DEGRADATION OF ORGANIC COMPOUNDS BY ACOUSTIC CAVITATION AND PULSED-POWER DISCHARGES

Thesis by

Ralf Höchemer

In Partial Fulfillment of the Requirements

for the Degree of

Doctor of Philosophy

California Institute of Technology

Pasadena, California

1996

(Submitted May 24, 1996)

Acknowledgments

I want to thank my advisor, Michael R. Hoffmann, for accepting me into his group and for giving me the once-in-a-lifetime opportunity to perform research in one of the best schools of the United States. Apart from the excellent education I received, it has been a dream come true to work and live in California for five years. To be able to view my home country from the outside has been an invaluable experience that will stay with me forever.

The last five years have been challenging ones. Everybody who went through Caltech knows that not every day feels like heaven when you are tackling tough research problems or struggle with homework assignments. I am indebted to many people—collegues and friends—for making my Caltech experience as pleasant and exciting as possible under the given "boundary conditions".

On my first day in Pasadena, Simo Pehkonen gave me a warm welcome and introduced me to much of the laboratory equipment in a matter of five minutes. In fact, I believe I was still carrying my two suitcases and carry-on bag when he explained to me the functions of his beloved pH-meter. His unique sense of humor was cause for many good laughs and a welcome break in the serious business of research.

It is not necessarily the easiest endeavour to form a powerful team out of four very different people with different backgrounds. For successfully pulling off a tough project I want to thank the pulsed-power gang, Axel Kratel, Patrick Lang, and Dean Willberg. None off the EHD experiments would have been possible without the help and determination of Dean Willberg.

Hartmut Herrmann sacrificed his summer vacation to help with the determination of the EHD spectrum. His practical experience and theoretical insight were invaluable. Apart from work, our adventures in the bars of Old Town Pasadena shall remain among

the more fun experiences of my time at Caltech. If I could only remember just how much fun we had. (I certainly can't recall how we got home.)

I want to thank Inez Hua for being a great co-worker and one of my closet friends at Caltech. Whenever I had something on my mind I wanted to discuss, be it private or professional, Inez was there to listen. Inez and I worked closely together, which made the work days much more fun than they would have been otherwise. The quality of a work place is defined largely by the relationships between colleagues. To me, Inez was a wonderful colleague, whose company I will miss both in the laboratory and during lunch at the Athenaeum, Subways or "Taco-Hell".

My other colleagues in the Hoffmann group, Won-Yong Choi, Anne Johannsen, Janet Kesselman, Scot Martin, Nicola Peill, Ron Siefert, and Linda Weavers have always been helpful whenever I was looking for lab equipment or needed someone to bounce ideas off. Tom Lloyd always found time for a serious discussion or to have a few good laughs.

Thank you to Peter Green who is always willing to answer questions about the vast collection of analytical equipment.

Nobody would finish a Ph.D. thesis without the generous help of secretaries, librarians, the crews in the machine and glass shops, and other supporting staff. Here I want to thank Linda Scott, Carmen Lopez, Fran Matzen, Shirley Anderson, Rayma Harrison, Susan Leising, Joe Fontana, Rich Eastvedt, Elena Escot, Rick Gerhart, Mike Gerfen, Glenn Wyne (CCO), Hai Duc Vu, Alan Goudy (GLACIT), and Lothar Kirk (JPL). Thank you all for your invaluable assistance and good cheer day in day out.

Finally I wish to thank my friends at MJ-House: Zeus, Kaiser (new and old), Sheighphough, Dream, Jewel, Raj, and Matt. You guys were a lot of fun!

To Jens, for being a great brother and a true friend.

To Sayuri, my partner in many things past and future.

To Ruth and Heinz, who gave me more strength than they can know.

Abstract

The exposure of organic chemical compounds to acoustically induced cavitation under various conditions in aqueous solution is studied. Emphasis is given to the degradation of undesired chemical compounds present at relatively low concentration.

The hydrolysis rate of p-nitrophenylacetate is enhanced in sonicated solution when compared to the reaction under ambient conditions. This rate enhancement is ascribed to the transient existence of supercritical water in sonicated aqueous solutions.

The degradation rate of 2,4,6-trinitrotoluene is shown to depend on the ultrasonic frequency and the nature of the background gas. Degradation products include nitrite, nitrate, carbon dioxide, and short-chain organic acids.

Ultrasonic irradiation of a mixture of nitro- and aminoaromatic compounds leads to competition of the substrates for reactive sites and rates of degradation scale with the electron density of the aromatic ring.

The near-field parallel-plate acoustical processor is investigated as an example of large-scale treatment a of dilute waste stream. Energy density and intensity have a pronounced effect on the overall degradation rate of p-nitrophenol. Most notably, the maximum reaction rate is found to be at an energy intensity of 1.2 W cm^{-2}. Higher intensities decrease the rate due to decoupling of the reaction mixture from the vibrating surface.

Electrical underwater discharges at relatively low electrical field strengths exhibit two distinct phases: the pre-breakdown, or initiation period, and the actual discharge itself. The length of the initiation period, the slope of the voltage transient, and the absolute and relative energy losses during initiation are investigated as a function of the electrical conductivity and temperature under various circuit parameters.

The temperature of the plasma-arc occurring during an electrical underwater discharge is estimated to be (9000 ± 300) K.

Table of Contents

List of Figures

Chapter VI

Chapter VIII

List of Tables

- Chapter I -

Thesis Overview

This thesis summarizes research performed in two separate areas: sonochemistry and pulsed-power discharges. Both projects have the common goal to more deeply understand and optimize the degradation of undesired chemical compounds using these advanced oxidation technologies. In Chapter II a brief introduction into both main areas is given. The introduction emphasizes the chemical effects of both acoustical cavitation in aqueous solution and high-voltage, high-current electrical underwater discharges.

Chapters III - VI discuss the chemical effects induced by ultrasound in both small- and larger-scale reactor systems. Physical measurements of underwater electrical discharges are presented in Chapters VII and VIII.

The hydrolysis of p-nitrophenylacetate (p-NPA) is subject of Chapter III. The reaction is studied in both sonicated and unsonicated aqueous solution. A rate enhancement in the sonicated system of two orders of magnitude is reported over the pH range of 3 - 8 when compared to the unsonicated solution. An argument is made for the transient existence of a supercritical water phase at the site of cavitational collapse and a simple mathematical model is presented for an estimation of the amount of supercritical water present in water exposed to high-power ultrasound.

In Chapter IV the ultrasonic degradation of 2,4,6-trinitrotoluene to nitrite, nitrate, carbon dioxide and short-chain organic acids (i.e., acetate, formate, glycolate, and oxalate) under different ultrasonic frequencies is reported. The observed first-order rate constants vary over a factor of 3 depending on the dissolved gasses and the ultrasound frequency. At 20 kHz, $k_{obs} = 1.67 \times 10^{-5}\ s^{-1}$ with O_2, $k_{obs} = 4.50 \times 10^{-5}\ s^{-1}$ with Ar, and $k_{obs} = 5.50 \times 10^{-5}\ s^{-1}$ with a O_2/O_3 (99/1 vol-%) mixture as cavitating background gases. The observed rate constants for 500 kHz are $k_{obs} = 2.00 \times 10^{-5}\ s^{-1}$ (O_2), $k_{obs} = 7.17 \times 10^{-5}\ s^{-1}$ (Ar), and $k_{obs} = 8.50 \times 10^{-5}\ s^{-1}$ (O_2/O_3). Ultrasonic irradiation at 500 kHz yielded consistently higher reaction rates than 20 kHz irradiation for all background gases.

Simultaneous irradiation with orthogonally-positioned 20 kHz and 500 kHz sound sources leads to a negative interference manifested in a diminished reaction rate compared to sonication with 500 kHz sound alone.

Research in the field of sonochemical degradation of hazardous chemical compounds is almost entirely focused on one compound at a time. However, real-life waste streams contain a mixture of various chemicals that have to be remediated simultaneously. In Chapter V a report on the sonochemical degradation of a mixture of 2,4,6-trinitrotoluene (TNT), 2,6-dinitrotoluene (DNT), 1,3,5-trinitrobenzene (TNB), 1,3-dinitroenzene (DNB), and m-nitroaniline (m-NA) at 500 kHz is presented. The compounds in the reaction mixture compete for the reactive sites at the bubble/solution interface. Their respective observed degradation rates appear to be proportional to the electron density of the aromatic ring: $k_{m\text{-}NA} > k_{DNT} > k_{TNT} > k_{DNB} > k_{TNB}$.

In addition, Chapter V includes a report on the degradation of m-NA in a near-field acoustical processor (NAP) at different concentrations.

The NAP is discussed in detail in Chapter VI. p-Nitrophenol (p-NP) has been chosen as a model compound to investigate its apparent degradation rate as a function of ultrasonic energy density (i. e., the ratio of introduced energy to irradiated volume) as well as energy intensity (i. e., ratio of energy to active area). The degradation rate is proportional to the energy density and exhibits a maximum at an energy-intensity of 1.2 W cm^{-2}. A mathematical model for the continous-flow loop reactor is presented. It allows for the extraction of k from the observed rate constant, k_{obs}.

The remaining two chapters summarize physical measurements performed with the electrohydraulic discharge (EHD) reactor. We believe direct photolysis plays a major role in the degradation of chemical compounds. It is therefore desirable to know the spectral distribution of the electromagnetic radiation during electrical discharges. In Chapter VII of this thesis the work towards the determination of the spectrum of the emitted light and an estimate of the plasma temperature is presented. Chapter VII

establishes that the electromagnetic radiation generated upon an underwater electrical discharge resembles radiation from a black-body source. A first-order estimation of the average plasma-arc temperature is given. The spectrum of the light flash has been measured using an optical multi-channel analyzer. Information about the generated radiation is essential to the further development of the EHD technology as a remediation technology, since its main chemical effects are caused by the emission of intense UV-light.

A main inefficiency of the EHD process is the energy leakage prior to electrical breakdown of the reaction solution. An extensive experimental database on the influence of various experimental parameters on the pre-initiation energy-loss is summarized in Chapter VIII. The investigated parameters include the solution's temperature and electrical condictivity, the electrode gap width, initially stored energy and the insulation of the reactor chamber from the hot electrode. Short electrode gaps and high initial energies minimize relative energy losses proir to breakdown. It is advantageous to perform discharges with an insulating liner installed and at elevated solution temperature in order to maximize energy utilization.

- Chapter II -

Introduction

Part of the text of this chapter appears in [Hoffmann, M. R., Hua, I., Höchemer, Willberg, D., Lang, P., Kratel, A., in *Chemistry Under Extreme or Non-classical Conditions,* Rudi van Eldik and Colin D. Hubbards, Editors, Springer Verlag, 1996.]

Ultrasonic Irradiation of Water and the Chemical Effects of Acoustical Cavitation

Background

The introduction of high power ultrasound (i. e., sound energy with frequencies in the range 15 kHz to 1 MHz) into liquid reaction mixtures is known to cause a variety of chemical transformations [1-47]. The chemical effects of ultrasound on chemical reactions were first reported by Richards and Loomis [48] in 1927. This early report was followed by a detailed investigation of the catalytic effect of ultrasonic irradiation on the autoxidation of iodide ion [49]. Since then, the application of ultrasound as a catalyst in chemical synthesis has become an important field of research.

In recent years, due to the growing need to eliminate undesirable chemical compounds, the utilization of high energy ultrasound for hazardous waste treatment has been explored with great interest [31,50-63].

Physical Principles

Ultrasonic irradiation of liquid reaction mixtures induces electrohydraulic cavitation, which is a process during which the radii of preexisting gas cavities in the liquid oscillate in a periodically changing pressure field created by the ultrasonic waves. These oscillations eventually become unstable, forcing the violent implosion of the gas bubbles. The rapid implosion of a gaseous cavity is accompanied by adiabatic heating of the vapor phase of the bubble, yielding localized and transient high temperatures and pressures. Temperatures on the order of 4200 K and pressures of 975 bar have been estimated [7]. Noltingk and Neppiras [64,65] estimate even higher temperature and pressure values that range up to 10,000 K and 10,000 bar. Experimental values of P = 313 atm and T = 3360 K have been reported [66] for aqueous systems, while temperatures in excess of 5000 K have been reported [16,67] for cavitation in organic

and polymeric liquids. Recent experimental results on the phenomenon of sonoluminescence [67-84] suggest that even more extreme temperatures and pressures are obtained during cavitational bubble collapse [85]. Thus, the apparent chemical effects in liquid reaction media are either direct or indirect consequences of these extreme conditions.

In a recent study, Riesz and co-workers [86] used the semiclassical model of the temperature dependence of the kinetic isotope effect for $H^{\cdot}$ and $D^{\cdot}$ atom formation to estimate the effective temperature of the hot cavitation regions in which $H^{\cdot}$ and $D^{\cdot}$ atoms are formed by ultrasound-induced pyrolysis of water molecules. The $H^{\cdot}$ and $D^{\cdot}$ atoms were formed in argon-saturated H_2O and D_2O mixtures (1:1) exposed to 50 kHz ultrasound and were detected by spin trapping with nitrone spin traps detected by and quantified by EPR. From these results, they estimated average cavitational collapse temperatures in the range of 2000 to 4000 K.

Equations describing the inception and dynamics of a single cavitation bubble have been developed [64,65,87,88]. Based on approximate solutions to the Rayleigh-Plesset equation, Noltingk and Neppras [64,65] gave the following equation to predict the temperature at the center of a collapsed cavitation bubble:

$$T_{max} = T_o \left\{ \frac{P_m (K-1)}{P} \right\} = T_o \left(\frac{R_o}{R_{min}} \right)^{3(K-1)} \qquad (1)$$

where T_O = temperature of the bulk solution, $K = C_p/C_v$ = polytropic index of the cavity medium, P = pressure in the bubble at its maximum size, P_m = pressure in the bubble at the moment of transient collapse. Thus, the relative temperature of bubble collapse can be adjusted by saturating the solution with gases characterized by substantially different specific heats, thermal conductivities, and solubilities. From eq. 1 we see that an important factor controlling the collapse temperature is the polytropic constant, K, of the

saturating gas. The value of K is associated with the amount of heat released from the gas inside the bubble during compression. As K increases, the heat released upon bubble collapse also increases. Additional physicochemical properties that may influence the temperature attained during bubble collapse include thermal conductivity (of both the liquid and gas), l, and gas solubility. A low thermal conductivity favors high collapse temperatures because the heat of collapse will dissipate less quickly from the cavitation site. Highly soluble gases should result in the formation of a larger number of cavitation nuclei and more extensive bubble collapse since gases with higher solubilities are more readily forced back into the aqueous phase. Thus, a gas with both a low thermal conductivity and high water solubility should yield the highest temperature upon cavitational bubble collapse. Based on known physical properties, krypton should reach the highest temperatures upon cavitational bubble collapse in aqueous solution. A list of background gases and their physicochemical properties is given in Table 1 of Chapter III.

Even though the basic physical and chemical consequences of cavitation are fairly-well understood, many fundamental questions about the cavitation site in aqueous solution remain unanswered. In particular, the dynamic temperature and pressure changes at the bubble interface and their effects on chemical reactions need further exploration. Since this region is likely to have transient temperatures and pressures in excess of 647 K and 221 bar for periods of microseconds to milliseconds, we [89] have proposed that supercritical water (SCW) provides an additional phase for chemical reactions during ultrasonic irradiation in water. Supercritical water exists above the critical temperature, T_c, of 647 K and the critical pressure, P_c, of 221 bar and has physical characteristics intermediate between those of a gas and a liquid [89,90] . The physicochemical properties of water such as viscosity, ion-activity product, density, and heat capacity change dramatically in the supercritical region. These changes favor substantial increases for rates of most chemical reactions. SCW has been used in industrial applications such

as extraction [91], enhanced hydrolysis [92,93] and for the oxidation of hydrocarbons [94] and phenols [95,96].

The transient temperatures and pressures within a collapsing cavitation bubble clearly exceed the critical point of water for some finite period of time. Based on previously estimated temperatures within a collapsed bubble and a smaller layer of surrounding liquid, one can describe the spatial and temporal temperature distribution around a bubble just after its collapse (see Chapter 3).

Chemical Consequences of Extreme Transient Conditions

Two distinct sites for chemical reaction exist during a single cavitation event [42]. They are the gas-phase in the center of a collapsing cavitation bubble and a thin shell of superheated liquid surrounding the vapor phase. The volume of the gaseous region is estimated to be larger than that of the thin liquid shell by a factor of $\approx 2\times10^4$ [97,98].

During cavitational-bubble collapse, which occurs within 100 ns, H_2O undergoes thermal dissociation within the vapor phase to give hydroxy radical and hydrogen atoms as follows:

$$H_2O \xrightarrow{\Delta} H^{\cdot} + {}^{\cdot}OH \qquad (2)$$

The concentration of $^{\bullet}OH$ at a bubble interface in water has been estimated to be 4×10^{-3} M [44] . Many of the chemical effects of ultrasonically induced cavitation have been attributed to the secondary effects of $^{\cdot}OH$ and $^{\cdot}H$ production [55,56,58,87,99-104].

Based on work in our laboratory [89], we believe that sonochemical reactions in water are characterized by the simultaneous occurrence of supercritical water reactions, direct pyrolyses and radical reactions especially at high solute concentrations. Volatile solutes such as carbon tetrachloride [105] and hydrogen sulfide [53] will undergo direct

pyrolysis reactions within the gas phase of the collapsing bubbles or within the hot interfacial region as shown below:

$$CCl_4 \xrightarrow{\Delta} CCl_3 + Cl^{\cdot} \quad (3)$$

$$CCl_3 \xrightarrow{\Delta} :CCl_2 + Cl^{\cdot} \quad (4)$$

$$H_2S \xrightarrow{\Delta} HS^{\cdot} + H^{\cdot} \quad (5)$$

while low-volatility solutes such as thiophosphoric acid esters [48] and phenylate esters [89] can react in transient supercritical phases generated within a collapsing bubble as follows:

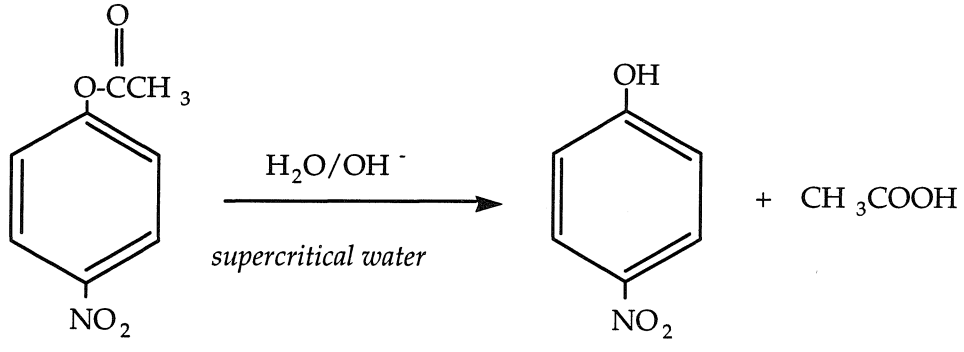

(6)

In the case of ester hydrolysis, reaction rates are accelerated 10^2 to 10^4 times the corresponding rates under controlled kinetic conditions (i.e., same pH, ionic strength, and controlled overall temperature). This effect can best be illustrated by the catalytic effect of ultrasonic irradiation on rate of hydrolysis of parathion in water at pH 7.

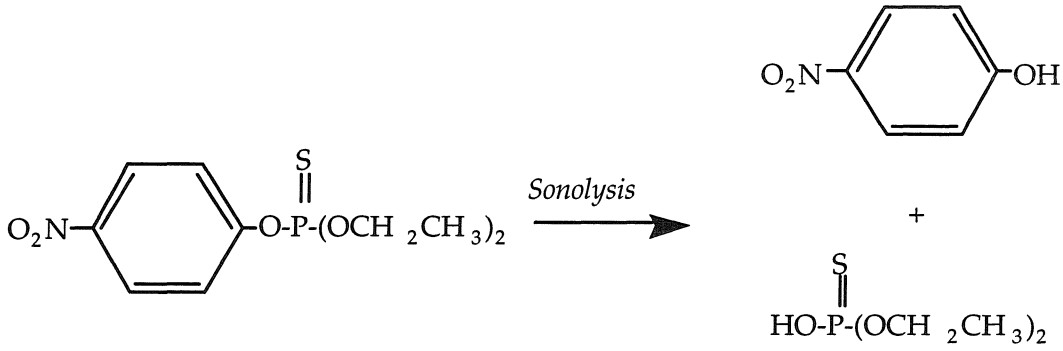

(7)

The half-life for parathion hydrolysis at pH 7.4, in the absence of ultrasound at 25 ^{o}C, is 108 days. However, in the presence of ultrasound the half-life is reduced to 20 minutes [52].

Pyrolysis (i.e., combustion) and supercritical water reactions in the interfacial region are predominant at high solute concentrations, while at low solute concentrations free radical reactions are likely to predominate. Depending on its physical properties, a molecule can simultaneously or sequentially react in both the gas and interfacial liquid regions.

In the specific case of hydrogen sulfide gas dissolved in water, both pyrolysis in the vapor phase of the collapsing bubbles and hydroxyl radical attack in the quasi liquid interfacial region occur simultaneously as follows:

$$H_2S \xrightarrow{\Delta} HS^{\cdot} + H^{\cdot} \qquad (8)$$

$$H_2S + {}^{\cdot}OH \longrightarrow HS^{\cdot} + H_2O \qquad (9)$$

The kinetics of reactions occurring during ultrasonic irradiation follow classical rate expressions. For example, Kotronarou *et al.* [53] determined that the experimentally-determined rate law for the autoxidation of H_2S in the presence of ultrasonic irradiation consisted of two terms, a first-order term, representing degradation initiated by the

pyrolytic decomposition of hydrogen sulfide in the hot vapor phase and a zero-order term representing the combined effects of hydroxyl radical attack in both the hot vapor phase (H_2S) and in the hot interfacial liquid domain (HS^-). The rate law expressed in terms of total sulfide ($[H_2S]_T = [H_2S] + [HS^-]$) where $pK_{a1} = 7.0$) is

$$-\frac{d[H_2S]_T}{dt} = k_o + k_1[H_2S]_T \qquad (10)$$

The integrated solution to eq. 20 is given below where k_o is the rate constant for hydroxyl radical attack, k_1 is the rate constant for pyrolysis, $[H_2S]_{T,t}$ is the concentration of total sulfide at time = t and $[H_2S]_{T,0}$ is the concentration of total sulfide at t = 0.

$$[H_2S]_{T,t} = \left([H_2S]_{T,o} + \frac{k_o}{k_1}\right)e^{-k_1 t} + \frac{k_o}{k_1} \qquad (11)$$

In addition to an apparent traditional kinetic dependence on concentration, pH, and ionic strength, a linear relationship between the applied power at a fixed frequency and the observed rate of loss of sulfide over the range from 10 to 120 W (10 to 120 W cm^{-2}) was reported [53].

Kotronarou and Hoffmann [106] have presented a detailed kinetic model for the sonolytic oxidation of HS^- by $^{\cdot}OH$ at high pH (in a pH domain where pyrolytic decomposition is negligible). The oxidation of S(-II) is initiated by reaction with hydroxyl radical but it is further propagated by a free-radical chain sequence involving O_2. Their mechanism can adequately model the observed oxidation of S(-II) in air-saturated aqueous solutions sonicated at 20 kHz and 75 W cm^{-2} at pH = 10, assuming a continuous and uniform hydroxyl radical input into solution from the imploding cavitation bubbles. These results suggest that the use of simplified approaches for modeling the liquid-phase sonochemistry of a well-mixed solution may be justified when

·OH radical reactions predominate. For the probe-type reactor utilized in their study, a uniform release rate of hydroxyl radical into the bulk solution was observed (3.5 μM min^{-1}) with a corresponding steady-state concentration of approx. 0.1 μM.

The most obvious evidence for the role of pyrolysis during ultrasonically-induced transient cavitation is the production of NO, NO_2, NO_2^-, NO_3^- and H_2O_2 during the sonolysis of water in the presence of N_2 and O_2 alone as background gases. The following mechanism [51], in which the first steps are analogous to those occurring during high-temperature combustion, appears to be operative:

$$O_2 \xrightarrow{\Delta} 2\,O^{\cdot} \tag{12}$$

$$N_2 + O^{\cdot} \xrightarrow{\Delta} NO + N^{\cdot} \tag{13}$$

$$N^{\cdot} + O_2 \rightarrow NO_2 \tag{14}$$

$$NO + O^{\cdot} \longrightarrow NO_2 \tag{15}$$

$$NO_2 + O^{\cdot} \longrightarrow NO_3 \tag{16}$$

$$NO_2 + NO_3 \longrightarrow N_2O_5 \tag{17}$$

$$N_2O_5 + H_2O \longrightarrow 2\,HNO_3 \tag{18}$$

$$NO + HO^{\cdot} \longrightarrow HONO \tag{19}$$

$$2\,NO_{2\,(aq)} + H_2O \longrightarrow HNO_3 + HNO_2 \tag{20}$$

Comparative rate thermometry, as described in Chapter III, employing p-nitrophenol (p-NP) as a probe molecule can be used in order to estimate the average effective temperatures achieved during bubble collapse. P-NP is a suitable probe molecule since its kinetics and mechanism of degradation are well understood [50,89].

The relative temperature of bubble collapse can be adjusted by saturating the solution with gases characterized by substantially different specific heats, thermal conductivities, and solubilities. As mentioned above, an important factor controlling bubble collapse temperature is the polytropic constant, K, of the saturating gas. From a knowledge of K we can estimate the maximum temperature obtained during bubble collapse from eq. 1.

Pulsed-Plasma Discharges in Water

Background

Pulsed-power plasma discharges into water are an electrohydraulic phenomena characterized by a periodic rapid release of accumulated electrical energy across a submerged electrode gap (1 -2 cm). The power source is a bank of charged capacitors capable of delivering a high voltage, high amperage electrical current to the submerged electrodes at a moderate frequency. Each electrical discharge produces a short (20 -50 μs) burst of electrical energy at a high power density within the electrode gap (i.e., 25 kJ). This highly ionized and pressurized plasma has the ability to transfer energy to wastewater via dissociation, excitation, and ionization (e.g., H_2O^+, $\bar{e}_{aq}$, $^{\cdot}OH$, $H^{\cdot}$, etc.) with a corresponding increase in temperature. The rapidly-expanding plasma produces a very high pressure shock wave (> 14,000 bar). If the propagating shock wave is reflected back from either a free surface or from a material with a different acoustic impedance, intense cavitation occurs with the associated chemical changes as described above for the

chemical effects of ultrasound. Thus, a pulsed-power discharge in water provides a unique method for promoting pyrolytic, ·OH radical, aquated electron and UV-promoted reactions. Additional reaction pathways result from the direct reactions of the rapidly expanding plasma gases with the chemical substrates of interest and from indirect production of ·OH radicals due to the release of soft X-rays and high energy UV radiation from the energized plasma.

The pulsed-plasma discharge processes or electrohydraulic discharge process (EHD) is a non-thermal technique to inject energy directly into an aqueous solution through a plasma channel formed by a high-current/high-voltage electrical discharge between two submersed electrodes [107-110]. A typical EHD system as shown in Fig. 1 consists of two major components, which are the pulsed-power electrical discharge circuit and the reaction chamber. Electrical energy is stored in a large capacitance (135 mF) pulsed-power circuit. This energy is released as a pulsed electrical discharge using fast ignitron switches. Each pulse can have energies ranging from 5 to 25 kJ with a duration of 20-100 ms. Peak powers are in the megawatt to gigawatt range. The reactor vessel (Fig. 1) contains an electrode assembly, and the aqueous solution to be treated. The reactor is designed to withstand intense shockwaves generated by the electrohydraulic discharges and to accommodate the high electrical currents and voltages required by the process.

The plasma channel formed during an electrohydraulic discharge reaches temperatures of 20,000-50,000 K [110] and thus functions as a blackbody radiation source with a maximum emittance in the vacuum ultraviolet (VUV) region of the spectrum. The VUV emitted from the hot plasma is absorbed by the water layer immediately surrounding the plasma channel [111], although UV light with $\lambda > 185$ nm penetrates into the bulk aqueous solution. During the formation of the plasma channel (1 -2 ms) an intense 5 to 20 kbar shockwave is generated, due to the rapidly expanding plasma [108]. The resulting shockwave can induce pyrolytic and free radical reactions

indirectly via cavitation as described above. As the plasma channel cools over 1 - 3 ms, thermal energy is transferred to the surrounding water resulting in the formation of a steam bubble [112]. Within a steam bubble, the temperatures and pressures are high enough for the formation of transient supercritical water [113].

Physical Principles

The underwater discharge can be separated into three distinct temporal phases. When the switch of the LRC circuit is closed with the subsequent buildup of a voltage across the underwater electrodes, a discharge initiation phase takes place during which a plasma channel is formed. During a second "energy transfer phase", the bulk of the energy stored in the capacitor is dissipated into the plasma channel. The plasma channel in turn does work against the surrounding fluid as it expands, and in the process, it generates a shockwave. Some of the energy discharged to the plasma channel is released as blackbody radiation with channel temperatures > 10,000 K. During the energy transfer phase, energy losses due to heat conduction are negligible, since the initial-event time scales are too fast for heat transfer to occur. The discharge enters its final phase once heat transfer is initiated and the plasma channel is converted into a spherical steam bubble, which behaves as a cavitating bubble, until all of the remaining energy is dissipated via acoustic radiation and viscous friction.

The general reactor system illustrated in Fig. 1 can be treated as a high-capacitance, low-inductance LRC circuit as described in Chapter VIII.

The energy transferred from the capacitor to the plasma channel is partitioned into three processes; they are the mechanical work on the surrounding fluid as the plasma channel expands, the internal energy of the plasma itself, and electromagnetic radiation as the channel heats up. That energy process is described by the following continuity equation:

$$\frac{dE_d(t)}{dt} = \frac{d}{dt}\left(W(t)V(t)\right) + P(t)\frac{dV(t)}{dt} + (1-f)\sigma_B T(t)^4 S \qquad (21)$$

The term on the left side of eq. 35 represents the rate of energy transferred to the plasma channel from the capacitor bank. The first term on the right describes the energy transferred to change the internal energy state of the plasma channel where W(t) denotes the internal energy density of the plasma, V(t) the volume and S(t) the surface area of the plasma channel. The second term on the right represents the work done by the channel on the surrounding fluid where P(t) is the pressure. The last term on the right represents the radiative transfer where σ_B is the Stephan-Boltzmann constant. Some of the black-body radiation fails to escape the plasma channel and this is factored into account by the term (1-f) where the fraction of the spectrum denoted by f represents radiation energy which is absorbed at the boundaries to ionize particles. The energy lost to these particles is recovered since these particles are inducted into the plasma channel.

Chemical Consequences of Transient Plasma Formation

In the EHD process, chemical degradation occurs within the plasma channel directly due to pyrolysis and free radical reactions. However, the small volume of the plasma channel (1 - 3 mL) limits the amount of solution that can be exposed directly to high-temperature processes in a large chamber reactor. On the other hand, experiments with exploding wires have shown that electrohydraulic discharges induce extreme electromagnetic and mechanical conditions in the bulk solutions outside of the plasma channel region [112]. These experiments have established that there are three primary physical processes (i.e., ultraviolet (UV) photolysis, electrohydraulic cavitation, and supercritical water oxidation) with the potential to induce significant oxidative chemistry in the bulk solution.

Since intense black-body radiation is emitted directly from the plasma channel into the secondary reaction volume of the reactor, we expect that direct photolysis will play a very important role in compound degradation. In the case of 0.5 L solution of 3,4-chloroaniline exposed to a series of 100 pulses in which each pulse had a total energy of 5.0 kJ, 74% of 3,4-dichloroaniline was degraded primarily by direct photolysis in 2 msec of power utilization according to the following stoichiometry [114]:

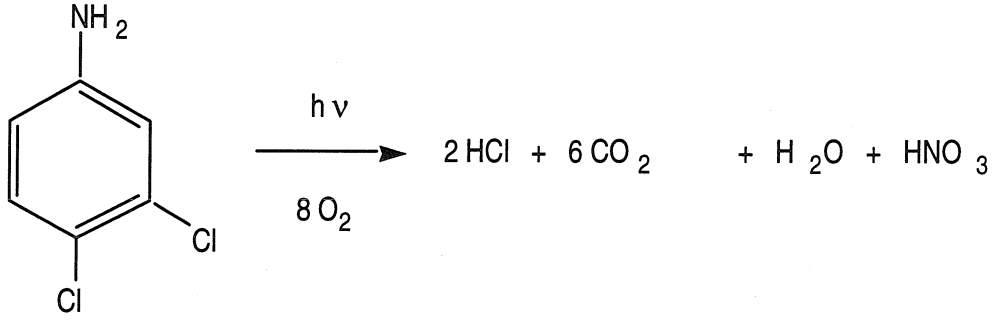

(22)

Direct photolysis reactions are quantified by the following rate equation:

$$-\frac{dC}{dt} = \Phi(\lambda)I_0(\lambda)\left(1 - \exp(-2.3\varepsilon lC)\right) \qquad (23)$$

where C is the concentration of the chromophoric reactant, $\Phi(\lambda)$ is the photolysis quantum yield, I_0 is the intensity of the UV source, ε is the extinction coefficient of the primary chromophore, and l is the pathlength of radiation. When $I_0(\lambda,t)$ is constant and in the case of long pathlengths, high concentrations, and/or large extinction coefficients eq. 23 reduces to the following zero-order expression,

$$-\frac{dC}{dt} = \Phi(\lambda)I_0(\lambda) \qquad (24)$$

Since the UV source in the EHD reactor is pulsed, $I_0(\lambda,t)$ varies significantly over the lifetime of the pulse. However, the total energy per discharge is a well defined quantity. Thus, one can assume that the total UV flux per discharge is relatively constant as long as the discharge conditions remain constant. Under these conditions t is replaced with N to obtain,

$$-\frac{dC}{dN} = \Phi(\lambda)Q(\lambda)\left(1 - \exp(-2.3\varepsilon lC)\right) \tag{25}$$

which for large values of εlC gives,

$$-\frac{dC}{dN} = \Phi(\lambda)Q(\lambda) = k_o \tag{26}$$

where $Q(\lambda)$ is the radiant energy per discharge. Since N is dimensionless, the rate constants will have non-conventional units. A zero-order rate constant, k_0, will have dimensions of μM, and a first-order rate constant, k_1, will be dimensionless. N-based kinetic constants can be readily transformed into intrinsic rate constants based on time.

If photochemical degradation is the only oxidative mechanism operative in the reactor, the process should exhibit zero-order behavior at sufficiently high substrate concentrations. However, under high concentrations strict zero-order behavior breaks down and the kinetics switch to apparent first-order behavior. To account for this transition, we consider the EHD system to be a two compartment reactor. The first reactor compartment is the bulk solution which is exposed to the extended effects (UV and shockwave radiation) generated by the EHD discharge. Discounting any cavitational effects generated by the shockwave, degradation in this region is due to purely photochemical effects and therefore can be treated as a zero-order process as discussed above.

The second reactor compartment is the small volume contained within and immediately surrounding the plasma channel. The solution in this region is exposed to the localized chemical effects. The substrate is oxidized within the high temperature plasma channel and by hydroxyl radicals generated by the VUV photolysis of water. Since the conditions in and around the plasma channel are so extreme, it is assumed that any substrate within this region will be completely oxidized. These combined processes will appear to be first-order in kinetic behavior, when they are considered over the scale of the entire reactor. If the solution in the reactor chamber is subsequently well-mixed after one discharge the measured concentration of the substrate will be:

$$C = \left(\frac{V_T - V_R}{V_T}\right) C_i - k_o \tag{27}$$

Where C_i is the initial concentration, V_T is the total solution volume, V_R is the plasma channel volume, and k_0 is the zero-order rate constant due to direct photolysis. After N discharges, it can be shown that the measured concentration will be:

$$C = a^N C_i - k_o \sum_{n=0}^{N-1} a^N = a^N C_i - k_o \left(\frac{1 - a^N}{1 - a}\right) \tag{28}$$

where,

$$a = \left(\frac{V_T - V_R}{V_T}\right) \tag{29}$$

Since N can be treated as a continuous variable for the kinetics analysis, the derivative of eq. 28 with respect to N yields:

$$\frac{dC}{dN} = e^{\ln(a)N}C_i + k_o\frac{\ln(a)e^{\ln(a)N}}{1 - a} \qquad (30)$$

Since $a \approx 1$ and $N < 40$, we can assume that $\ln(a) = (a-1)$ and $\exp(\ln(a)N) = (1 + \ln(a)N)$ to obtain

$$\frac{dC}{dN} = \ln(a)C_i - k_o - k_o\ln(a)N + \ln^2(a)C_i \qquad (31)$$

The last two terms of eq. 31 can be neglected since they are much smaller in magnitude than the first two terms and are much smaller than the experimental error. Therefore, the final differential equation that describes the initial rate of degradation in an EHD reactor can be described as the sum of zero and first-order terms as follows:

$$-\frac{dC}{dN} = k_1C_i + k_o = k_A \qquad (32)$$

The observed first-order rate constant will be $k_1 = -\ln(a)$. The value of k_1 is a function of the ratio of V_R to V_T. In our reactor $V_R << V_T$, and therefore k_1 has a small ($\approx 9 \times 10^{-4}$ discharge^{-1}) but significant effect.

References

(1) Berlan, J.; Mason, T. J. *Ultrasonics* **1992**, *30*, 203-212.

(2) Lindley, J.; Mason, T. J. *Chem. Soc. Rev.* **1987**, *16*, 275-311.

(3) Lindley, J.; Mason, T. J.; Lorimer, J. P. *Ultrasonics* **1987**, *25*, 45-48.

(4) Lorimer, J. P.; Mason, T. J. *Chem. Soc. Rev.* **1987**, *16*, 239-274.

(5) Lorimer, J. P.; Mason, T. J.; Fiddy, K. *Ultrasonics* **1991**, *29*, 338-343.

(6) Mason, T. J. *Chem. Brit.* **1986**, *22*, 661-661.

(7) Mason, T.; Lorimer, J. *Sonochemistry: Theory, Applications, and Uses of Ultrasound in Chemistry*; Ellis Norwood, Ltd.: New York, 1988.

(8) Mason, T. J.; Lorimer, J. P. *Endeavour* **1989**, *13*, 123-128.

(9) Mason, T. J.; Lorimer, J. P.; Paniwnyk, L.; Harris, A. R.; Wright, P. W. *Syn. Comm.* **1990**, *20*, 3411-3420.

(10) *Advances in Sonochemistry*; Mason, T. J., Ed.; JAI Press Ltd.: London, 1990; Vol. 1.

(11) Mason, T. J. *Ultrasonics* **1992**, *30*, 192-196.

(12) Mason, T. J.; Lorimer, J. P.; Bates, D. M. *Ultrasonics* **1992**, *30*, 40-42.

(13) Mason, T. J. *Chem. Ind.* **1993**, 47-50.

(14) Walton, D. J.; Chyla, A.; Lorimer, J. P.; Mason, T. J. *Syn. Commun.* **1990**, *20*, 1843-1852.

(15) Walton, D. J.; Phull, S. S.; Bates, D. M.; Lorimer, J. P.; Mason, T. J. *Ultrasonics* **1992**, *30*, 186-191.

(16) Flint, E. B.; Suslick, K. S. *J. Am. Chem. Soc.* **1989**, *111*, 6987-6992.

(17) Suslick, K. S.; Schubert, P. F.; Wang, H. H.; Goodale, J. W. in *Inorganic Chemistry: Toward the 21st Century*, Chisholm, M. A., ed., Amer. Chem. Soc., Washington, DC, **1983**, p. 550.

(18) Suslick, K. S.; Grinstaff, M. W.; Kolbeck, K. J.; Wong, M. *Ultrasonics Sonochemistry* **1994**, 1, S65.

(19) Suslick, K. S., Fang, M. M.; Hyeon, T.; Cichowlas, A. A. in *Molecularly Designed Nanostructures, Gonsalves*, K. E.; Chow, G. M.; Xiao, T. O.; Cammarata, R. C., eds. Materials Research Society: Pittsburgh, **1994**, pp. 443-448.

(20) Suslick, K. S.; Schubert, P. F. *J. Am. Chem. Soc.* **1983**, *105*, 6042-6044.

(21) Suslick, K. S.; Gawienowski, J. J.; Schubert, P. F.; Wang, H. H. *Journal Of Physical Chemistry* **1983**, *87*, 2299-2301.

(22) Suslick, K. S.; Goodale, J. W.; Schubert, P. F.; Wang, H. H. *J. Am. Chem. Soc.* **1983**, *105*, 5781-5785.

(23) Suslick, K. S.; Schubert, P. F.; Wang, H. H.; Goodale, J. W. *Acs Symposium Series* **1983**, *211*, 550-550.

(24) Suslick, K. S.; Johnson, R. E. *J. Am. Chem. Soc.* **1984**, *106*, 6856-6858.

(25) Suslick, K. S.; Hammerton, D. A. *Ultrasonics Intl.* **1985**, 231.

(26) Suslick, K. S.; Gawienowski, J. J.; Schubert, P. F.; Wang, H. H. *Ultrasonics* **1984**, *22*, 33-36.

(27) Suslick, K. S.; Cline, Jr., R. E.; Hammerton, D. A. *J. Am. Chem. Soc.* **1986** *108*, 5641.

(28) Suslick, K. S. *Modern Synthetic Methods* **1986**, *4*, 1-60.

(29) Suslick, K. S. *Adv. Organometallic Chem.* **1986**, *25*, 73-119.

(30) Suslick, K. S. *ACS Symp. Ser.* **1987**, *333*, 191-208.

(31) *Ultrasound: Its Chemical, Physical and Biological Effects*; Suslick, K. S., Ed.; VCH Publishers, Inc.: New York, 1988.

(32) Suslick, K. S.; Doktycz, S. J. *J. Am. Chem. Soc.* **1989**, *111*, 2342-2344.

(33) Suslick, K. S. *Science* **1990**, *247*, 1439-1445.

(34) Suslick, K. S.; Choe, S. B.; Cichowlas, A. A.; Grinstaff, M. W. *Nature* **1991**, *353*, 414-416.

(35) Grinstaff, M. W.; Cichowlas, A. A.; Choe, S. B.; Suslick, K. S. *Ultrasonics* **1992**, *30*, 168.

(36) Tuncay, A.; Dustman, J. A.; Fisher, G; Tuncay, C. I.; Suslick, K. S. *Tetrahedron Lett.* **1992**, *33*, 7647.

(37) Suslick, K. S.; Flint, E. B.; Grinstaff, M. W.; Kemper, K. A. *J. Phys. Chem.* 1993, **97**, 7216.

(38) Henglein, A.; Herburger, D.; Gutierrez, M. *J. Phys. Chem.* **1992**, *96*, 1126-1130.

(39) Buttner, J.; Gutierrez, M.; Henglein, A. *J. Phys. Chem.* **1991**, *95*, 1528-1530.

(40) Fischer, C. H.; Hart, E. J.; Henglein, A. *J. Phys. Chem.* **1986**, *90*, 3059-3060.

(41) Fischer, C. H.; Hart, E. J.; Henglein, A. *J. Phys. Chem.* **1986**, *90*, 222-224.

(42) Gutierrez, M.; Henglein, A.; Fischer, C.-H. *Int. J. Radiation Biol.* **1986**, *50*, 313-321.

(43) Gutierrez, M.; Henglein, A. *J. Phys. Chem.* **1990**, *94*, 3625-3628.

(44) Gutierrez, M.; Henglein, A.; Ibanez, F. *J. Phys. Chem.* **1991**, *95*, 6044-6047.

(45) Hart, E. J.; Henglein, A. *J. Phys. Chem.* **1987**, *91*, 3654-3656.

(46) Henglein, A. *Ultrasonics* **1987**, *25*, 6-16.

(47) Henglein, A.; Gutierrez, M. *J. Phys. Chem.* **1990**, *94*, 5169-5172.

(48) Richards, W. T.; Loomis, A. L. *J. Am. Chem. Soc.* **1927**, *49*, 3086-3100.

(49) Weissler, A. C.; Snyder, S. J. *J. Am. Chem. Soc.* **1950**, *72*, 1769-1775.

(50) Kotronarou, A.; Mills, G.; Hoffmann, M. R. *J. Phys. Chem.* **1991**, *95*, 3630-3638.

(51) Kotronarou, A. Thesis, California Institute of Technology, 1991.

(52) Kotronarou, A.; Mills, G.; Hoffmann, M. R. *Environ. Sci. Technol.* **1992**, *26*, 1460-1462.

(53) Kotronarou, A.; Mills, G.; Hoffmann, M. R. *Environ. Sci. Technol.* **1992**, *26*, 2420-2428.

(54) Hua, I.; Höchemer, R. H.; Hoffmann, M. R. *Environ. Sci. Technol.* **1995**, in press.

(55) Olson, T. M.; Barbier, P. F. *Water Res.* **1994**, *28*, 1383-1391.

(56) Petrier, C.; Lamy, M. F.; Francony, A.; Benahcene, A.; David, B.; Renaudin, V.; Gondrexon, N. *J. Phys. Chem.* **1994**, *98*, 10514-10520.

(57) Petrier, C.; Micolle, M.; Merlin, G.; Luche, J. L.; Reverdy, G. *Environ. Sci. Technol.* **1992**, *26*, 1639-1642.

(58) Serpone, N.; Terzian, R.; Hidaka, H.; Pelizzetti, E. *J. Phys. Chem.* **1994**, *98*, 2634-2640.

(59) Serpone, N.; Terzian, R.; Colarusso, P.; Minero, C.; Pelizzetti, E.; Hidaka, H. *Res. Chem. Intermed.* **1992**, *18*, 183-202.

(60) Wu, J. M.; Huang, H. S.; Livengood, C. D. *Environ. Prog.* **1992**, *11*, 195-201.

(61) Price, G.; Matthias, P.; Lenz, E. J. *Process Safety Environ. Protection: Trans. Instit. Chem. Eng. Part B.* **1994**, *72*, 27-31.

(62) Johnston, A. J.; Hocking, P. *ACS Sympos. Series* **1993**, *518*, 106-118.

(63) Cost, M.; Mills, G.; Glisson, P.; Lakin, J. *Chemosphere* **1993**, *27*, 1737-1743.

(64) Noltingk, B. E.; Nepprias, E. A. *Proc. Phys. Soc. B.* **1950**, *63B*, 674-685.

(65) Nepprias, E. A.; Noltingk, B. E. *Proc. Phys. Soc. B.* **1951**, *63B*, 1032-1038.

(66) Sehgal, C.; Steer, R. P.; Sutherland, R. G.; Verrall, R. E. *J. Phys. Chem.* **1979**, *70*, 2242-2248.

(67) Flint, E. B.; Suslick, K. S. *Science* **1991**, *253*, 1397-1399.

(68) Becker, L.; Bada, J. L.; Kemper, K.; Suslick, K. S. *Marine Chem.* **1992**, *40*, 315-320.

(69) Barber, B. P.; Hiller, R.; Arisaka, K.; Fetterman, H.; Putterman, S. *J. Acoust. Soc. Amer.* **1992**, *91*, 3061-3063.

(70) Barber, B. P.; Weninger, K.; Lofstedt, R.; Putterman, S. *Phys. Rev. Lett.* **1995**, *74*, 5276-5279.

(71) Chendke, P. K.; Fogler, H. S. *J. Phys. Chem.* **1983**, *87*, 1362-1369.

(72) Crum, L. A.; Roy, R. A. *Science* **1994**, *266*, 233-234.

(73) Crum, L. A. *Phys. Today* **1994**, *47*, 22-29.

(74) Crum, L. A. *J. Acoust. Soc. Amer.* **1994**, *95*, 559-562.

(75) Didenko, Y. T.; Pugach, S. P. *J. Phys. Chem.* **1994**, *98*, 9742-9749.

(76) Flint, E. B.; Suslick, K. S. *J. Phys. Chem.* **1991**, *95*, 1484-1488.

(77) Henglein, A.; Gutierrez, M. *J. Phys. Chem.* **1993**, *97*, 158-162.

(78) Kamath, V.; Prosperetti, A.; Egolfopoulos, F. N. *J. Acoust. Soc. Amer.* **1993**, *94*, 248-260.

(79) Margulis, M. A. *Ultrasonics* **1985**, *23*, 157-169.

(80) Seghal, C.; Steer, R. P.; Sutherland, R. G.; Verrall, R. E. *J. Chem. Phys.* **1979**, *70*, 2242-2248.

(81) Suslick, K. S.; Doktycz, S. J.; Flint, E. B. *Ultrasonics* **1990**, *28*, 280-290.

(82) Suslick, K. S.; Kemper, K. A. *Ultrasonics* **1993**, *31*, 463-465.

(83) Suslick, K. S.; Flint, E. B.; Grinstaff, M. W.; Kemper, K. A. *J. Phys. Chem.* **1993**, *97*, 3098-3099.

(84) Young, F. R. *J. Acous. Soc. Am.* **1976**, *60*, 100-104.

(85) Putterman, S. *Scientific Am.* **1995**, *272*, 46-51.

(86) Misik, V.; Miyoshi, N.; Riesz, P. *J. Phys. Chem.* **1995**, *99*, 3605-3611.

(87) Naidu, D.; Rajan, R.; Kumar, R.; Gandhi, K. S.; Arakeri, V. H.; Chandrasekaran, S. *Chem. Eng. Sci.* **1994**, *49*, 877-888.

(88) Rayleigh, L. *Philos. Mag.* **1917**, *34*, 94-98.

(89) Hua, I.; Höchemer, R. H.; Hoffmann, M. R. *J. Phys. Chem.* **1995**, *99*, 2335-2342.

(90) Shaw, R. W.; Brill, T. B.; Clifford, A. A.; Eckert, C. A.; Franck, E. U. *Chem. Eng. News* **1991**, *69*, 26-39.

(91) Li, L. L.; Egiebor, N. O. *Energy Fuels* **1992**, *6*, 34-40.

(92) Klein, M. T.; Mentha, Y. G.; Torry, L. A. *Ind. Eng. Chem.* **1992**, *31*, 182-187.

(93) Lee, D. S.; Gloyna, E. F. *Environ. Sci. Technol.* **1992**, *26*, 1587-1593.

(94) Townsend, S. H.; Abraham, M. A.; Huppert, G. L.; Klein, M. T.; Paspek, S. C. *Ind. Eng. Chem. Res.* **1988**, *27*, 143-149.

(95) Yang, H.; Eckert, C. A. *Ind. Eng. Chem. Res.* **1988**, *27*, 2009-2014.

(96) Thornton, T. D.; LaDue, D. E.; Savage, P. E. *Environ. Sci. Technol.* **1991**, *25*, 1507-1510.

(97) Suslick, K. S.; Hammerton, D. A.; Cline, R. E. *J. Am. Chem. Soc.* **1986**, *108*, 5641-1510.

(98) Suslick, K. S.; Hammerton, D. A. *IEEE Trans. Ultrasonics* **1986**, *2*, 143-147.

(99) Kondo, T.; Kodaira, T.; Kano, E. *Free Rad. Res. Commun.* **1993**, *19*, S 193-S 200.

(100) Kondo, T.; Kirschenbaum, L. J.; Kim, H.; Riesz, P. *J. Phys. Chem.* **1993**, *97*, 522-527.

(101) Petrier, C.; Jeunet, A.; Luche, J. L.; Reverdy, G. *J. Amer. Chem. Soc.* **1992**, *114*, 3148-3150.

(102) Price, G. J.; Lenz, E. J. *Ultrasonics* **1993**, *31*, 451-456.

(103) Riesz, P.; Kondo, T. *Free Rad. Biol. Med.* **1992**, *13*, 247-270.

(104) Riesz, P.; Kondo, T.; Carmichael, A. J. *Free Rad. Res. Commun.* **1993**, *19*, S 45-S 53.

(105) Hua, I.; Hoffmann, M. R. *Environ. Sci. Technol.* **1995**, in press.

(106) Kotronarou, A.; Hoffmann, M. R. *Adv. Chem. Ser.* **1995**, *244*, 233-251.

(107) Robinson, J. W. *J. Appl. Phys.* **1973**, *44*, 76.

(108) Martin, E. A. *J. Appl. Phys.* **1958**, *31*, 255.

(109) Robinson, J. W. *J. Appl. Phys.* **1967**, *38*, 210.

(110) Robinson, J. W.; Ham, M.; Balaster, A. N. *J. Appl. Phys.* **1973**, *44*, 72-75

(111) Jakob, L.; Hashem, T. M.; Burki, S.; Guidny, N. M.; Braun, A. M. *Photochem. Photobiol. A: Chem.* **1993**, *7*, 97.

(112) Buntzen, R. R. *Exploding Wires*; Plenum Press: New York, 1962, pp 195.

(113) Ben'kovskii, V. G.; Golubnichii, P. I.; Maslennikov, S. I. *Phys. Acoust.* **1974**, *20*, 14-15.

(114) Willberg, D. M.; Lang, P. S.; Höchemer, R. H., Kratel, A.; Hoffmann, M. R. *Environ. Sci. Technol.* **1995**, submitted.

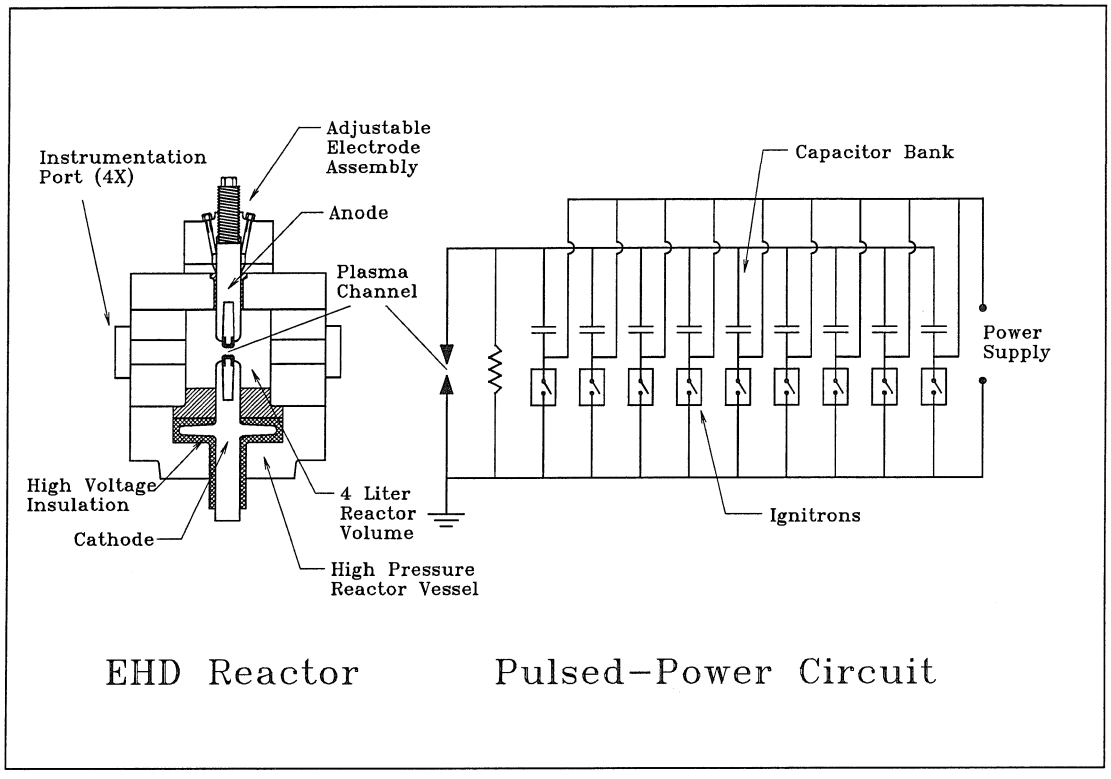

Fig. 1: Schematic diagram of the EHD reactor and the corresponding electronic circuit.

- Chapter III -

The Sonolytic Hydrolysis of p-Nitrophenylacetate: The Role of Supercritical Water

The text of this chapter appears in [Hua, I., Höchemer, R. H., Hoffmann, M. R., *J. Phys. Chem.*, 1995, *99* (8), 2335-2342.]

Abstract

Ultrasonic irradiation is shown to accelerate the rate of hydrolysis of p-nitrophenylacetate (PNPA) in aqueous solution by two orders of magnitude over the pH range of 3 to 8. In the presence of ultrasound, the observed first-order rate constant for the hydrolysis of PNPA is found to be independent of pH and ionic strength with $k_{obs} = 7.5 \times 10^{-4}$ s^{-1} with Kr as the cavitating gas, $k_{obs} = 4.6 \times 10^{-4}$ s^{-1} with Ar as the cavitating gas, and $k_{obs} = 1.2 \times 10^{-4}$ s^{-1} with He as the cavitating gas. The apparent activation parameters for sonolytic catalysis are $\Delta H^{\neq}$(sonified) = 211 kJ/mol, $\Delta S^{\neq}$(sonified) = - 47 J/(mol K), and $\Delta G^{\neq}$(sonified) = 248 kJ/mol. Under ambient conditions and in the absence of ultrasound, k_{obs} is a strong function of pH where $k_{obs} = k_{H_2O}[H_2O] + k_{OH^-}[OH^-]$ with $k_{H_2O} = 6.0 \times 10^{-7}$ s^{-1} and $k_{OH^-} = 11.8$ $M^{-1}s^{-1}$ at 25 °C. The corresponding activation parameters are $\Delta H^{\neq} = 71.5$ kJ/mol, $\Delta S^{\neq} = -107$ J/(mol K) and $\Delta G^{\neq} = 155$ kJ/mol.

During cavitational bubble collapse high temperatures and pressures exceeding the critical values of water ($T > T_c = 647$ K and $P > P_c = 221$ bar) occur in the vapor phase of the cavitating bubbles and at the interfaces between the hot vapors and the cooler bulk aqueous phase. The formation of transient supercritical water (SCW) appears to be an important factor in the acceleration of chemical reactions in the presence of ultrasound.

The apparent activation entropy, $\Delta S^{\neq}$, is decreased substantially during the sonolytic catalysis of PNPA hydrolysis, while $\Delta G^{\neq}$ and $\Delta H^{\neq}$ are increased. The decrease $\Delta S^{\neq}$ is attributed to differential solvation effects due to the existence of supercritical water (e.g., lower ρ and ε) while the increases in $\Delta G^{\neq}$ and $\Delta H^{\neq}$ are attributed to changes in the heat capacity of the water due to the formation of a transient supercritical state.

A dynamic heat-transfer model for the formation, lifetime and spatial extent of transient supercritical water at cavitating bubble interfaces is presented.

Introduction

The application of ultrasonic irradiation for the controlled degradation of chemical contaminants in water has been investigated recently using several model compounds (1-5). Upon the passage of ultrasonic waves, water molecules are exposed to alternative compression and rarefaction cycles. During a rarefaction cycle, the liquid density is low enough to form a cavitation bubble containing water vapor, dissolved gases, and high vapor-pressure solutes. During a compression cycle, a pre-existing cavity is compressed resulting in localized high temperatures and pressures. Equations describing the inception and dynamics of a cavitation bubble have been developed (6-8). With these equations, a theoretical temperature of 4200 K and a pressure of 975 atm have been predicted for a collapsing cavitation bubble in an aqueous solution saturated with N_2 (9). Experimental values of P = 313 atm and T = 3360 K have been reported (10). Cavitation temperatures in excess of 5000 K in organic and polymeric liquids have been reported (11, 12).

Two distinct sites for chemical reaction exist during a single cavitation event (13). They are the gas-phase in the center of a collapsing cavitation bubble and a thin shell of superheated liquid surrounding the vapor phase. The volume of the gaseous region is estimated to be larger than that of the thin liquid shell by a factor of ~2 x 10^4 (14) in organic liquids.

Chemical transformations are initiated predominantly by pyrolysis at the bubble interface or in the gas-phase, and attack by hydroxyl radicals generated from the decomposition of water. The concentration of $^{\bullet}OH$ at a bubble interface in water has been estimated to be 4 x 10^{-3} M (15). Depending on its physical properties, a molecule can simultaneously or sequentially react in both the gas and interfacial liquid regions.

P-nitrophenol (p-NP) is degraded completely by sonolysis to yield short-chain carboxylic acids, CO_2, NO_3^- and NO_2^- (1). Intermediate products resulting from both

hydroxyl radical attack and thermal bond cleavage are detected. Hydroxyl radical attack on p-NP is thought to occur in a region of the bubble interface with T < 440 K, while pyrolysis occurs in a hotter interfacial region with an average temperature of 900 K (1). On the other hand, H_2S (2) appears to be degraded primarily by pyrolytic decomposition within the compressed vapor phase.

Even though the basic physical and chemical consequences of cavitation are understood, many fundamental questions about the cavitation site in aqueous solution remain unanswered. In particular, the dynamic temperature and pressure changes at the bubble interface and their effects on chemical reactions need to be explored. Since this region is likely to have transient temperatures and pressures in excess of 647 K and 221 bar for periods of microseconds to milliseconds, we propose that supercritical water (SCW) provides an additional phase for chemical reaction. This phase of water exists above the critical temperature, T_c, of 647 K and the critical pressure, P_c, of 221 bar and has physical characteristics intermediate between those of a gas and a liquid (16). The physicochemical properties of water such as viscosity, ion-product, density, and heat capacity change dramatically in the supercritical region (16,17). These changes favor substantial increases for rates of most chemical reactions. SCW has been used in industrial applications such as extraction (18), hydrolysis (19, 20) and for environmental applications such as the destruction of hydrocarbons (21), and phenols (22, 23).

In this paper, we present experimental results on the kinetics of p-nitrophenylacetate (p-NPA) hydrolysis in support of our hypothesis of the existence of transient SCW during ultrasonic irradiation in water. In addition, we present an elementary heat transfer model for the estimation of the lifetime and spatial extent of supercritical water during cavitational bubble collapse.

Experimental Methods

Sonication was performed with a direct immersion-probe system (VCX-400 from Sonics and Materials). The irradiation horn was immersed reproducibly (3 cm below the surface) into the sample solution. The average power delivered to the aqueous phase was 115 W, which corresponds to an intensity of approximately 96 W/cm^2. Solutions of 100 μM p-NP were adjusted to pH 4.8-5.2 with phosphoric acid and sonolysis reactions were performed in a modified stainless-steel cell on a total volume of 25 mL. The cell was modified by the addition of stainless-steel gas dispersion and sampling tubes. A small Teflon tube with "luer-lok" connection (Aldrich) was inserted through the sampling tube. The reaction chamber was stirred with a magnetic stirring-bar and stirring motor. Compressed air was blown continuously through the converter to minimize changes in temperature of the piezoelectric crystal. pH was adjusted to the range pH 4.8-5.2 to ensure that all of the p-NP (pK_a = 7.16 at I = 0.05 M) (1) was in the neutral form such that it would preferentially partition to the gas bubble interfaces. The reaction solution was sparged for 15 min at a flow-rate of 10-15 mL/min with the appropriate gas. Constant temperature was maintained with a Haake A80 temperature - control system. 0.5 mL aliquots were withdrawn via syringe through the sampling tube at variable time-intervals. Even though the total reaction volume was not maintained constant during sonication, dV/dt was determined to be small and thus did not have an effect on the value of the measured rate constant. The pH of the sample aliquots was adjusted to ~12 with 5 N NaOH and then filtered through 0.2 μm syringe filters (PFTE, Gelman). The degradation of p-NP was monitored spectrophotometrically at λ = 400 nm (ε = 17,900 M^{-1} cm^{-1}) with an HP8542a UV/VIS Spectrophotometer.

The rates of p-NPA hydrolysis in the absence of ultrasound were determined in a temperature-controlled optical cell using an HP8450a UV/VIS Spectrophotometer. The appearance of p-nitrophenolate ion was monitored at λ = 360 nm or 400 nm. p-NPA was

dissolved in a small volume of methanol before dilution in water; and solutions were used immediately after preparation. The ionic strength was maintained at μ = 0.4 M with NaCl and over the pH range of 2 to 11, three different buffers (i. e., CH_3COOH/CH_3COO^-, $CO_2 \cdot H_2O/CO_3^-$; HCO_3^- / CO_3^{2-}) and concentrations were used at each pH and the observed rate constants were extrapolated to zero buffer concentration to correct for the influence of general acid and base catalysis on the hydrolysis rate. Experiments were carried out in duplicate with an uncertainty of $\leq$ 5 %.

Solutions of 100 μM p-NPA were sonicated and analyzed in an identical fashion as p-NP. However, in the case of the p-NPA, the aliquots were adjusted to pH 7 by the addition of 0.2 mL pH 7 buffer to 0.5 mL of sample. The samples were filtered and the absorbance at λ = 272nm (ε = 8452 M^{-1} cm^{-1}) was measured. The contribution to the absorbance at 272 nm by p-NP (ε=1777 $M^{-1}cm^{-1}$) was subtracted from the total absorbance. The use of methanol as a co-solvent was shown to substantially decrease the observed rate constant. Thus, no further experiments were done with this co-colvent. P-NPA dissolved in water after approximately two hours of stirring and mild heating. The pH dependency of the reaction rate was established by a variation in buffer concentration or by using phosphoric acid. Ionic strength was varied with NaCl. NO_3^- and NO_2^- concentrations were determined by capillary electrophoresis (Dionex Capillary Electrophoresis System I) using a silica column (~60 cm) and a standard method for anion analysis (24).

Water with 18.2 mΩ resistivity (MilliQ UV Plus System) was used in the preparation of all aqueous solutions. P-NP and p-NPA (Aldrich, 99 %+ and 97 % purity respectively) were used without further purification. Phosphoric acid, sodium chloride, and potassium phosphate monobasic were reagent grade and used without further purification.

Results and Discussion

Comparative rate thermometry employing p-NP as a probe molecule can be used in order to estimate the effective temperatures achieved during bubble collapse (25). P-NP (1) is a suitable probe molecule since its kinetics and mechanism of degradation are well understood. The primary step during the sonolytic degradation of p-NP has been shown to be (1):

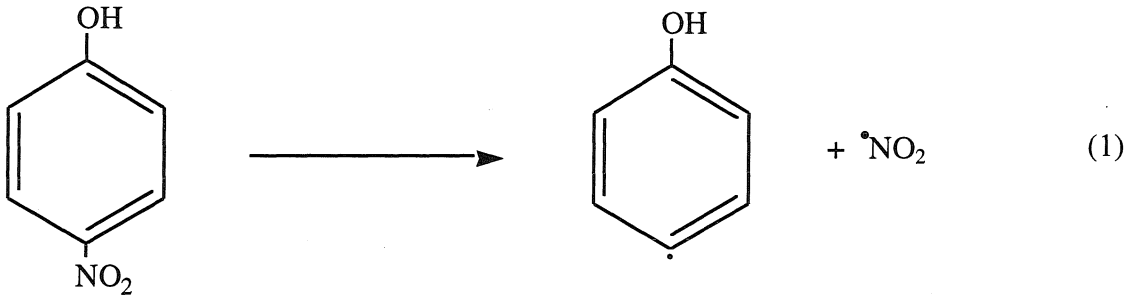

(1)

Another possible reaction is the addition of •OH with subsequent NO_2 generation:

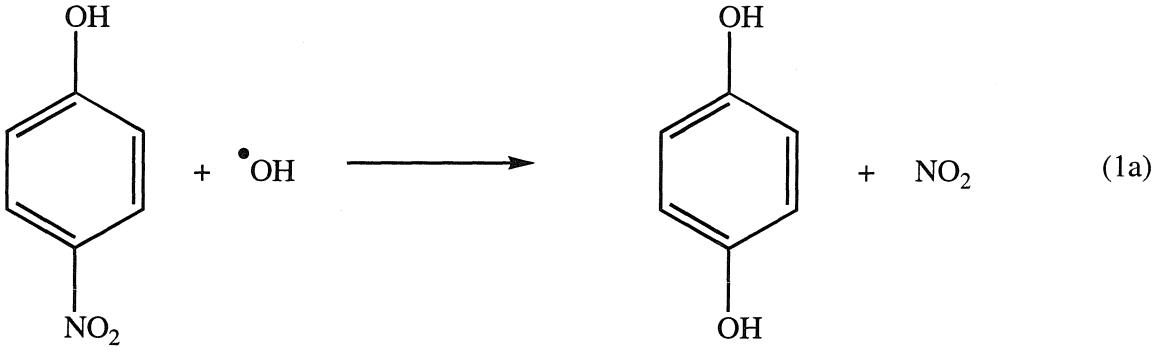

(1a)

The activation energy for the main pathway of degradation, which involves carbon-nitrogen bond cleavage, can be estimated from shock-tube studies of nitrobenzene decomposition (25). The reaction rate constant for carbon-nitrogen bond-cleavage in nitrobenzene has been determined to be:

$$k = A\exp\left\{\frac{-E_a}{RT}\right\} \qquad (2)$$

where $A = 1.9 \times 10^{15}\ s^{-1}$ and $E_a/R = 33026$ K, and the stoichiometry is given by:

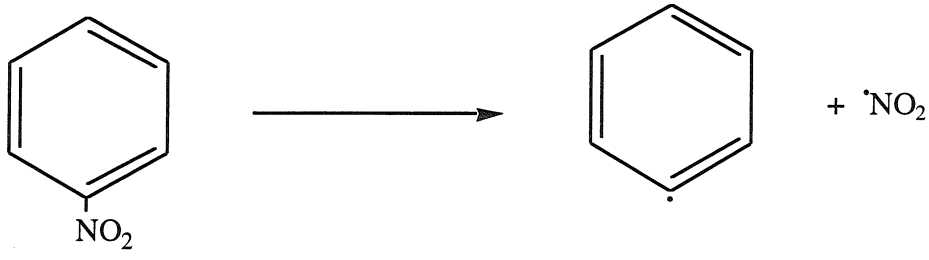

(3)

Using these values for A and E_a/R, we can estimate the effective temperature of the cavitation as follows:

$$T_{eff} = \frac{-E_a / R}{\ln\left(\frac{k}{A}\right)} = \frac{-33026}{\ln\left(\frac{k}{1.9\times10^{15}}\right)} \quad [K] \qquad (4)$$

The relative temperature of bubble collapse can be adjusted by saturating the solution with gases characterized by substantially different specific heats, thermal conductivities, and solubilities. An important factor controlling bubble collapse temperature is the polytropic factor, K, of the saturating gas (9). From a knowledge of K we can estimate the maximum temperature obtained during bubble collapse from Eq. 5:

$$T_{max} = T_0\left\{(K-1)\frac{P_m}{P}\right\} \qquad (5)$$

where T_{max} = temperature of bubble upon collapse, T_0 = temperature of the bulk solution, P = pressure in the bubble at its maximum size (i. e., the vapor pressure of the

solvent); P_m = pressure in liquid at moment of transient collapse and $K = C_p/C_v$. The value of K is associated with the amount of heat released from the gas inside the bubble during adiabatic compression. As K increases, the heat released upon bubble collapse also increases. Additional physicochemical properties that may influence the temperature attained during bubble collapse include thermal conductivity, λ, and gas solubility. Values for the relevant physical properties (26, 27) of gases used in this study are listed in Table I.

Thermal conductivities of the dissolved gases have been inversely correlated to sonoluminescence intensity (28) as well as with variable rates of free-radical formation (29, 30) during sonolysis. A low thermal conductivity favors high collapse temperatures because the heat of collapse will dissipate less quickly from the cavitation site. Highly soluble gases should result in the formation of a larger number of cavitation nuclei and more extensive bubble collapse since gases with higher solubilities are more readily forced back into the aqueous phase. Thus, a gas with both a low thermal conductivity and high water solubility should yield the highest temperature upon cavitational bubble collapse. Based on physical properties, we predict that krypton will yield the highest rate of p-NP degradation, while helium should yield the lowest relative rate.

The sonolytic degradation of p-NP is found to be a first-order reaction for all gases as shown in Fig. 1. Using the rate constants obtained from this data and Eq. 3 we estimate the effective average temperatures at the interface of the collapsing bubbles for each gas (Table II). The highest effective temperature is achieved in a Kr-saturated solution, whereas a He-saturated solution results in the lowest effective temperature, as predicted above. Although the value of K is similar for all three gases, helium has an unusually high thermal conductivity and a relatively low solubility in comparison to Ar and Kr. Thus, the difference in the resulting effective temperature is also larger than that between Ar and Kr.

Probing for Supercritical Water During Cavitation

Furthermore, the reaction does not involve hydroxyl radical and thus the interpretation of the observed reaction rate constants should not be complicated by formation rates of radicals produced during cavitation. Observed rate constants are highly pH dependent and range from 10^{-6} to 10^{-3} s^{-1} in the pH range 2-10 for this reaction under ambient conditions (Fig. 2). Above pH 6.5, the hydrolysis of p-NPA is base-catalyzed:

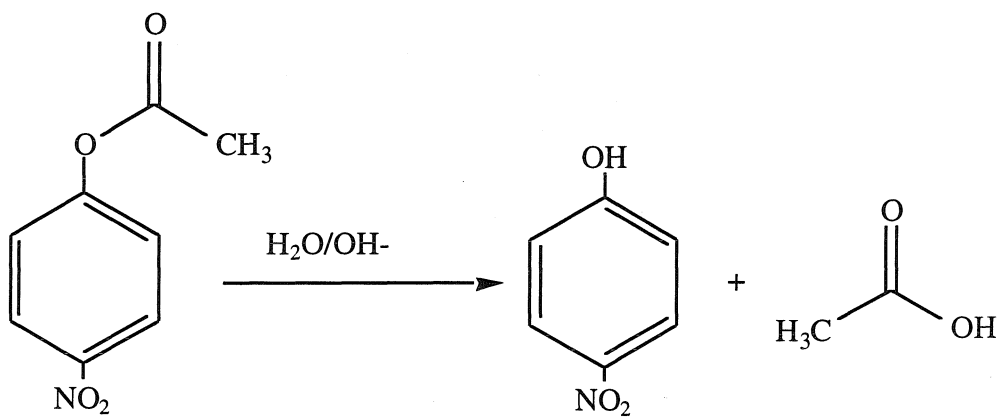

(6)

The rate law for p-NPA hydrolysis is written as:

$$v = k_{obs}\ [\text{p-NPA}] = \frac{-d[p-NPA]}{dt} \tag{7}$$

where

$$k_{obs} = k_{H_2O}[H_2O] + k_{OH^-}[OH^-] + k_{H^+}[H^+] \tag{8}$$

with $k_{H^+} \approx 0$.

The pH dependency of the control reaction is shown in Fig. 2.

The overall first-order rate constant for p-NPA hydrolysis contains two terms that account for the uncatalyzed reaction with water and for the base - catalyzed pathway.

Under normal conditions, the concentration of the water and OH^- (at a constant pH) remain constant and thus the overall rate constant is treated as a pseudo-first order constant. The observed rate constants were found to be $k_{H_2O} = 6.0 \times 10^{-7}\ s^{-1}$ and $k_{OH^-} = 11.8 \pm 0.5\ M^{-1}s^{-1}$ and were determined from standard analysis of spectrophotometric data as a function of time.

The sonolytic acceleration of p-NPA hydrolysis has been reported previously by Kristol (31). He noted that several esters with widely different activation energies showed approximately the same relative enhancements in hydrolysis rates in the presence of ultrasound. Esters with substantially different activation energies for hydrolysis should show different relative rate enhancements, if these apparent enhancements were due only to the very high microscopic temperatures generated by cavitational bubble collapse. Our basic hypothesis, in this case, is that a change in the thermodynamics of the formation of the activated complex may account for changes in the observed reaction rates and reflect a change in either the microscopic environment and/or the mechanism. For a bimolecular reaction we can use the following activation parameters:

$$\Delta S^{\neq} = R\left(\ln A - \ln\left(\frac{k_B T}{h}\right) - 1\right) \tag{9}$$

$$\Delta H^{\neq} = E_a - RT$$

$$\Delta G^{\neq} = \Delta H^{\neq} - T\Delta S^{\neq} \tag{11}$$

to characterize the overall rate of reaction, where E_a is the intrinsic activation energy, A is the pre-exponential factor, $R = 8.31\ J\ mol^{-1}\ K^{-1}$, $k_B = 1.38 \times 10^{-23}\ J\ K^{-1}$ and $h = 6.626 \times 10^{-34}\ J\ s$. E_a and A are determined experimentally from kinetic data.

The measured rate constant for hydrolysis of p-NPA at the bubble interface should

be different from the rate constant determined from analysis of the bulk solution since the solution is not homogeneous. In order to determine a rate constant that is as close as possible to the intrinsic rate constant at the bubble interfaces, several other bulk solution parameters must be considered, including ionic-strength, co-solvent effects, and pH.

Given that the interface between the hot gas in the bubble and the surrounding cooler liquid is hydrophobic (32), organic compounds will partition to that region much more effectively than ions. Thus, a variation in the ionic strength of the bulk solution should have a negligible influence on the hydrolysis rate constant. As shown in Fig. 3, the observed hydrolysis rate constants do not vary appreciably over the range of ionic strength from 0.0 and 0.3M.

Methanol, when used as a co-solvent can be present at a large excess compared to p-NPA. Under these conditions, methanol may preferentially accumulate at the bubble interface. In this way, a methanol co-solvent is predicted to slow down the rate of sonolysis of most organic molecules. This prediction is supported by the data shown in Fig. 4 which provides a comparison of the rate constants observed in irradiated solutions in the absence (_, □) and presence (x, +) of 0.25% (v/v) methanol. The rate constants are found to be significantly larger in solutions that were prepared without methanol.

Over a pH range of 3 to 8, the overall first-order rate constants are essentially invariant in a sonicated solution as shown in Fig. 5. This pH-dependency is consistent with the tendency for water in a dense supercritical state to have a higher ion activity product relative to normal-phase water; a higher value for K_W should result in a higher concentration of both OH^- and H^+ for a given set of conditions. Thus, we expect that the $k_{OH^-}[OH^-]$ term of k_{obs} (Eq. 8) should be enhanced significantly in the presence of transient SCW. Selected properties of supercritical water and water under ambient conditions compared in Table IV.

The optimal set of conditions for determination of intrinsic rate constants proved to be an unbuffered solution of 100 μM p-NPA in the absence of a co-solvent. The

amount of NO_2^- and NO_3^- produced during p-NPA sonolysis was insignficant. This indicates that the main reaction pathway for p-NPA was hydrolysis of the ester linkage rather than pyrolytic denitration of the nitro group. Fig. 6 compares the relative values of k_{obs} in the presence of different saturating gases. The hydrolysis rate constants vary from 9.8×10^{-5} s^{-1} to 3.8×10^{-4} s^{-1}, depending on the nature of the dissolved gas.

The Arrhenius plots for sonicated and unsonicated solutions are shown in Figs. 7 and 8. Using the overall activation energies determined from these plots, the respective activation parameters can be calculated. As shown in Table III, the activation free energy, $\Delta G^{\neq}$, for hydrolysis appears to increase in the sonicated system compared to the unsonicated solution primarily due to an increase in the value of $\Delta H^{\neq}$. The higher value of $\Delta H^{\neq}$ in the sonicated system may result in part from its correlation with heat capacity which is a function of temperature. The heat capacity of water greatly increases in the supercritical regime (13) and thus may contribute to an increase in $\Delta H^{\neq}$ during sonolysis. However, the corresponding reaction rate constant is also higher because of the net effect of an increasing effective reaction temperature. On the other hand $\Delta S^{\neq}$ for hydrolysis appears to decrease in the presence of ultrasound. The apparent change in $\Delta S^{\neq}$ can be explained by considering changes in both the transition state and reactant interactions with the solvent, which are affected by the lower density and dielectric constant of the supercritical phase. Because the solute molecules are further apart in the supercritical domain, fewer are available for solvation of the polar transition state compared to the number which can cluster near the transition state in water at its normal density. In addition, the lower dielectric constant implies that when the organic solute is introduced into the supercritical phase, disruption of the solvent structure should be less compared to the disruption in the hydrogen bonds when an organic solute is introduced into liquid water.

Estimation of the Total Amount of Supercritical Water During Sonolysis

In light of the above results, we now proceed to estimate the fraction of an individual cavitating bubble, and total fraction of a cavitating solution, that is in the transient supercritical regime.

Flint and Suslick (12) and Sehgal et al. (10) have clearly demonstrated that temperatures and pressures within a collapsing cavitation bubble exceed the critical point of water. Based on previously estimated temperatures within a collapsed bubble and a smaller layer of surrounding liquid (33), we now attempt to describe the spatial and temporal temperature distribution around a bubble just after its collapse. In order to obtain a simple first-order approximation of the heat transport from the interior of a hot bubble to the surrounding bulk liquid we need to make several severe assumptions. Thus, we caution that this model should be viewed as a qualitative estimation rather than a precise description of the real physical phenomenon. Our goal is to show qualitatively, conditions occur around a collapsed bubble that are in accord with existence of supercritical water as suggested by our experimental results and to estimate the total volume of supercritical water present in a typical solution exposed to ultrasound.

The hydrodynamic life of the bubble before collapse is excluded from this analysis. Thus, we assume that the collapsed bubble is an instantaneous point source of heat embedded in an infinite matrix at ambient temperatures, as shown in Fig. 9. Furthermore, we assume that conduction provides the only means of heat transfer, and thus we ignore heat transport by convection and radiation. We also assume that the bubble retains its spherical shape after collapse. The heat capacity, thermal conductivity and density of the collapsed bubble are assumed to be the same as of the surrounding water at room temperature. In addition we assume that a uniform temperature is attained within the bubble immediately after collapse.

The following values for the physical properties of liquid water at 303 K are used in the calculation. The heat capacity, C_p, 4178.4 J/kg K, the thermal conductivity, λ,

0.6154 J/s m K, the density, ρ, 995.65 kg/m^3 were taken from the Handbook of Chemistry and Physics (34). The initial radius, a = 150 μm and the initial temperature of the collapsed bubble, T_0 = 5000 K have previously been estimated by Suslick (12, 33). The temperature of the water surrounding the collapsed bubble, T_{med} = 300 K.

The severe assumptions that are made in order to keep the mathematical treatment simple allow at best an order of magnitude estimation. A precise physical model would have to take into account the deviations of single bubble dynamics in cloud of cavitating bubbles. Also, the physical properties vary widely around the critical point. The calculations have been carried out using room-temperature properties.

Given all these assumptions, we can write the heat transport equation as

$$\frac{\partial T}{\partial t} = k\nabla^2 T \tag{13}$$

where the thermal diffusivity, k, in units of [m^2/s] is given as $\lambda/(\rho\, C_p)$. The Laplacian, written in spherical polar coordinates

$$\nabla^2 = \frac{1}{r^2}\frac{\partial}{\partial r}\left[r^2\frac{\partial}{\partial r}\right] + \frac{1}{r^2\sin\theta}\frac{\partial}{\partial\theta}\left[\sin\theta\frac{\partial}{\partial\theta}\right] + \frac{1}{r^2\sin^2\theta}\frac{\partial^2}{\partial\phi^2} \tag{14}$$

can be simplified, since we have assumed that the collapsed bubble retains its spherical shape and that it has a uniform initial temperature T_0. The resulting temperature distribution, T(r), is, therefore, only a function of the distance from the bubble center and is independent of the angles θ and ϕ. With these assumptions we can write:

$$\frac{1}{k}\frac{\partial T}{\partial t} = \frac{\partial^2 T}{\partial r^2} + \frac{2}{r}\frac{\partial T}{\partial r} \tag{15}$$

For the initial conditions, $T = T_0$, for $t = 0$, $0 < r < a$ and $T = T_{med}$, for $t = 0$, $r > a$ and the boundary condition T = finite, for $r = 0$, the solution to Eq. 14 is given (35, 36) as:

$$T_{red} = \frac{1}{2}\left[\operatorname{erf}\left(\frac{\frac{r}{a}+1}{2\sqrt{k\frac{t}{a^2}}} \right) - \operatorname{erf}\left(\frac{\frac{r}{a}-1}{2\sqrt{k\frac{t}{a^2}}} \right) \right] \ldots$$

$$\ldots - \frac{a}{r\sqrt{\pi}}\sqrt{k\frac{t}{a^2}}\left[\exp\left(-\left(\frac{\frac{r}{a}-1}{2\sqrt{k\frac{t}{a^2}}} \right) \right) - \exp\left(-\left(\frac{\frac{r}{a}+1}{2\sqrt{k\frac{t}{a^2}}} \right) \right) \right] \tag{16}$$

where the error function is given by

$$\operatorname{erf}(x) = \frac{2}{\sqrt{\pi}} \int_0^x \exp\left[-y^2 \right] dy \tag{17}$$

while the reduced temperature is defined as

$$T_{red} = \frac{T - T_{med}}{T_0 - T_{med}} \tag{18}$$

In Eq. 17 T_0 is the initial temperature of the collapsed bubble, T_{med} is the initial temperature of the surrounding water, T_{red} is the reduced temperature as a function of the distance from the center of the bubble, r, at an elapsed time, t. The actual temperature can be calculated from the definition of the reduced temperature. In Fig. 10 we show a plot of T_{red} versus r/a, obtained from the numerical solution of Eq. 15. The maximum radius of a shell around the collapsed bubble with a temperature exceeding the critical value T_c

= 647 K can also be calculated for each given time interval after collapse. The times and corresponding reduced distances are given in Table V. The estimated lifetime and spatial extent of the supercritical phase at a single cavitation site are on the order of milliseconds and microns. After 10 msec the radius of the supercritical region around a collapsed bubble extends about 40 % farther into the bulk solution than the original cavity. The radius of the supercritical shell expands up to 160 % of the original bubble radius at 50 msec after collapse.

We can also estimate the fraction of the total volume of a sonified aqueous solution that is actually in the supercritical state. The volume $V_{shell}(t_i)$ of the hot layer, where $T > T_c$, around a collapsed cavity can now be calculated as a function of time.

$$V_{shell}(t_i) = \frac{4}{3}\pi a^3 \left[\left(\frac{r(t_i)}{a} \right)^3 - 1 \right] \tag{19}$$

If N is the number of cavities that collapse per unit volume per unit time, the fraction of the aqueous solution that is in the supercritical state, x_{scw}, is given as

$$\frac{V_{scw}}{V_{total}} \equiv x_{scw} = N \sum_i V_{shell}(t_i)[t_i - t_{i-1}] \tag{20}$$

The number density of nuclei and their size distribution has been measured by Katz and Acosta (37). However there are no experimental data for the number density of nuclei or actual cavitation bubbles in water during ultrasonic irradiation. Suslick and Hammerton (14) give an estimate for the number of collapsing bubbles per time and volume. If we use their estimate of $N = 4 \times 10^8$ $sec^{-1}m^{-3}$, we determine that $x_{scw} = 0.0015$.

Our simple model predicts that approximately 0.15 percent of the irradiated water is in the supercritical state at any point in time. Depending on the extent to which

supercritical water accelerates chemical reactions, this fraction may represent a substantial contribution to reaction rate enhancements that have been reported previously for chemical reactions in the presence of ultrasound. The very nature of our simple model and its severe assumptions preclude a precise treatment of the heat transfer processe occuring during cavitation. Akamatsu and co-workers (38, 39) have investigated the heat and mass transfer in cavitating bubbles in more thepretic detail than is possible within the scope of our experimental study.

Conclusions

p-NPA hydrolysis in an ultrasonically irradiated solution exhibits an observed rate constant which is enhanced by about two orders of magnitude in comparison to the same hydrolysis under ambient conditions at 25 ^{o}C. Furthermore k_{obs} is found to be relatively insensitive to the solution pH in the presence of ultrasound while k_{obs} under ambient conditions is a strong function of pH, i. e., $k_{obs} = k_o + k_{OH^-}[OH^-]$. The latter result is distinct from that observed in unsonified solutions and suggests that the reaction rate enhancement occurs at the cavitation bubble interface. Both the enhanced hydrolysis rate and its pH independence may be explained by the existence of supercritical water around the collapsing cavitation bubbles. Hydrolysis may be accelerated, in part, by a higher concentration of OH^- at the hot bubble interface, which results from the higher ion-product, K_w, of SCW. The apparent decrease of $\Delta S^{\neq}$ in the presence of ultrasound suggests that the rate enhancement might be due to a physical change in the microscopic environment surrounding the substrate. In addition to our experimental evidence, a simple heat transfer model predicts that approximately 0.15% of the irradiated water is in the supercritical state at any point in time, giving further evidence for the proposed existence of SCW in cavitating aqueous solutions. Based on these experimental findings and our semi - quantitative calculations, we argue that supercritical water represents a potentially important component of sonochemistry, in addition to the free-radical reactions and thermal/pyrolytic effects (1-3) that have been demonstrated previously.

The existence of the SCW phase during acoustic cavitation has significant implications for hydrolysis reactions of environmental interest. Because the reaction occurs at or close to the bubble/water interface, compounds more hydrophobic than p-NPA are expected to exhibit even higher hydrolysis rate enhancements because the compound that is concentrated around the bubble will, once the bubble collapses, be embedded in supercritical water. The sonolysis of parathion at 25 ^{o}C results in complete

hydrolysis within 30 min (3), whereas at 20 °C and pH 7.4 the non-catalyzed hydrolysis has a half-life of 108 days (40).

Finally, the existence of the supercritical phase in an ultrasonically irradiated solution suggests a modification of the conventional view of the reactive area at a cavitation site. This region is normally considered to consist of two discrete phases: a high temperature, low density gas phase, and a more condensed and lower temperature liquid shell. An alternative description would include a structural change of the collapsing bubble due to the existence of SCW with properties more characteristic of water vapor than liquid water. The presence of SCW in a collapsing bubble may help to explain the observed fragmentation of a single bubble into a bubble cloud consisting of many smaller bubbles (41).

The application of SCW oxidation to wastewater treatment has been investigated in recent years (21-23). One drawback of the large scale application of SCW oxidation is the inherently aggressive nature of water in the supercritical state, which results in extensive corrosion of reaction vessels. Corrosion of the reactor chamber lessens the economic feasibility of this method. We believe that the treatment of hazardous organic compounds with ultrasound could be a possible alternative to oxidation processes in bulk supercritical water. Due to the local confinement of supercritical water as generated during the collapse of gas cavities, the bulk solution remains at ambient pressures and temperatures, thus avoiding extensive damage to the reaction vessel.

Acknowledgments: The authors are grateful to EPRI (contract # RP8003-36) and ARPA (Grant # NAV 5HFMN N0101492J1901) for generous financial support. We appreciate the support and encouragement of Drs. Ira Skurnick and Myron Jones and the helpful discussions provided by Professor Kenneth Suslick.

References

(1) Kotronarou A., Mills, G., Hoffmann, M. R., *J. Phys. Chem.*, 1991, *95*, 3630-3638.

(2) Kotronarou, A., Mills, G., Hoffmann, M. R., *Environ. Sci. and Technol.*, 1992,*26,* 12, 2430-2428.

(3) Kotronarou, A., Mills, G., Hoffmann, M. R., *Environ. Sci. and Technol.,* 1992, *26,* 7, 1469-1462.

(4) Petrier C., Micolle, M., Merlin, G., Luche, J. L., Reverdy, G., *Environ. Sci. and Technol.*, 1992, *26*, 8, 1639-1642.

(5) Wu, J. M., Huang, H. S., Livengood, C. D., *Environmental Progress*, 1992, *11*, 3 , 195-201.

(6) Lord Rayleigh, *Philos. Mag.*, 1917, 34, 94-98.

(7) Noltingk, B. E., Neppiras, E. A., *Proc. Phys. Soc. B.*, 1950, *63B*, 674-685

(8) Noltingk, B. E., Neppiras, E. A., *Proc. Phys. Soc. B.*, 1951, *64B*, 1032-1038.

(9) Mason, T. and Lorimer, J., *Sonochemistry: Theory, Applications, and Uses of Ultrasound in Chemistry*; Ellis Norwood, Ltd., New York, 1988.

(10) Sehgal, C., Steer, R. P., Sutherland, R. G., Verrall, R. E., *J. Chem. Phys.,* 1979, *70, 5*, 2242-2248.

(11) Flint, E. B., Suslick K. S., *J. Am. Chem. Soc.*, 1989, *111*, 18, 6987-6992.

(12) Flint, E. B., Suslick, K. S., *Science*, 1991, *253*, 5026, 1397-1399.

(13) Gutiérrez, M., Henglein, A., Fischer, Ch.-H., *Int. J. Radiat. Biol.*, 1986, *50*, 313-321.

(14) Suslick, K. S., Hammerton, D. A., *IEEE Trans Ultrasonics Ferroelec Freq. Contr,* 1986, *UFCC-33* , 2, 143-147.

(15) Gutiérrez, M., Henglein, A., Ibañez, F., *J. Phys. Chem.,* 1991, *95,* 6044-6047.

(16) Shaw, R. W., Brill, T. B., Clifford, A. A., Ecker, C. A, Franck, E. U., *Chemical and Engineering News*, 1991, 69, 51, 26-39.

(17) Marshall, W. L. and Franck, E. U., *J. Phys. Chem. Ref. Data,* 1981, *10*, 295-304.

(18) Li, L. L., Egiebor, N. O., *Energy and Fuels*, 1992, *6*, 1, 35-40.

(19) Lee, D. S., Gloyna, E. F., *Eviron. Sci. and Technol.*, 1992, *26*, 8, 1587-1593.

(20) Klein, M. T., Mentha, Y. G., Torry, L. A., *Ind. Eng. Chem.*, 1992, *31*, 182-187.

(21) Townsend, S. H., Abraham, M. A., Huppert, G. L., Klein, M. T., Paspek, S. C., *Ind. Eng. Chem. Res.*, 1988, *27*, 143-149.

(22) Yang, H., Eckert, C. A., *Ind. Eng. Chem. Res.*, 1988, *27*, 2009-2014.

(23) Thornton, T. D., LaDue, III, D. E., Savage, P. E., *Environ. Sci. and Technol.*, 1991, *25*, 1507-1510.

(24) Harrold, M. P., Wojtusik, M., Riviello, J., and Henson, P., *J. Chrom.,* 1993, *640,* 463-471.

(25) Tsang, W., Robaugh, D., Mallard, G. W., *J. Phys. Chem.*, 1986, *90*, 5968-5973.

(26) Kaye, G. W. C. and Labye, T. H., *Tables of Physical and Chemical Constants and Some Mathematical Functions,* 14th Ed., Longman Group Limited, London, 1973, p. 54.

(27) Braker, W. and Mossman, A., *Gas Data Book*, 6th Ed., Matheson Gas Products Inc., United States of America, 1980.

(28) Young, F. R., *J. Acoust. Soc. Am.*, 1976, *60,* 100-104.

(29) Kondo, T., Kirschenbaum, L. J., Kim, H., Riesz, P., *J. Phys. Chem.*, 1993, *97*, 522-527.

(30) Makino, K., Mossoba, M. M., Riesz, P., *J. Phys. Chem.*, 1983, *87*, 1369-1377.

(31) Kristol, D. S., Klotz, H., Parker, R. C., *Tett. Lett.*, 1981, *22*, 907-908.

(32) Henglein, A., Kormann, C., *Int. J. Radiat. Biol.*, 1985, *48*, 251-258.

(33) K.S. Suslick, D. A. Hammerton, and R. E. Cline, Jr. *J. Am. Chem. Soc.*, 1986, *108*, 5641-5642.

(34) *Handbook of Chemistry and Physics*, 71st Ed., CRC Press, Ohio,1990.

(35) Crank, J., *The Mathematics of Diffusion*, 1st Ed., Clarendon Press, Oxford, 1956.

(36) Carslaw, H. S., Jaeger, J. C.,*Conduction of Heat in Solids*, 2nd Ed., Clarendon Press, Oxford, 1959.

(37) Katz, J., Acosta, A., *Appl. Sci. Res.*, 1982, 38, 123-132.

(38) Fujikawa, S., Akamatsu, T., *J. Fluid Mech.*, 1980, *97*, 481.

(39) Fujikawa, S., Akamatsu, T. *Bull. J. Sci. Mech. Eng.*, 1985, *28*, 286, 267-273.

(40) Faust, S. D., Gomaa, H. M., *Environ. Lett.*, 1972, *3*, 171-201.

(41) Neppiras, E. A. and Coakley, W. T., *J. of Sound and Vibration*, 1976, *45*, 341-373.

Table 1

Physical properties of selected gases used during sonolysis.

Gas	Polytropic Index, κ	Thermal Conductivity, λ [mW/m K]	Solubility in Water [m^3/m^3]
Kr	1.66	17.1	0.0594
Ar	1.66	30.6	0.032
He	1.63	252.4	0.0086

* @ 600 K

Table 2

Calculated effective temperature from comparative rate thermometry with p-NP as reacting system.

Dissolved Gas	Rate Constant, $[s^{-1}]$	Calculated Temperature, [K]
Kr	7.5×10^{-4}	779
Ar	$4.6. \times 10^{-4}$	772
He	1.2×10^{-5}	750

Table 3

Thermodynamics of p-NPA hydrolysis in sonicated and unsonicated solutions.[a)]

Thermodynamic Property	Sonicated	Unsonicated
$\Delta S^{\neq}$	-47 J/mol K	-107 J/mol K
$\Delta H^{\neq}$	211 kJ/mol	71.5 kJ/mol
$\Delta G^{\neq}$	248 kJ/mol	155 kJ/mol

a) Quantities calculated using representative interfacial temperature of 780 K.

Table 4

Selected properties of different phases of water.

Physical State	ρ, [g/ml]	ε	log K_w, [mol^2/L^2]	μ, [mPa/s]
supercritical	0.3	~6	-11.4 [a)]	~10^2
ambient	1	78.5	-14	~10^3

At the critical point: T_c = 647 K, P_c = 221 bar

Under ambient conditions: T = 298 K, P = 1 bar

ρ = density, ε = dielectric constant, K_w = ion-activity product, μ = viscosity

a) Calculated from equation in (17). All other values from (16).

Table 5

Reduced radii and volumes of the hot layer around a collapsed cavity and corresponding elapsed times.

No, i	Time elapsed since collapse [msec]	Reduced distance from center, $r(t_i)/a$, with $T > T_c$	Volume of hot shell $V_{shell}(t_i)$ [pL]
0	0	1.000	0
1	1	1.147	7.2
2	2	1.200	10.3
3	5	1.307	17.4
4	10	1.400	24.7
5	15	1.467	30.5
6	30	1.573	40.9
7	50	1.613	45.2
8	70	1.573	40.9
9	90	1.467	30.5
10	110	1.307	17.4
11	120	1.200	10.3
12	130	1.067	3.04

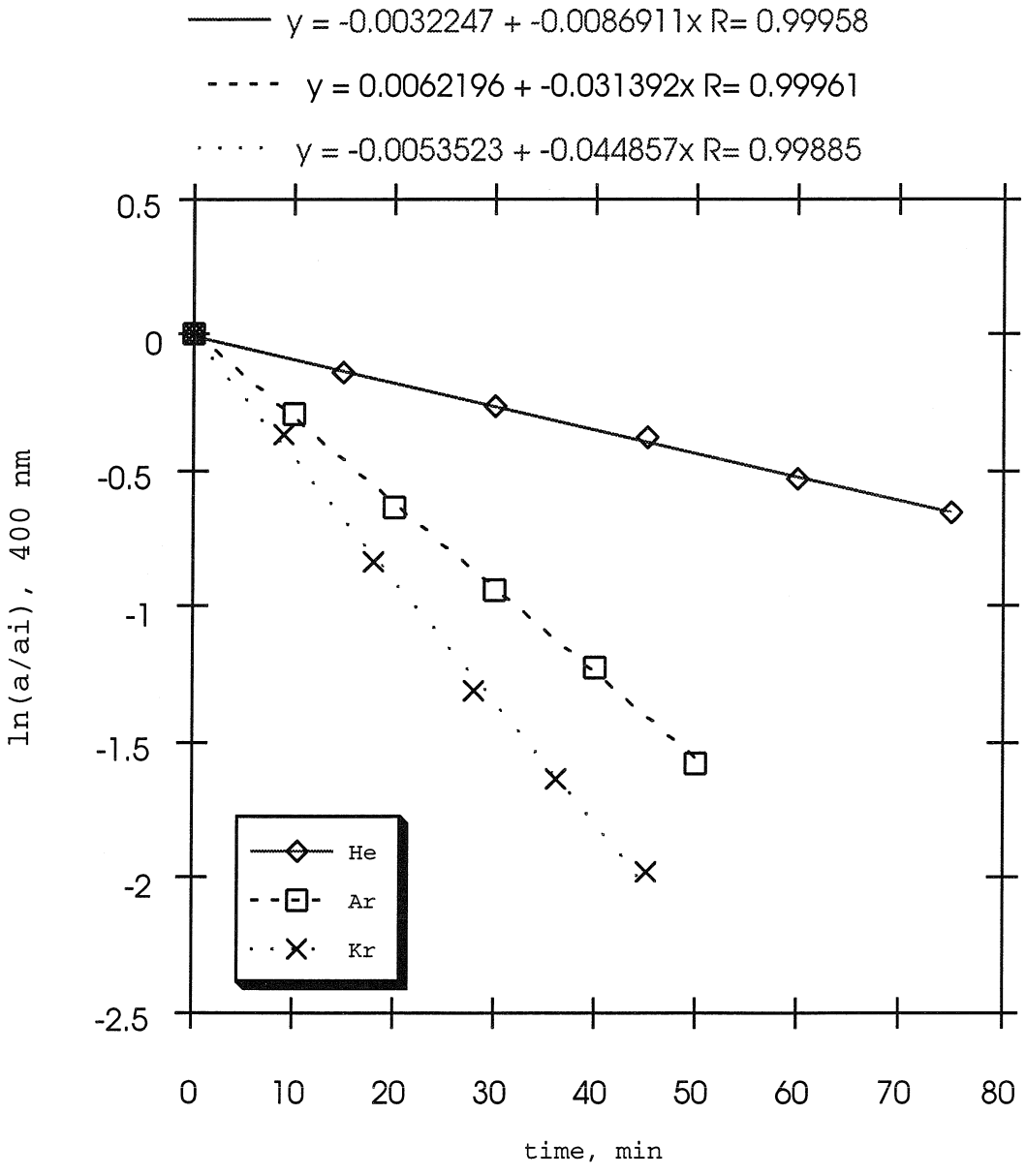

Fig. 1: First-order plot of p-NP degradation with different saturating gases.

Rate constants (s^{-1}): a) Kr: 7.5×10^{-4} b) Ar: 5.2×10^{-4} c) He: 1.4×10^{-4}.

a = absorbance at 400 nm at time, t. a_i = absorbance at 400 nm, t = 0.

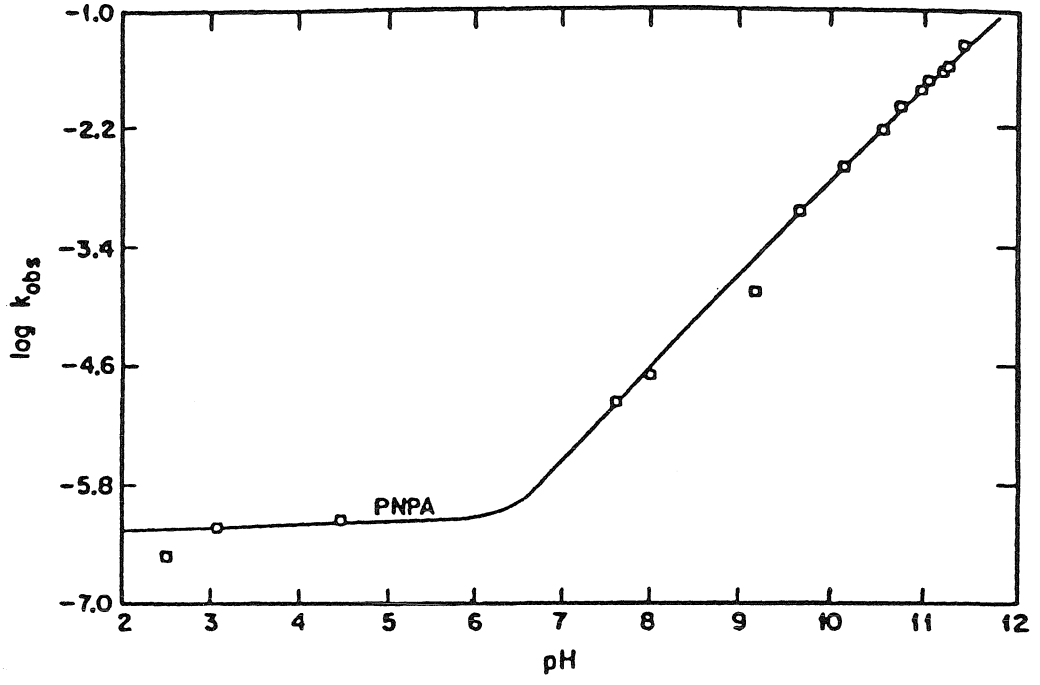

Fig. 2: pH dependence of k_{obs} for the hydrolysis of p-NPA under ambient conditions.

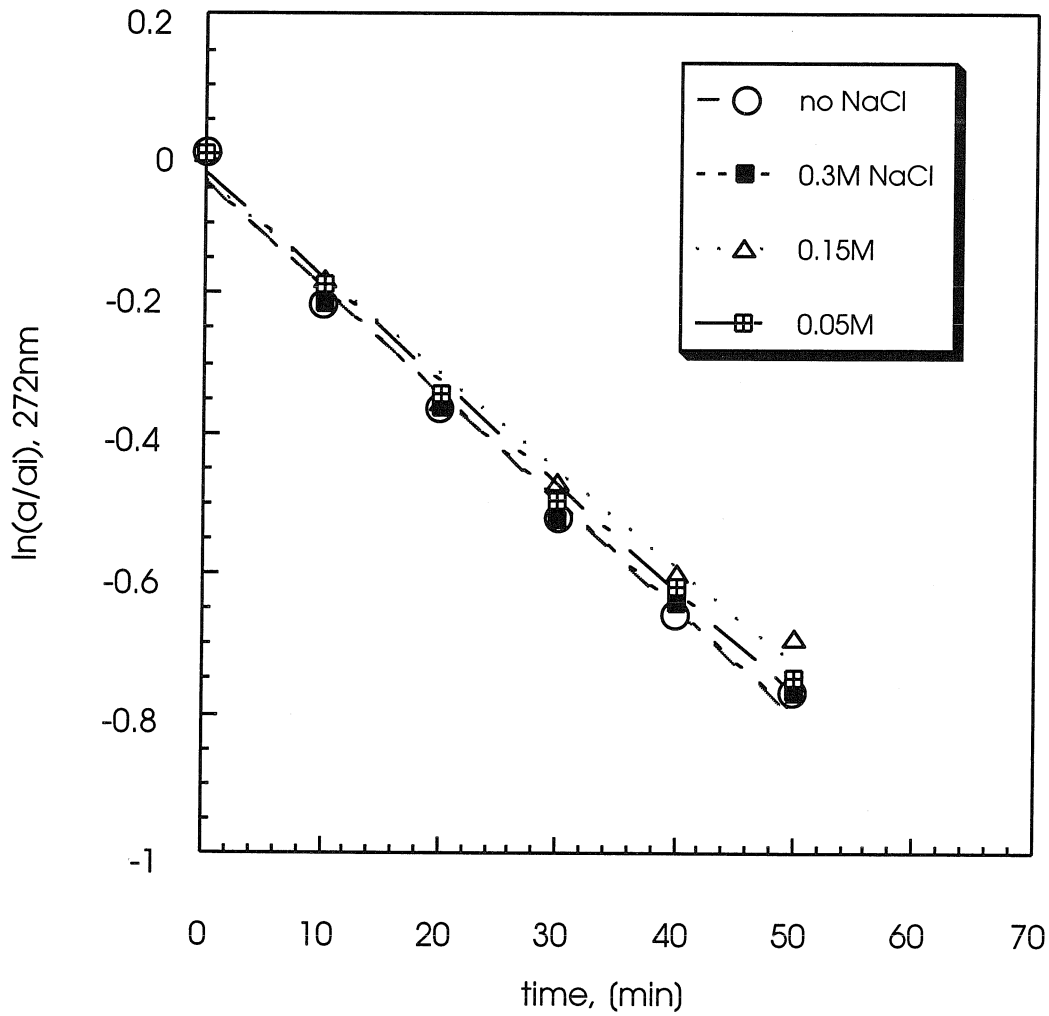

Fig. 3: Effect of ionic strength on hydrolysis kinetics. $[p\text{-NPA}]_i = 100\ \mu M$.

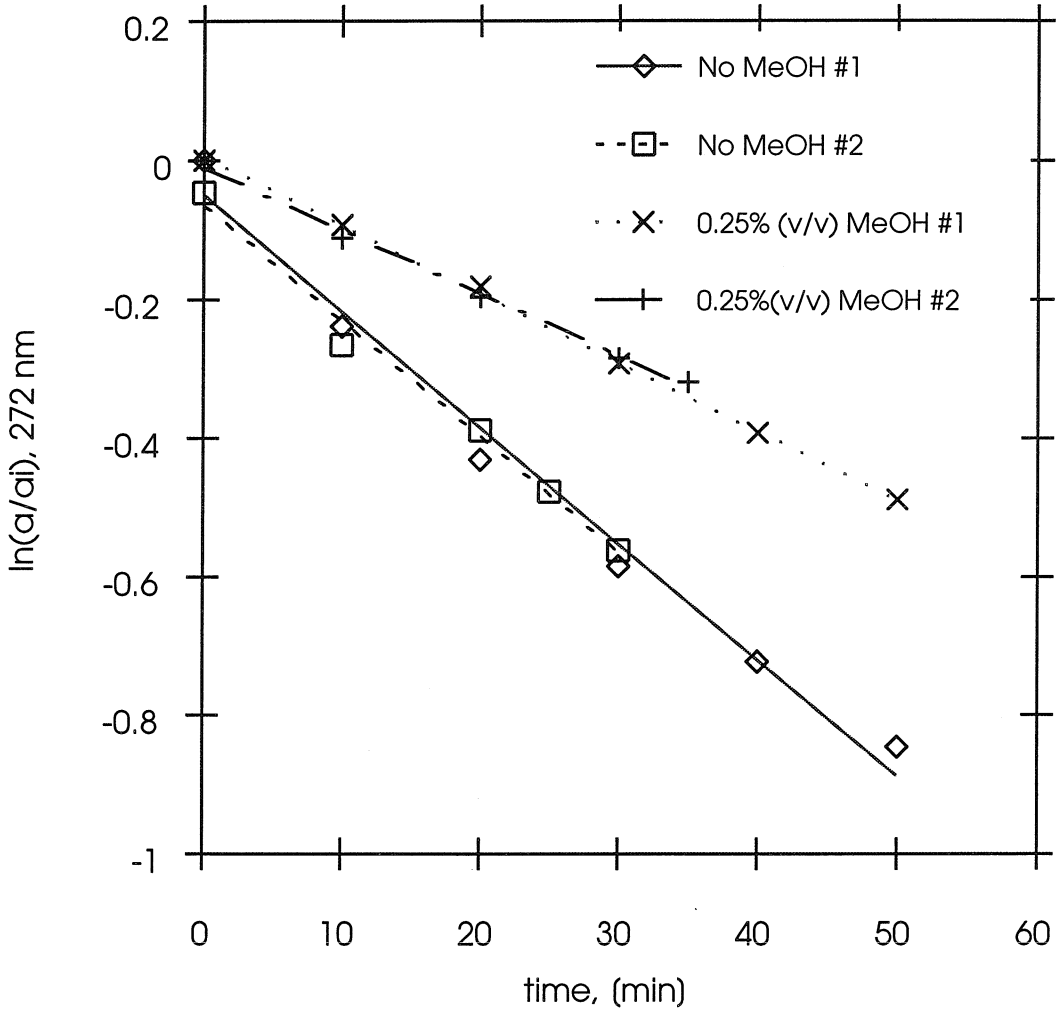

Fig. 4: Effect of co-dissolved methanol on hydrolysis kinetics. $[p\text{-NPA}]_i = 100\ \mu M$. The solution is Ar-saturated.

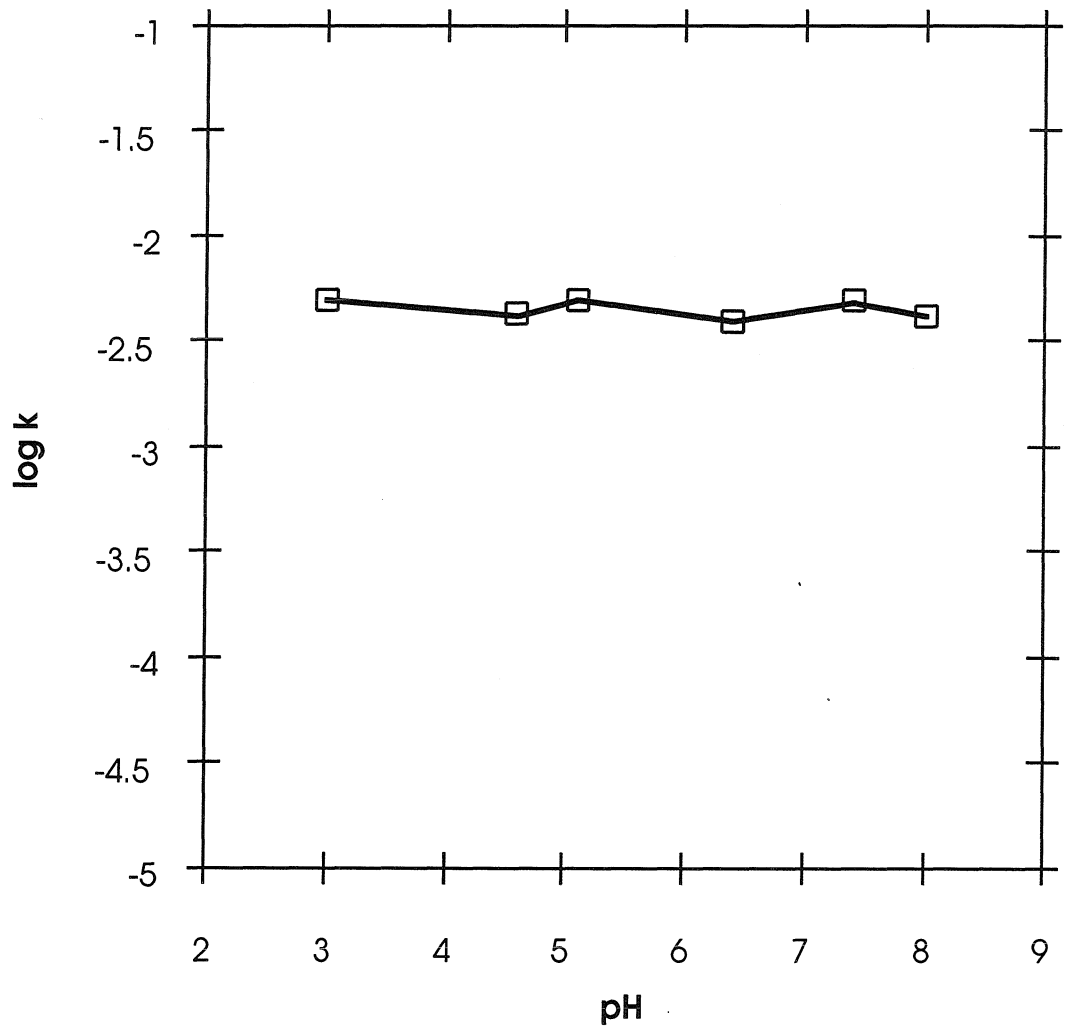

Fig. 5: p-NPA hydrolysis rate constant as a function of pH.

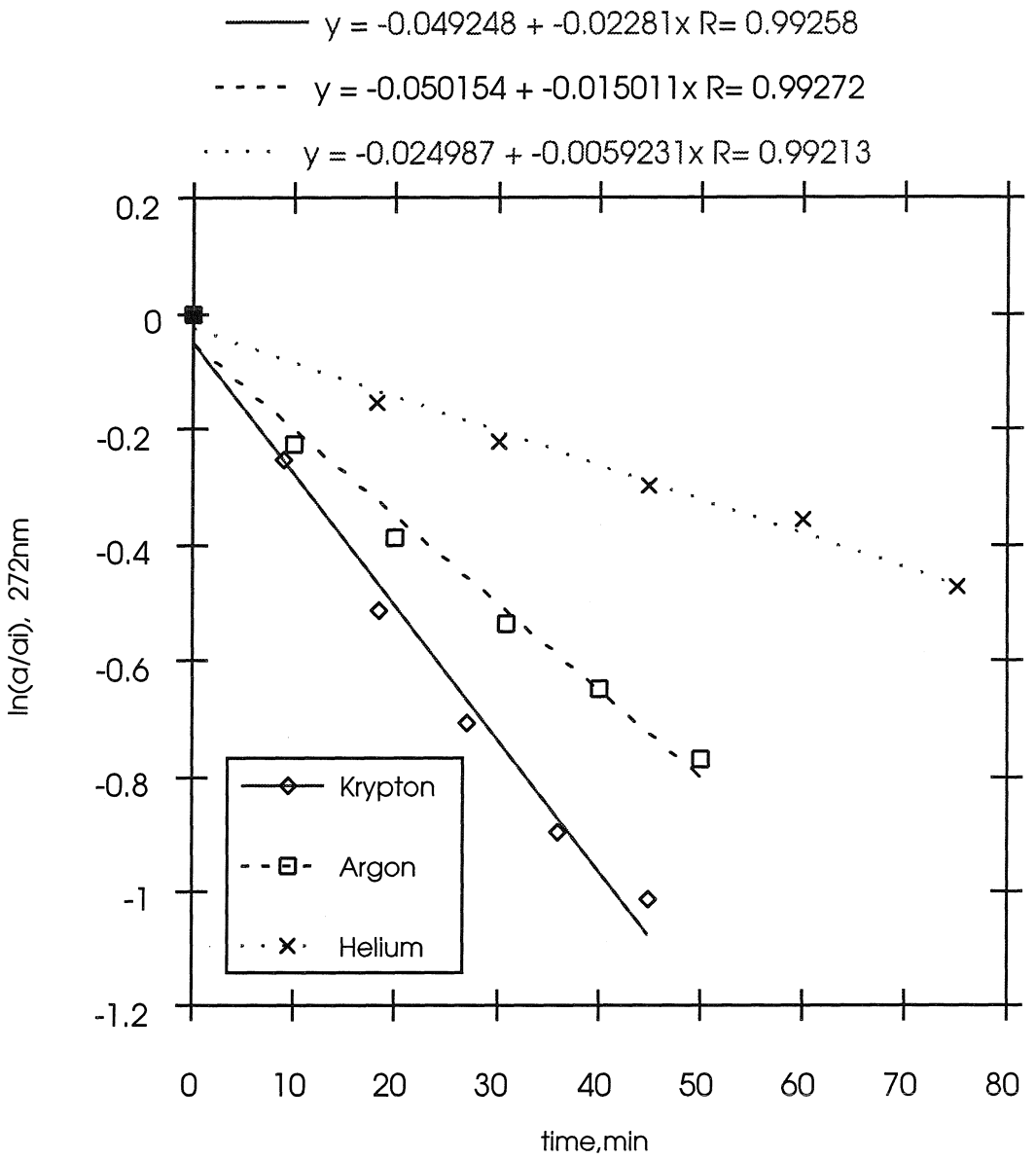

Fig. 6: First-order plot of p-NPA hydrolysis in a sonicated solution with different saturating gases.

Rate constants (s^{-1}): a) Kr: 3.8×10^{-4} b) Ar: 2.5×10^{-4} c) He: 9.8×10^{-5}.

a = absorbance at 272 nm at time, t. a_i = absorbance at 272 nm at t=0.

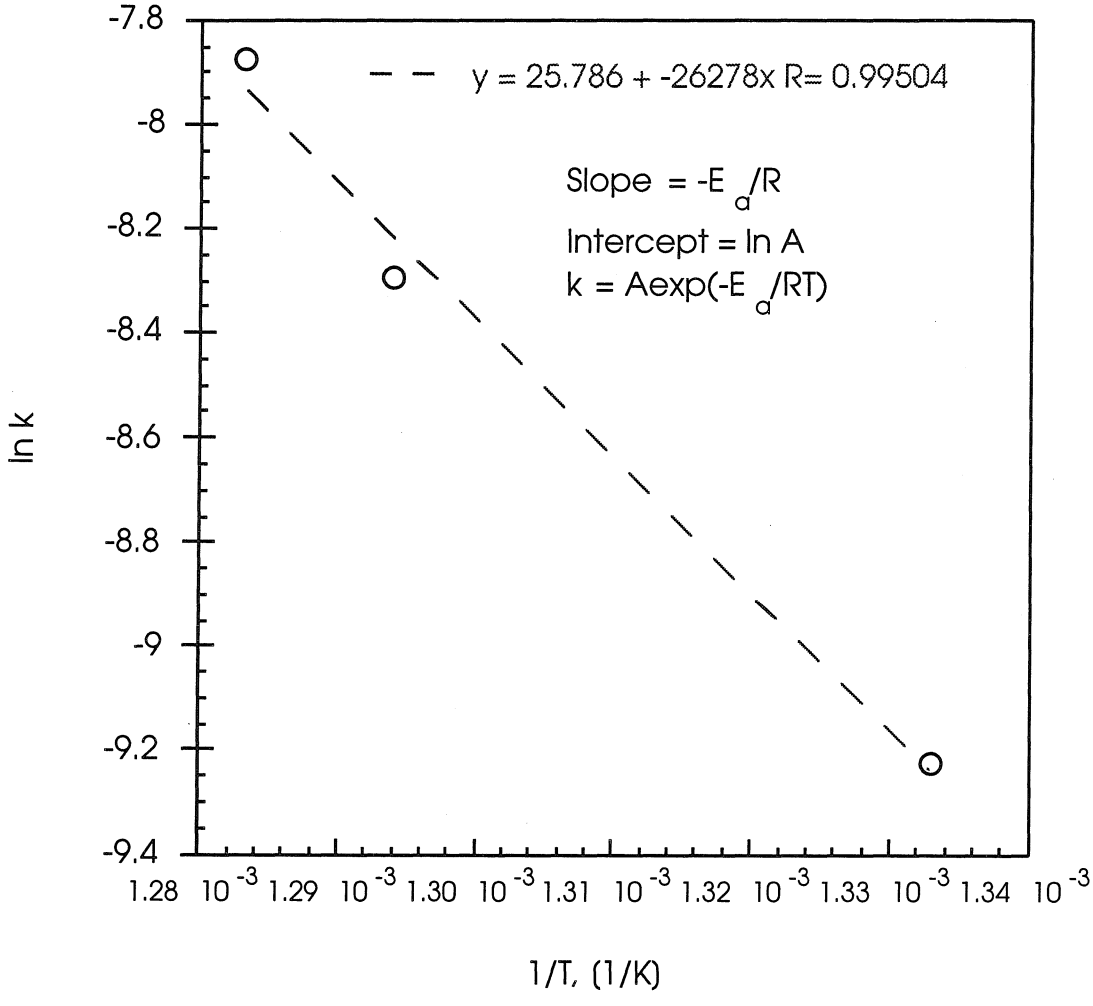

Fig. 7: Arrhenius plot of kinetics of hydrolysis of p-NPA in a sonicated solution.

$pH_i = 6.1$, $[p\text{-NPA}]_i = 100\ \mu M$.

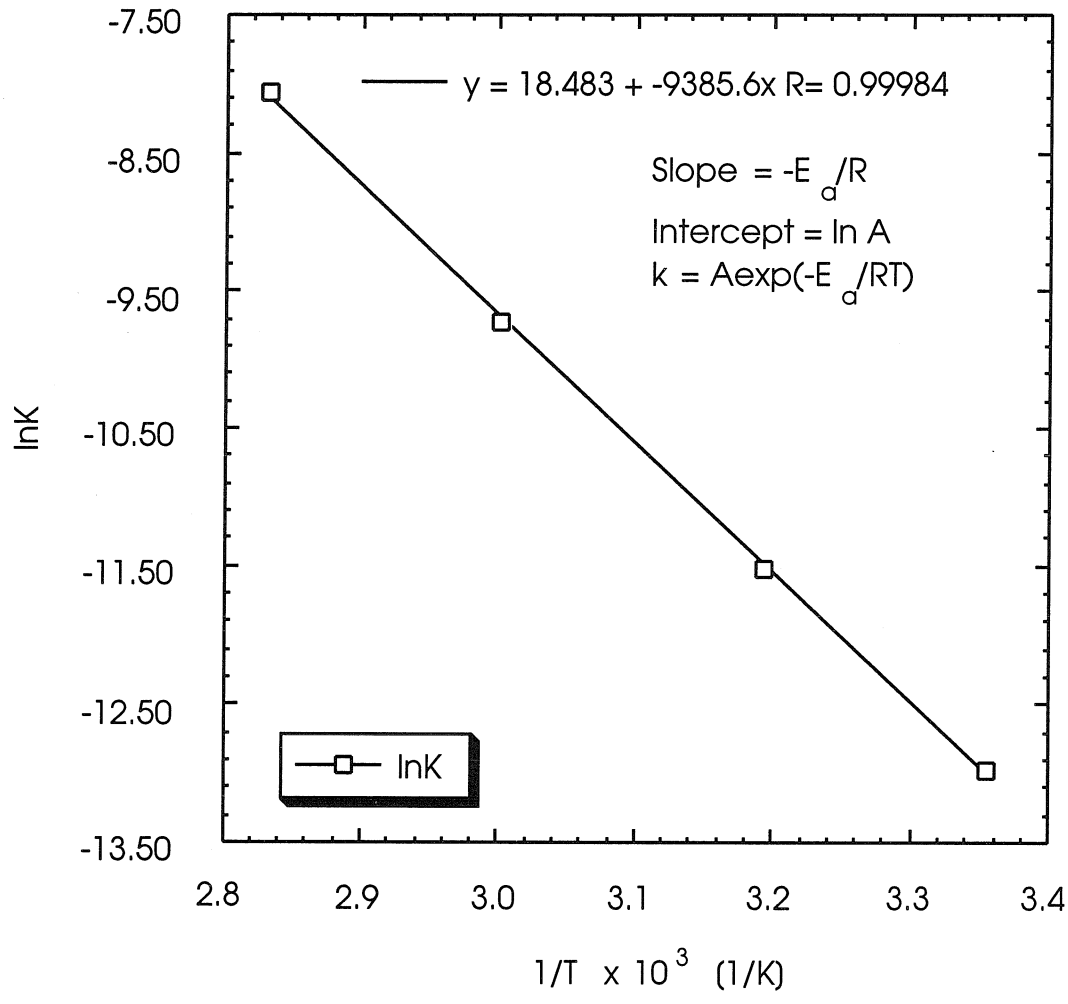

Fig. 8: Arrhenius plot of kinetic data for hydrolysis of p-NPA in an unsonicated solution. $[p\text{-NPA}]_i$ = 100 μM, I = 0.4 M (NaCl), pH = 6.

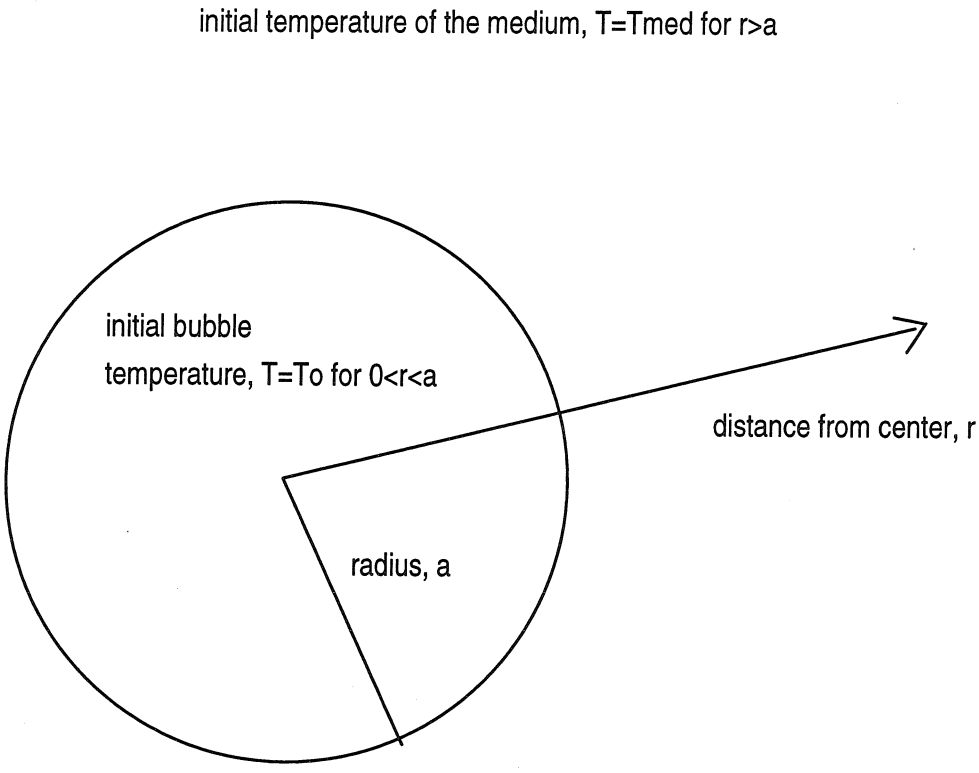

Fig. 9: Schematic of the heat transfer model with initial conditions.

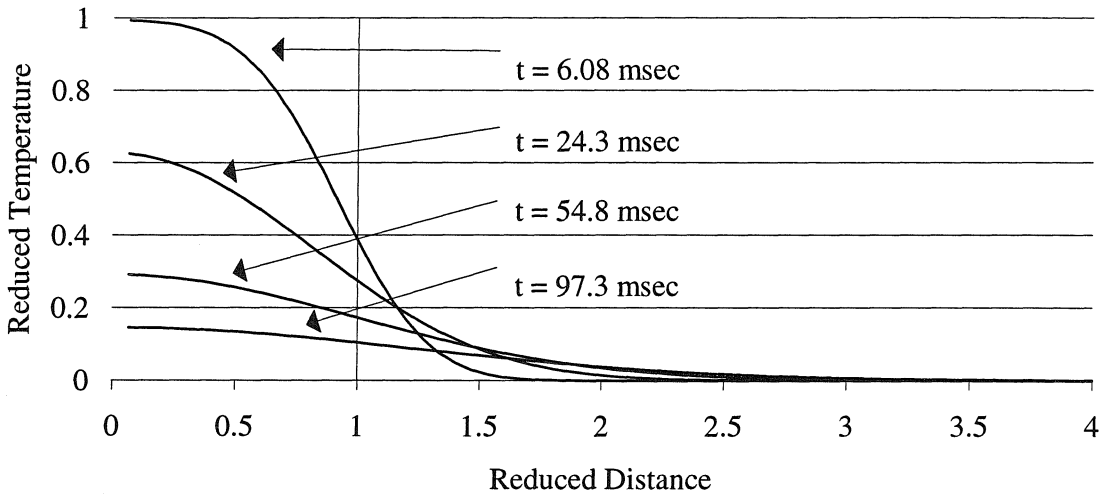

Fig. 10: Plot of the reduced temperature, T_{red}, versus the distance from the center of the bubble, r, for various times after bubble collapse.

- Chapter IV -

The Degradation of 2,4,6-Trinitrotoluene in Aqueous Solution by Ultrasonic Irradiation at Different Frequencies

The text of this chapter has been submitted for publication. [Höchemer, R. H., Hoffmann, M. R., Environ. Sci. Technol., May, 1996.]

Abstract

2,4,6-Trinitrotoluene (TNT) is degraded in the presence of ultrasonic irradiation to acetate, formate, glycolate, oxalate, carbon dioxide, nitrite, and nitrate. The degradation reaction follows apparent first-order kinetics. 1,3,5-trinitrobenzene appears to be the principal reaction intermediate based on its HPLC retention time and electrospray/MS evidence.

The observed first-order kinetics vary over a factor of 3 depending on the nature of the dissolved gases and the ultrasonic frequency. At 20 kHz, $k_{obs} = 1.67 \times 10^{-5}\ s^{-1}$ with O_2, $k_{obs} = 4.50 \times 10^{-5}\ s^{-1}$ with Ar, and $k_{obs} = 5.50 \times 10^{-5}\ s^{-1}$ with a O_2/O_3 (99/1 vol-%) mixture as cavitating background gases. The observed rate constants for 500 kHz are $k_{obs} = 2.00 \times 10^{-5}\ s^{-1}$ (O_2), $k_{obs} = 7.17 \times 10^{-5}\ s^{-1}$ (Ar), and $k_{obs} = 8.50 \times 10^{-5}\ s^{-1}$ (O_2/O_3). Ultrasonic irradiation at 500 kHz yielded consistently higher reaction rates than 20 kHz irradiation for all background gases.

Simultaneous irradiation with orthogonally-positioned 20 kHz and 500 kHz sound sources leads to a negative interference manifested in a diminished reaction rate compared to sonication with 500 kHz sound alone.

Introduction

The introduction of high power ultrasound (i. e., sound energy with frequencies in the range 15 kHz to 1 MHz) into liquid reaction mixtures is known to cause a variety of chemical transformations (*1-9*). In addition, the application of ultrasound as a physical catalyst in chemical synthesis has become an important field of research (*1-7*). In recent years, due to the growing need to eliminate undesirable chemical compounds, the utilization of high energy ultrasound for hazardous waste treatment has been explored (*3,7,10-24*).

Ultrasonic irradiation of liquid reaction mixtures induces electrohydraulic cavitation, a process that is characterized by the oscillation of preexisting gas cavities (i. e., cavitation nuclei) in a periodically changing pressure field created by the ultrasonic waves. These oscillations, which eventually become unstable, result in the violent implosion of the gas bubbles. This rapid implosion is accompanied by an adiabatic heating of the vapor phase of the bubble, that yields localized and transient high temperatures and pressures. Temperatures on the order of 4200 K and pressures of 975 bar have been estimated (*3*). Noltingk and Neppiras estimate even higher temperature and pressure values that range up to 10,000 K and 10,000 bar (*25-27*).

Upon ultrasonic irradiation organic compounds in water are degraded via several mechanisms, due to the extreme transient conditions. Three main pathways involving hydroxyl radical, pyrolytic degradation and supercritical water have been identified (*15*). In the case of an aqueous solution, water vapor present in the bubble is homolytically split to yield $OH^{\bullet}$ and $H^{\bullet}$ radicals. Chemical substrates that are present within or in close vicinity to the collapsed bubbles are subject to direct attack by $OH^{\bullet}$ (*12,13,16*). Volatile compounds such as H_2S and CCl_4 partition into the gas phase (i.e., into the gaseous bubbles within the aqueous solution) and undergo pyrolysis (*10,11*). Furthermore, it has been found that hydrolysis reactions are accelerated by several orders of magnitude in the

presence of ultrasound (*15*). These accelerated reaction rates have been attributed to the existence of transient supercritical water (*15*) during ultrasonic irradiation.

This paper focuses on the potential use of high energy ultrasound for the degradation of 2,4,6-trinitrotoluene (TNT) in aqueous solution. TNT is the most commonly used high-energy explosive. TNT contamination of ground and surface waters in the vicinity of former production sites is a major problem in the U. S. (*28-33*) and in Europe (*34-37*). Exposure to TNT causes liver damage (*38*); and its presence in natural waters represents a serious threat to common health.

A variety of analytical techniques for the qualitative and quantitative detection of TNT have been reported, including GC/MS (*32,33,39-42*) , HPLC (*43-46*), biological monitoring (*47,48*), and others (*46,49-53*). The majority of research into the treatment of wastewater containing explosives (i.e., effluents from munitions production plants or contaminated natural water bodies) has been focused on microbial treatment (*54-66*) with either aerobic or anaerobic organisms. However, biological processes for TNT degradation are characterized by relatively long retention times (e. g., days to weeks) and are sensitive to the specific composition of the waste.

Several physico-chemical processes for the treatment of TNT contaminated waters have been investigated. They include wet air oxidation (*67*), UV-photolysis (*68,69*), and UV irradiation with H_2O_2 and O_3 (*31,70-73*). The treatment of TNT solutions with O_3/ultrasound has been reported (*74*). However no reaction was observed when ultrasound was applied without an added oxidant. The enhancement of the oxidation of TNT by H_2O_2 with ultrasound was attributed to the improved mass transport in ultrasonically irradiated solutions (*74*).

To our knowledge, the work presented in this paper is the first investigation of the application of high power ultrasound to the degradation of TNT. The present kinetic study includes a characterization of intermediate and final products and a comparison of

the treatment efficiencies as a function of ultrasonic frequency and the nature of the cavitating gas.

Experimental Methods

Chemicals

2,4,6-Trinitrotoluene (Chem Service, 99 % + 10 % water added), 1,3,5-trinitrobenzene, TNB, (Chem Service, 99%), sodium oxalate (Baker Analyzed, >99.98 %), sodium acetate (Mallinckrodt, analytical reagent), pyruvic acid (Sigma, 99+%), sodium formate (Mallinckrodt, analytical reagent), glycolic acid, (Fluka, 99 %), sodium nitrate, (Mallinckrodt, analytical reagent), and sodium nitrite (Baker Analyzed, reagent grade) were used without further purification. TNT used in the preparation of quantitative standards was dried for two days in a desiccator before use. All solutions and calibration standards were prepared with deionized water (Millipore, Milli-Q UV plus, R=18.2 MΩ cm^{-1}).

Sonochemistry

Ultrasonic irradiations of dilute aqueous solutions of TNT were conducted at frequencies of 20 kHz and 500 kHz. The applied power, P, power densities, P_V, and power intensities, P_A, for the various reactor setups are based on wall-wattage and on the power that is actually introduced into the solution (Table 1). The ultrasonic power transmitted into irradiated solutions was estimated calorimetrically by measuring the temperature rise o fa known mass of water, m. The temperature rise is linear with time over the first 10 minutes of irradiation. The power introduced into solution was estimated using eq. 1,

$$P = m \cdot C_m \cdot \frac{\Delta T}{\Delta t} \qquad (1)$$

where C_m = 4.18 J K^{-1} g^{-1} is the specific heat of water at 25 °C, and $\Delta T/\Delta t$ is the initial slope of the temperature/time curve.

For the generation of ultrasound at 20 kHz, two different ultrasonic devices were used. One system consisted of an ultrasonic horn (Sonics & Materials, VCX 400) and a detachable stainless steel reactor. Entrance and exit ports allowed for the continuous gas sparging and sampling during experiments. The other system involved a glass reactor (Orthoreactor, Undatim), using a different ultrasonic probe (20 kHz transmitter, Undatim). Reaction volumes were 50 mL for the stainless steel reactor and 650 mL for the Orthoreactor. Both reactors were equipped with cooling jackets. The temperature was held constant at 10 °C throughout all experiments.

The Orthoreactor is characterized by a wide opening at the side to which a 500 kHz transmitter (Undatim) is attached. A standard ultrasonic horn is inserted through the top port of the vessel. This orthogonal configuration allows for the investigation of simultaneous irradiation at two different frequencies, in this case 500 kHz and 20 kHz. In order to investigate synergistic effects of ultrasound at 20 and 500 kHz, simultaneous as well as separate irradiations were conducted in the Orthoreactor. The geometrical setup of the reactor setup for all three experiments (i. e., simultaneous irradiation at 20 kHz and 500 kHz, irradiation at 20 kHz, and irradiation at 500 kHz) were held constant.

Ultrasonic irradiations were performed using Ar, O_2 and an O_2/O_3 (99/1 vol-%) mixture, respectively, as cavitating gas. The O_2/O_3 mixture was supplied by an ozone generator (OREC, V10-0). Throughout all experiments the sparging rate was maintained at 100 mL min^{-1} (Gilman Instruments flow meter).

Since the partitioning of TNT between the bulk aqueous solution and the bubble/solution interface was not expected to depend on the pH, neither buffers nor other electrolytes were added to the reaction solution in order to avoid possible interferences.

Chemical Analysis

The decrease in the TNT concentration and the generation of nitroaromatic intermediates was monitored using high performance liquid chromatography, HPLC, (Hewlett Packard, Series II 1090) coupled with photodiode array detection. In a typical analysis, 25 μL of the filtered (Gelman, 0.2 μm PFTE filters) sample solution were injected and separated with a 3 μm, 100×4 mm, C-18 Hypersil column (Hewlett Packard). Chromatograms were recorded using the absorbance at λ = 235 nm. The eluent peaks were identified by their retention time and absorbance spectra. In order to facilitate peak identification an existing H_2O/MeOH gradient method was used (*75*).

For quantitative determination of TNT, standards were prepared by dissolving dried TNT in deionized water. The HPLC was calibrated using the integrated peak areas of a concentration series of TNT chromatograms. The TNT calibration was found to be reproducable and very stable.

In order to identify intermediate degradation products, fractions of the HPLC effluent were collected and concentrated by partial evaporation of the H_2O/MeOH solvent mixture. Samples of the preconcentrated fractions were injected into an ESI/MS (i. e., electrospray ionization/mass spectroscopy) instrument (VG ProSpec, Fisons Instruments) at a flow rate of 7 μL/min using a syringe injection pump (Harvard Apparatus 22) with 1μL injection loop. A H_2O/MeOH (50/50-vol-%) mixture containing 1% AcOH served as the spray liquid. In comparison to more conventional ionizing methods (i. e., electron ionization, EI, and chemical ionization, CI), electrospray ionization (ESI) is a relatively mild method of introducing a charged analyte sample into a mass spectrometer (MS),

allowing for the direct detection of a charged parent compound molecule rather than its fragmentation products.

The generation of inorganic and organic ions was followed by ion chromatography, IC, (Dionex, Bio-LC) with electrical conductivity detection. The stationary phase was an Omnipax analytical column PAX-500, and the mobile phase consisted of 1 mM NaOH, 200 mM NaOH and 5% MeOH at a combined flow rate of 1 mL min^{-1} with 20 mM H_2SO_4 at 15 mL min^{-1} as regenerating solution.

The pH was determined with a Beckman Φ 71 pH meter.

Results and Discussion

Ultrasonic irradiation of aqueous solutions of TNT results in a decrease in the TNT concentration according to first-order kinetics for all reaction conditions. The magnitude of the observed first-order degradation rate constants, k_{obs}, depends on the applied frequency as well as on the nature of the cavitating background gas as shown in Figs. 1 and 2. The combination of the 500 kHz sonicator and O_3 (i. e., 500 kHz/O_3) exhibited the highest rate. Table 2 summarizes the measured values of k_{obs} under the various conditions. In the absence of ultrasound, no TNT degradation was observed under Ar and O_2. In the presence of aqueous O_3, a slow degradation of TNT was observed. This reaction was accelerated significantly with ultrasound. Introduction of 500 kHz sound resulted in a more pronounced acceleration of the TNT degradation than that observed at 20 kHz. The slow oxidation of TNT by O_3 in the absence of ultrasound is most likely due to the strong electron withdrawing effect of the three nitro groups which deactivates TNT for attack by electrophiles (*68*).

A typical HPLC chromatogram with detection at λ = 235 nm shows two intermediate reaction products at retention times of 4.37 min and 5.65 min in addition to the TNT peak at 10.23 min. The peak at 5.65 min is identified on basis of its retention

time and ESI/MS evidence (peak at -m/z = 211) as 1,3,5-trinitrobenzene (TNB). The following mechanism is proposed for the generation of TNB. $OH^{\bullet}$ attacks the methyl group of TNT, yielding a TNT radical, which is stabilized by delocalization of the unpaired electron over the three nitro groups.

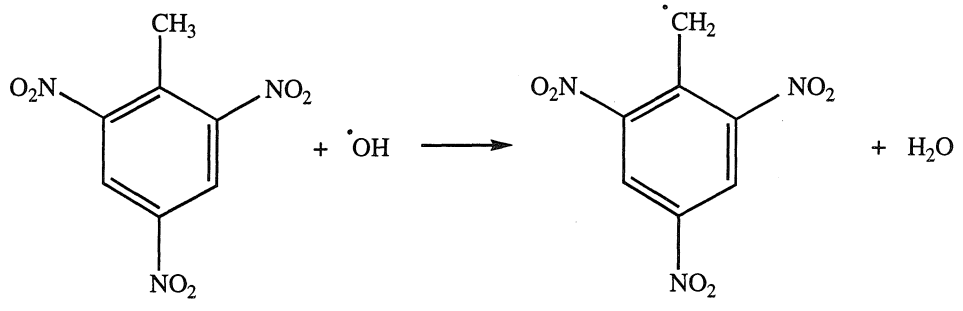

(2)

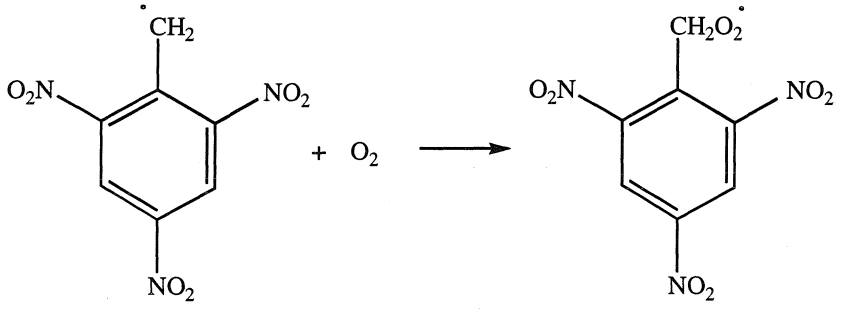

(3)

The peroxy radical intermediate of eq. 3 is oxidized by $OH^{\bullet}$ to 2,4,6-trinitrobenzoic acid, TNBA as follows:

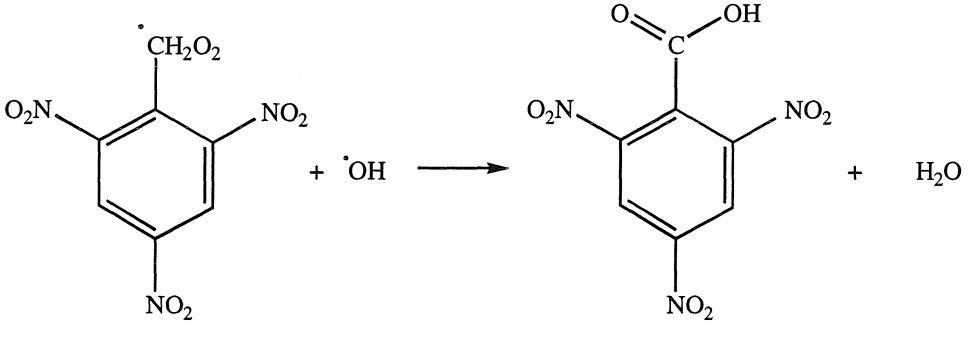

(4)

Decarboxylation of TNBA yields TNB.

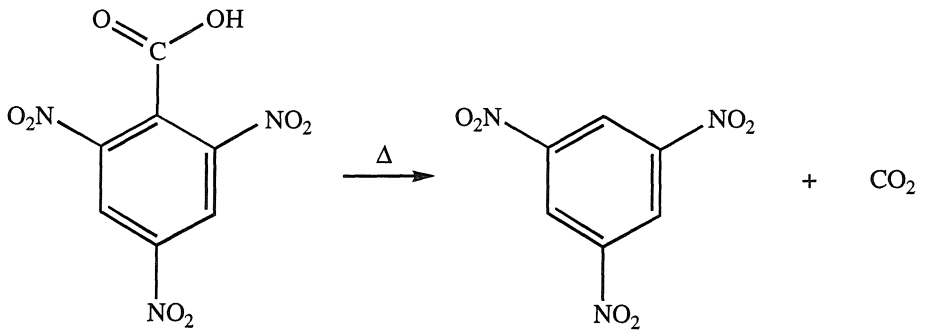

(5)

A similar mechanism has been proposed for TNT degradation induced by TiO_2 photocatalysis (*68*) suspension. Ho (*76*) proposed an analog mechanism for the oxidation of 2, 4 - dinitrotoluene to 1, 3 -dinitrobenzene in aqueous solution in the presence of H_2O_2 by photogenerated $OH^{\bullet}$ radical attack. We propose that the $OH^{\bullet}$ radicals produced during the ultrasonically induced cavitation lead to the same mechanism for the transformation of TNT to TNB. $OH^{\bullet}$ radical attack of the ring rather than the methyl group leads to hydroxylated TNT derivatives.

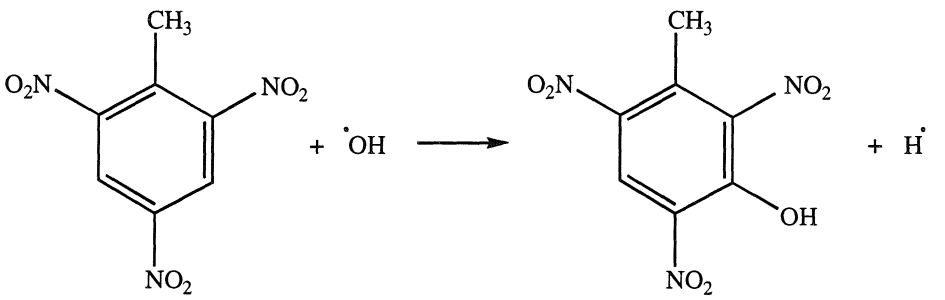

(6)

In addition to the $OH^{\bullet}$ radical pathway, pyrolytic cleavage of an NO bond is also expected to occur in TNT molecules that are in close vicinity of the hot bubble/solution interface as follows:

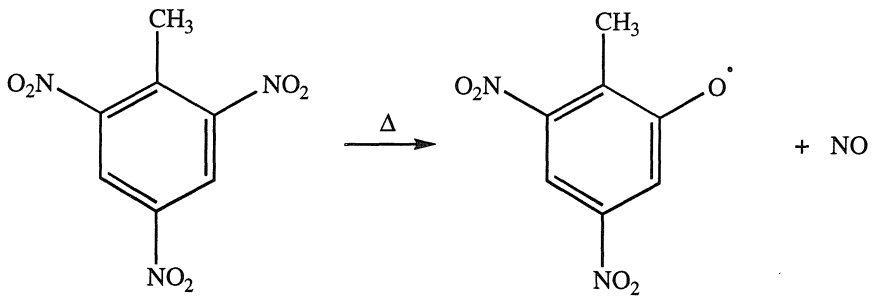

(7)

The nitrous oxide is then further oxidized to yield NO_2^- and NO_3^-.

$$NO + {}^{\bullet}OH \rightarrow HONO \Leftrightarrow H^+ + NO_2^- \quad (8)$$

$$HONO + {}^{\bullet}OH \rightarrow {}^{\bullet}NO_2 + H_2O \quad (9)$$

$${}^{\bullet}NO_2 + {}^{\bullet}OH \rightarrow HNO_3 \quad (10)$$

Awad and Stanbury (*77*) have shown that NO is subject to autoxidation in the presence of O_2 in aqueous solution:

$$2NO + O_2 \rightarrow 2NO_2 \quad (11)$$

$$NO_2 + NO \rightarrow N_2O_3 \quad (12)$$

$$N_2O_3 + H_2O \rightarrow 2NO_2^- + 2H^+ \quad (13)$$

Sonication leads to the generation of short chain organic acids, including acetic, glycolic, formic, and oxalic acid, under both frequencies, and is shown for the 500 kHz sonicator using Ar, O_3 and O_2 in Fig. 3. The corresponding stoichiometric equations for complete TNT degradation with either O_2, O_3, and $OH^{\bullet}$ as the oxidizing agents are given in eqs 13-15.

$$C_7H_5(NO_2)_3 + 9O_2 \xrightarrow{)))} 7CO_2 + H_2O + 3H^+ + 3NO_3^- \quad (14)$$

$$C_7H_5(NO_2)_3 + 6O_3 \xrightarrow{)))} 7CO_2 + H_2O + 3H^+ + 3NO_3^- \quad (15)$$

$$C_7H_5(NO_2)_3 + 36OH^\bullet \xrightarrow{)))} 7CO_2 + 19H_2O + 3H^+ + 3NO_3^- \quad (16)$$

While sonication of Ar- or O_2-sparged TNT solution leads to the production of both NO_3^- and NO_2^-, Fig. 4, no NO_2^- was detected when using O_3 as a background gas. The production of acids is accompanied by a change in the solution pH. The initial pH value of 5.6 drops to values between 3.8 - 4.6 depending on the extent of the TNT degradation. Acetate and nitrate are the main contributors to the production of acidity. A typical degradation experiment generates 80 μM acetate and 40 μM nitrate. The pH of an aqueous solution that has these concentrations in acetate and in nitrate can be calculated to 4.1, which agrees well with the observed pH.

A synergistic effect between multiple frequencies in the Orthoreactor is not observed as is observed in multiple frequency parallel-plate reactors (*16*). On the other hand, simultaneous irradiation with 500 kHz and 20 kHz results in slightly lower degradation rates than observed for the 500 kHz system alone (Fig. 5). This effect may be due to negative interference of the sound waves, which will diminish the amount of energy that is available for inducing cavitation. The possibility of synergistic effects between multiple frequencies is interesting from a scientific and an economic standpoint. However factors such as the relative positioning of the sound sources (orthogonal, parallel, or at different angles), the power density within the irradiated solution, and the power intensity of the sound sources have to be taken into account.

The power delivered to solution as well as the actual solution volume is different for each irradiation configuration (Table 1). In order to compare the relative efficiencies of TNT degradation under the different experimental conditions, we introduce the concept of a G-value for sonolysis, which is most often used in radiolysis (*78,79*), where it is defined as the number of molecules converted per 100 eV of energy absorbed by the

reaction medium (*80*). We define the G-value in eq. 17 as the number of TNT molecules degraded per J energy input,

$$G-\text{value} \equiv \frac{N_A \cdot V}{P} \frac{d[TNT]}{dt} \tag{17}$$

where $N_A = 6.023 \times 10^{23}\ mol^{-1}$ is the Avogadro constant, V is the reaction solution volume in units of L, and P is the power input in units of W. The derivative, d[TNT]/dt, represents the initially observed rate of TNT degradation. Table 3 summarizes the G-values for all of the irradiation conditions. The calculations for the G-values have been carried out for P equal to the wall-wattage as well as for P equal to the power transmitted into solution. The acoustical power which actually produces cavitation of the aqueous solution could be significantly less than the power estimates based on either wall-wattage or calorimetric measurements. The G-values given in Table 3 are therefore lower bounds for the efficiency. TNT degradation appears to be more efficient for 500 kHz ultrasound than for 20 kHz ultrasound. The higher efficiency at 500 kHz may be the result of several factors involving the power intensity, P_A. As has been shown previously, the efficiency depends strongly on P_A (*16*). If a certain intensity threshold is reached, further increases of P_A lead to a decrease in efficiency due to decoupling of the solution from the transmitter. The power intensity of the 500 kHz sound source is relatively low (P_A = 4.98 W cm^{-2} or 1.67 W cm^{-2}, based on wall-wattage or calorimetry respectively). The 20 kHz probe omthe other hand, exhibits a relatively high power intensity (P_A = 116 W cm^{-2} or 43.6 W cm^{-2}, based on wall-wattage or calorimetry respectively) and the observed low G-value is in part caused by decoupling of energy transmission between the probe tip and the solution. In addition, since TNT is preferentially attacked by $OH^{\bullet}$ radical, the frequency that produces $OH^{\bullet}$ radicals at a higher rate is expected to be the more efficient one for TNT degradation. Cavitation induced by 500 kHz is more stable than that

induced by lower freqencies. Stable cavitation (500 kHz) results in a higher $OH^{\bullet}$ radical production rate whereas transient cavitation (20 kHz) leads to the enhancement of pyrolitic reactions. Furthermore, the resonant radius of a cavitating bubble is smaller at the higher frequency, causing the $OH^{\bullet}$ radical to be more effectively ejected into the solution surrounding a cavitation bubble, which leads to a decreased recombination rate and thus a higher overall generation rate of $OH^{\bullet}$ radicals (*20*). The $OH^{\bullet}$ radical generation for 20 and 500 kHz is shown in Fig. 6 (*81*). The 500 kHz ultrasonic transmitter exhibits a higher production rate for $OH^{\bullet}$ radicals, which attack the TNT in the initial step of the degradation reaction.

Conclusion

It has been shown that ultrasonic irradiation of aqueous TNT solutions results in the degradation of TNT to yield short chain organic acids, CO_2 NO_3^- and NO_2^-. TNB has been identified as a main reaction intermediate. The formation of TNB is the result of $OH^{\bullet}$ radical oxidation of TNT and subsequent decarboxylation of the trinitrobenzoic acid (TNBA) intermediate. In order to fully understand the mechanism of the sonochemical degradation of TNT, other possible reaction intermediates need to be identified. This is a difficult task due to the very low steady-state concentrations of potential reaction intermediates during irradiation. We are currently working on the determination of additional nitroaromatic degradation products.

Sonochemical degradation of TNT at 500 kHz is more efficient than at 20 kHz by at least one order of magnitude, due to the more effective energy coupling at low power intensities and the higher rate of $OH^{\bullet}$ radical production.

The negative synergistic effect of irradiation with 20 kHz and 500 kHz transmitters simultaneously can be explained by the occurrence of destructive interference of the two ultrasonic sound wave fields. In designing an ultrasonic reactor, care has to be

taken in order to avoid the possible diminishing return in chemical effects when the power input is increased.

Acknowledgment: The authors wish to thank Inez Hua for making the $OH^{\bullet}$ generation data available, and Ronald L. Siefert for the introduction to the IC. Peter Green and Yuanda Zhang are gratefully acknowledged for their help with the ESI/MS analysis. The authors are grateful for financial support from the Advanced Research Projects Agency, ARPA, and the Office of Naval Research, ONR, (Grant # NAV 5HFMN N0001492J1901), and the Electric Power Institute, EPRI, (Grant # RP 8003-37).

References

(1) Berlan, J.; Mason, T. J. *Ultrasonics* **1992**, *30*, 203-212.

(2) De Souza Barboza, J. C.; Petrier, C.; Luche, J. L. *J. Org. Chem.* **1988**, *53*, 1212-1218.

(3) Mason, T. J.; Lorimer, J. P. *Sonochemistry: Theory, Applications and Uses of Ultrasound in Chemistry*; Ellis Horwood Ltd.: Chichester, 1988.

(4) Mason, T. J. *Advances in Sonochemistry*; Mason, T. J., Ed.; JAI Press Ltd.: London, 1990; Vol. 1.

(5) Mason, T. J. *Practical Sonochemistry: User's Guide to Applications in Chemistry and Chemical Engineering*; Ellis Horwood: Chichester, 1991.

(6) Mason, T. J. *Ultrasonics* **1992**, *30*, 192-196.

(7) Suslick, K. S. *Ultrasound: Its Chemical, Physical and Biological Effects*; Suslick, K. S., Ed.; VCH Publishers, Inc.: New York, 1988.

(8) Richards, W. T.; Loomis, A. L. *J. Am. Chem. Soc.* **1927**, *49*, 3086-3100.

(9) Weissler, A.; Cooper, H. W.; Snyder, S. *J. Am. Chem. Soc.* **1950**, *72*, 1769-1775.

(10) Kotranarou, A.; Mills, G.; Hoffmann, M. R. *Environ. Sci. Technol.* **1992**, *26*, 2420-2428.

(11) Kotronarou, A. *Ph. D. Thesis*; Kotronarou, A., Ed.; California Institute of Technology, Pasadena, 1991.

(12) Kotronarou, A.; Mills, G.; Hoffmann, M. R. *J. Phys. Chem.* **1991**, *95*, 3630-3638.

(13) Kotronarou, A.; Mills, G.; Hoffmann, M. R. *Environ. Sci. Technol.* **1992**, *26*, 1460-1462.

(14) Cost, M.; Mills, G.; Glisson, P.; Lakin, J. *Chemosphere* **1993**, *27*, 1737-1743.

(15) Hua, I.; Höchemer, R. H.; Hoffmann, M. R. *J. Phys. Chem.* **1995**, *99*, 2335-2342.

(16) Hua, I.; Höchemer, R. H.; Hoffmann, M. R. *Environ. Sci. Technol.* **1995**, *29*, 11, 2790-2796.

(17) Koskinen, W. C.; Sellung, K. E.; Baker, J. M.; Barber, B. L.; Dowdy, R. H. *J. Environ. Sci. Health Part B* **1994**, *29*, 581-590.

(18) Olson, T. M.; Barbier, P. F. *Wat. Res.* **1994**, *28*, 1383-1391.

(19) Petrier, C.; Micolle, M.; Merlin, G.; Luche, J. L.; Reverdy, G. *Environ. Sci. Technol.* **1992**, *26*, 1639-1642.

(20) Petrier, C.; Lamy, M. F.; Francony, A.; Benahcene, A.; David, B.; Renaudin, V.; Gondrexon, N. *J. Phys. Chem.* **1994**, *98*, 10514-10520.

(21) Serpone, N.; Terzian, R.; Colarusso, P.; Minero, C.; Pelizzetti, E.; Hidaka, H. *Res. Chem. Intermed.* **1992**, *18*, 183-202.

(22) Serpone, N.; Terzian, R.; Hidaka, H.; Pelizzetti, E. *J. Phys. Chem.* **1994**, *98*, 2634-2640.

(23) Wu, J. M.; Huang, H. S.; Livengood, C. D. *Environ. Prog.* **1992**, *11*, 195-201.

(24) Price, G. J.; Matthias, P.; Lenz, E. J. *Process Safety and Environmental Protection: Transactions of the Institution of Chemical Engineers Part B* **1994**, *72*, 27-31.

(25) Noltingk, B. E.; Neppiras, E. A. *Proc. Phys. Soc. B. (London)* **1950**, *63B*, 674-685.

(26) Neppiras, E. A.; Noltingk, B. E. *Proc. Phys. Soc. B (London)* **1951**, *64B*, 1032-1038.

(27) Putterman, S. *Sci. Am.* **1995**, *272*, 46-51.

(28) Chen, T. H.; Campbell, C.; Fisco, W. J. "Characterization of Pollutants at Holston Army Ammunition Plant," US Army ARRADCOM, 1981.

(29) Conley, K. A.; Mikucki, W. J. "Migration of Explosives and Chlorinated Pesticides in a Simulated Sanitary Landfill," Construction Engineering Research Laboratory, 1976.

(30) Hall, T. N.; Lawrence, G. W. "A Study of the Organic Components of Red Water," Naval Surface Weapons Center, 1976.

(31) Kobylinski, E. A.; Burrows, W. D. "Tertiary Treatment of Effluent from Holston AAP Industrial Liquid Waste Treatment Facility II. Corona Oxidation Studies: TNT, RDX, HMX, TAX, and SEX," US Army Medical Bioengineering Research and Development Laboratory, 1983.

(32) Spanggord, R. J.; Gibson, B. W.; Keck, R. G.; Thomas, D. W.; Barkley, J. J. J. *Environ. Sci. Technol.* **1982**, *16*, 229-232.

(33) Spanggord, R. J.; Suta, B. E. *Environ. Sci. Technol.* **1982**, *16*, 233-236.

(34) Haas, R. ;. v. L., E. *Grundwasserbelastung durch eine Altlast. Die Folgen einer ehemaligen Sprengstoffproduktion für die heutige Trinkwassergewinnung*; Haas, R. ;. v. L., E., Ed., 1986; Vol. 37, pp 33-43.

(35) Haas, R.; Schreiber, I.; Löw, E. v.; Storck, G. *Fresenius J. Anal. Chem.* **1990**, *338*, 41-45.

(36) Haas, R.; Storck, G. *Fresenius Z. Anal. Chem.* **1989**, *335*, 839-846.

(37) Haas, R.; Schreiber, I.; Storck, G. *Z. Umweltchem. Ökotox.* **1990**, *2*, 139-141.

(38) Li, G. Y.; Wang, T.; Shams, N. K. B.; Davis, J. F.; Calkins, J. H.; Hornung, C. A.; Altekruse, J. M.; Sigel, M. M. *J. Med.* **1992**, *34*, 930-933.

(39) Hable, M.; Stern, C.; Asowata, C.; Williams, K. *J. Chrom. Sci.* **1991**, *29*, 131-135.

(40) Lee, M. R.; Chang, S. C.; Kao, T. S.; Tang, C. P. *J. Res. Nat. Bur. Stand.* **1988**, *93*, 428-431.

(41) Laramee, J. A.; Deinzer, M. L. *Anal. Chem.* **1994**, *66*, 719-724.

(42) Feltes, J.; Levsen, K.; Volmer, D.; Spiekermann, M. *J. Chromatogr.* **1990**, *518*, 21-40.

(43) Emmrich, M.; Kaiser, M.; Ruden, H.; Sollinger, S. *J. Chromatogr.* **1993**, *645*, 89-94.

(44) Bouvier, E. S. P.; Oehrle, S. A. *LC-GC* **1995**, *13*, 120-130.

(45) Major, M. A.; Checkai, R. T.; Phillips, C. T.; Wenstel, R. S.; Nwanguma, R. O. *Intern. J. Anal. Chem.* **1992**, *48*, 217-227.

(46) Walsh, M. E.; Jenkins, T. F. *Anal. Chim. Acta* **1990**, *231*, 313-315.

(47) Shriver-Lake, L. C.; Breslin, K. A.; Charles, P. T.; Conrad, D. W.; Golden, J. P.; Ligler, F. S. *Anal. Chem.* **1995**, *67*, 2431-2435.

(48) Whelan, J. P.; Kusterbeck, A. W.; Wemhoff, G. A.; Bredehorst, R.; Ligler, F. S. *Anal. Chem.* **1993**, *65*, 361-3565.

(49) Lemire, G. W.; Simeonsson, J. B.; Sausa, R. C. *Anal. Chem.* **199**, *65*, 529-533.

(50) McLuckey, S., A.; Van Berkel, G., J.; Goeringer, D.; Glish, G. G. *Anal. Chem.* **1994**, *66*, 737-743.

(51) Simeonsson, J. B.; Lemire, G. W.; Sausa, R. C. *Appl. Spectr.* **1993**, *47*, 1907-1912.

(52) Goeringer, D. E.; Asano, K. G.; McLuckey, S. A.; Hoeckman, D.; Stiller, S. W. *Anal. Chem.* **1994**, *6*, 313-318.

(53) Boumsellek, S.; Alajajian, S. H.; Chutjian, A. *J. Am. Soc. Mass. Spectrom.* **992**, 243-247.

(54) Pennington, J. C. *Chemosphere* **1995**, *30*, 429-38.

(55) Bradley, P. M.; Chapelle, F. H.; Landmeyer, J. E.; Schumacher, J. G. *Appl. Environ. Microbiol.* **1994**, *60*, 2170-2175.

(56) Michels, J.; Gottschalk, G. *Appl. Environ. Microbiol.* **1994**, *60*, 187-194.

(57) Boopathy, R.; Kulpa, C. F.; Wilson, M. *Appl. Microbiol. Biotechnol.* **1993**, *39*, 270-275.

(58) Bumpus, J. A.; Tatarko, M. *Curr. Microbiol.* **1994**, *28*, 185-190.

(59) Spiker, J. K.; Crawford, D. L.; Crawford, R. L. *Appl. Environ. Microbiol.* **1992**, *58*, 3199-3202.

(60) Duque, E.; Haidour, A.; Godoy, F.; Ramos, J. L. *J. Bactriol.* **1993**, *175*, 2278-2283.

(61) Sulette, K. L.; Ganapathy, E. V.; Schwartz, S. *Appl. Biochem. Biotech.* **1992**, *34/35*, 709-723.

(62) Preuss, A.; Fimpel, J.; Diekert, G. *Arch. Microbiol.* **1993**, *159*, 345-353.

(63) Boopathy, R.; Kulpa, C. F. *Curr. Microbiol.* **1992**, *25*, 235-241.

(64) Boopathy, R.; Manning, J.; Montemagno, C.; Kulpa, C. *Curr. Microbiol.* **1994**, *28*, 131-137.

(65) Boopathy, R. *Arch. Microbiol.* **1994**, *162*, 167-172.

(66) Fernando, T.; Aust, S. D. *Biodegradation of Munition Waste, TNT (2,4,6-Trinitrotoluene), and RDX (Hexahydro-1,3,5-Trinitro-1,3,5-Triazine) by Phanerochaete chrysospium*; Fernando, T.; Aust, S. D., Ed., 1991, pp 214-232.

(67) Hao, O. J.; Phull, K. K.; Chen, J. M. *Wat. Res.* **1994**, *28*, 283-290.

(68) Dillert, R.; Brandt, M.; Fornefett, I.; Siebers, U.; Bahnemann, D. *Chemosphere* **1995**, *30*, 2333-2341.

(69) Wang, Z.; Kutal, C. *Heterogeneous Photocatalytic Degradation of 2,4,6-Trinitrotoluene in an Aqueous Titanium Dioxide Dispersion*; Wang, Z.; Kutal, C., Ed., 1994.

(70) Farrel, F. C.; Zeff, J. D.; Crase, T. C.; Boylan, D. T. "Development Effort to Design and Describe Pink Water Abatement Processes," Westgate Research Corporation, 1977.

(71) Noss, C. I.; Chyrek, R. H. "Tertiary Treatment of Effluent from Holston AAP Industrial Liquid Waste Treatment Facility IV. Ultraviolet Radiation and Hydrogen Peroxide Studies: TNT, RDX, HMX, TAX, and SEX," US Army Medical Bioengineering Research and Development Laboratory, 1984.

(72) Andrews, C. C.; Klausmeier, R. E.; Osmon, J. L. *Method for Degrading Aromatic Explosive Solutions*; Andrews, C. C.; Klausmeier, R. E.; Osmon, J. L., Ed., 1977.

(73) Hong, A.; Zappi, M.; Kuo, C. H. *Kinetics and Mechanism of UV/H2O2/O3 Treatment for Explosive-Contaminated Groundwater*; Hong, A.; Zappi, M.; Kuo, C. H., Ed.: London, Ontario, Canada, 1994, pp 231-233.

(74) Sierka, R. A. *Ozone: Sci. Eng.* **1985**, *6*, 275-290.

(75) Schuster, R. *Hewlett-Packard application note,* **1993**, *12-5091-7626E.*

(76) Ho, P. C. *Environ. Sci. Technol.* **1986**, *20*, 260-267.

(77) Awad, H. H.; Stanbury, D. M. *Int. J. Chem. Kinet.* **1993**, *25*, 375-381.

(78) Armstrong, W. A.; Humphreys, W. G. *Can. J. Chem.* **1965**, *43*, 2576-2584.

(79) Todd, J. H. *Ultrasonics* **1970**, *8*, 234-238.

(80) Allen, A. O. *The Radiation Chemistry of Water and Aqueous Solutions*; Van Nostrand: Princeton, New Jersey, 1961.

(81) Hua, I. *Ph.D. Thesis*; Hua, I., Ed.; California Institute of Technology, Pasadena, 1995.

Table 1

Power densities, P_V, and intensities, P_A, for the various ultrasonic reactor setups. Power values are given as determined form wall-wattages and, in parantheses, from calorimetry.

	Vibrating Area [cm^2]	Solution Volume	Power Input [W]	P_A [W cm^{-2}]	P_V [W mL^{-1}]
20 kHz, Sonics Materials	1.20	50	139 (52.3)	116 (43.6)	2.78 (1.05)
20 kHz, Orthoreactor, Undatim	2.50	650	127 (57.2)	50.8 (22.9)	0.195 (0.088)
500 kHz, Orthoreactor, Undatim	25.5	650	127 (42.6)	4.98 (1.67)	0.195 (0.066)
20 & 500 kHz, Orthoreactor, Undatim	-	650	254 (99.8)	-	0.390 (0.154)

Table 2

Summary of the pseudo first-order rate constants for TNT degradation, k_{obs} [10^{-5} s^{-1}].

	O_2	Ar	O_2/O_3
w/o ultrasound, Sonics Materials	0.00	0.00	0.33
20 kHz, Sonics Materials	1.67	4.50	18.8
w/o ultrasound, Orthoreactor, Undatim	0.00	0.00	3.33
20 kHz, Orthoreactor, Undatim	-	0.33	-
500 kHz, Orthoreactor, Undatim	2.00	7.92	8.50
20 & 500 kHz, Orthoreactor, Undatim	-	7.00	-

Table 3

TNT degradation efficiencies in terms of G-values [10^{11} molecules J^{-1}]. Values are given in terms of wall-wattages and, in parantheses, in terms of calorimetric power estimates. The corresponding radiation chemistry G-values [molecules $(100\ eV)^{-1}$] are given in square brackets, and are based on calorimetric power estimates.

	O_2	Ar	O_2/O_3
20 kHz, Sonics Materials	3.62 (9.62) [1.54×10^{-5}]	9.75 (25.9) [4.15×10^{-4}]	40.7 (108) [1.73×10^{-4}]
20 kHz, Orthoreactor, Undatim	- (-) [-]	10.2 (22.6) [3.62×10^{-5}]	- (-) [-]
500 kHz, Orthoreactor, Undatim	61.7 (184) [2.94×10^{-4}]	244 (728) [1.17×10^{-3}]	262 (781) [1.25×10^{-3}]
20 & 500 kHz, Orthoreactor, Undatim	- (-) [-]	108 (275) [4.40×10^{-4}]	- (-) [-]

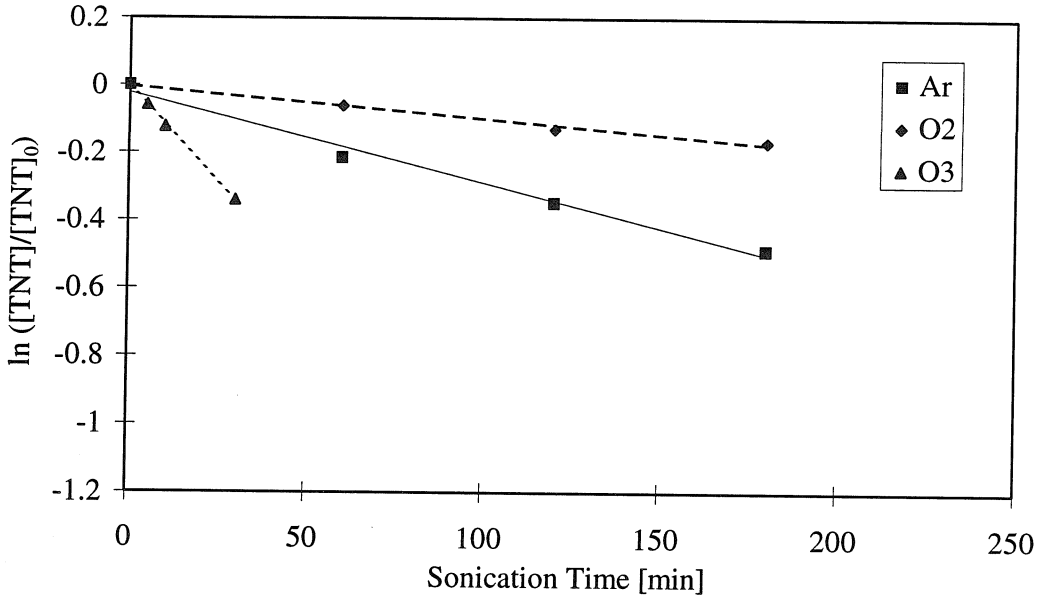

Fig. 1: Influence of the background gas on the ultrasonic TNT degradation at 20 kHz.

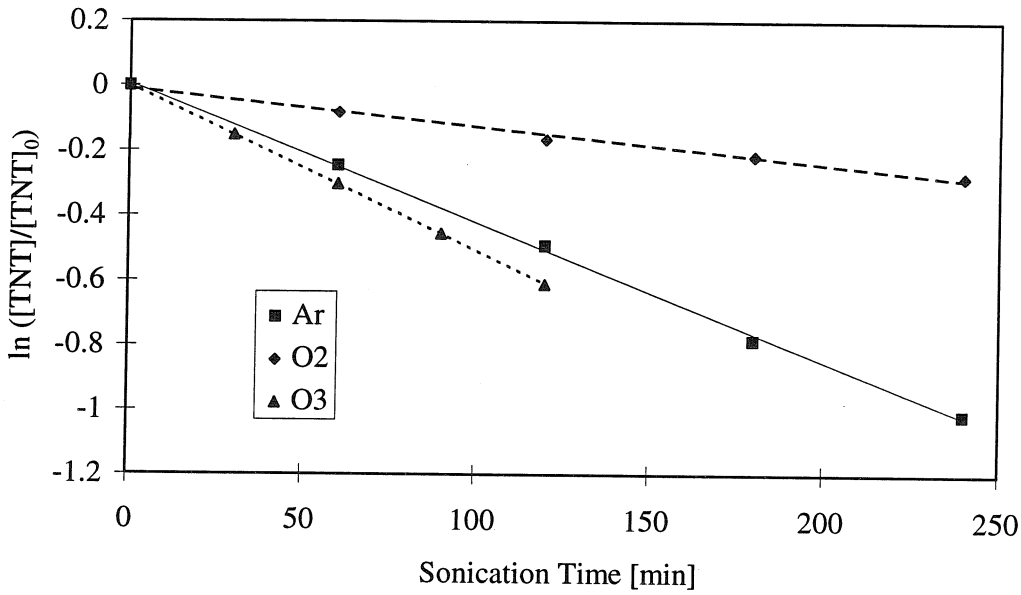

Fig. 2: Influence of the background gas on the ultrasonic TNT degradation at 500 kHz.

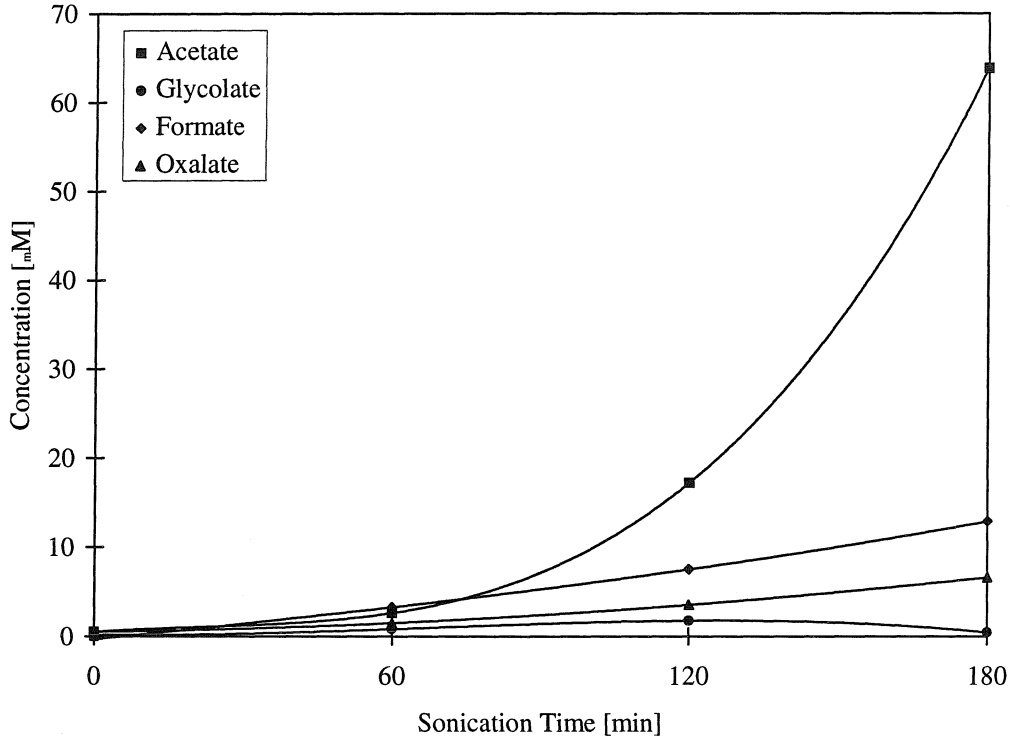

Fig. 3: Generation of short chain organic acids.

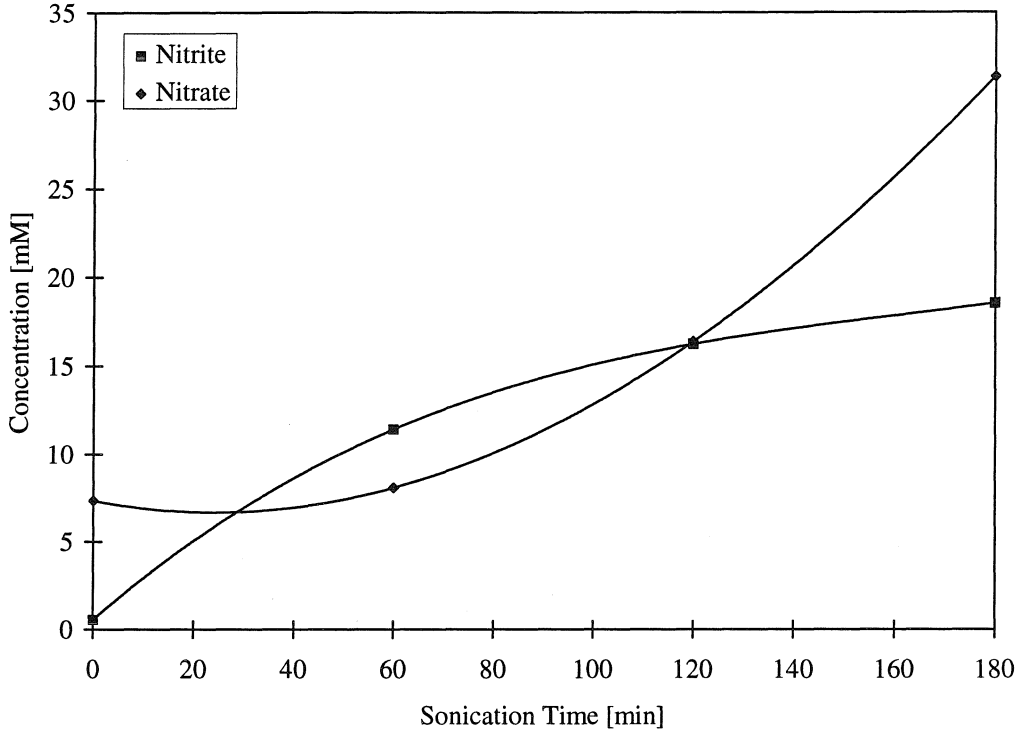

Fig. 4: Generation of NO_3^- and NO_2^-.

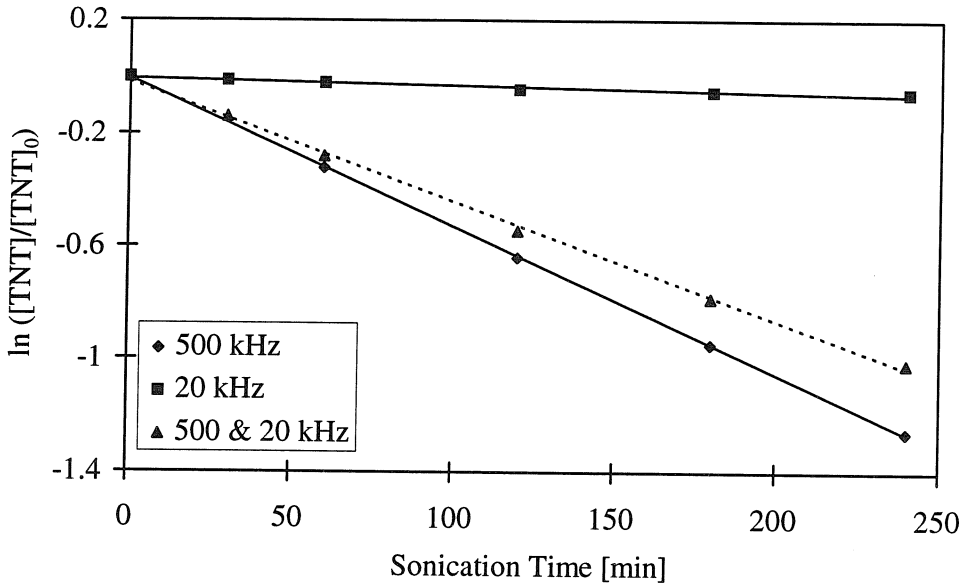

Fig. 5: Effect of frequency combination.

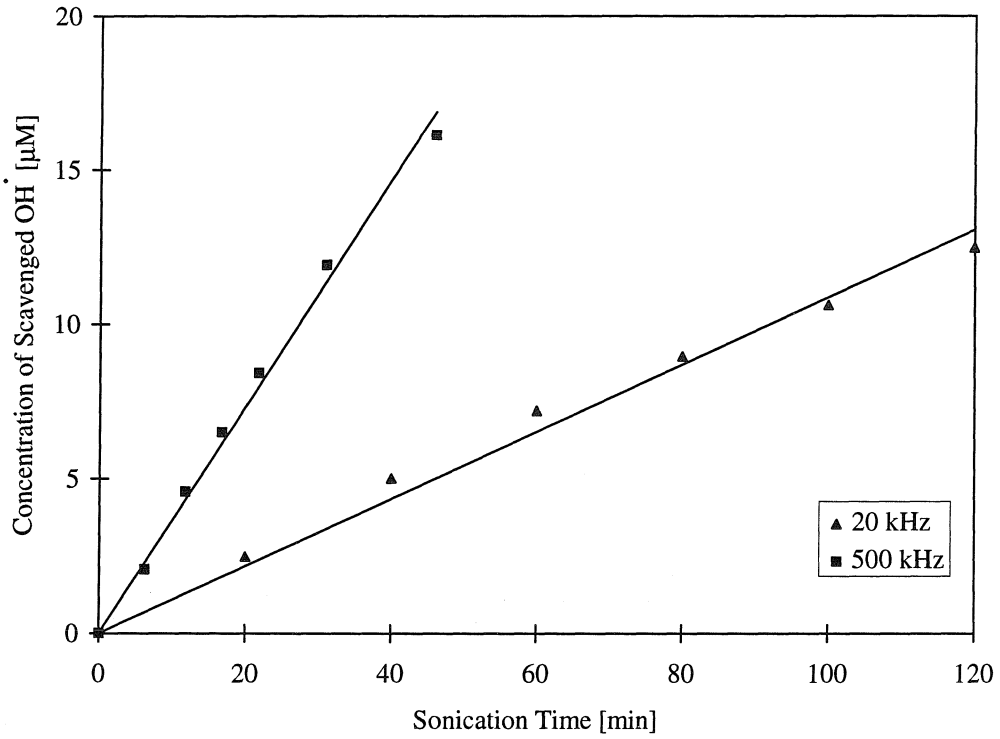

Fig. 6: Generation of $OH^{\bullet}$ radical at 20 and 500 kHz (*81*).

- Chapter V -

Ultrasonic Irradiation of a Mixture of Nitro- and Amino-aromatic Compounds

Introduction

In recent years there has been a growing interest in remediating ground- and wastewaters contaminated with undesirable chemical compounds. The need for novel treatment processes prompted the development of many advanced oxidation technologies, AOT's, (1). These technologies include treatment processes with ozone, hydrogen peroxide and UV radiation, heterogeneous photocatalysis (2), non-thermal plasmas, supercritical water oxidation, electron beam irradiation, electrohydraulic discharges (3), and sonolysis. The common oxidant in all AOT's is the hydroxyl radical. The argument behind these novel technologies is that the potent oxidizing species $OH^{\bullet}$ attacks dissolved organic compounds and degrades them to innocuous substances, eventually breaking them down to inorganic acids and carbon dioxide.

The work presented in Chapters III - VI of this thesis focuses on basic research towards the utilization of high-power ultrasound for hazardous waste treatment. Research on this field has been performed almost exclusively on solutions containing only one compound (4-18). Real-life waste streams, however, are commonly composed of a variety of different chemicals. As an example, the effluent from munitions production plants contain a complicated mixture of nitro- and amino-aromatic compounds (19-22, 23-26).

In Chapter IV the degradation of 2,4,6-tirnitrotoluene by ultrasonic irradiation has been described in detail. In order to more realistically evaluate the potential use of high-power ultrasound for the remediation of real-world ground-, and wastewaters, this chapter summarizes research on the sonochemical degradation of a mixture of four nitroaromatic compounds plus m-nitroaniline.

Experiments have been performed in a 500 kHz bench-top reactor and in a continuous flow near-field acoustical processor at lower frequencies (16 and 20 kHz).

Experiments

Chemicals

2,4,6-Trinitrotoluene, TNT, (Chem Service, 99 % + 10 % water added), 2,4-dinitrotoluene, DNT, (Chem Service, 98 %), 1,3,5-trinitrobenzene, TNB, (Chem Service, 99 % + 10 % water added), 1,3-dinitrobenzene, DNB, (Chem Service, 99 %), and m-nitroaniline, m-NA, (Chem Service, 99 %) were used without further purification. TNT and TNB used in the preparation of quantitative standards were dried for two days in a desiccator before use. All solutions and calibration standards were prepared with deionized water (Millipore, Milli-Q UV plus, $\rho = 18.2\ M\Omega\ cm^{-1}$).

Sonochemical Reactors

The degradation experiments at 50 and 500 μM initial m-NA concentration were performed in a parallel-plate near-field acoustical processor, NAP, (Lewis Corporation, Oxford, CT). In a NAP reactor mechanical energy of vibration is transferred to the reaction mixture via two parallel stainless steel plates that are bolted together. The vibrations of the plates is driven by seven magnetostrictive transducers that are bonded onto each plate. The two plates vibrate at frequencies of 16 and 20 kHz respectively. The total sonoactive area is 1262 cm^2. The total power input is set 1521 W (wall-wattage). A stainless steel spacer is placed between the two vibrating plates in order to define the reaction volume. The seal between spacer and plates is provided by a Goretex gasket. The reaction volume, 577 mL, was constant throughout all NAP experiments. The reaction mixture in the NAP reactor was maintained at constant temperature (25 °C) using a VWR Scientific (Model 1176) refrigeration unit. The NAP reactor is incorporated in a closed-loop setup (Fig. 1 in Chapter VI) in which the reaction mixture is continuously recirculated via a peristaltic pump (Masterflex, Model 7591-50) through a

well-stirred mixing reservoir and the reactor itself. Throughout the study, a volumetric flow rate of 3.2 L min^{-1} was maintained.

Since the NAP reactor is part of a continuous-flow closed-loop system, the reaction rate has to be extracted from an observed reaction rate, k_{obs} according to the following equation in which V_S is the sonicated volume and V_R is the volume of the reservoir:

$$k = \frac{V_S + V_R}{V_S} k_{obs}, \; V_S = 577\,mL, \; V_R = 3423\,mL \tag{1}$$

A detailed derivation of eq. 1 is presented in Chapter VI which contains a detailed introduction to the NAP system.

For the investigation of parent compound degradation in a mixture of nitro-aromatic compounds, each present at a concentration of 50 μM, a 500 kHz bench-top reactor (Orthoreactor, Undatim) was used. The orthoreactor has a wide opening at one side of its glass vessel to which a 500 kHz transmitter is attached. The volume of the reaction mixture was 650 mL throughout all experiments. The 500 kHz reactor was equipped with cooling jackets. The temperature was held constant at 10 °C throughout all experiments.

The applied power, P, power densities, P_V, and power intensities, P_A, for the NAP and the 500 kHz reactor are based on wall-wattage and on the power that is actually introduced into the solution (Table 1 in Chapter IV). The power introduced into the reaction mixture was estimated calorimetrically as described in Chapter IV.

Chemical Analysis

The decrease in the concentrations of TNT, TNB, DNT, DNB, and m-NA and the generation of intermediate compounds were monitored using high performance liquid

chromatography, HPLC, (Hewlett Packard, Series II 1090) coupled with photodiode array detection. In a typical analysis, 25 μL of the filtered (Gelman, 0.2 μm PFTE filters) sample solution were injected and separated with a 3 μm, 100 × 4 mm, C-18 Hypersil column (Hewlett Packard). Solutions with high concentrations of m-NA (0.2 - 0.5 mM) were analyzed by injecting 5 μL of the filtered sample solution. Chromatograms were recorded using the absorbance at the wavelengths λ = 214 nm, λ = 135 nm, and λ = 233 nm. The eluent peaks were identified by their retention times and UV/vis absorbance spectra.

In order to facilitate peak identification an existing HPLC method was used (27). The method employed a H_2O/MeOH gradient with the following time table: t = 0 min, H_2O = 74 %; 10 min, 60 %; 20 min, 45 %; 21 min, 74 %. The flow was constant throughout the 23 min run at 0.72 mL/min. The oven temperature was set to 38 °C.

For the quantitative determination of all nitro- and amino-aromatic compounds, standards were prepared by dissolving known amount of dried TNT and TNB, DNT, DNB, and m-NA in deionized water. The HPLC was calibrated using the integrated peak areas at λ = 235 nm of a concentration series of chromatograms (Fig. 1). The calibration curves for all compounds were found to be reproducable and stable (Fig. 2).

The TOC of various samples was determined using a Shimadzu (model 5000A) total organic carbon analyzer.

Results and Discussion

TNT, DNT, TNB, DNB, and m-NA, have been irradiated individually and in a mixture containing all five compounds with 500 kHz ultrasound. First-order plots show the degradation of each compound when present as single solute (Fig. 3) and in the mixture (Fig. 4). The obtained rate constants for degradation when present as single solute, k_1, and in a mixture, $k_{1,m}$, are summarized in Table 1. Degradation is faster by a

factor of 1.2 - 2.2 in single solute solutions. m-NA shows the greatest decrease in reaction rate when comparing the single-pollutant solution to a mixture containing all five compounds. The slower reaction rate of all compounds in the mixture can be explained by competition between the different solutes. Since all compounds investigated have a low vapor pressure, the main reaction leading to degradation occurs at the bubble/liquid interface and not within the collapsed bubble. The space that is available for reaction is given by the number and the size of collapsing bubbles, which are a function of the ultrasonic frequency and the physical properties of the irradiated solution. Since the space that is available for reaction remains constant, the reactants compete against each other. This leads to the observed lower rates for solutes in a mixture.

The degradation rate constants increase in the following order: $k_{TNB} < k_{DNB} < k_{TNT} < k_{DNT} < k_{m\text{-}NA}$. In order to elucidate this order, the rate constants for degradation in the mixture are plotted against $\sum\sigma$ in Fig. 5 (Fig. 6 for the single compounds). The basis for the determination of the σ's is nitrobenzene. The procedure of ascribing σ's to the various groups attached to the nitrobenzene moiety is explained for the case of TNB: TNB can be described as a nitrobenzene core with nitro groups in each of its two meta positions. The σ value for a m-NO_2 group is 0.71 ± 0.04. Therefore, for TNB, $\sum\sigma = 1.42 \pm 0.08$. Accordingly, the values for the other compounds have been derived (28,29) For TNT, $\sum\sigma = 1.28 \pm 0.11$, DNB ($0.71 \pm 0.04$), DNT ($0.57 \pm 0.07$), m-NA ($-0.09 \pm 0.05$). (Values for groups in sigma position have been estimated with those for the para-position).

The linear free energy relationships (LFER) in Figs. 5 and 6 suggest that the reaction rate is proportional to the electron density of the aromatic ring: TNB with three strongly electron-withdrawing nitro groups reacts more slowly than DNT, which has only two nitro groups and a slightly electron-pushing methyl group. In Chapter IV it has been pointed out that the main pathway for TNT degradation is •OH attack. •OH is a strong electrophile which attacks preferentially substrates with high electron-density. The

observed LFER between electron densities and rate constants is further evidence for a degradation mechanism that involves •OH attack in its rate limiting step.

Also, when the reaction is performed in the NAP reactor, which operates at frequencies of 16 and 20 kHz, the degradation rates for the nitro-aromatic compounds drop significantly, Fig. 7. As shown in Fig. 6 of Chapter IV, ultrasound at 500 kHz generates significantly more •OH than lower-frequency ultrasound.

The final series of experiments involved the sonication of aqueous solutions of m-NA in the NAP. Fig. 8 shows the decrease of the parent compound from an initial concentration of 500 μM to levels below the detection limit over the course 170 min of effective sonication. The x-axis represents the effective sonication time, (i. e., the time each fluid parcel actually resides in the sonoactive volume). By the same reasoning that led to eq. 1, the actual time, t, and effective sonication time, t_S, are related by eq. 2:

$$t_S = \frac{V_S}{V_S + V_R} t \qquad (2)$$

It is apparent from Fig. 8 that the decrease in parent-compound concentration does not follow a single reaction order over the entire duration of the experiment. In Fig. 9 the decrease in [m-NA] is plotted for the first part of the experiment. It shows an apparent zero-order mechanism. Later in the experiment, the reaction becomes first-order as shown in Fig. 10.

While for the case of an initial m-NA concentration, $[m\text{-}NA]_0$, of 500 μM the reaction changes from a apparent zero- to a first- order mechanism, the reaction follows an apparent first-order mechanism from start to finish when $[m\text{-}NA]_0$ = 50 μM, Fig. 11. This behavior may be explained by the limited interfacial area where reaction can take place. When [m-NA] is high, the rate is limited by the available active interface, leading to an apparent zero-order mechanism. On the other hand, when the reactant concentration

is relatively low, the degradation rate is limited by its partitioning to the bubble/solution interface, wich leads to apparent first-order kinetics. The argument is the same as for the competition among several different reactants. In one case m-NA competes with other reactants (i. e., TNB, TNT, DNB. DNT), in the other case it competes with itself when present at high enough concentration.

The degradation of m-NA is accompanied by a decrease in total organic carbon, TOC, Fig. 12. TOC decreases by 50 % over the time of the experiment. The remaining TOC consists of short-chain organic acids. These are difficult to oxidize to CO_2 due to the fact that they are present as charged ions that do not preferentially partition to the bubble surface. However, these compounds are harmless and a complete mineralization is not necessary for detoxification.

Various intermediate compounds are formed during the irradiation of m-NA, Fig. 13. However, all of them are subsequently degraded. Fig. 14 shows the chromatogram of a solution with $[m\text{-}NA]_0$ = 500 μM, that has been irradiated in the NAP reactor for an effective time of 72 minutes. The identification of these intermediate products is difficult, since they are present at very low concentrations. Figs. 15a -f show their respective UV/vis spectra.

Conclusions

Nitroaromatic compounds are degraded by ultrasonically induced cavitation in aqueous solution. The degradation appears to occur via an initial •OH attack. In general, the rate constant increase with increasing electron density of the aromatic ring (i. e., the more nitro groups the slower the reaction). It may be advantageous to reduce nitro-aromatic compounds to their amino-analogues prior to sonication.

In the case of high initial concentration or when more than one reactant is present, the reactant will compete for the limited interfacial area of collapsing bubles. This

In the case of high initial concentration or when more than one reactant is present, the reactant will compete for the limited interfacial area of collapsing bubles. This competition consistently leads to lower degradation rates for a compound that is present in a mixture when compared to a solution containing only one compound. This has to be taken into account when applying ultrasound to the remediation of real-world waste streams, which in general contain a complex mixture of pollutants.

References

(1) Second International Symposium on Advanced Oxidation Technologies, San Francisco, California, February 28 - March 1, 1996.

(2) Hoffmann, M. R.; Martin, S. T.; Choi, W. Y.; Bahnemann, D. W. *Chem. Rev.* **1995**, *95*, 1, 69-96.

(3) Willberg, D. M.; Lang, P. S.; Höchemer, R. H.; Kratel, A.; Hoffmann, M. R.; *Environ. Sc. Technol.* **1995**, submitted.

(4) Kotranarou, A.; Mills, G.; Hoffmann, M. R. *Environ. Sci. Technol.* **1992**, *26*, 2420-2428.

(5) Kotronarou, A. *Ph. D. Thesis*; Kotronarou, A., California Institute of Technology, Pasadena, 1991.

(6) Kotronarou, A.; Mills, G.; Hoffmann, M. R. *J. Phys. Chem.* **1991**, *95*, 3630-3638.

(7) Kotronarou, A.; Mills, G.; Hoffmann, M. R. *Environ. Sci. Technol.* **1992**, *26*, 1460-1462.

(8) Cost, M.; Mills, G.; Glisson, P.; Lakin, J. *Chemosphere* **1993**, *27*, 1737-1743.

(9) Hua, I.; Höchemer, R. H.; Hoffmann, M. R. *J. Phys. Chem.* **1995**, *99*, 2335-2342.

(10) Hua, I.; Höchemer, R. H.; Hoffmann, M. R. *Environ. Sci. Technol.* **in press**.

(11) Koskinen, W. C.; Sellung, K. E.; Baker, J. M.; Barber, B. L.; Dowdy, R. H. *J. Environ. Sci. Health Part B* **1994**, *29*, 581-590.

(12) Olson, T. M.; Barbier, P. F. *Wat. Res.* **1994**, *28*, 1383-1391.

(13) Petrier, C.; Micolle, M.; Merlin, G.; Luche, J. L.; Reverdy, G. *Environ. Sci. Technol.* **1992**, *26*, 1639-1642.

(14) Petrier, C.; Lamy, M. F.; Francony, A.; Benahcene, A.; David, B.; Renaudin, V.; Gondrexon, N. *J. Phys. Chem.* **1994**, *98*, 10514-10520.

(15) Serpone, N.; Terzian, R.; Colarusso, P.; Minero, C.; Pelizzetti, E.; Hidaka, H. *Res. Chem. Intermed.* **1992**, *18*, 183-202.

(16) Serpone, N.; Terzian, R.; Hidaka, H.; Pelizzetti, E. *J. Phys. Chem.* **1994**, *98*, 2634-2640.

(17) Wu, J. M.; Huang, H. S.; Livengood, C. D. *Environ. Prog.* **1992**, *11*, 195-201.

(18) Price, G. J.; Matthias, P.; Lenz, E. J. *Process Safety and Environmental Protection: Transactions of the Institution of Chemical Engineers Part B* **1994**, *72*, 27-31.

(19) Chen, T. H.; Campbell, C.; Fisco, W. J. "Characterization of Pollutants at Holston Army Ammunition Plant," US Army ARRADCOM, 1981.

(20) Conley, K. A.; Mikucki, W. J. "Migration of Explosives and Chlorinated Pesticides in a Simulated Sanitary Landfill," Construction Engineering Research Laboratory, 1976.

(21) Hall, T. N.; Lawrence, G. W. "A Study of the Organic Components of Red Water," Naval Surface Weapons Center, 1976.

(22) Kobylinski, E. A.; Burrows, W. D. "Tertiary Treatment of Effluent from Holston AAP Industrial Liquid Waste Treatment Facility II. Corona Oxidation Studies: TNT, RDX, HMX, TAX, and SEX," US Army Medical Bioengineering Research and Development Laboratory, 1983.

(23) Haas, R.; Löw., E. v. *Grundwasserbelastung durch eine Altlast. Die Folgen einer ehemaligen Sprengstoffproduktion für die heutige Trinkwassergewinnung*; Haas, R.;. Löw., E. v. , Ed., 1986; Vol. 37, pp 33-43.

(24) Haas, R.; Schreiber, I.; Löw, E. v.; Storck, G. *Fresenius J. Anal. Chem.* **1990**, *338*, 41-45.

(25) Haas, R.; Storck, G. *Fresenius Z. Anal. Chem.* **1989**, *335*, 839-846.

(26) Haas, R.; Schreiber, I.; Storck, G. *Z. Umweltchem. Ökotox.* **1990**, *2*, 139-141.

(27) Schuster, R. *Hewlett-Packard application note,* **1993**, *12-5091-7626E.*

(28) Wells, P. R. *Linear Free Energy Relationships;* Academic Press; Ltd.: London, 1968, pp. 116.

(29) Chapman, N. B.; Shorter, J. *Correlation Analysis in Chemistry;* Plenum Press; New York, 1978, pp. 546.

Table 1

First-order rate constants for the degradation of the parent compound in a mixture and as single component. Irradiations were performed in the 500 kHz Orthoreactor.

Compound	Mixture, $k_{1,m}$ [10^{-3} min^{-1}]	Single reactant, k_1 [10^{-3} min^{-1}]	$k_1/k_{1,m}$ [-]
1,3,5-TNB	0.65 ± 0.04	1.0	1.6 ± 0.08
1,3-DNB	2.8 ± 0.23	3.3	1.2 ± 0.10
2,4,6-TNT	3.2 ± 0.22	4.5	1.4 ± 0.09
2,4-DNT	7.4 ± 0.33	11.6	1.6 ± 0.07
m-NA	9.3 ± 0.27	20.7	2.2 ± 0.06

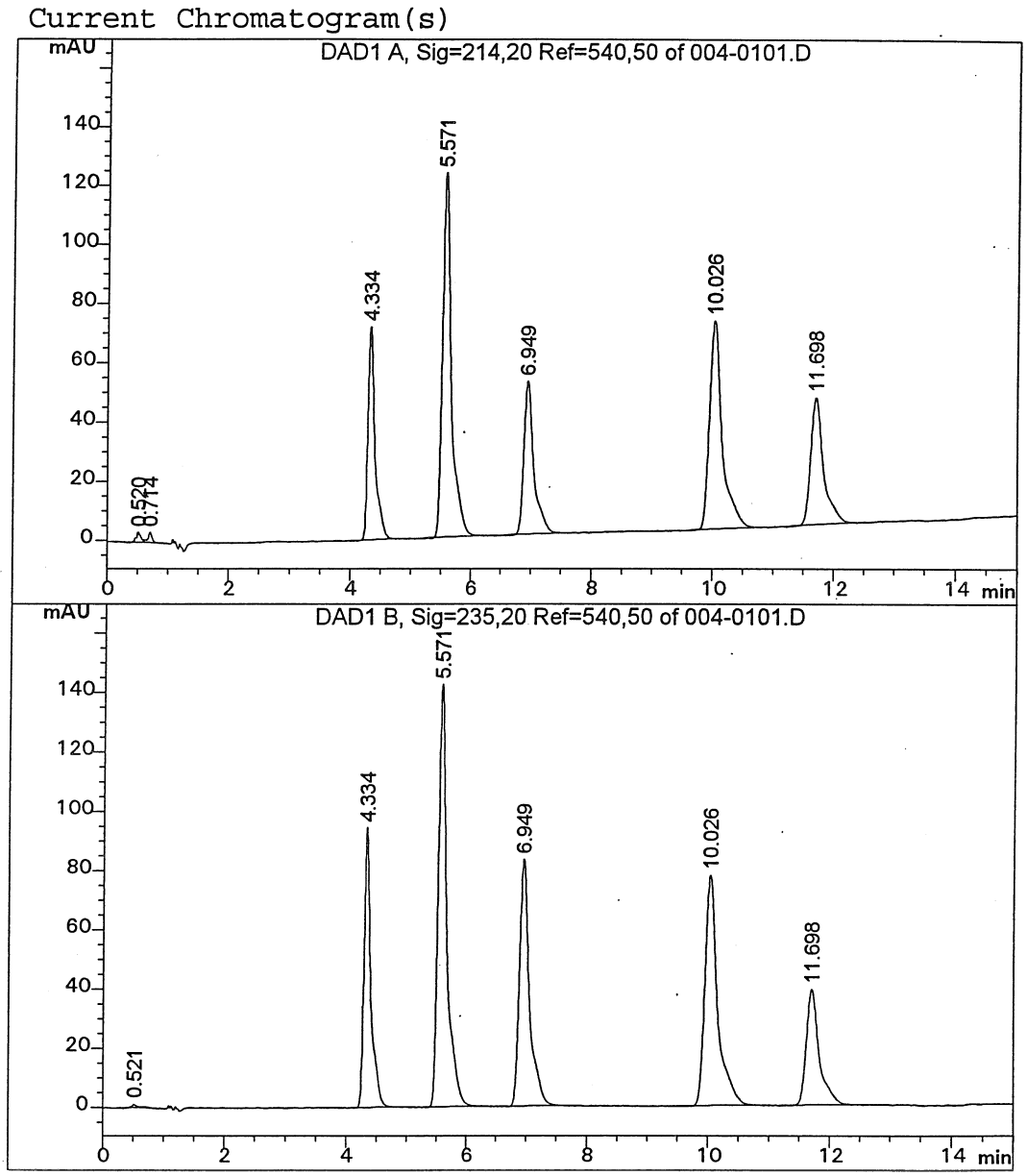

Fig. 1: Chromatogram of a 50 µM nitro-aromatic standard solution. The peaks correspond to the following compounds respectively: m-NA (4.33 min retention time), 1,3,5-TNB (5.57 min), 1,3-DNB (6.95 min), 2,4,6-TNT (10.03 min), 2,4-DNT (11.70 min). Detection wavelength: 214 and 235 nm.

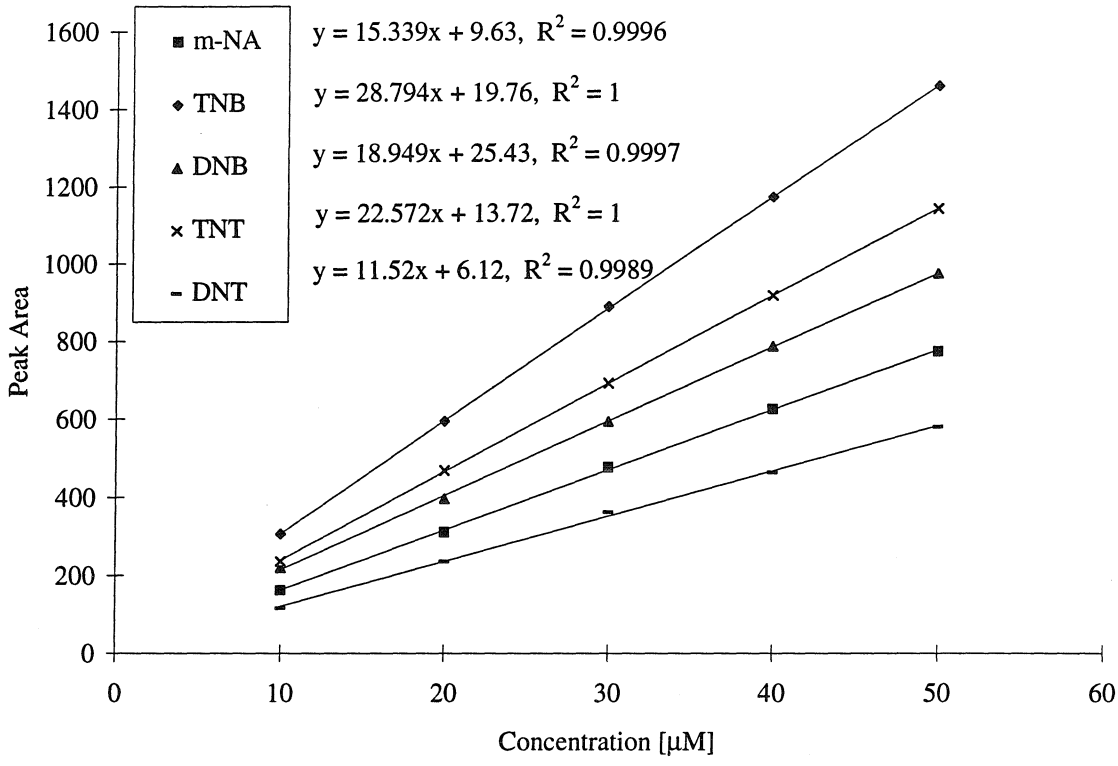

Fig. 2: Calibration curves for selected nitro-aromatic compounds and m-NA. Basis for the calibration are the respective peak areas of the HPLC-chromatograms.

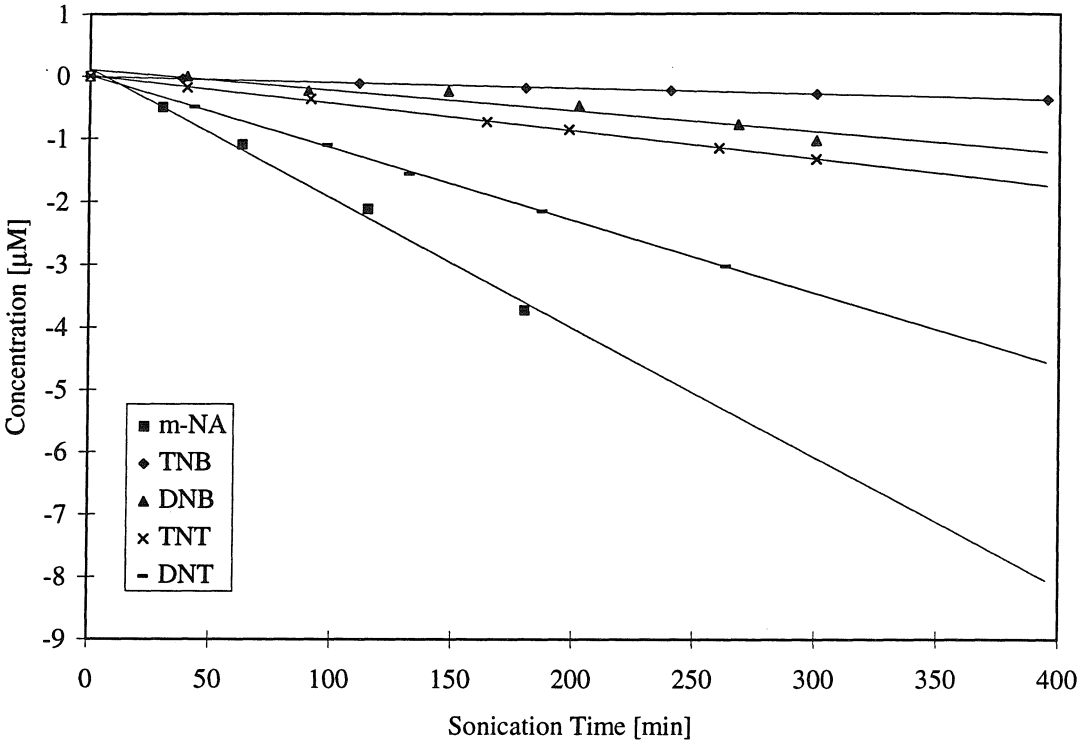

Fig. 3: First-order plot for the degradation of single compounds. The irradiations have been performed in the 500 kHz Orthoreactor. The reaction mixture was maintained at a temperature of 10 °C.
Initial concentration of all chemicals was 50 µM.

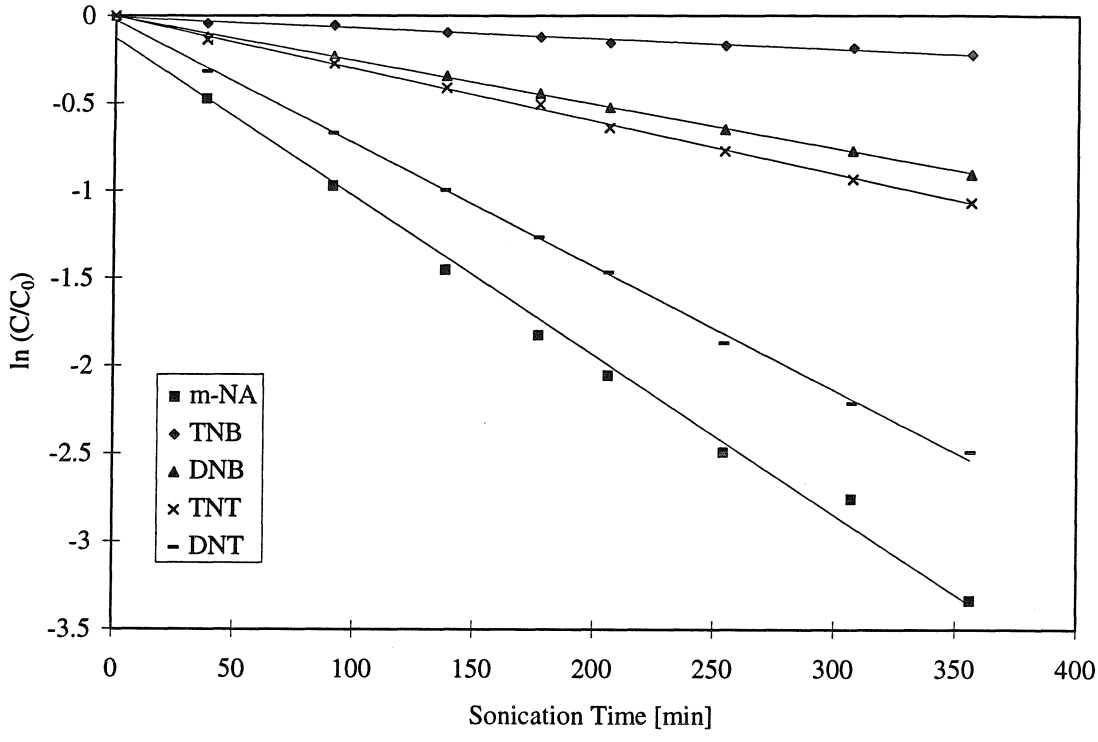

Fig. 4: First-order plot for the degradation of a mixture of compounds. The irradiations have been performed in the 500 kHz Orthoreactor. The reaction mixture was maintained at a temperature of 10 °C.

Initial concentration of all chemicals was 50 μM.

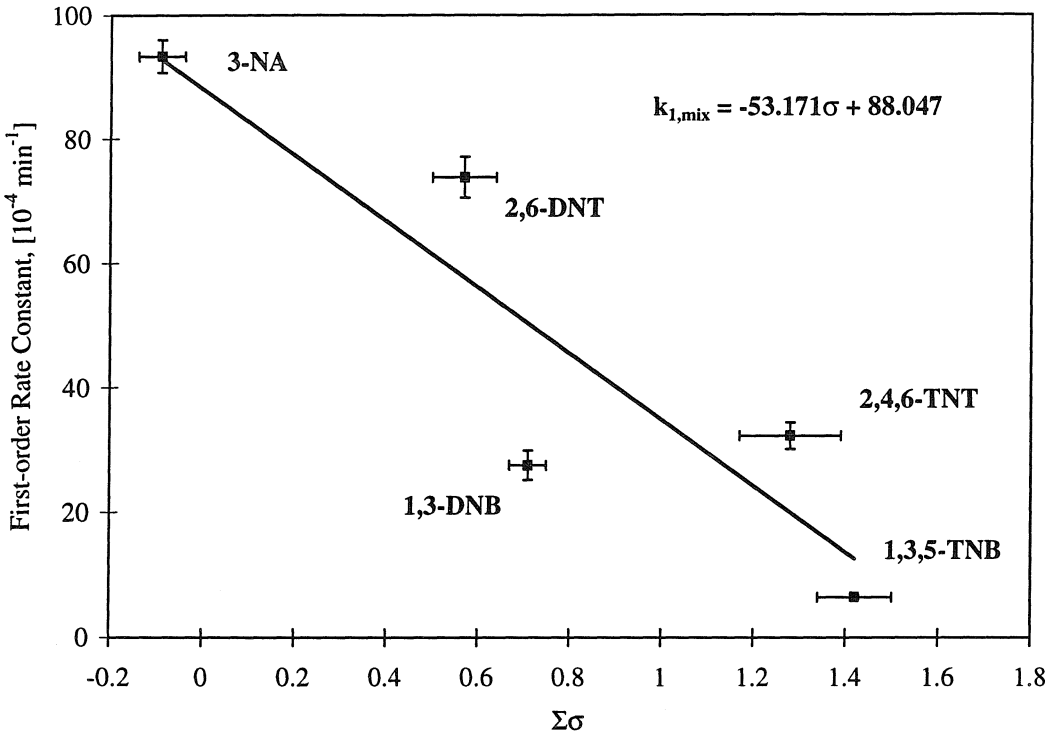

Fig. 5: LFER for the first-order degradation rates in a mixture of compounds. The basis for comparison of the different molecules is nitrobenzene. The irradiations have been performed in the 500 kHz Orthoreactor. The reaction mixture was maintained at a temperature of 10 °C.

Initial concentration of all chemicals were 50 μM.

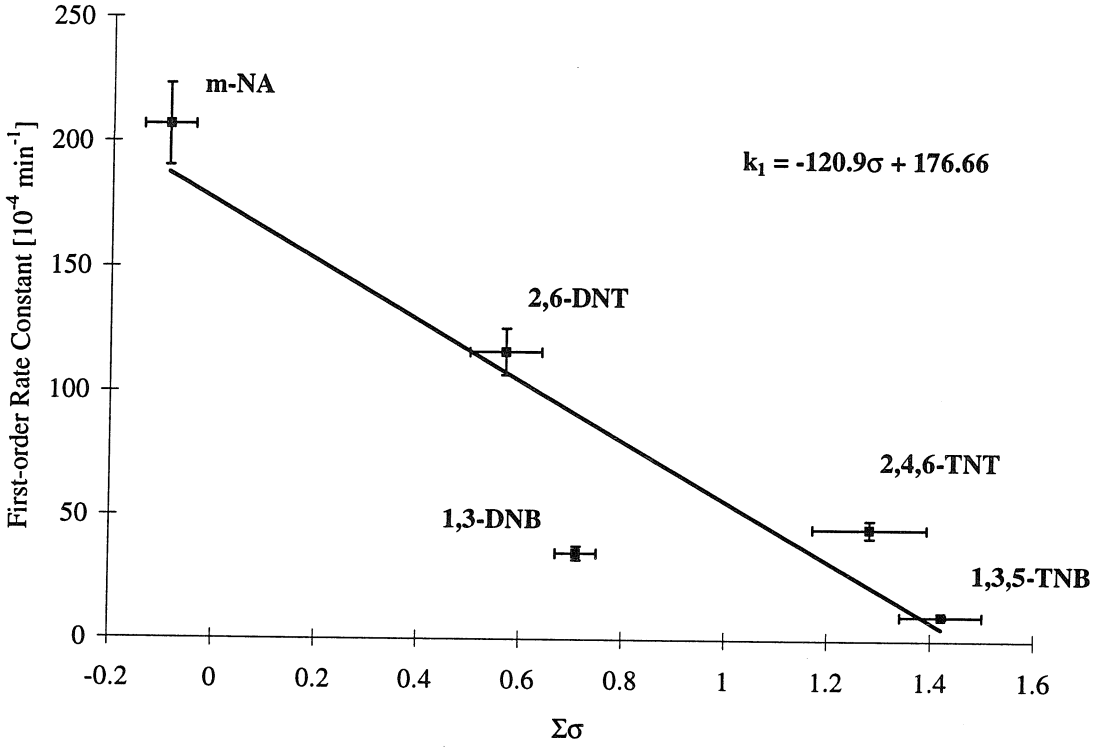

Fig. 6: LFER for the first-order degradation rates in single-compound solution. The basis for comparison of the different molecules is nitrobenzene. The irradiations have been performed in the 500 kHz Orthoreactor. The reaction mixture was maintained at a temperature of 10 °C.

Initial concentration of all chemicals were 50 μM.

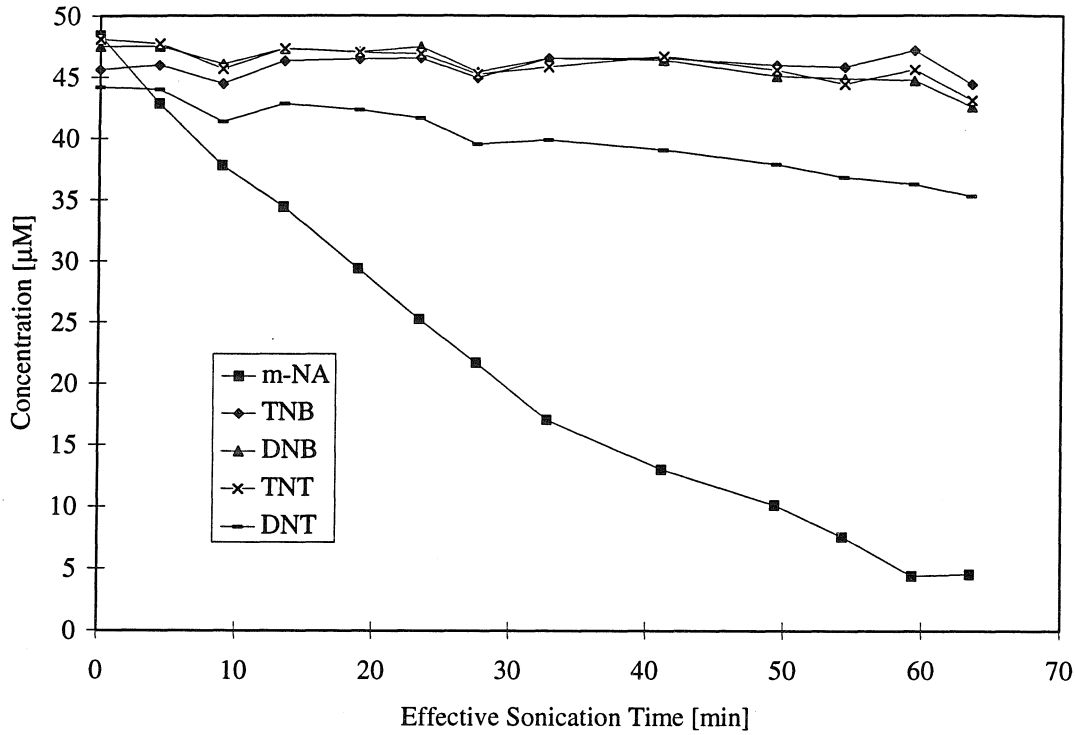

Fig. 7: Degradation of a mixture of nitro-aromatic compounds in the NAP reactor. Initial concentration of all chemicals were 50 µM.

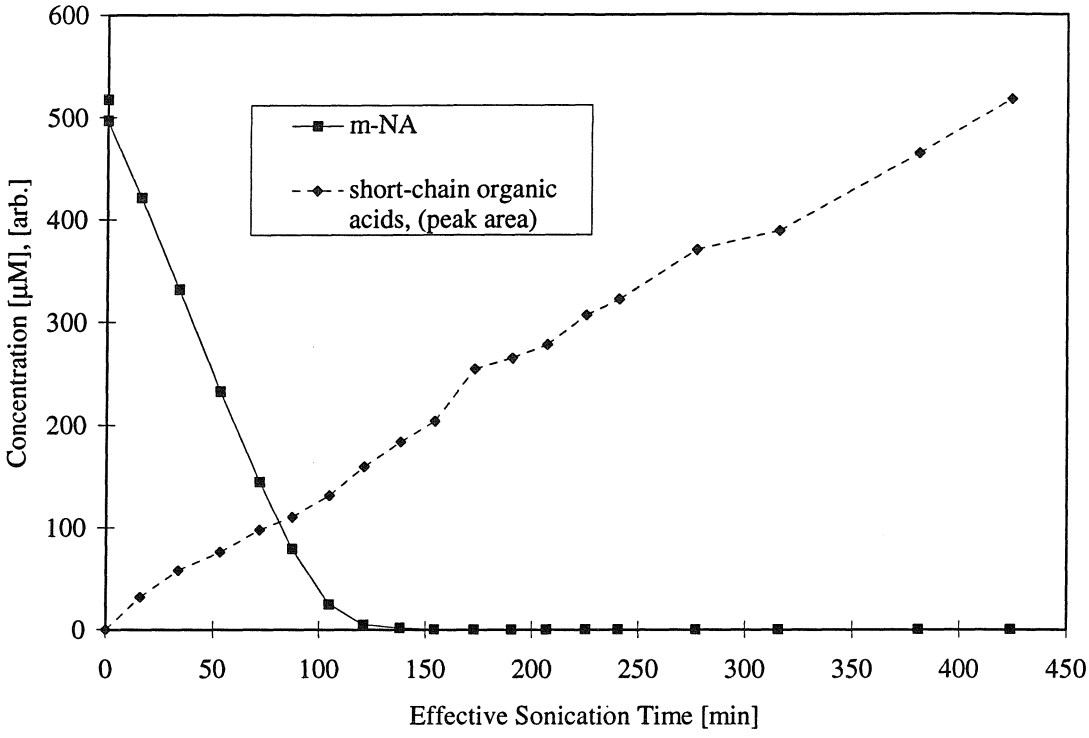

Fig. 8: Degradation of m-NA in the NAP reactor.

Initial concentration, $[m\text{-}NA]_0 = 500\ \mu M$.

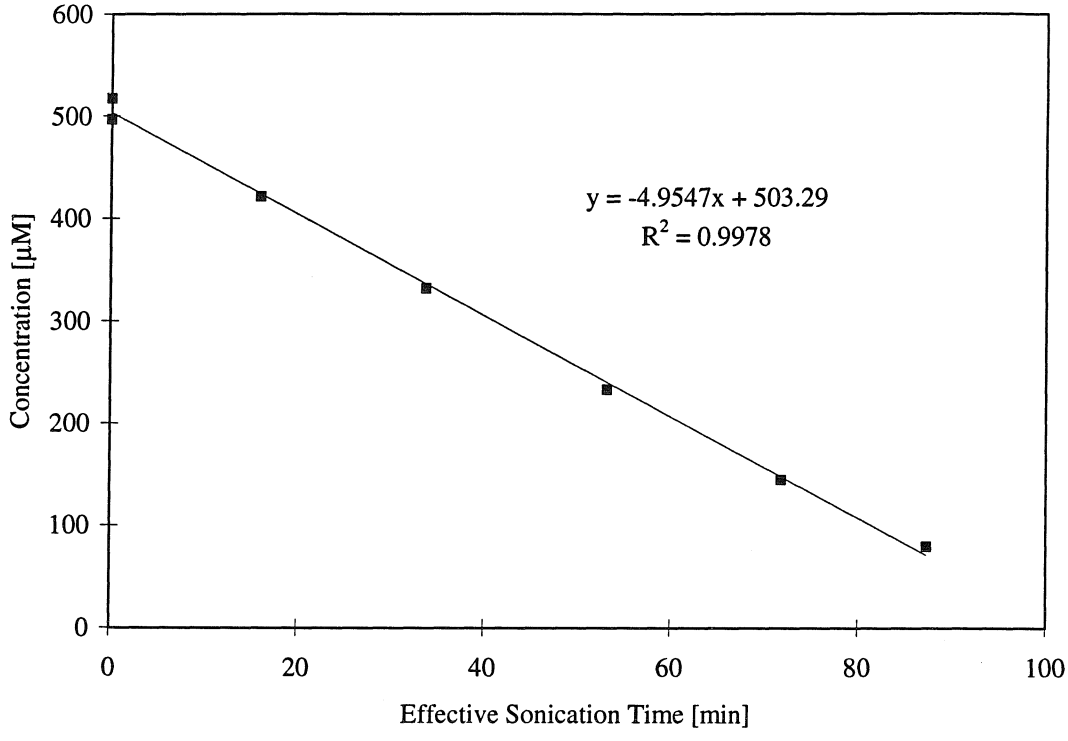

Fig. 9: Zero-order plot for the degradation of m-NA in the NAP reactor. $k_0 = 4.9\ \mu M\ min^{-1}$. Initial concentration, $[m\text{-}NA]_0 = 500\ \mu M$.

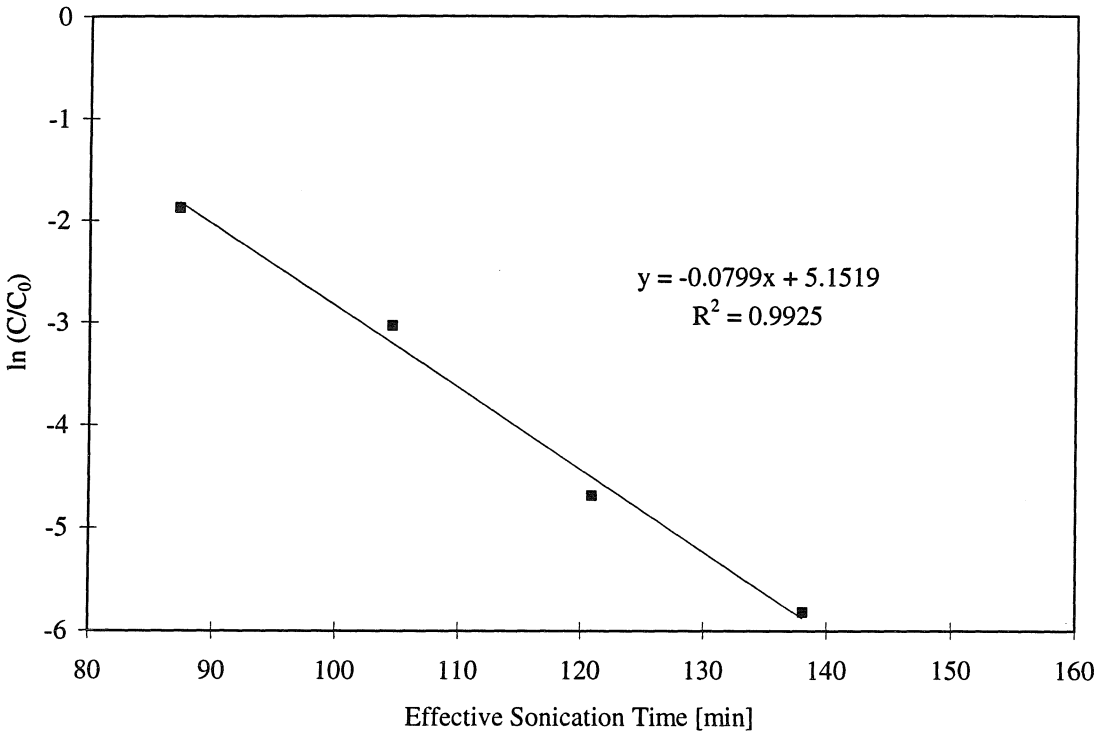

Fig. 10: First-order plot for the degradation of m-NA in the NAP reactor.

$k_1 = 0.08\ min^{-1}$. Initial concentration, $[m\text{-}NA]_0 = 500\ \mu M$.

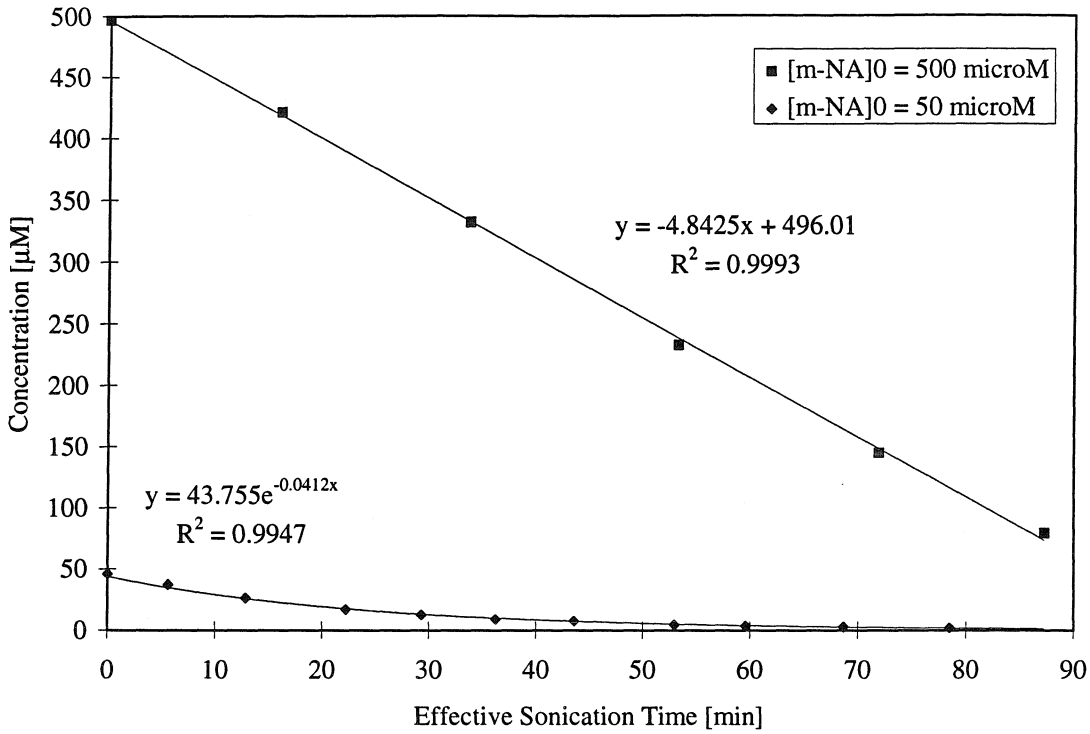

Fig. 11: Influence of the initial m-NA concentration on the apparent order and rate of the degradation reaction.

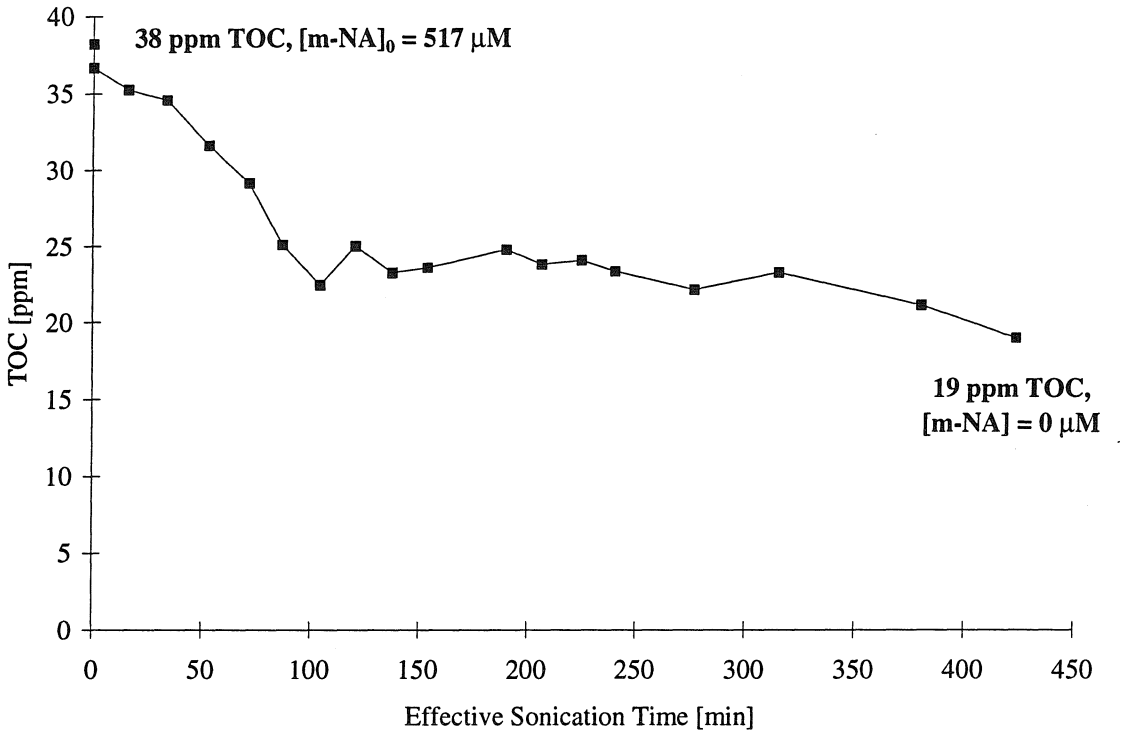

Fig. 12: Decrease of total organic carbon, TOC, during the sonication of m-NA in the NAP reactor. Initial concentration, $[\text{m-NA}]_0 = 500\ \mu M$.

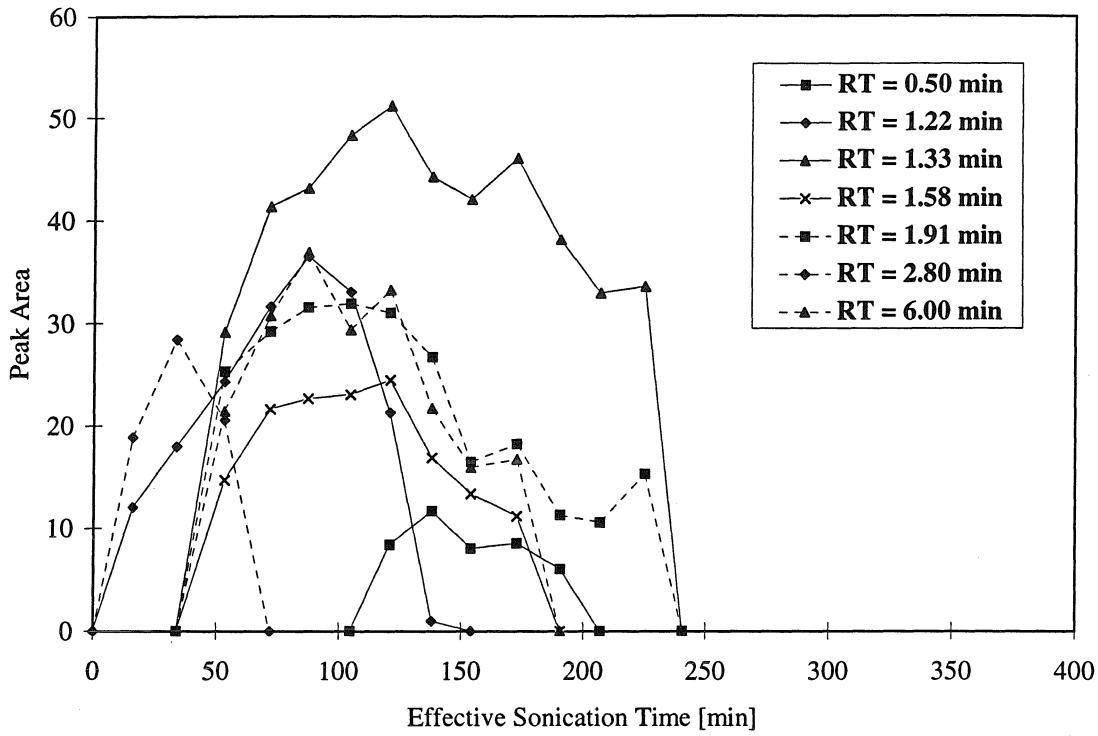

Fig. 13: Generation and dissapearance of aromatic intermediates during the ultrasonic irradiation of m-NA in the NAP reactor.

Initial concentration, $[\text{m-NA}]_0 = 500\ \mu M$.

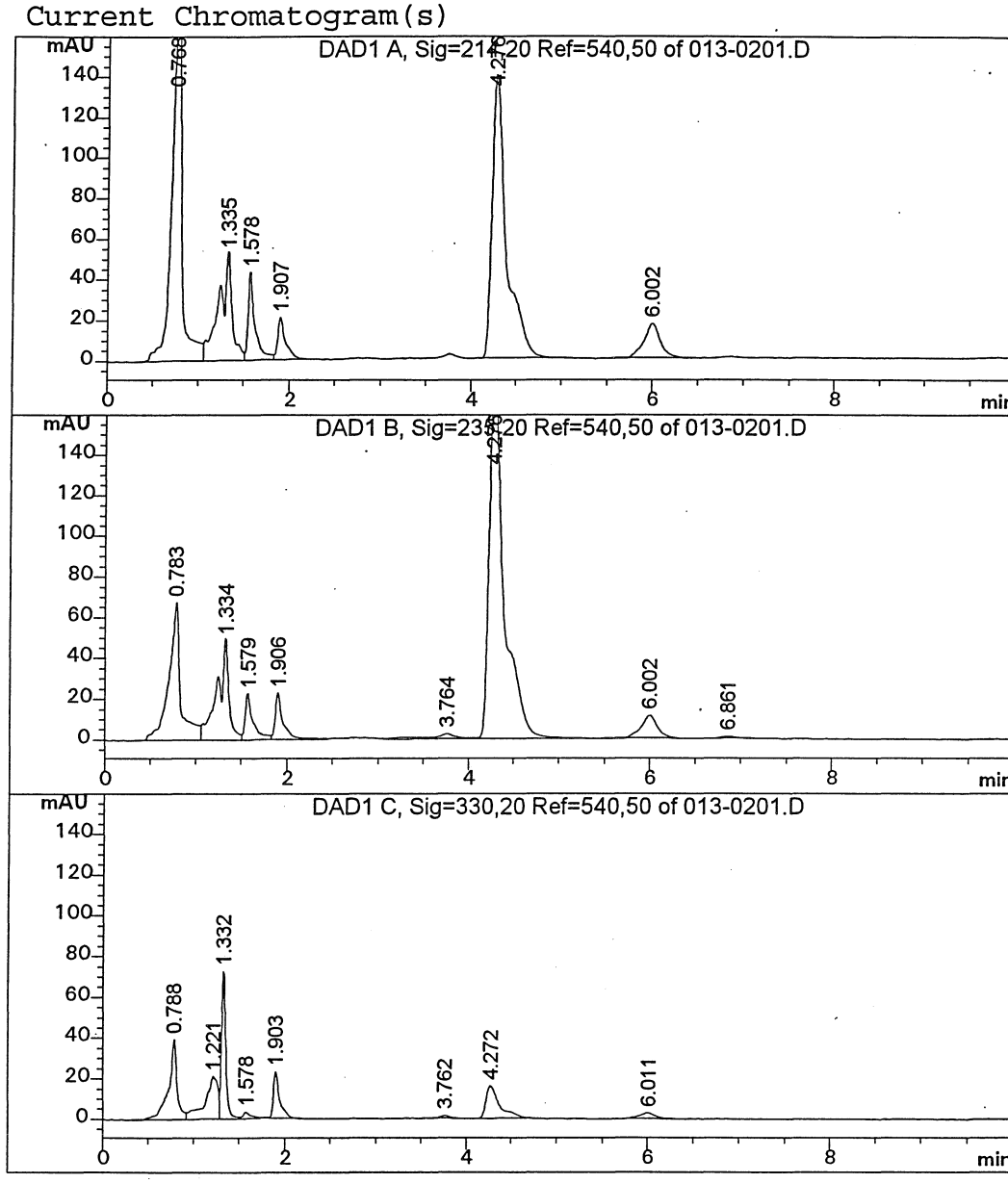

Fig. 14: Chromatogram of a reaction mixture after an effective sonication time of 72 minutes in the NAP. Initial concentration, $[\text{m-NA}]_0 = 500\ \mu\text{M}$.

Fig. 15a: UV/vis spectra of the unidentified aromatic compound shown in Fig. 14 at retention time 1.22 minutes.

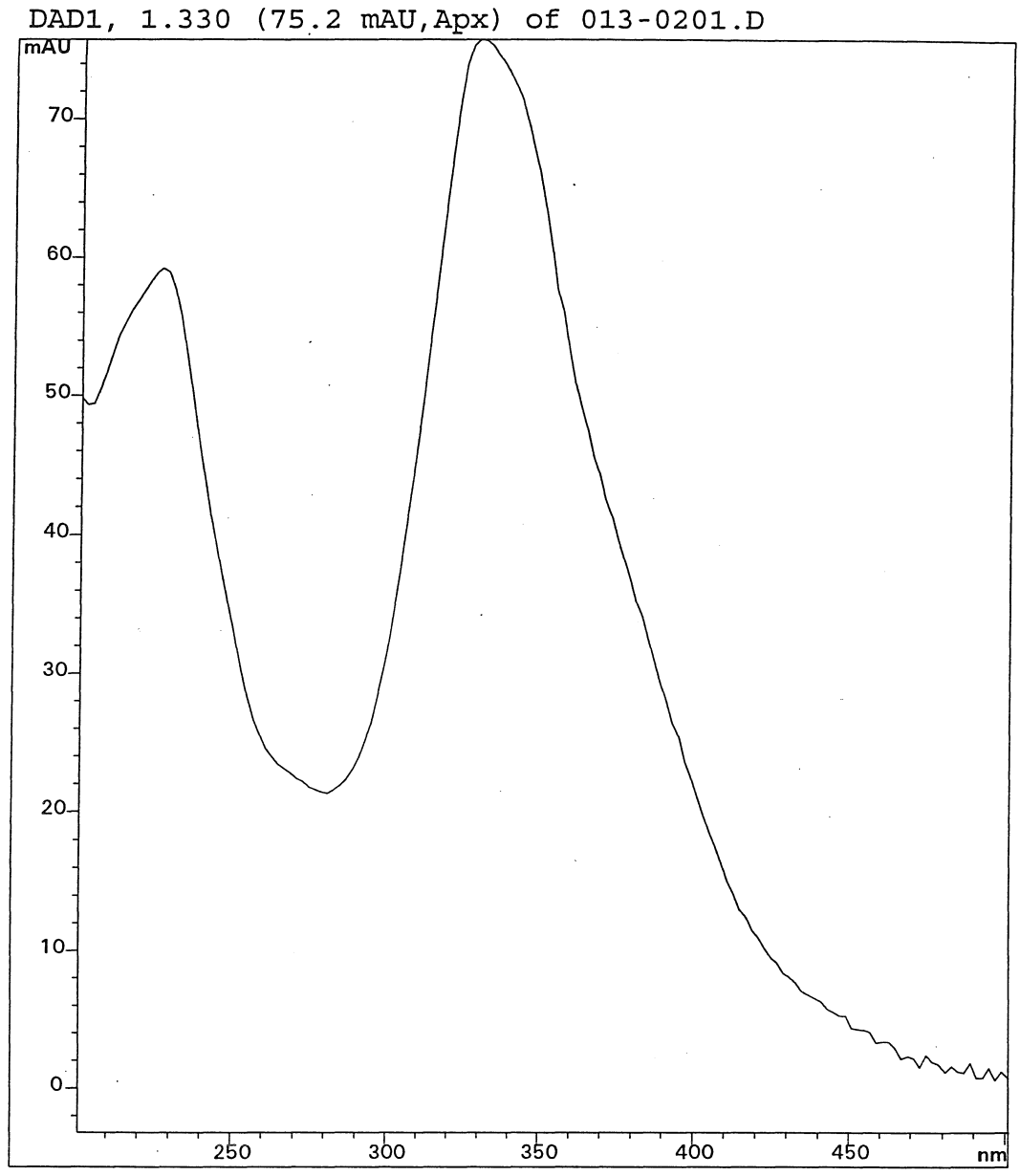

Fig. 15b: UV/vis spectra of the unidentified aromatic compound shown in Fig. 14 at retention time 1.33 minutes.

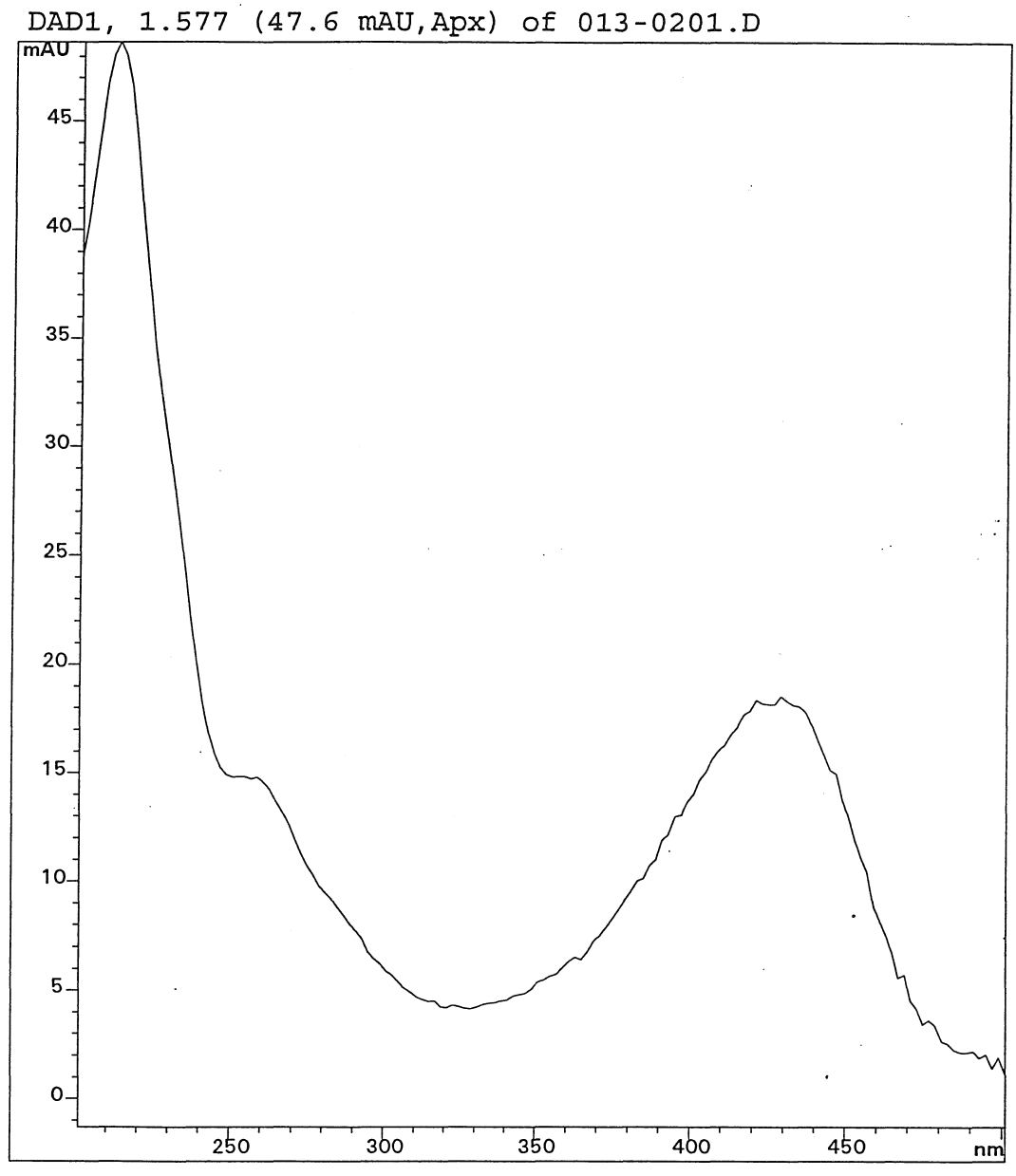

Fig. 15c: UV/vis spectra of the unidentified aromatic compound shown in Fig. 14 at retention time 1.58 minutes.

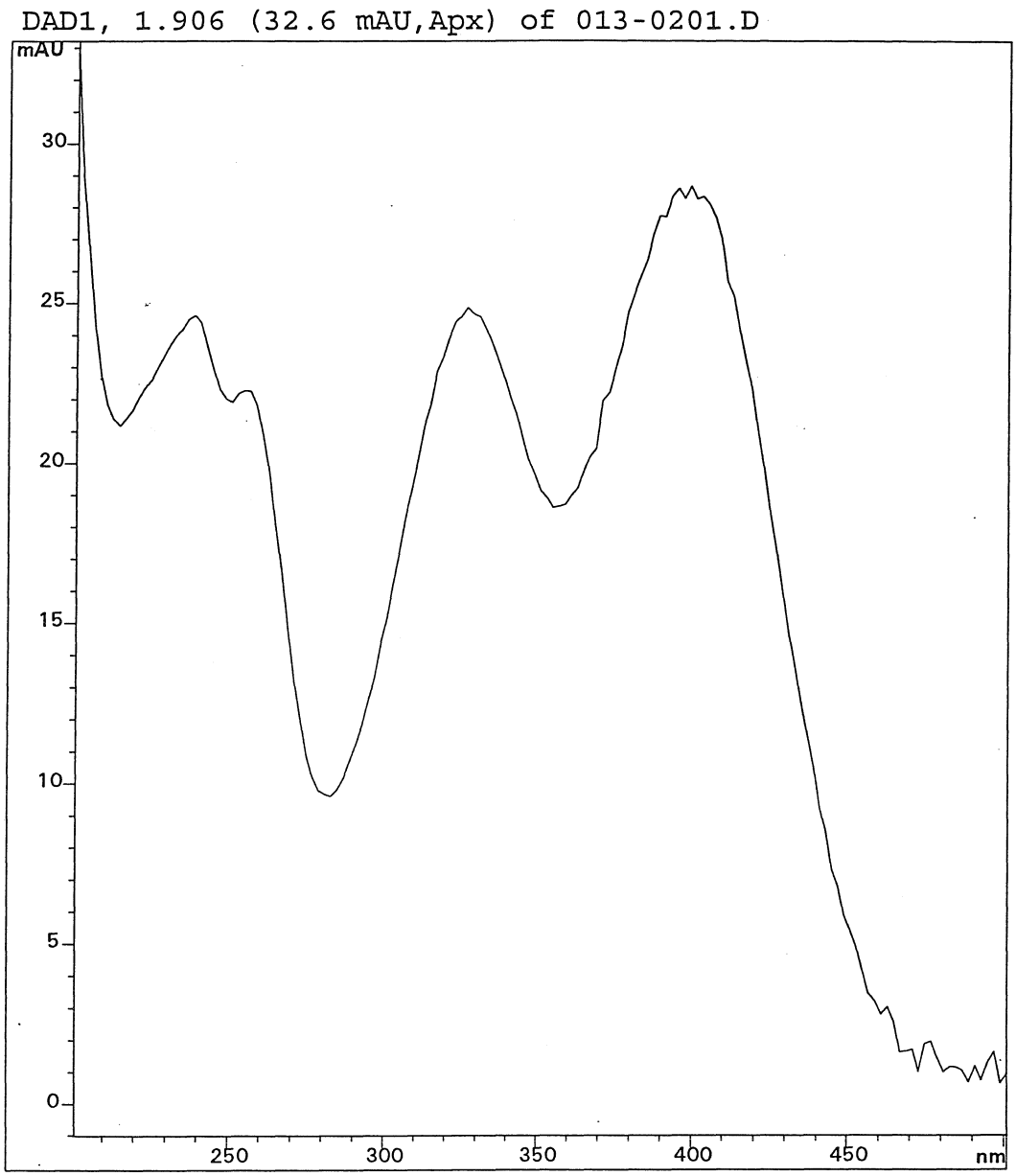

Fig. 15d: UV/vis spectra of the unidentified aromatic compound shown in Fig. 14 at retention time 1.91 minutes.

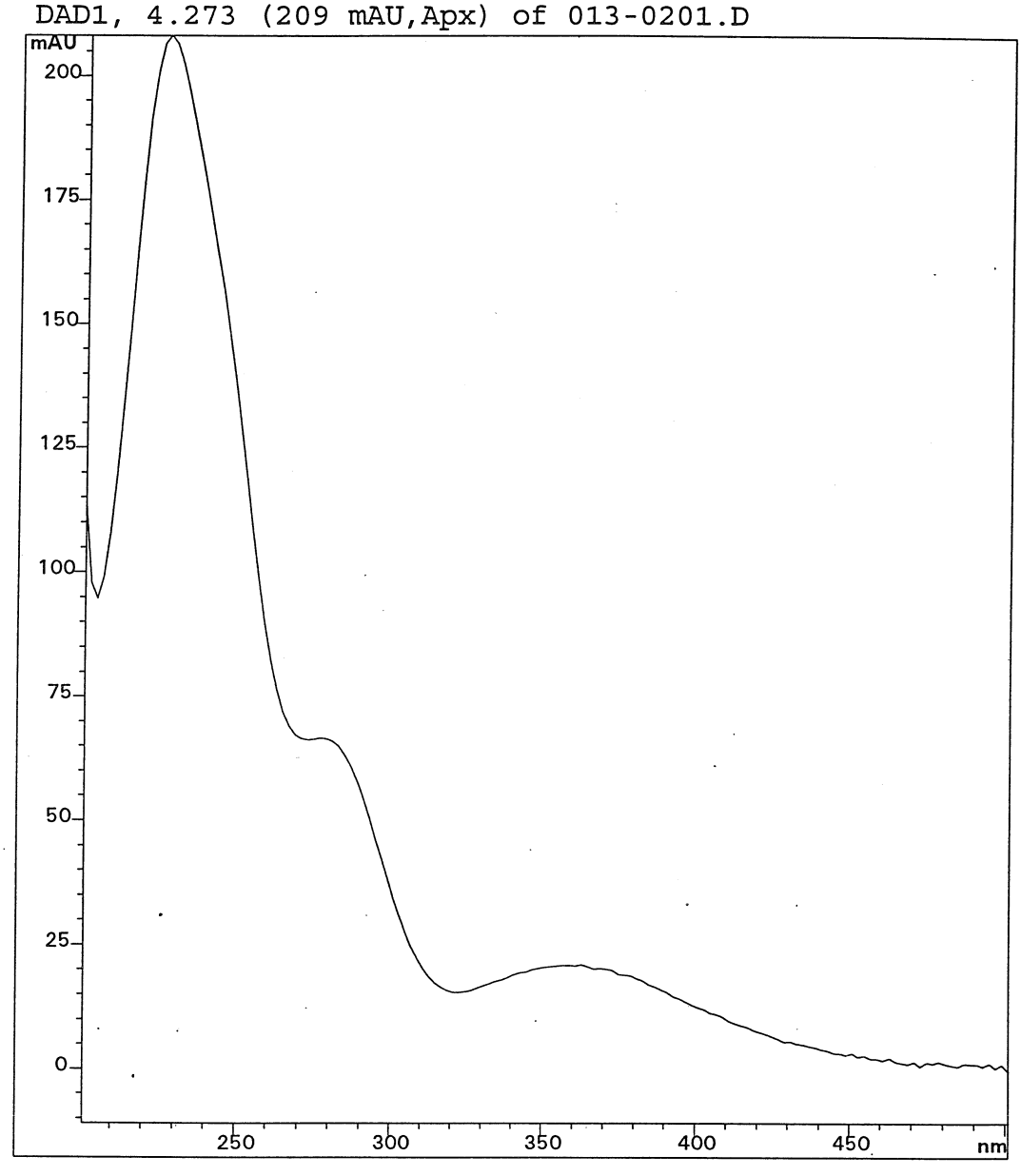

Fig. 15e: UV/vis spectra of the m-nitroaniline peak shown in Fig. 14 at retention time 4.27 minutes.

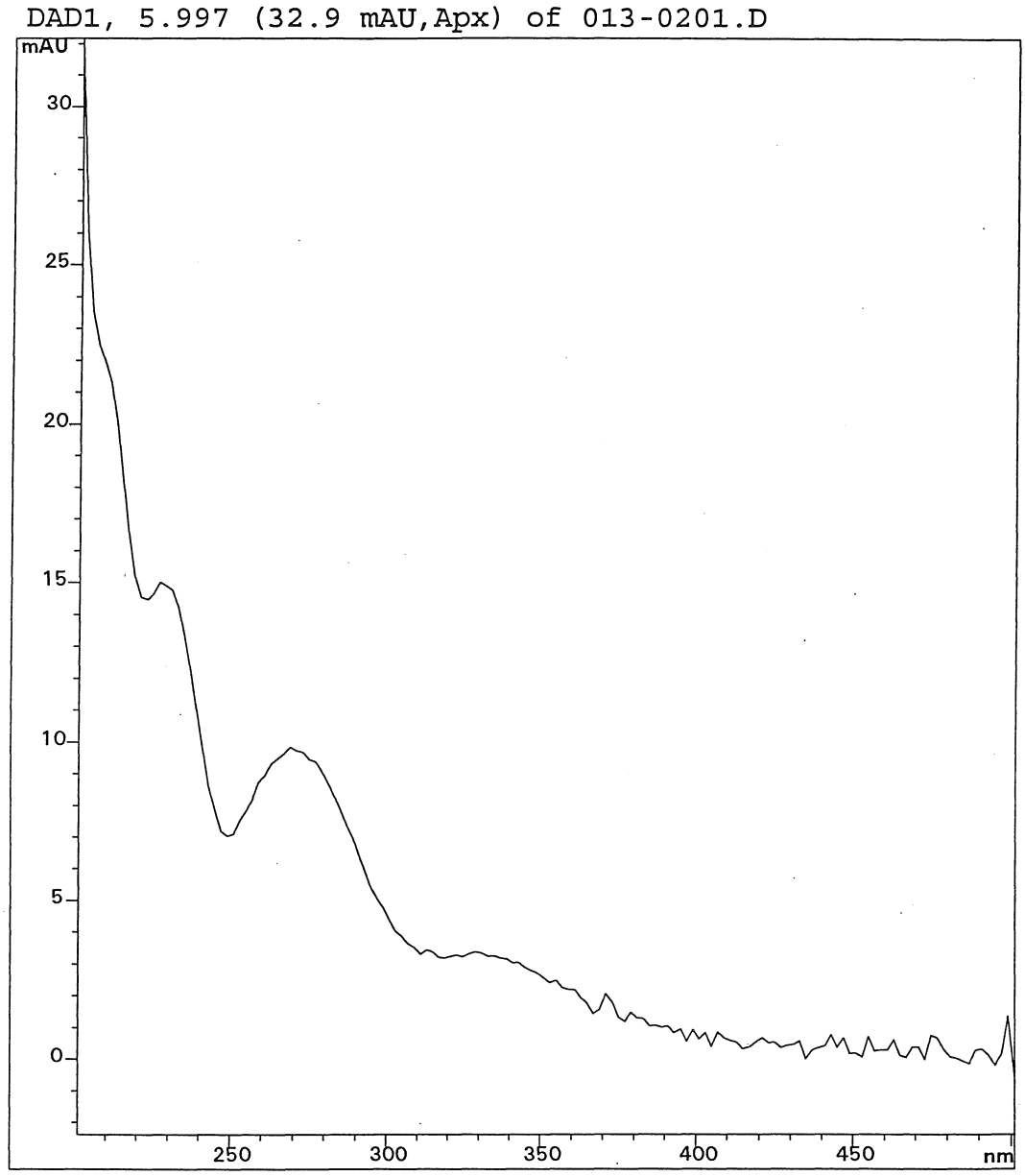

Fig. 15f: UV/vis spectra of the unidentified aromatic compound shown in Fig. 14 at retention time 6.00 minutes.

- Chapter VI -

The Sonochemical Degradation of p-Nitrophenol in a Parallel-plate Near-field Acoustical Processor

The text of this chapter appears in [Hua, I., Höchemer, R. H., Hoffmann, M. R., Environ. Sci. Technol., 1995, 29 (11), 2190-2796.]

Abstract

The sonochemical degradation of p-nitrophenol (p-NP) in a near-field acoustical processor (NAP) is investigated. The pseudo first-order rate constant, k, for p-NP degradation increases proportionally from $1.00\times10^{-4}s^{-1}$ to $7.94\times10^{-4}s^{-1}$ with increasing power-to-volume density over the range of 0.98-7.27 W/cm^3. An increase in the power-to-area density (i.e., sound intensity), results in an increase in k up to a maximum value of 8.60×10^{-4} s^{-1} at a sound intensity of 1.2 W/cm^2. A mathematical model for a continuous-flow loop reactor configuration is required in order to extract k from the experimentally observed rate constant, k_{obs}, which is a function of the relative volumes of reactor and reservoir.

The nature of the cavitating gas (Ar, O_2) is found to influence the overall degradation rate and the resulting product distribution. The rate constant for p-NP degradation in the presence of pure O_2, $k_{O_2} = 5.19\times10^{-4}s^{-1}$, is lower than in the presence of pure Ar, $k_{Ar} = 7.94\times10^{-4}s^{-1}$. A 4:1 (v/v) Ar/$O_2$ mixture yields the highest degradation rate, $k_{Ar/O_2} = 1.20\times10^{-3}s^{-1}$.

Results of these experiments demonstrate the potential application of large-scale, high power ultrasound to the remediation of hazardous compounds present at low concentrations. The NAP is a parallel-plate reactor which allows for a lower sound intensity but a higher acoustical power per unit volume than conventional probe-type reactors.

Introduction

The sonochemical degradation of a variety of chemical contaminants in aqueous solution has been previously reported (1-14). Substrates such as chlorinated hydrocarbons, pesticides, phenols, and esters are transformed into short-chain organic acids, CO_2, and inorganic ions as the final products. Time scales of treatment in simple batch reactors are reported to range from minutes to hours for complete degradation (3,4,9). For example, the total elimination of H_2S at pH 7 was achieved within 10 minutes (4) while parathion required 120 min to achieve complete degradation (6). Ultrasonic irradiation appears to be an effective method for the destruction of organic contaminants in water because of localized high concentrations of oxidizing species such as hydroxyl radical and hydrogen peroxide in solution, high localized temperatures and pressures, and the formation of transient supercritical water (2).

The scale-up of sonochemical reactors for practical waste water treatment applications has not been addressed to date. However, ultrasonic irradiation has been demonstrated to be effective in several large-scale, industrial processes such as sludge-dewatering (15), coal benefication (16), fossil fuel recovery (17,18), de-foaming (19) and the cleaning of jet-engine parts (16). Martin (20) has identified important scale-up parameters for sonochemical reactors (e.g., volume of the cavitating zone and the liquid flow-rate) and compared the effectiveness of a batch-scale probe reactor with a cylindrical duct reactor for the hydrolysis of methyl benzoate.

Large-scale reactor configurations include the conventional vibrating probe batch reactors and continuous flow reactors such as the near-field acoustical processor (NAP), in which the flowing solution is irradiated between two vibrating, parallel plates. Other reactor configurations include pentagonal or hexagonal tube reactors with magnetostrictive ultrasonic transducers mounted on each of the sides of the polygon (21).

In this paper we demonstrate the feasibility of utilizing large-scale ultrasonic reactors for the degradation of chemical contaminants in water. The effects of the ultrasonic power-to-area and power-to-volume densities on the degradation rate of p-nitrophenol (p-NP) and the effects of the physical and chemical properties of dissolved gases are explored. The net energy efficiency of the NAP is compared to a conventional probe reactor.

Experimental Methods

Chemical Procedures

p-NP (Aldrich, 99%+), phosphoric acid (EM Science) and NaOH (EM Science) were used as received. Solutions of p-NP were made with water obtained from a MilliQ-UV-Plus System (R = 18.2 MΩ cm^{-1}). All experiments were performed on 3-5 L of 100 μM p-NP in water. The pH was adjusted to the range of 4.5-5.0 with phosphoric acid. Solutions were saturated with the appropriate gas (flow rate 1.9 L min^{-1}) by bubbling the gas through four glass fritted dispersion tubes (Kontes, New Jersey), which were immersed into the liquid, for at least 20 minutes before and during sonication. Ar and O_2 and a mixture of the two gases were used as the saturating gases. The flow rates of O_2 and Ar in the gas mixture were 688 mL min^{-1} and 2434 mL min^{-1}, respectively. The solution temperature within the reactor reservoir was maintained at 22-25 ^{o}C during the course of sonication. 10 mL aliquots of solutions were removed from the reservoir at appropriate time intervals (ranging from 15 to 60 min) and adjusted to pH 11 with 100 μL of 5 N NaOH, filtered through 0.2 μm PFTE filters (Gelman), and analyzed spectrophotometrically (Hewlett-Packard UV/Vis, 8452A). The degradation of p-NP was followed at λ = 400 nm (ε = 17,900 M^{-1} cm^{-1}), and the formation of 4-nitrocatechol (4-NC) was followed at λ = 512 (ε = 12,300 M^{-1} cm^{-1}). The absorbance at λ = 400 nm is

corrected for interference by 4-NC by subtracting the relatively small absorbance due to the by-product ($\varepsilon = 6500\ M^{-1}\ cm^{-1}$) at 400 nm.

The Near-Field Acoustical Processor (NAP)

In a near-field acoustical processor (Lewis Corporation, Oxford, CT) the vibrational energy is transferred to the reaction mixture via two parallel stainless steel plates which are bolted together (Fig. 1). Each plate is vibrationally driven by seven magnetostrictive transducers that are bonded onto each plate. The transducers convert the electrical energy which is delivered by two power generators, operating at 16 and 20 kHz respectively, into the mechanical energy of vibration. The total sonoactive area is 1261.8 cm^2, and the length and width are 81.25 and 7.76 cm respectively.

A stainless steel spacer is placed between the two vibrating plates, in order to define the reaction volume, V_S. The seal between spacer and plates is provided by a Gore-tex gasket. Spacers of different thicknesses were employed to study the apparent reaction rate as a function of volume (244-1807 mL), and thus at different power-to-volume densities. Power input into the two frequency generating units was varied from 0 W to 1775 W in order to investigate the dependence of degradation rates on energy densities per area. Due to energy transformation losses within the system, the acoustical power transferred to the reaction mixture is less than the overall power put into the power generators (i.e., the power drawn from the wall supply). Efficiency calculations were based on the total power drawn from the wall outlet. The NAP reactor was maintained at constant temperature (30 ^oC) using a VWR Scientific (Model 1176) refrigeration unit.

Since the NAP system does not allow for direct cooling of the plates and transducers, the reaction mixture flowing through the reactor itself is thermostated externally as shown in the schematic diagram (Fig. 1). This reactor configuration involves the continuous flow of the reaction solution from the reservoir through the NAP

and back into the reservoir. A Pyrex glass vessel holding up to 8 L of reactant solution is used as reservoir. Stainless steel cooling coils were immersed into the reservoir solution to attain temperature control during sonication. Various ports in the top lid of the reservoir vessel allow for purging of the reaction mixture with the background gases during an experiment as well as sample withdrawal. NAP and reservoir were connected by a corrugated Teflon tubing (3/8'' i.d.). The reaction mixture is continuously circulated through the system via a peristaltic pump (Masterflex, model 7591-50) operating with Viton tubing. Throughout the entire study a volumetric flow rate of 3.2 L min^{-1} was maintained.

Results

Even though the reactor configuration of Fig. 1 can be viewed as a pseudo-batch reactor, observed kinetic data may depend on the time a given volume element actually resides within the irradiation zone and thus on the relative volume of NAP and its reservoir, and on the actual residence-time distribution (22-24) .

By choosing a flow through mode as opposed to a true batch mode, in which all of the solution would remain in one vessel and is at all times exposed to the ultrasonic irradiation, we introduce several additional reactor parameters. These parameters include the volumetric flow rate, Q, and the volumes of the reservoir, V_R, and the NAP, V_S. In order to obtain empirical rate constants for p-NP degradation that are independent of these three parameters (i.e., to extract first-order rate constants, k, from the observed rate constants, k_{obs}), we need to understand the dynamic behavior of the reactor system. A mathematical model is needed to give the concentration of p-NP as a function of time in both the reservoir and the NAP.

In order to obtain a convenient mathematical description of the reactor system of Fig. 1, we can consider two ideal reactors according to general reactor design principles

(22-24). We assume that the reservoir is a continuously stirred tank reactor (CSTR). This assumption is justified, since the solution in the reservoir vessel is vigorously stirred via a magnetic stirrer during the course of all experiments, ensuring efficient mixing. Control experiments show that there is no degradation occurring in the reservoir; thus it appears to be a perfect mixer without chemical reaction.

For reactions with a kinetic order ≥ 1, the conversion per pass through a reactor is a function of the residence-time distribution. We address this problem by considering the NAP to be two ideal reactors, that exhibit opposite extremes of residence time distributions (i.e., the CSTR and the plug flow reactor, PFR) and incorporate them into two different models. If both modeling approaches predict the same temporal behavior of the p-NP concentration in the reservoir (i.e., the same k_{obs} for a given reaction rate constant, k), then the residence time distribution of the NAP has no important influence on the system dynamics in this particular case and either approach may be used to find the k_{obs} to k conversion factor.

Our first approach is to assume the NAP to be an ideal CSTR (CSTR model) and then assume it to be an ideal PFR (PFR model) and subsequently solve the resulting differential equations for both cases.

CSTR Model

The mass balance equation for the reservoir is given as

$$\frac{dC_R(t)}{dt} = \frac{Q}{V_R}\left[C_S(t) - C_R(t)\right] \qquad (1)$$

where $C_R(t)$ and $C_S(t)$ are the concentrations of p-NP in the reservoir and in the NAP respectively and Q is the volumetric flow rate of the reaction mixture. Assuming ideal CSTR-behavior, the mass balance equation for the NAP is given as

$$\frac{dC_S(t)}{dt} = \frac{Q}{V_S}\left[C_R(t) - C_S(t)\right] + \nu r(k,c) \tag{2}$$

where V_S is the sonicated volume in the NAP, $\nu = -1$ is the stoichiometric coefficient for the reactant p-NP, and r(k, c) is the first-order reaction rate, which is given as:

$$r(k, C_S) = kC_S(t) \tag{3}$$

where k is the intrinsic first-order rate constant for the rate-limiting step in the degradation reaction as shown by (5)

$$HOC_6H_4NO_2 \xrightarrow{k,\Delta} HOC_6H_4O^{\bullet} + NO \tag{4}$$

The initial conditions for Eqns. (1, 2) are given as $C_R(t = 0) = C_S(t = 0) = C_0$.

We can make the problem non-dimensional as follows:

$$\tau \equiv kt, \quad \gamma \equiv \frac{V_S}{V_R}, \quad g \equiv \frac{C_R}{C_0}, \quad f \equiv \frac{C_S}{C_0}, \quad \alpha \equiv \frac{1}{Da} = \frac{Q}{kV_S}, \tag{5}$$

where Da is the Damkoehler number. Da represents the ratio of the mean hydrodynamic residence time, V_S/Q, over the characteristic time constant of the reaction, k^{-1}, under the NAP entrance conditions (22).

With these terms eqs. (1, 2), can be written in dimensionless form as follows:

$$\dot{g}(\tau) = \gamma\left[f(\tau) - g(\tau)\right] \tag{6}$$

$$\dot{f}(\tau) = \alpha g(\tau) - (1 + \alpha) f(\tau) \tag{7}$$

The dimensionless initial conditions are thereby given as $g(\tau = 0) = f(\tau = 0) = 1$, with the solution for g being

$$g(\tau) = \frac{1}{\lambda_2 - \lambda_1}\left[\lambda_2 \exp(\lambda_1) - \lambda_1 \exp(\lambda_2)\right] \tag{8}$$

and with λ_i given by

$$\lambda_1 = -\frac{\tau}{2}\left[1 + \alpha(1+\gamma) - \sqrt{\alpha^2(1+\gamma)^2 + 2\alpha(1-\gamma) + 1}\right] \tag{9}$$

$$\lambda_2 = -\frac{\tau}{2}\left[1 + \alpha(1+\gamma) + \sqrt{\alpha^2(1+\gamma)^2 + 2\alpha(1-\gamma) + 1}\right] \tag{10}$$

The actual operation conditions for volumetric flow rate, reaction rate constants and volume of NAP and reservoir allow us to simplify eq.(8). For $\tau \geq \frac{10}{\alpha}$ and $\alpha >> 1$ (i.e. Da << 1) g (i.e., the dimensionless p-NP concentration in the reservoir) can be written in terms of γ:

$$g(\tau) = \exp\left\{-\left(\frac{\gamma}{1+\gamma}\right)\tau\right\} \tag{11}$$

In dimensional form eq. (11) is given as

$$\frac{C_R(t)}{C_0} = \exp\left[-\left(\frac{V_S}{V_S + V_R}\right)kt\right] \tag{12}$$

where the observed first-order rate constant for p-NP degradation, k_{obs}, given by:

$$k_{obs} = \frac{V_S}{V_S + V_R} k \tag{13}$$

Eq. (13) relates the observed rate constant, k_{obs}, to the intrinsic rate constant in eq. (4), k.

PFR Model

Assuming ideal plug-flow behavior for the NAP, its mass balance equation is given by the partial differential equation

$$\left(\frac{\partial C_S(V,t)}{\partial t}\right)_{V=const} = -Q\left(\frac{\partial C_S(V,t)}{\partial V}\right)_{t=const} + vr(V,t) \tag{14}$$

and the mass balance equation for the reservoir is given by eq. (1).

Using the same dimensionless quantities as above, eq. (5), and by defining

$$f_\tau(x,\tau) \equiv \left(\frac{\partial f(x,\tau)}{\partial \tau}\right)_{x=const} \text{ and } f_x(x,\tau) \equiv \left(\frac{\partial f(x,\tau)}{\partial x}\right)_{\tau=const} \tag{15}$$

the mass balances for the reservoir and the NAP, Eqns (1, 12), respectively, can be written in dimensionless form as

$$\dot{g}(\tau) = \gamma[f(\tau) - g(\tau)] \tag{16}$$

$$f_x(x,\tau) + Da\, f_t(x,\tau) = -Da\, f(x,\tau) \tag{17}$$

with initial conditions $g(\tau = 0) = f(\tau = 0) = 1$, and the boundary condition of

$f(x,\tau) = g(\tau)$. Employing the method of characteristics, the differential equations can be solved analytically to obtain an expression for g,

$$g(\tau) = e^{-\lambda\tau} \tag{18}$$

where

$$\lambda = 1 + \frac{1}{Da}\ln\left(1 + Da\frac{\lambda}{\gamma}\right) \tag{19}$$

For $Da\frac{\lambda}{\gamma} << 1$ we expand eq. (19) into a MacLaurin series yielding a series expression for λ.

$$\lambda = \frac{\gamma}{1+\gamma} + O(Da) \tag{20}$$

Eq. (18) can be written in dimensional form by substituting eq. 20 for λ,

$$C_R(t) = C_0 \exp\left[-\left(\frac{V_S}{V_S + V_R}\right)kt\right] \tag{21}$$

The relation between the intrinsic rate constant, k, and the observed rate constant, k_{obs}, is found to be given as:

$$k_{obs} = \frac{V_S}{V_S + V_R}k \tag{22}$$

which is identical to eq. (11). We conclude, that by assuming the NAP to exhibit ideal PFR-behavior versus ideal CSTR-behavior we do not affect the final mathematical relationship between k_{obs} and k under the given conditions for Da and γ. Therefore, the

interpretation of the present results is possible without incorporating a residence time distribution within the NAP.

The initial reactions (5) in the degradation pathway of p-NP in an ultrasonically irradiated solution are shown below :

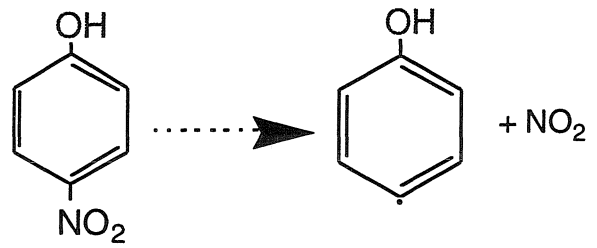

(1)

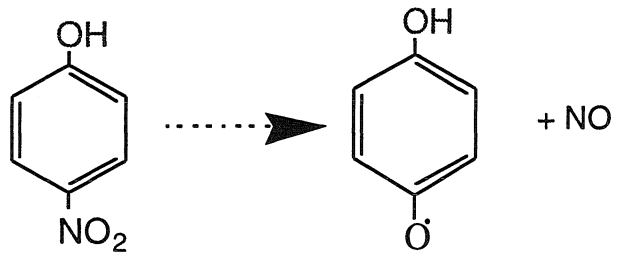

(2)

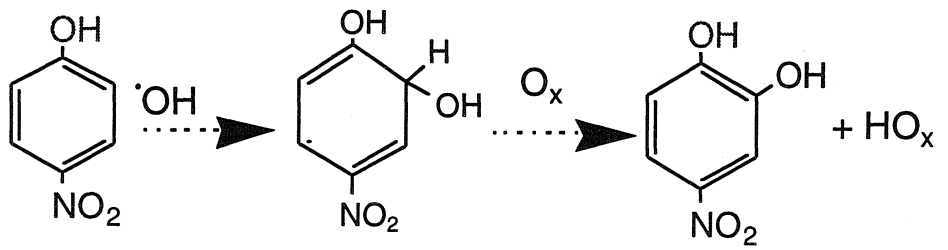

(3)

The predominant step, inferred from shock-tube studies (25) of analogous compounds is pyrolytic cleavage of the C-NO_2 bond which occurs at the hot bubble interface. Attack by hydroxyl radical (26-30) and subsequent reaction with other oxidizing species can lead to the formation of 4-NC and benzoquinone. A detailed discussion of the degradation by-products of p-NP in a sonicated solution is provided by Kotronarou et al. (5).

First-order plots of ln[p-NP] vs. time for an Ar saturated solution of p-NP sonicated at a gap-width of 1.45 mm are shown in Fig. 2. The rate constants for three identical runs were reproducible within 3-5 %.

A second set of experiments was performed to examine a variable gap-width between the plates (i. e., a variable reaction volume), with a constant power input of 1775 W. This variation allowed for a range of energy densities per unit volume while the energy per unit area (i.e., sound intensity) was maintained constant. The energy required to expand a population of bubbles in solution can be estimated with Eq. (26) (31):

$$E = (4/3)PNR_{max}^3 \tag{26}$$

where P = the magnitude of the hydrostatic and acoustic pressure; N = number of bubbles in solution; R_{max} = the maximum radius of the bubble before it collapses. Because P and therefore R_{max} vary only when the intensity changes, increasing the energy per unit volume in this set of experiments increases N, the number of bubbles which are forced to expand and then implode. Eq. (26) predicts that the number of bubbles will increase linearly with energy density. Although the number of chemical events per bubble is not known, it is reasonable to expect a linear correlation of chemical reactivity with the amount of energy transferred into solution. Fig. 3 illustrates the linear correlation of the observed degradation rate constant for p-NP with the volume energy density in an Ar saturated solution. The value of k ranges from $1.00 \times 10^{-4} s^{-1}$ at the lowest power-to-volume-density (0.98 W mL^{-1}) to $7.94 \times 10^{-4} s^{-1}$ at the highest power-to-volume density (7.27 W mL^{-1}). Faster degradation rates at higher energy densities result from a higher number of reactive sites (i.e., cavitation events) in solution.

In order to examine the dependence of k on the energy per unit area, the NAP reactor was operated at a fixed gap - width of 1.45 mm, while the power output was varied. Fig. 4 shows the variation of k as a function of the energy per unit area. k

increases with increasing sound intensity until a maximum value is obtained at 1.2 W cm^{-2} and then k decreases with further increases in intensity. This behavior has been observed previously, in both aqueous (31-33) and organic (34) solutions. The intensity, or energy per unit area, is correlated with the acoustic amplitude of the ultrasonic wave, Eq. (27) (7), as follows:

$$I = P_A^2 / 2\rho c \tag{27}$$

where I = amount of energy emitted per unit area per unit time, P_A = acoustic pressure amplitude, ρ is the density of water, and c is the speed of sound in water (~1500 m s^{-1}). The importance of the acoustic amplitude in determining the final temperature and pressure within the collapsed bubble can be estimated with Eqs. (28-29) (35,36).

$$P_{max} = P\left(\frac{P_m (K-1)}{P}\right)^{K/(K-1)} \tag{28}$$

$$T_{max} = T_0\left(\frac{P_m (K-1)}{P}\right) \tag{29}$$

where P_m = pressure in the liquid at moment of collapse; P = pressure in the bubble at its maximum size; $K = C_p/C_v$, the adiabatic index of the saturating gas; T_0 = temperature of bulk liquid. P_m is the sum the hydrostatic and acoustic pressures. A higher pressure during the rarefaction cycle will result in the growth of a bubble with a larger final bubble radius. During the compression cycle, however, a higher amplitude will result in a more complete implosion and thus more extreme the final conditions. This translates into higher reactivity at each bubble as the acoustic amplitude increases. However, the cavitation intensity cannot be increased without limit because as the vibrational amplitude (and thus the acoustic amplitude) increases, decoupling occurs between the vibrating

plate and the solution, thus energy transfer efficiency decreases (37). Also, the formation of a bubble shroud (13) may occur at the surface of the vibrating plates at high intensities, resulting in attenuation of the sound wave.

The effect of dissolved gases on k was determined. Since the chemical reactivity at a cavitation site is determined by the final temperature and pressure of bubble collapse as well as the nature of the oxidizing species produced, k should depend on the nature and properties of the dissolved gases. In the presence of Ar, water vapor in the high - temperature regions decomposes as follows (38):

$$H_2O \rightarrow H^{\bullet} + HO^{\bullet} \quad (30)$$

$$2\ HO^{\bullet} \rightarrow H_2O_2 \quad (31)$$

$$2\ H^{\bullet} \rightarrow H_2 \quad (32)$$

to produce $^{\bullet}OH$ and H_2O_2.

In addition to pyrolytic decomposition of water, the following reactions also occur in oxygen saturated solutions:

$$O_2 \rightarrow 2\ O^{\bullet} \quad (33)$$

$$O^{\bullet} + O_2 \rightarrow O_3 \quad (34)$$

$$H^{\bullet} + O_2 \rightarrow HO_2 \quad (35)$$

Thus, a solution saturated only with Ar (K_{Ar} = 1.66) would be expected to favor pyrolytic reactions (39,40) because of the higher final temperature, whereas an oxygen (K_{O_2} = 1.4) saturated solution would result in a greater number of oxidizing radicals but a lower temperature upon bubble collapse. The variation of k as a function of background gas compositions is shown in Fig. 5. The degradation of p-NP occurs most rapidly in a solution saturated with a 80%/20% (v/v) Ar/O_2 mixture and least rapidly in a solution saturated only with oxygen. This result is reasonable because the initiation of p-NP degradation occurs in two parallel reactions: pyrolytic cleavage of the C-NO_2 moiety and attack by $^{\bullet}OH$. In a solution saturated with either Ar or O_2 alone, only one of the

parallel pathways is accelerated. In a solution containing both gases, more extreme conditions can be achieved, as well as higher concentrations of oxidizing species and thus, the overall reaction rate constant increases.

The effect of the saturating gas on the formation of 4-nitrocatechol, a reaction intermediate, is less predictable. In Fig. 6 a plot of the fraction of p-NP degraded to 4-NC as a function of the percentage of p-NP degraded is shown. In an Ar saturated solution, the fraction of p-NP degraded to yield 4-NC is the highest. However, in solutions saturated with O_2 or the Ar/O_2 mixture, 4-NC is present in much lower concentrations. These lower concentrations of 4-NC most likely result from faster degradation due to attack by $HO_2^{\bullet}$, which is formed in significant quantities only in the presence of oxygen.

Sonication of solutions with $[p\text{-}NP]_i$ = 25 μM resulted in degradation rates constants which were about twice as large as those observed in solutions with $[p\text{-}NP]_i$ = 100 μM (Fig. 7). The slower degradation rate at a higher initial concentration demonstrates that the cavitation sites approach saturation with increasing bulk solute concentrations. A similar correlation between initial concentration and degradation rate constant is reported by Kotranarou (5).

Discussion

A summary of the rate constants and reactor conditions is given in Table I. The power-to-area ratio was maintained constant while the power-to-volume ratio was varied. However, when the power-to-area ratio was varied, the reactor volume was maintained constant, and thus the power-to-volume ratio varied simultaneously. The effect of these two parameters can be decoupled to conclude that a maximum value of the rate constant is obtained when the solution is exposed to an optimal intensity, rather than an optimal power-to-volume ratio.

The observed degradation rate constants show an increase in chemical reactivity at bubble interfaces as the ultrasonic intensity is increased but also indicate an uncoupling between the solution and the energy source at higher intensities (13). The number of reactive sites in solution can be controlled via the power-to-volume density, while the optimal reactivity at each site can be achieved by varying the power-to-area density. Furthermore, the enhancement of p-NP degradation in the presence of dissolved gas mixtures is consistent with previous studies. Hart (41) and Büttner (42) have studied free-radical formation in Ar/O_2 mixtures and also found an optimal percentages of each gas for oxidation of different substrates.

The energy efficiency of an advanced oxidation technology must be determined in order to determine its practical potential for hazardous waste treatment. In order to make this comparison, we employ the concept of efficiency, measured in terms of a G-value, which is often used in radiation chemistry (43,44). The G-value is defined for our purposes as the number of molecules degraded per unit of energy input into the system:

$$G - \text{value} = \frac{\Delta C \times N_o \times V}{\Delta T \times W} \text{ [molecules/kJ]} \qquad (36)$$

ΔC = change in the solute concentration over a given time interval ΔT; N_O = 6.023 x 10^{23} molecules/mol; V = volume of solution; W = wall voltage. Because the energy input is based on the wall-voltage, and the energy transduction process is not 100% efficient, the G-values calculated in this study (Table II) represent a lower limit for the G-values (based on energy absorbed) in the NAP reactor. As shown in Fig. 8, the G-value in the NAP is a function of the saturating gas.

The G-values for p-NP degradation in a probe reactor and NAP reactor under various conditions are compared in Table II. The standard bench top reactor configuration for sonochemistry consists of a vibrating horn (or 'probe') immersed in solution. This configuration was chosen for comparison to the NAP. Experimental

methods for collection of this data are described in Hua et al. (2) and specific reactor conditions are listed in Table II. The G-value for the probe reactor is approximately an order of magnitude less than in the NAP although the rate constants are of the same order of magnitude. This is due to the more even dispersal of energy in the NAP system. Because of the larger emitting area of the plates in a NAP, all of the reactant solution is directly exposed to ultrasound whereas in the probe reactor, the actual cavitating volume represents a small fraction of the total solution (37). In addition, attenuation of the sound wave in the NAP is minimal because the distance at any point in the solution from the emitting surface is only several mm or at most ~1.25 cm. Finally, because the NAP operates at two different frequencies, a greater number of bubbles in a given population can be excited. Sound waves emitted from two opposing plates can undergo constructive interference, given the superposition principle (45). The amplitude of the resulting wave can be larger than the two individual sound waves, resulting in more intense cavitational collapse. Given two waves traveling in opposite directions, with amplitude A, frequencies ω_1 and ω_2, and wave numbers k_1 and k_2, the behavior of the resulting wave as a function of time, t and position, x can be derived from the superposition principle:

$$f(x,t) = 2A\cos\left[\frac{(k_1+k_2)x+(\omega_1-\omega_2)t}{2}\right]\cos\left[\frac{(k_1-k_2)x+(\omega_1+\omega_2)t}{2}\right] \quad (37)$$

The NAP reactor operates at two different frequencies, but the sound field is the result of complex interactions.

The sonochemical degradation of p-NP in aqueous solutions can be successfully scaled-up from laboratory scale bench-top volumes to more practical operational volumes. The G-value obtained in the larger-scale NAP reactor is approximately 20 times higher than in a conventional probe reactor. The reaction rate retains its overall first-order character, and the observed rate constant exhibits an inverse relation to the

initial substrate concentration similar to that observed in the probe system. The parallel-plate design of the NAP reactor allows for a lower sound intensity but higher irradiation energy per unit volume. Furthermore, this configuration gives a more even distribution of cavitation events in the solution flowing through the NAP.

Optimization of p-nitrophenol degradation rates within the NAP can be achieved by adjusting the energy density, the energy intensity; and the nature and properties of the saturating gas in solution. The observed first-order degradation rate constant increases as the energy density and intensity are increased up to a saturation value. Manipulation of these macroscopic parameters leads to enhancement of the cavitation chemistry as the number of cavitation bubbles and the chemical events at each bubble are varied. A seven-fold increase in energy density results in an approximately equivalent increase in observed rate constant for degradation, whereas k reaches a maximum value upon increasing the intensity four-fold. The specific nature of the saturating gas influences the relative proportion of pyrolytic or free-radical reaction steps. Simultaneous acceleration of these pathways results in the maximum rate observed in solutions saturated in an Ar/O_2 mixture.

In our present investigations, the NAP reactor was integrated into a recycle system due to the need for temperature control which could only be achieved by thermostating the reaction mixture itself outside the reactor. The need for continuous recycling at a relative high volumetric flow rate together with the reactor volume and the first-order rate constants leads to small Damkoehler numbers, $Da = k V_R / Q << 1$. The mathematical analysis of the reactor system shows that for small Da (i.e., small conversion per pass), the residence time distribution of the NAP has no influence on the observed rate constants. This result justifies the use of the simple volume correction factor in determining k from k_{obs}.

Increasing the rate constant and/or the reactor volume, and decreasing the volumetric flow rate result in an increased Damkoehler number. Under these conditions,

the residence time distribution of the NAP has to be known in order to extract k from k_{obs}.

To operate the NAP as a steady-state continuous-flow reactor, a higher conversion per pass is needed by either decreasing the volumetric flow rate or increasing the reactor volume. During operation at small flow rates, the prevention of heat build-up within the reactor is achieved by circulating water through bores in the plates themselves, independent of the reaction mixture.

The degradation p-NP by ultrasonic degradation compares favorably to other modern treatment methods, including bacterial reduction (46) or oxidation (47), carbon adsorption (48), membrane solvent extraction (49), ozonolysis (50), and the Fenton reaction (51). Because reactor configurations (batch vs. flow-through) and reactor volumes vary greatly among these studies, direct comparison of rate constants cannot be made. Most of the techniques result in >90% degradation or removal of p-NP on the time scale of hours. However, ultrasonic irradiation offers the advantage over carbon adsorption and membrane extraction of complete compound destruction. Degradation occurs over concentration ranges varying by orders of magnitude (5), unlike certain biological systems (47) which are inhibited by relatively low substrate concentrations. Furthermore, the cavitation chemistry of p-NP does not exhibit complex pH effects which are observed during ozonolysis of the substrate (50) .

Acknowledgments: The authors wish to thank Sayuri Desai for preliminary experiments and the power input measurements and Douglas A. Varela for his assistance with solving the partial differential equation. Financial support from the Advanced Research Projects Agency, ARPA, (Grant # NAV 5HFMN N0001492J1901), the Office of Naval Research, ONR, and the Electric Power Institute, EPRI, (Grant # RP 8003-37) is gratefully acknowledged.

References

(1) Cost, M.; Mills, G.; Glisson, P.; Lakin, J. *Chemosphere,* **1993**, *27*, 1737-1743.

(2) Hua, I.; Höchemer, R. H.; Hoffmann, M. R. *J. Phys. Chem.,* **1995**, *9*,

(3) Koskinen, W. C.; Sellung, K. E.; Baker, J. M.; Barber, B. L.; Dowdy, R. H. *J. Environ. Sci. Health Part B,* **1994**, *29*, 581-590.

(4) Kotranarou, A.; Mills, G.; Hoffmann, M. R. *Environ. Sci. Technol.,* **1992**, *26*, 2420-2428.

(5) Kotronarou, A.; Mills, G.; Hoffmann, M. R. *J. Phys. Chem.,* **1991**, *95*, 3630-3638.

(6) Kotronarou, A.; Mills, G.; Hoffmann, M. R. *Environ. Sci. Technol.,* **1992**, *26*, 1460-1462.

(7) Mason, T. J.; Lorimer, J. P. *Sonochemistry: Theory, Applications and Uses of Ultrasound in Chemistry*; Ellis Horwood Ltd.: Chichester, 1988.

(8) Olson, T. M.; Barbier, P. F. *Wat. Res.,* **1994**, *28*, 1383-1391.

(9) Petrier, C.; Micolle, M.; Merlin, G.; Luche, J. L.; Reverdy, G. *Environ. Sci. Technol.,* **1992**, *26*, 1639-1642.

(10) Petrier, C.; Lamy, M. F.; Francony, A.; Benahcene, A.; David, B.; Renaudin, V.; Gondrexon, N. *J. Phys. Chem.,* **1994**, *98*, 10514-10520.

(11) Serpone, N.; Terzian, R.; Colarusso, P.; Minero, C.; Pelizzetti, E.; Hidaka, H. *Res. Chem. Intermed.,* **1992**, *18*, 183-202.

(12) Serpone, N.; Terzian, R.; Hidaka, H.; Pelizzetti, E. *J. Phys. Chem.,* **1994**, *98*, 2634-2640.

(13) *Ultrasound: Its Chemical, Physical and Biological Effects*; Suslick, K. S., Ed.; VCH Publishers, Inc.: New York, 1988.

(14) Wu, J. M., Huang, H. S., Livengood, C. D. *Environ. Prog.,* **1992**, *11*, 195-201.

(15) Bien, J. *Acustica,* **1991**, *74*, 279-283.

(16) Hunicke, R. L. *Ultrasonics,* **1990**, *28*, 291-294.

(17) Lin, J.-R.; Yen, T. F. *Energy and Fuels,* **1993**, *7*, 111-118.

(18) Sadeghi, K. M.; Lin, J. R.; Yen, T. F. *Energy Sources,* **1994**, *16*, 439-449.

(19) Berlan, J.; Mason, T. J. *Ultrasonics,* **1992**, *30*, 203-212.

(20) Martin, P. D.; Ward, L. D. *Chem. Eng. Res. Des.,* **1992**, *70*, 296-303.

(21) Mason, T. J. *Ultrasonics,* **1992**, *30*, 192-196.

(22) Baerns, M., Hofmann, H., Renken, A. *Chemische Reaktionstechnik;* 1 ed.; Georg Thieme Verlag: Stuttgart, New York, 1987; Vol. 1, pp 428.

(23) Denbigh, K. G. *Chemical Reactor Theory*; University Press: Camebridge, 1965.

(24) Dialer, K., Loewe, A. *Chemische Reaktionstechnik*; Carl Hanser Verlag: Muenchen, Wien, 1975, pp 108.

(25) Tsang, W.; Robaugh, D.; Mallard, W. G. *J. Phys. Chem.,* **1986**, *90*, 5968-5973.

(26) O'Neill, P., Steenken, S., Van Der linde, H., Schulte-Frohlinde, D.*Radiat. Phys. Chem.,* **1978**, *12*, 13-17.

(27) Volkert, O., Termens, G., Schulte-Frohlinde, D. *Z. Phys. Chem. N F,* **1967**, *56*, 261-267.

(28) Grässlin, D., Merger, F., Schulte-Frohlinde, D., Volkert, O. *Z. Phys. Chem. N F,* **1966**, *51*, 84-94.

(29) Suarez, C. L., F.;Günther, K.; Eiben, K. *Tetrahedron Lett,* **1970**, 575-578.

(30) Cercek, B.; Ebert, M. *Adv. Chem. Ser.,* **1968**, *81*, 210-221.

(31) Shutilov, V. A. *Fundamental Physics of Ultrasound*; OPA: Amsterdam, 1988, pp 378.

(32) Couppis, E. Z., Klinzing, G. E. *AIChE. J.,* **1974**, *20*, 485-491.

(33) Henglein, A., Gutierrez, M. *J. Phys. Chem.,* **1990**, *94*, 5169-5172.

(34) De Souza Barboza, J. C.; Petrier, C.; Luche, J. L. *J. Org. Chem.,* **1988**, *53*, 1212-1218.

(35) Neppiras, E. A., Noltingk, B. E. *Proc. Phys. Soc. B (London),* **1951**, *64B*, 1032-1038.

(36) Noltingk, B. E., and Neppiras, E. A. *Proc. Phys. Soc. B. (London),* **1950**, *63B*, 674-685.

(37) Mason, T. J. *Practical Sonochemistry: User's Guide to Applications in Chemistry and Chemical Engineering*; Ellis Horwood: Chichester, 1991, pp 186.

(38) *Advances in Sonochemistry*; Mason, T. J., Ed.; JAI Press Ltd.: London, 1990; Vol. 1.

(39) Kondo, T.; Riesz, P. *Free Radical Biol. Med.,* **1989**, *7*, 259-268.

(40) Kondo, T.; Kirschenbaum, L. J.; Kim, H.; Riesz, P. *Abstr. A C S Meeting,* **1992**, *204*, 246-INOR.

(41) Hart, E. J., Henglein, A. *J. Phys. Chem.,* **1985**, *89*, 4342-4347.

(42) Büttner, J., Gutiérrez, M., Henglein, A. *J. Phys. Chem.,* **1991**, *95*, 1528-1530.

(43) Armstrong, W. A., Humphreys, W. G. *Can. J. Chem.,* **1965**, *43*, 2576-2584.

(44) Todd, J. H. *Ultrasonics,* **1970**, *8*, 234-238.

(45) Ohanian, H. C. *Physics*; W. W. Norton and Co., Inc.: New York, 1985; Vol. 1, pp 594.

(46) Gurevich, P.; Oren, A.; Sarig, S.; Henis, Y. *Water Sci. Technol.,* **1993**, *27*, 89-96.

(47) Spain, J. C.; Gibson, D. T. *Appl. Environ. Microbiol.,* **1991**, *57*, 812-819.

(48) Calleja, G.; Serna, J.; Rodríguez, J. *Carbon,* **1993**, *31*, 691-697.

(49) Tompkins, C. J.; Michaels, A. S.; Peretti, S. W. *J. Membr. Sci.,* **1992**, *75*, 277-292.

(50) Beltrán, F. J.; V., G.-S.; Durán, A. *Wat. Res.,* **1991**, *26*, 9-17.

(51) Kochany-Lipczynska, E. *Chemosphere,* **1992**, *24*, 1369-1380.

Table 1

First-order rate constants for different power-densities with Ar as background gas.

Rate Constants, [10^{-4} s^{-1}]	Gap-Width, [mm]	Irradiated Volume, [mL]	Power/Area-Density, [W cm^{-2}]	Power/Volume-density, [W mL^{-1}]
7.94	1.45	244	1.41	7.27
5.39	3.25	376	1.41	4.72
3.93	6.30	568	1.41	3.12
1.98	9.50	834	1.41	2.12
1.00	25.17	1807	1.41	0.98
8.16	1.45	244	1.41	7.27
8.50	1.45	244	1.33	6.86
8.60	1.45	244	1.23	6.35
6.50	1.45	244	0.93	4.80
4.00	1.45	244	0.55	2.82
1.99	1.45	244	0.33	1.74

Table 2

Energy efficiencies of the NAP and probe systems.[a)]

Reactor	Energy Density, W/mL	Energy Intensity, W/cm^2	G-value x 10^{-15}, molecules/kJ	k, s^{-1}
Probe	4.8	10	2.3	5.2×10^{-4}
NAP	7.27	1.4	43	7.9×10^{-4}

[a)] For an Ar saturated solution; pH ~5 and $[p\text{-}NP]_i$ = 100 mM. Probe reactor manufactured by Sonics and Materials: Model VCX-400; operated at an average output of 130 W; sonicated volume 25 mL; T = 30 °C.

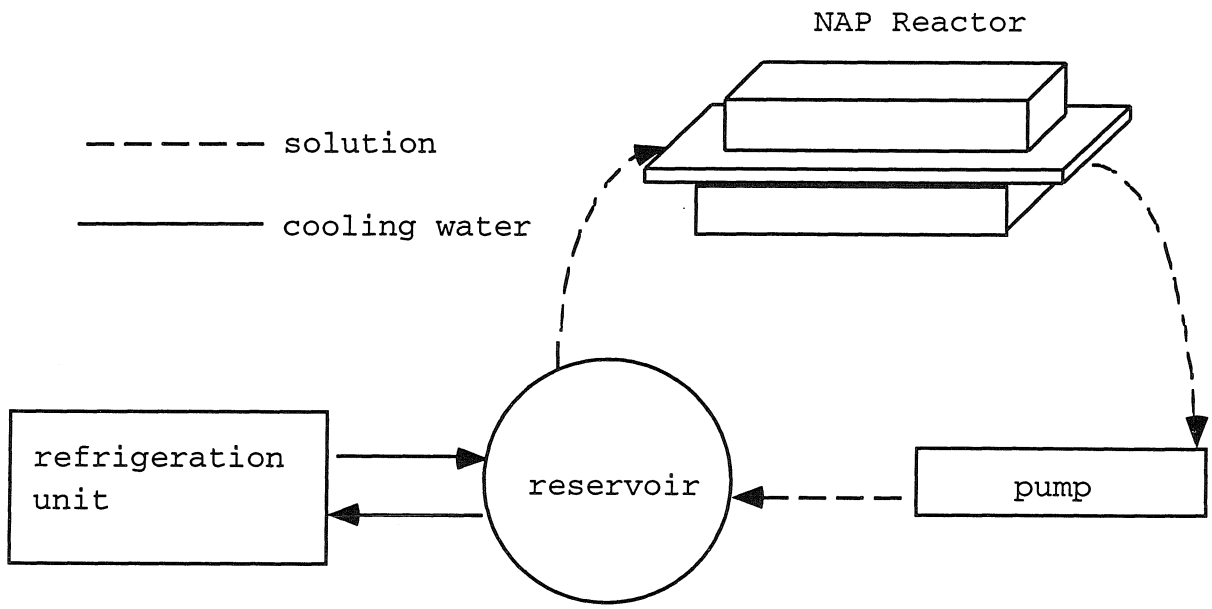

Fig. 1: Schematic of the reactor system setup.

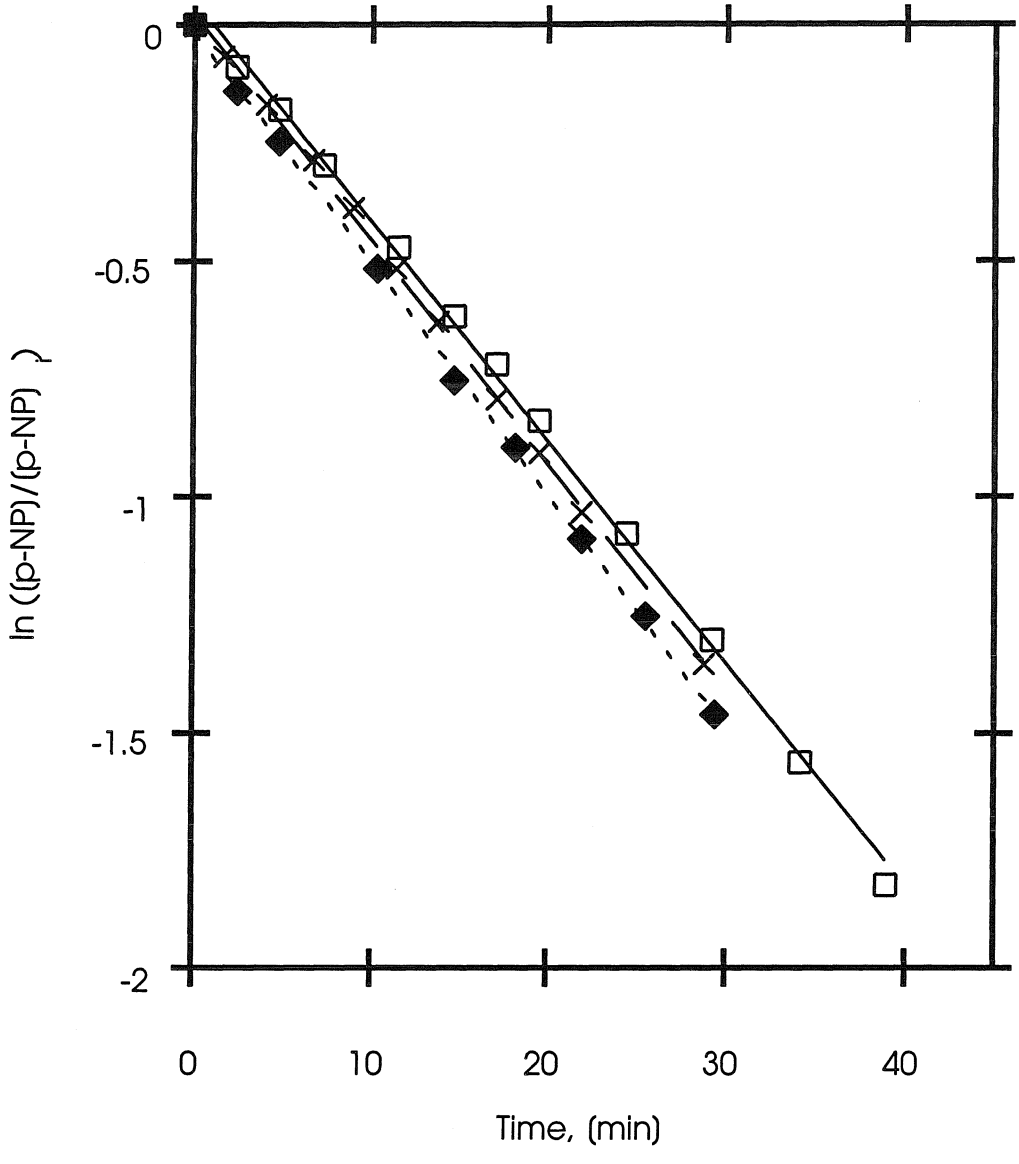

Fig. 2: First-order plot for p-NP degradation in an Ar saturated solution irradiated at 100 % (1775 W) power and a gap width of 1.45 mm. $[p\text{-NP}]_0 = 100\ \mu M$, $T = 30 \pm 2\ ^{o}C$, $pH = 5.0 \pm 0.2$, $\mu < 30 \mu M$. $k = (7.96 \pm 0.2) \times 10^{-4}\ s^{-1}$.

——— y = 0.044594 + -0.046645x R= 0.99896

—— - y = 0.01909 + -0.047664x R= 0.99973

- - - - - y = -0.015497 + -0.048965x R= 0.99973

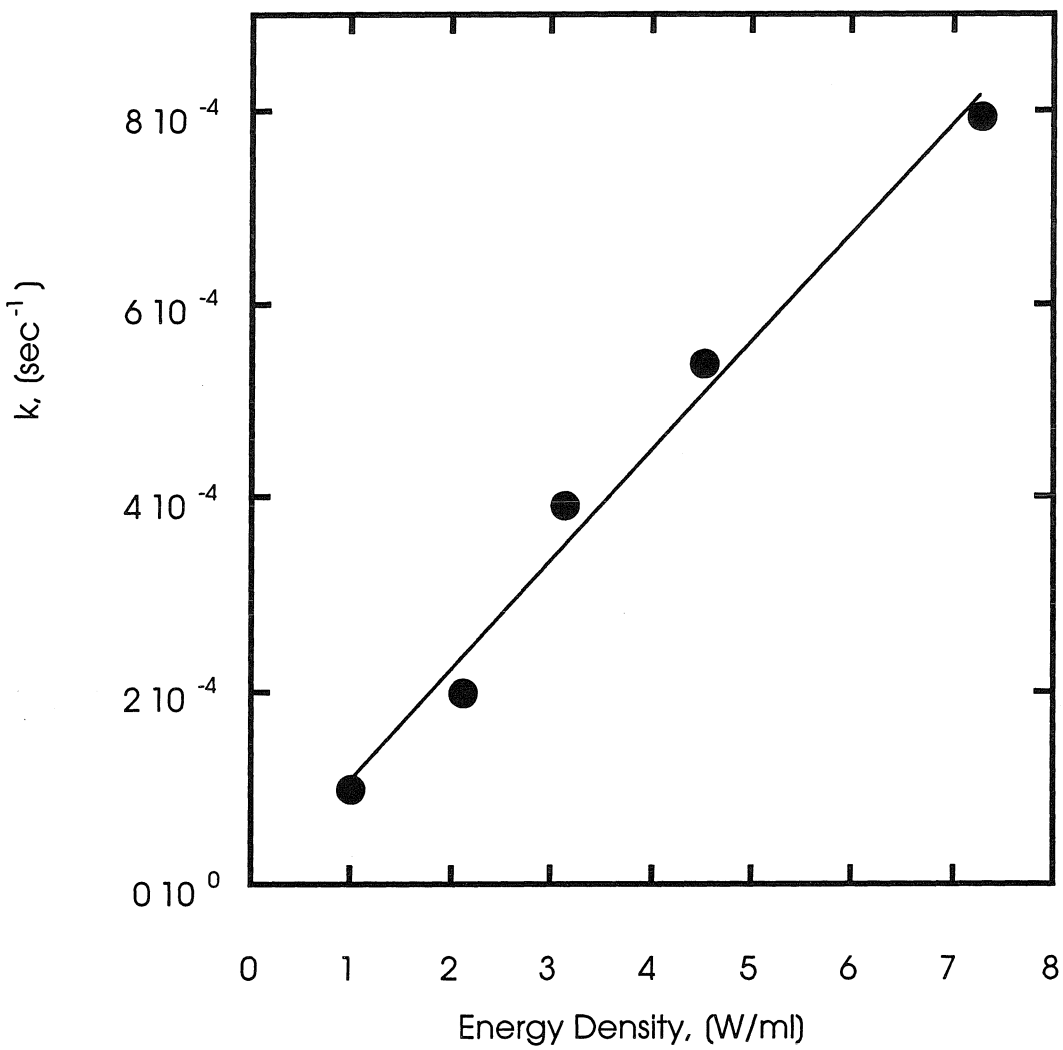

Fig. 3: p-NP degradation rate constant as a function of ultrasound power-to-volume-density. Variable reaction volume with constant power (1775 W). $[p\text{-}NP]_0$ = 100 μM, T = 30 ± 2 °C, pH = 5.0 ± 0.2, μ < 30 μM.

——— y = -1.6917e-06 + 0.00011282x R= 0.99185

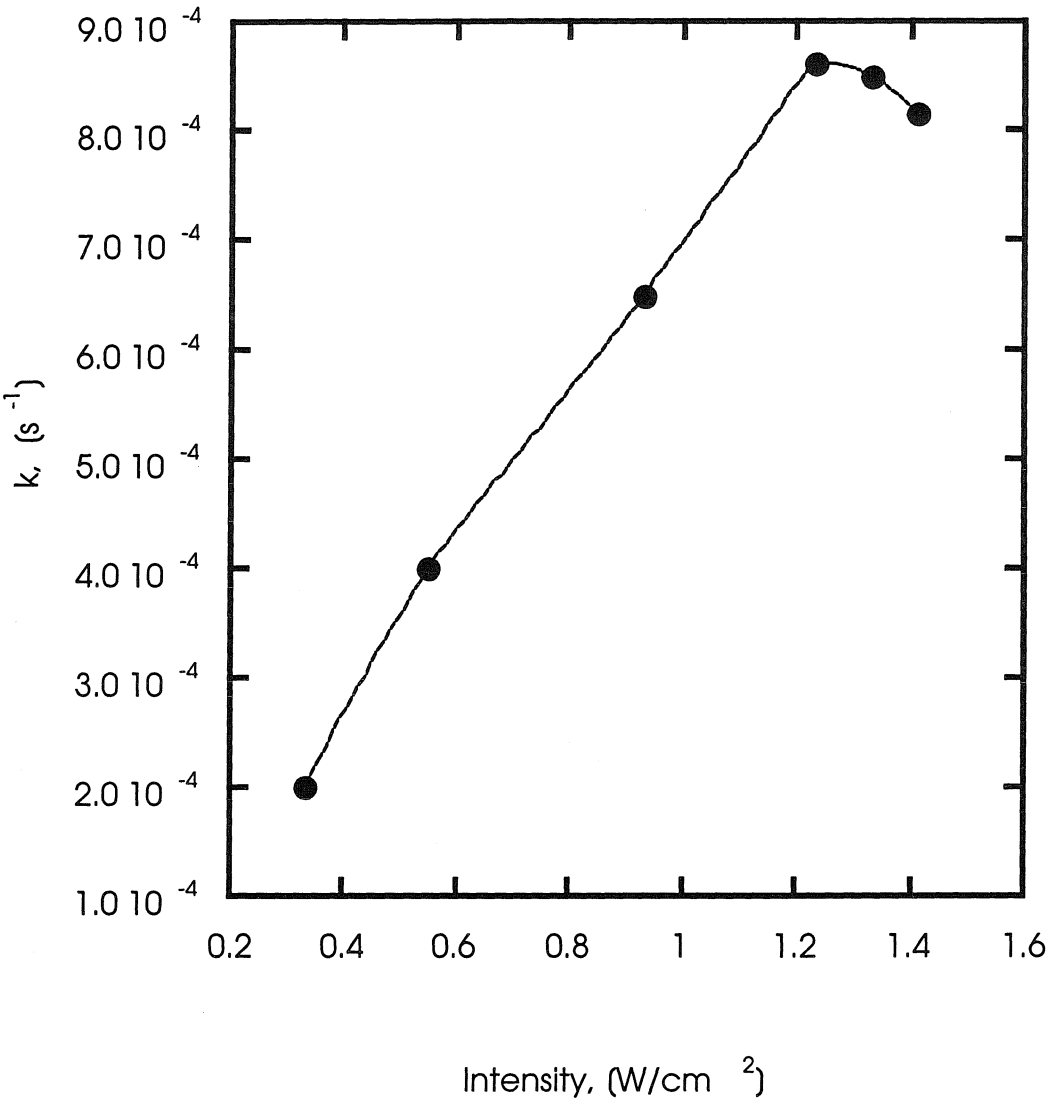

Fig. 4: p-NP degradation rate constant as a function of ultrasound power-to-area-density. Variable power with constant reaction volume (244 mL). $[p\text{-}NP]_0 = 100\ \mu M$, $T = 30 \pm 2\ ^{o}C$, $pH = 5.0 \pm 0.2$, $\mu < 30\ \mu M$.

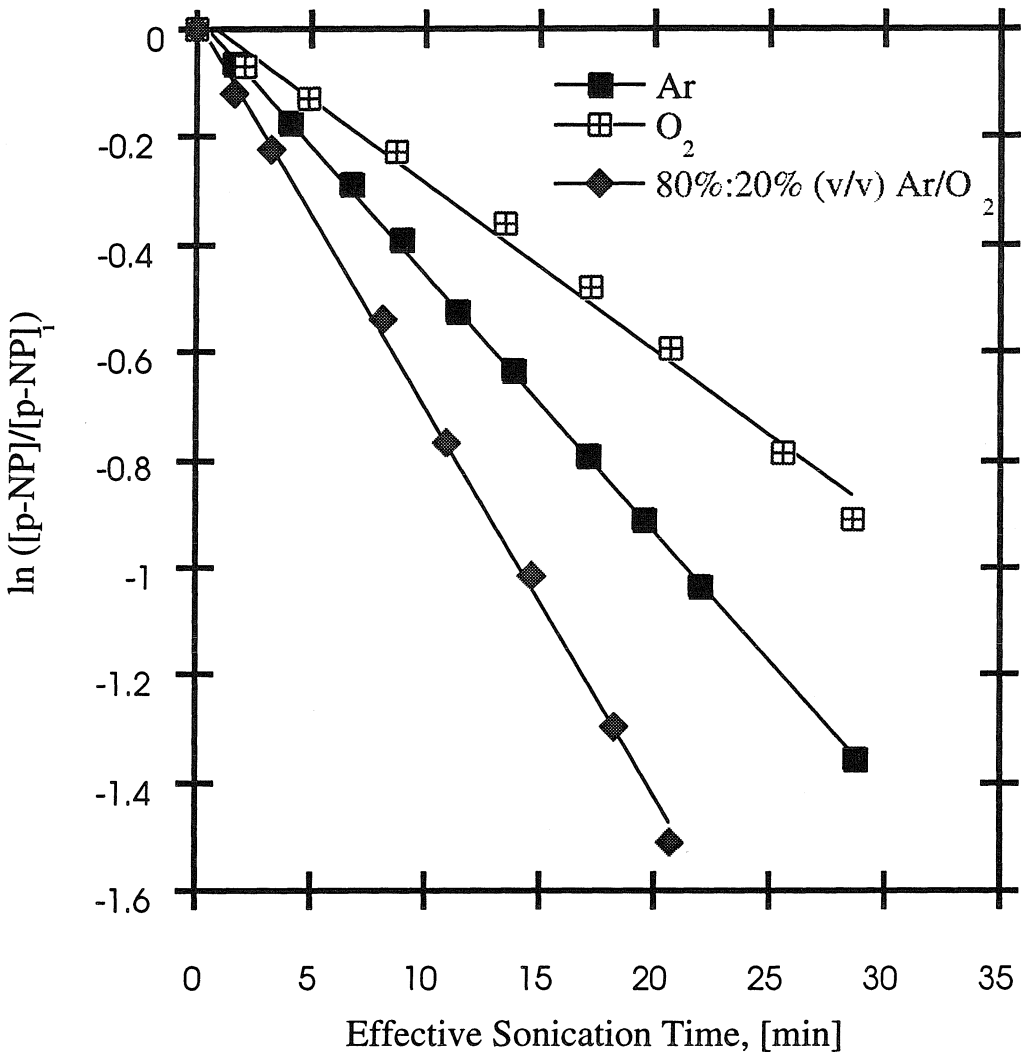

Fig. 5: First-order plot of p-NP degradation in solutions saturated with different gases at 1775 W power and 1.45 mm gap width. $k_{O_2} = 5.19 \times 10^{-4} s^{-1}$, $k_{Ar} = 7.94 \times 10^{-4} s^{-1}$, $k_{Ar/O_2} = 1.20 \times 10^{-3} s^{-1}$. $[p\text{-}NP]_0 = 100\ \mu M$, $T = 30 \pm 2\ ^{o}C$, $pH = 5.0 \pm 0.2$, $\mu < 30\ \mu M$.

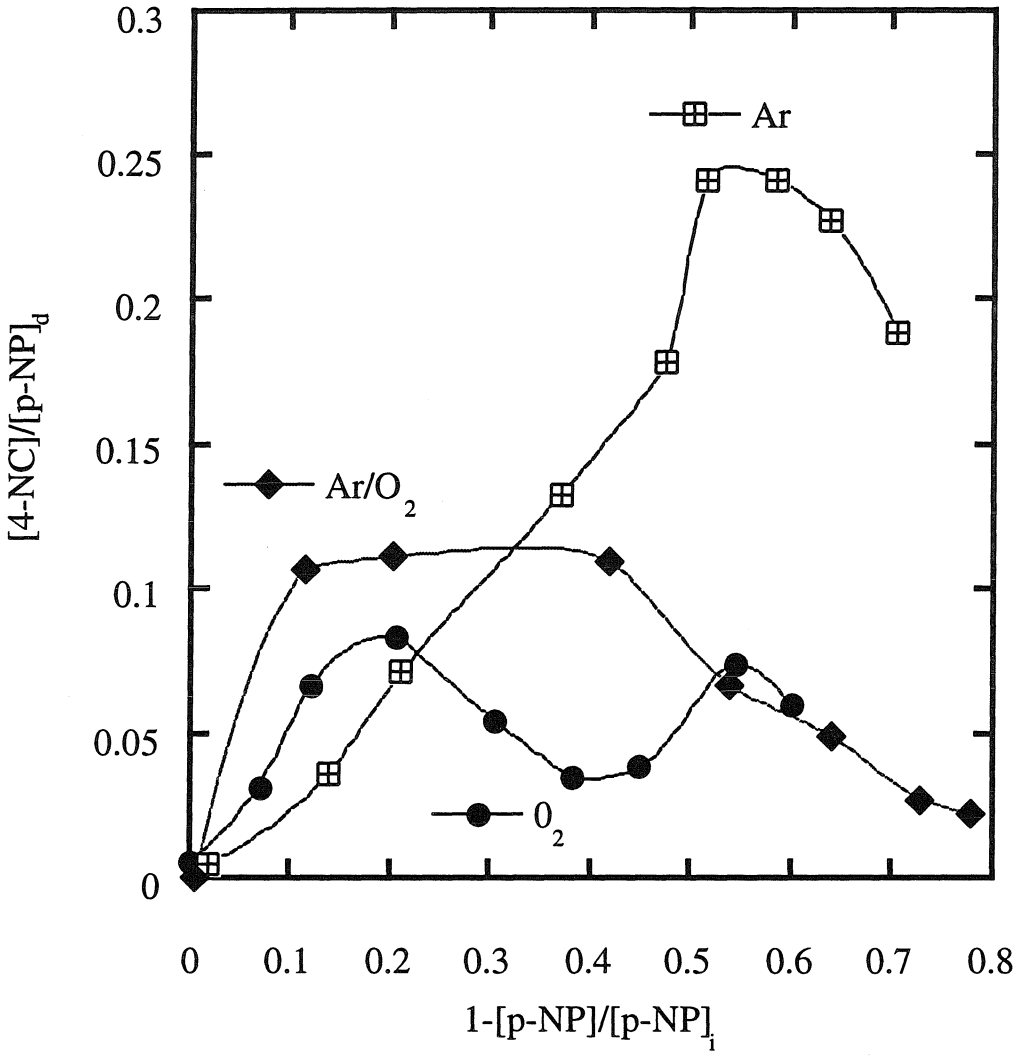

Fig. 6: Fraction of degraded p-NP which has been transformed into 4-NC as a function of the fraction of p-NP degraded. 7.27 W/mL and 3.2 W/cm^2.

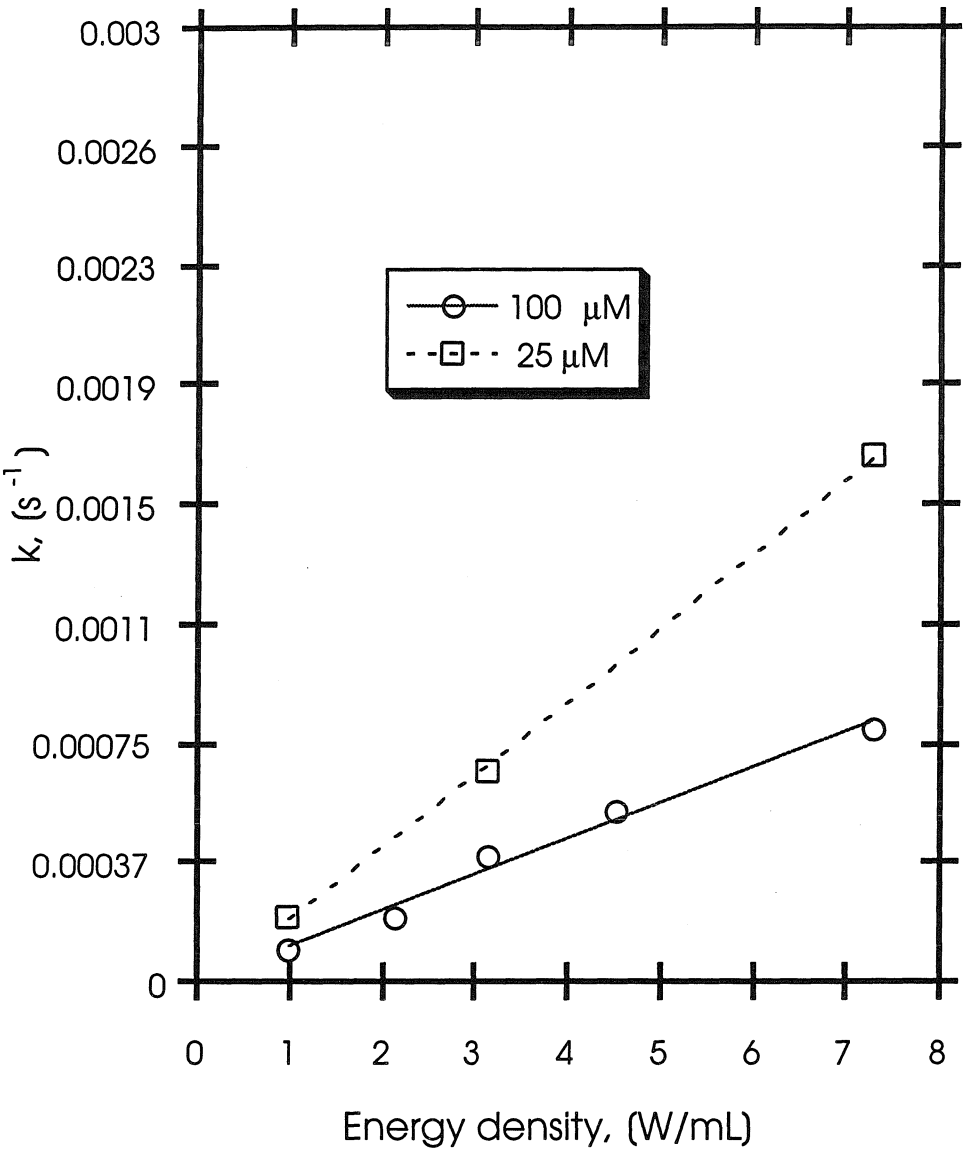

Fig. 7: Influence of initial concentration on p-NP degradation rate constant in Ar saturated solution. Power-to-volume density = 7.27 W mL^{-1} and power-to-area density = 1.45 W cm^{-2}. $[p\text{-}NP]_0$ = 100 and 25 µM, T = 30 ± 2 °C, pH = 5.0 ± 0.2, µ < 30 µM.

——— y = -1.6917e-06 + 0.00011282x R= 0.99185

- - - - - y = -3.4653e-05 + 0.00023077x R= 0.9997

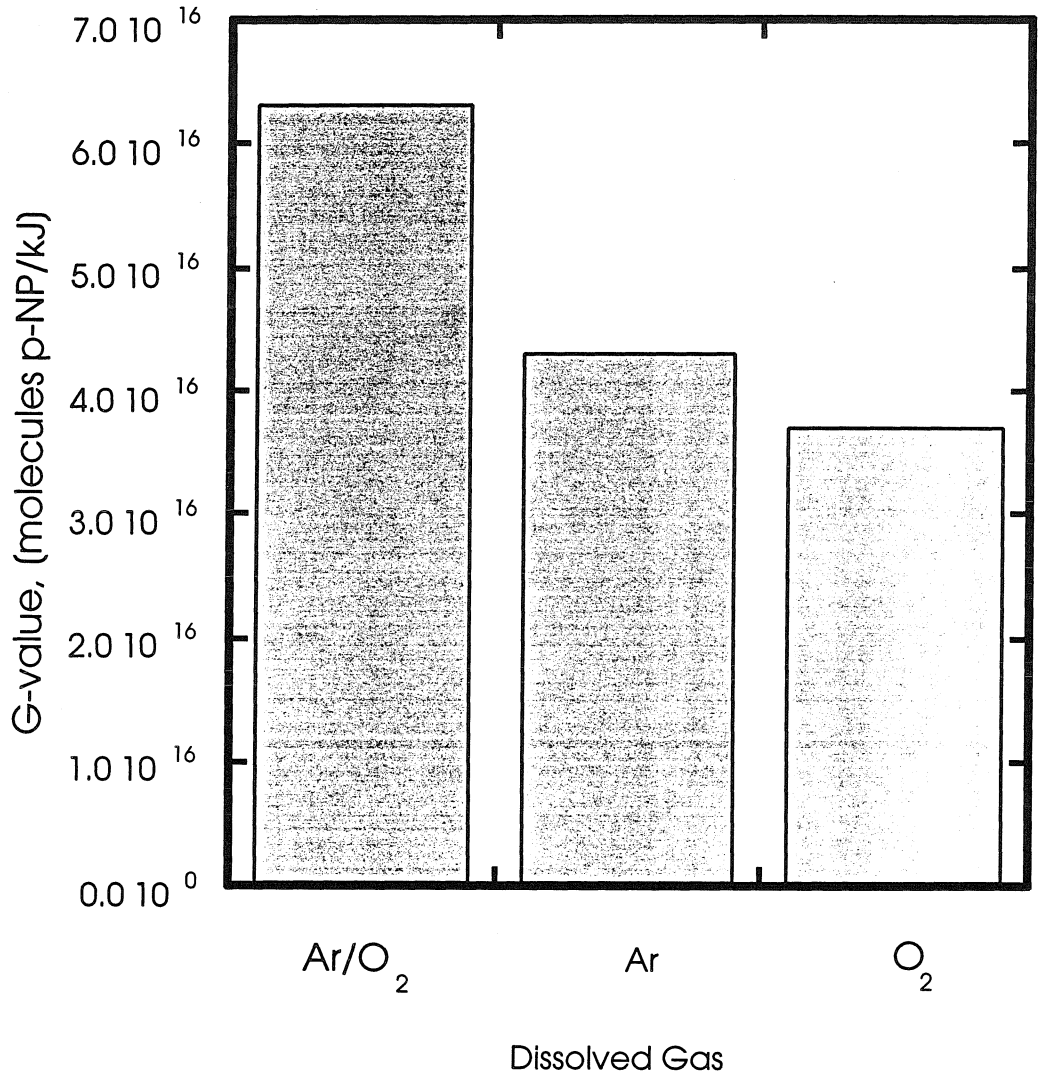

Fig. 8: The effect of the cavitating gas on the energy efficiency of p-NP degradation.

- Chapter VII -

The Pulsed-Power Plasma Reactor: Emission Spectrum and an Estimation of the Plasma-Arc Temperature

Abstract

The electromagnetic radiation emitted from the plasma channel formed during electrical underwater discharges within a pulsed-power reactor was determined over the wavelength range 416 to 635 nm. The spectrum was found to be continuous over the observed wavelength interval representing the radiative emission of a black-body source. The observed spectrum was approximated employing a nonlinear least square fit of a modified Planck distribution in order to estimate the temperature of the discharge arc. From this, a temperature of $T = (9500 \pm 300)$ K of the underwater discharge investigated was derived. The temperature of the plasma arc is an important physical input parameter in modeling electrical underwater processes.

Introduction

As we become increasingly aware of the scarcity of our natural resources new and less wasteful ways of production and utilization are gaining the interest of researchers in all fields of science and engineering. In particular, new technologies suitable for the remediation of hazardous wastes have in recent years attracted an increasing amount of interest.

Over the last decade, interest in the development of advanced oxidation technologies (AOTs) for the treatment of hazardous chemical wastes has grown enormously. Several AOTs involve the introduction of energy into aqueous solution via non-thermal processes. TiO_2 photocatalysis (1), electron-beam irradiation (2,3), sonochemistry (4-7), and UV/perozone photolysis (8) are examples of this strategy.

The electrohydraulic discharge process (EHD) is a non-thermal plasma technology, that injects energy into an aqueous solution through a plasma channel formed by a high-current/high-voltage electrical discharge between two submersed electrodes (9-15, 16). Industrial applications of the basic technology have included the simulation of underwater explosions (15), metal forming (17), rock fragmentation (18), and lithotripsy (19).

Basic pulsed-power technology has been incorporated into other AOT*s* such as in nonthermal plasma and corona discharge treatment of hazardous wastes (2,3). However, they depend on substantially different chemical mechanisms than the EHD process to achieve compound destruction. Nonthermal plasma technology has been applied primarily to gas phase-waste streams. This approach relies on high-energy collisions of molecules with electrons to generate free radicals and lower-energy electrons, which subsequently react with the chemical contaminants. The corona discharge method is similar in this operation to nonthermal plasmas, although it has also been applied to the treatment of liquid-phase wastes (20).

The emitted light flash plays a major role in compound degradation within the EHD reactor (16). This work focuses on the investigation of the high-intensity electromagnetic radiation emitted during an EHD event. In particular, we determined the spectral distribution of the light flash and estimated the average temperature over the lifetime (30-50 μs) of the plasma.

It has been previously reported that the low-temperature (i.e. below 100,000 K) dense plasma formed during the discharge resembles a black-body radiation source to good approximation (9-11). In addition the occurrence of sonoluminescence of the pulsating cavity occurring at the site of a high-voltage discharge has been reported (21). One goal of the present paper is to characterize the electrical underwater discharge in terms of its electromagnetic emission, i.e. the determination of the emission spectrum and the temperature of the plasma arc. Information about the generated radiation is necessary in determining the effectiveness of the high-voltage electrical discharge process for degrading chemical compounds via photochemical pathways. Photochemical degradation of organic compounds is a wide field of research (1) and the potential application of the pulsed-power plasma technology as a UV light and also a hydroxyl ($OH^{\bullet}$) radical source is promising. The absence of quartz surfaces, which separate the light source from the reaction medium in conventional UV lamps, is of advantage. In underwater high-voltage discharges, the possibility of obstructing the path of light by dirty interfaces is ruled out, since the light flash is generated directly in the reaction mixture.

Experimental

The emission spectrum was measured using an optical multi-channel analyzer (OMA), a schematic of which is shown in fig. 1. The system consists of a monochromator (SPEX Industries, 1681 0.22 m Spectrometer) without exit slit, a gated diode array detector (Princeton Instruments, IRY-700), a detector control unit (Princeton

Instruments, ST-120) and a pulse generator (Princeton Instruments, PG-10). Light dispersion within the monochromator was achieved by a planar diffraction grating with 1200 grooves/nm, which allowed for the observation of the emitted spectrum over a wavelength region of 30 nm at a time.

In order to synchronize the recording of the discharge emission spectrum with the ignition of the discharge a photodiode (Thorlabs, 10 ns rise time) was employed, which triggered the detector control unit off the generated light flash itself. In the present study emission data were collected by sampling light over the whole duration of the plasma arc, which has a lifetime of 30-50 μs (16). The spectra were measured with a gate time of at least 2 ms. Data acquisition and processing were performed using commercially available software. The emission lines from two low pressure mercury lamps (Pen-Ray SCT-1, Ultra-Violet Products, San Gabriel, Ca; Electro-Technic, SP-200, Chicago) were used for a linear wavelength-to-pixel assignment.

The generated light was observed through a 2 mm thick quartz window, which was mounted onto a stainless steel tube using a modified Swagelok assembly. The tube was inserted into a feed through port within the reactor lid. A quartz fiber (1 mm diameter, 2 m length) was used as a light guide in order to transport the emitted radiation from the discharge reactor to the entrance slit (0.05-0.5 mm) of the monochromator. Within the investigated wavelength regime transmission coefficients of the quartz fiber were close to unity, ranging from 0.9974 at 635 nm to 0.9921 at 416 nm. Therefore the detected spectra were not corrected for the transmission of the fiber.

The electrical discharges were carried out in 700 mL of aqueous (deionized water, MilliQ-UV-Plus System, R = 18.2 M cm^{-1}) 0.02 M $NaClO_4$ (Fisher Scientific, HPLC grade) solution. Since the solution showed increasing light scattering and absorption due to electrode tip erosion, the solution was replaced after 2-4 discharges. The experiments were performed with 5 kJ nominal energy per discharge using conical Ta electrode tips. The electrode gap width was 1 cm.

Results and Discussion

The relative emission intensity over the range λ = 416 - 635 nm was experimentally determined in intervals of 20 nm per spectrum. The observed emission intensity at λ = 635 nm was arbitrarily chosen as baseline. The overall spectrum was obtained by adding appropriate constants to the single narrow range spectra. This data treatment results in a baseline shift, but it does not introduce an artificial bias to the data analysis, since this present investigation is restricted to the relative emission intensities of the plasma arc. In this work no attempt was made to calibrate the data aquisition apparatus in order to obtain absolute intensity values.

The obtained spectrum, Fig. 2, lacks sharp emission peaks and the relative intensity is monotonically decreasing, which is consistent with the emission spectrum of a black-body radiation source. In order to get an estimate for the arc temperature of the discharge plasma, a modified Planck distribution was fitted to the observed pulsed-power emission curve. The Planck distribution for a black-body (22) is given by

$$I(\lambda) = \frac{8\pi hc}{\lambda^5}\left\{\frac{\exp\left[-\frac{hc}{\lambda kT}\right]}{1-\exp\left[-\frac{hc}{\lambda kT}\right]}\right\} \qquad (1)$$

Eq. 1 represents the energy density distribution, $I(\lambda)$, of a black-body radiation source, where $h = 6.626\times10^{-34}\,J\,s$, $c = 2.997925\times10^{8}\,m\,s^{-1}$, $k = 1.38066\times10^{-23}\,J\,K^{-1}$ are the Planck constant, the speed of light and the Boltzmann constant, respectively. The wavelength, λ, and the temperature, T, are independent variables. For the purpose of fitting the Planck distribution with T as a parameter to the observed emission curve it is convenient to rewrite eq. 1 as

$$I(\lambda) = \frac{A}{\lambda^5}\left\{\frac{\exp\left[-\frac{B}{T\lambda}\right]}{1-\exp\left[-\frac{B}{T\lambda}\right]}\right\} \qquad (2)$$

where the constants A and B are defined as

$$A \equiv 8\pi hc, \qquad B \equiv \frac{hc}{k} \qquad (3), (4)$$

In order to compare the observed spectrum to a calculated black-body emission spectrum at various temperatures, the observed emission curve is transformed by multiplication with a factor given as, C_{obs} = I_{obs}(416 nm) - I_{obs}(635 nm), such that $0 \le I(\lambda) \le 1$, and $416\,nm \le \lambda \le 635\,nm$. Similarly the values obtained through eq. 2 have to be transformed onto the same $I(\lambda)$, λ domain. Furthermore an additive fitting parameter, I_0, was introduced in order to account for baseline shifts in the experimental determination of the spectrum and for the non-zero emission at λ = 635 nm. The modified Planck distribution can then be written as

$$I(\lambda) = \frac{1}{C_T}\left\{\frac{\exp\left(-\frac{B}{T\lambda}\right)}{1-\exp\left(-\frac{B}{T\lambda}\right)}\right\} + I_0 \qquad (5)$$

where the transformation factor, C_T, is defined as

$$C_T \equiv \left(\frac{\lambda}{416\,\mathrm{nm}}\right)^5 \left\{\frac{\exp\left(-\frac{B}{416\,\mathrm{nm\,T}}\right)}{1-\exp\left(-\frac{B}{416\,\mathrm{nm\,T}}\right)}\right\} - \left(\frac{\lambda}{635\,\mathrm{nm}}\right)^5 \left\{\frac{\exp\left(-\frac{B}{635\,\mathrm{nm\,T}}\right)}{1-\exp\left(-\frac{B}{635\,\mathrm{nm\,T}}\right)}\right\} \quad (6)$$

The observed emission spectrum is approximated by performing a nonlinear least square fit of eq. 5 with T and I_0 as fitting parameters. The black-body temperature that best approximates the experimental emission curve is found to be

$$T = (9500 \pm 300)\ \mathrm{K} \quad (7)$$

A comparison between the observed emission curve and its best black-body fit with the emissions of a black-body source at two different temperatures is given in Fig. 3. The quality of approximation significantly decreases if the temperature deviates from its best fit value of 9500 K.

According to Wien's displacement law (22),

$$T\lambda_{max} = 2.9 \times 10^{-3}\,\mathrm{mK} \quad (8)$$

the obtained value for the temperature would lead to an emission maximum at λ_{max} = (315 ± 10) nm, Fig. 4.

An estimation of the total power emitted per area, P, can be obtained by using Stefan's Law (22),

$$M = a\,T^4 \quad (9)$$

with the Stefan-Boltzmann constant, $a = 5.67 \times 10^{-8} W\,m^{-2}\,K^{-4}$, and T = 9500 K, the total power per area emitted by the discharge arc is estimated to be

$$M = 4.62 \times 10^{8} W\,m^{-2} \qquad (10)$$

The surface area, S, of the plasma arc can be estimated from independent experiments (23) to be: $3\,mm^2 < S < 30\,mm^2$. Then the total power, P, summed over all wavelengths of the plasma arc is estimated to

$$1.4\ kW < P < 14\ kW \qquad (11)$$

Conclusions and Outlook

In the present work, the time-averaged emission spectrum of the electromagnetic radiation generated upon underwater electrical discharges was determined. The absence of sharp emission peaks has been established, thus verifying the general black-body behavior as expected for a dense plasma (9-11). Using the Planck distribution for a black-body radiation source we were able to estimate the temperature of the plasma arc, T = (9500 ± 300) K.

The current reactor setup restricted the determination of the emission spectrum to the 416 - 635 nm wavelength regime. In order to extend the measurements further into the UV region we are currently designing a reactor setup that allows for collecting light directly from the plasma arc, rather than using scattered light. In addition the data acquisition apparatus will be modified in order to enable the determination of time resolved emission spectra. Clean spectra at different instances over the entire lifetime of the plasma arc will yield its black-body temperatures as it evolves from its hot early

stages to the cooler temperatures later in the discharge. Such information is an important input into a mathematical description of the discharge process.

Acknowledgments: This study was financially supported by ARPA and ONR (Grant # NAV 5HFMN N0001492J1901). I would like to thank Frank Cosso in Dr. Bellan's research group in Applied Physics at Caltech for lending us the optical multi-channel analyzer. Without the practical experience and insight of Dr. Hartmut Herrmann (Universität Essen, Germany) this work would not have been possible.

References

(1) Hoffmann, M. R.; Martin, S. T.; Choi, W. Y.; Bahnemann, D. W. *Chemical Reviews* **1995**, *95*, 69.

(2) *Non-Thermal Plasma Techniques for Pollution Control Part A: Overview, Fundamentals and Supporting Technology*; Penetrante, B. M.; Schultheis, S. E.; Eds. Springer-Verlag: New York, 1993.

(3) *Non-Thermal Plasma Techniques for Pollution Control Part B: Electron Beam and Electrical Discharge Processing*; Penetrante, B. M.; Schultheis, S. E.; Eds. Springer-Verlag: New York, 1993.

(4) Kotronarou, A.; Mills, G.; Hoffmann, M. R. *J. Phys. Chem* **1991**, *95*, 3630.

(5) Hua, I.; Höchemer, R. H.; Hoffmann, M. R. *Environ. Sci. Tech.* **1995**, (In Press).

(6) Hua, I.; Höchemer, R. H.; Hoffmann, M. R. *J. Phys. Chem.* **1995**, *99*, 2335.

(7) Serpone, N.; Terzian, R.; Hidaka, H.; Pelizzetti, E. *J. Phys. Chem.* **1994**, *98*, 2634.

(8) Legrini, O.; Oliveros, E.; Braun, A. M. *Chem. Rev.* **1993**, *93*, 671.

(9) Martin, E. A. *J. Appl. Phys.* **1958**, *31*, 255.

(10) Robinson, J. W. *J. Appl. Phys.* **1967**, *38*, 210.

(11) Robinson, J. W.; Ham, M.; Balaster, A. N. *J. Appl. Phys.* **1973**, *44*, 72.

(12) Robinson, J. W. *J. Appl. Phys.* **1973**, *44*, 76.

(13) Naugolnykh, K. A.; Roy, N. A. *Electrical Discharges in Water. A Hydrodynamic Description.* technical report FTD-HC-2049-74, Foreign Technology Division, Wright-Patterson Air Force Base, Ohio. 1974.

(14) Radovanov, S. B. *A Spectroscopic and Thermodynamic Study of Pulsed Underwater Discharges.* In: *The Physics of Ionized Gases*; Tanovic', L.; Konjevic', N.; Tanovic', N. Eds. Nova Science Publishers: 1988.

(15) Buntzen, R. R. *The Use of Exploding Wires in the Study of Small-Scale Underwater Explosions*. In: *Exploding Wires, Vol 2;* Chace, W. G.; Moore, H. K. Eds. Plenum Press: New York, NY, 1962; pp. 195.

(16) Willberg, D. M.; Lang, P. S.; Höchemer, R. H., Kratel, A.; Hoffmann, M. R. *Environ. Sci. Technol.* **1995**, submitted.

(17) Smith, K. F. *Electro-Hydraulic Forming*. In: *High-Velocity Forming of Metals*; Wilson, F. W. Ed. Prentice Hall: Englewood Cliffs, N. J. 1964; pp. 77.

(18) Wesley, R. H.; Ayres, R. A. *U. S. Patent No. 4,479,680* **1984**.

(19) Coleman, A. J.; Saunders, J. E.; Crum, L. A.; Dyson, M. *Ultrasound in Med. & Biol.* **1987**, *13*, 69.

(20) Sharma, A. K.; Locke, B. R.; Arce, P.; Finney, W. C. *Hazardous Waste and Hazardous Materials* **1993**, *10*, 209.

(21) Ben'kovskii, V. G.; Golubnichii, P. I.; Maslennikov, S. I. *Sov. Phys. Acoust.* **1974**, *20*, 14.

(22) Atkins, P.W., Physical Chemistry, 3rd ed., **1986**.

(23) Lang, P., personal communication, **1994**.

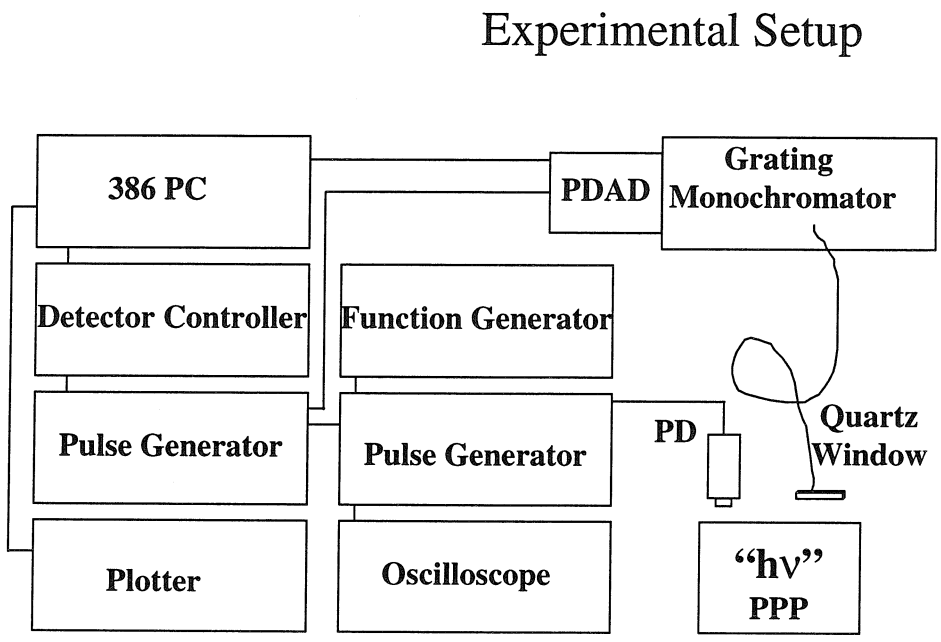

Fig. 1: Schematic diagram of the data aquisition and triggering apparatus.

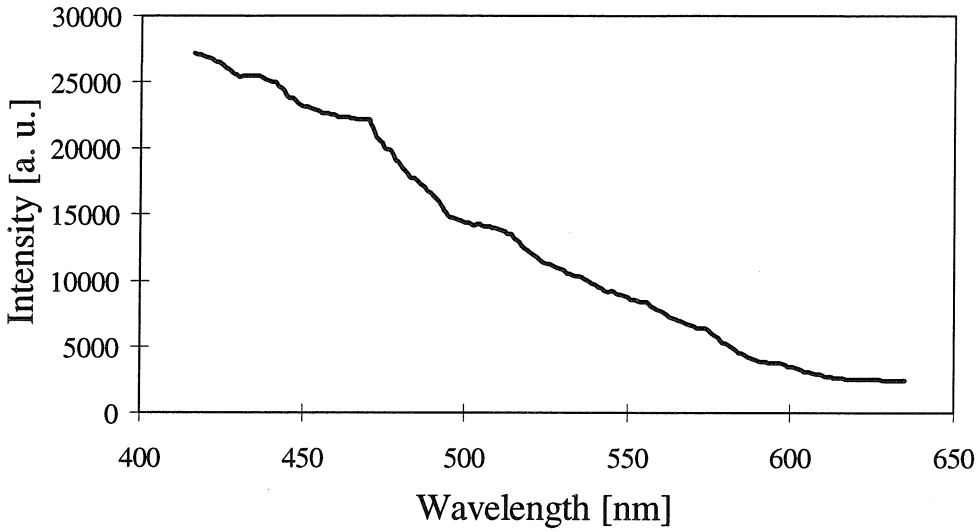

Fig. 2: Spectrum of the observed electromagnetic emission of the plasma arc.

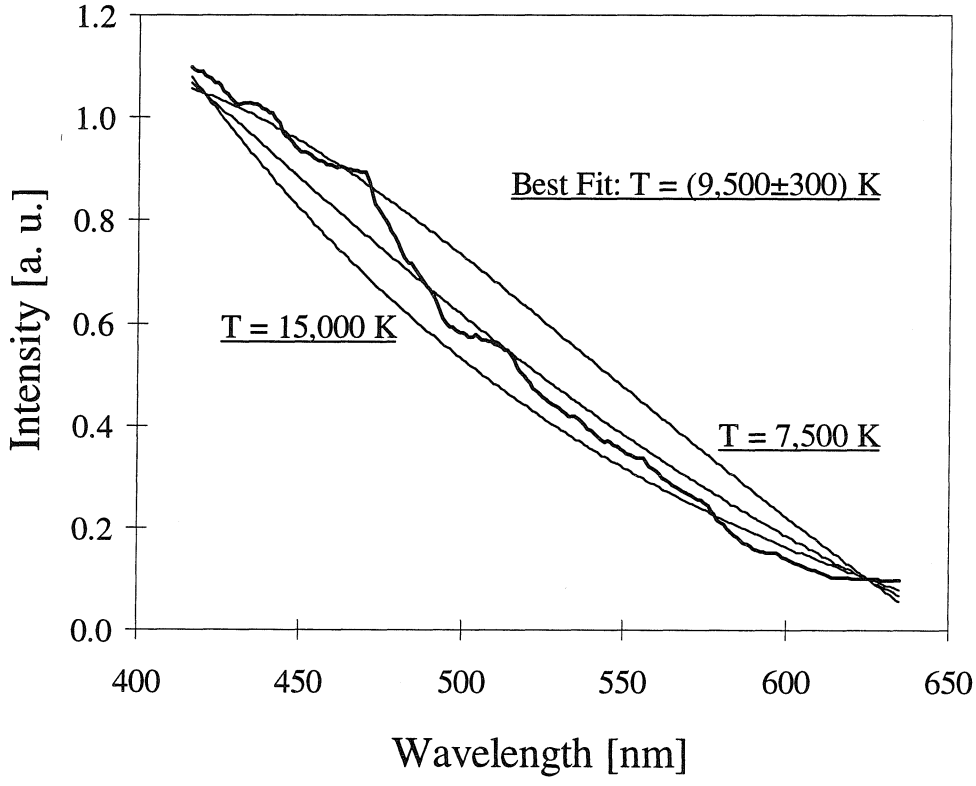

Fig. 3: Black-body at different temperatures compared to the observed emission spectrum.

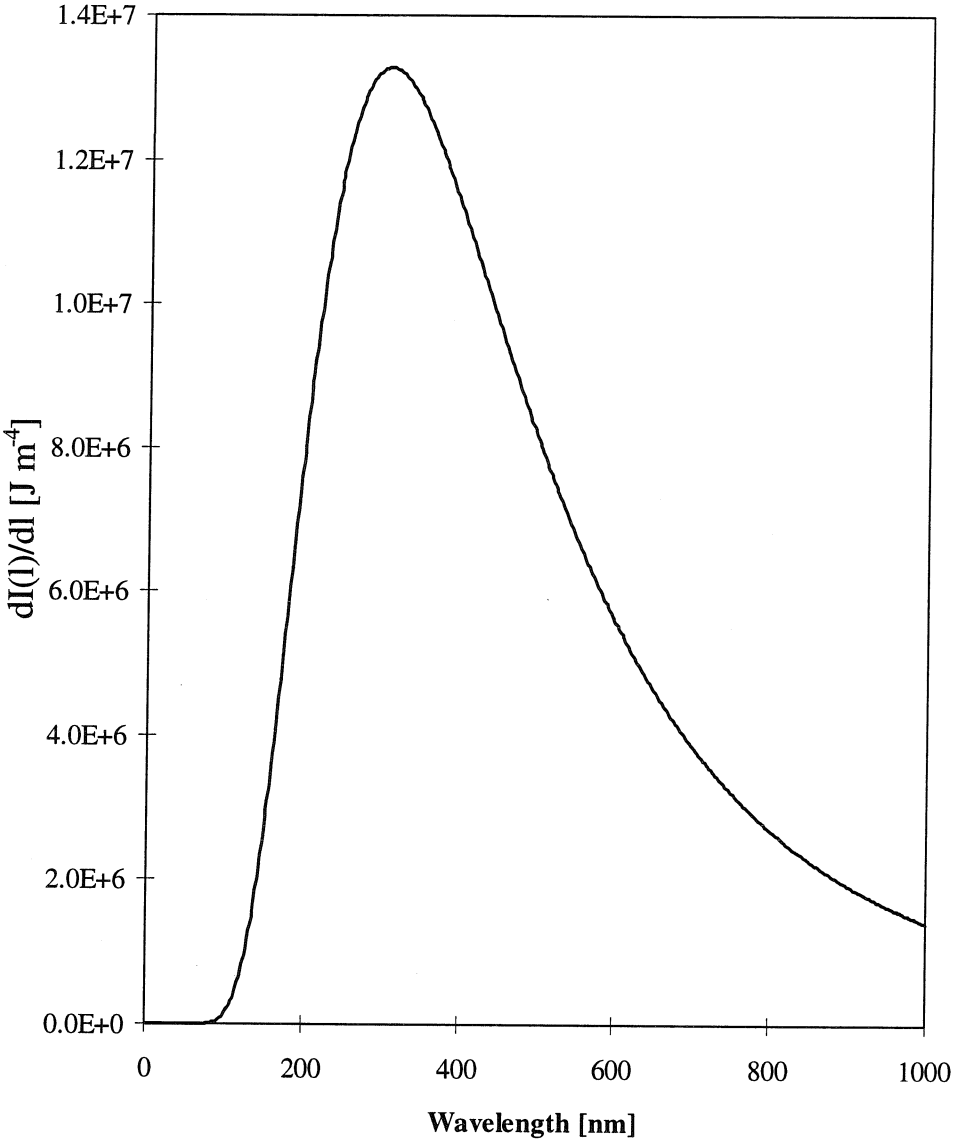

Fig. 4: Theoretical black-body emission at 9500 K.

- Chapter VIII -

Electrohydraulic Discharge Initiation as a Function of the Circuit Parameters: The Influence of the Solution's Electrical Conductivity and Temperature

Introduction

The electrohydraulic discharge (EHD) process is currently being investigated as a possible technology for water remediation. It has been shown that the intense radiation generated during an EHD is capable to degrade chemical compounds such as 2,4,6-trinitrotoluene, 4-chlorophenol, and 3,4-dichloroaniline (1). One main challenge on the way to technical application is the minimization of the amount of energy that is required by the process. This study presents a first step in minimizing inefficiencies due to energy leakage prior to electrical breakdown.

During an electrical discharge energy stored in a capacitor bank is rapidly released into the dielectric medium of an electrode gap. In order for the discharge to occur, the electrical insulation of the medium has to break down. The electrical potential required for breakdown depends on the nature of the insulating medium filling the electrode gap. In the case of pure water the necessary field strength for instantaneous electrical breakdown is on the order of 100 kV/cm (2). Since, in our reactor, the electrodes are submersed into water and the maximum applied potential is 19.2 kV with electrode gaps in the range 4 to 16 mm, the electrical breakdown is not instantaneous. Instead, at these relatively low electrical field strengths, the electrical discharge may be preceded by the formation of a gas pocket in the electrode gap (2, 3). The initiation of that type of electrical discharge is a stochastic process. As such it exhibits rather large shot-to-shot variability in discharge energy, current, and potential even if all the circuit parameters are held constant. The addition of an electrolyte facilitates electrical breakdown and keeps the shot-to-shot variability relatively small compared to low-voltage discharges in pure water.

Any evolving new technology that seeks practical application has to be optimized with respect to energy efficiency. In the particular case of underwater electrical discharges one main inefficiency is the leakage of energy from the hot electrode to ground

during the initiation period prior to electrical breakdown of the solution. Energy leakage from the hot electrode occurs along two distinct paths: directly to the ground electrode and to the reactor wall, which is at the same potential as ground. This second pathway does not exist when a high-density polyethylene- (HDPE-) liner is installed in the chamber: The liner insulates the chamber wall from the hot electrode. Other inefficiencies are related to the energy partitioning during the actual discharge.

This study focuses on the pre-breakdown period. In particular, we investigated the influence of a variety of parameters on the length of the initiation period and the slope of the voltage transient prior to electrical breakdown. The parameters under investigation include the electrical conductivity of the solution, the electrode gap width, the initially applied potential, and the solution temperature. In addition we examined the pre-breakdown period with and without a HDPE-liner.

The goal of this study is to gather systematic experimental data such that we are in a position to predict, within our chosen parameter space, the voltage transient prior to the actual discharge. The insight gained from this investigation will help minimize inefficiencies due to energy leakage during the pre-breakdown period.

Experiments

The Electrohydraulic Discharge Reactor

A schematic of the important features of the Caltech EHD system is shown in Fig. 1 of chapter II. The electrohydraulic discharge (EHD) reactor consists of two major components: a pulsed-power electrical discharge circuit and a reaction chamber. The reactor chamber contains the two electrodes which are immersed in the aqueous solution that is to be treated. The pulsed-power circuit package has been designed and built by Pulsed-Power Technologies, Inc. (PPTI, San Diego). It has been specifically designed with a low inductance, L = 250 - 300 nH, and a high capacitance, C = 135 μF, to generate

short high-energy pulses. It is capable of storing energies in the range of 1 to 25 kJ. Upon closing the electrical circuit, the hot electrode is brought to an electrical potential of 3.85 to 19.2 kV. In order to ensure rapid energy release, fast ignitron switches (300 ns risetime) are used. The charging of the hot electrode is a virtually instantaneous process on the timescale of an actual discharge (10 -100 μs).

The reactor vessel has been designed to withstand the extreme electrical and mechanical stresses that are generated during an electrical underwater discharge. In particular, the reactor vessel has to withstand intense shockwaves generated during the expansion of the plasma channel formed during an EHD event. In addition, the reactor has to accommodate the high electrical current peaks of up to 1 GW and the high potentials that are required for the process. Furthermore, the reactor chamber has been designed to provide reproducible conditions over many discharges (> 10.000) in order to enable systematic studies. The high-voltage cathode bulkhead assembly is a critical component. The electrical insulation of the cathode holds off a potential in excess of 25 kV in order to avoid electrical shorting. The insulation is also resistant to the erosive effects of intense shockwaves.

An opposing electrode design was selected for shock resistance. The ground electrode assembly penetrates the reaction chamber from the top. A tight compression connection between the electrode and the reactor chamber allows for the high-current pulses to occur without external discharges. In order to allow for discharge experiments at various different gap widths as well as to offset tip erosion, the ground electrode has been designed for adjustability. It allows for precise control of the spark-gap length to within ± 0.1 mm, while maintaining the structural integrity of the reactor.

In order to minimize erosion of the electrodes, the refractory metal tantalum (mp = 2996 °C) was chosen as electrode-tip material. In addition, tantalum as well as its oxides are inert with respect to chemical reactions with organic compounds, which minimizes a potential interference with the chemistry under investigation. The tantalum

tips are joined to the stainless steel electrodes by incorporating them into locking Morse (PPTI and Jerames Tools, San Diego) taper assemblies. The tips are cylindrical and flat on order to minimize the effects of tip erosion during an experiment.

Potential and Current Measurements

The electric current during a discharge was measured using a self-built Rogowski coil (4) on the hot electrode bus, i.e., the connection of the capacitor bank to the cathode. The high-intensity current induces a potential in the Rogowski coil. Voltage transients were measured on the cathode bus bar using a high voltage probe (North Star Research Corp.) with a calibration constant of 2000 V per unit. Both signals were monitored on an oscilloscope (LeCroy, model 9304). Discharge triggering and data collection were controlled remotely using a 486-PC with customized process control software (LabView, National Instruments).

Throughout all experiments the circuit's inductance, L = 275±25 nH, and capacitance, C = 135 μF, were kept constant. The investigated parameter space included the solution's electrical conductivity, κ, the electrode gap width, l, the energy initially stored in the capacitor bank, E_0, and the solution temperature, T. In a typical experiment the reactor chamber is filled with a solution of known conductivity and at least five discharges are performed, keeping l and E_0 constant. The temperature change over five discharges is negligible. We repeated the experiment under three different initial E_0, while keeping all the other parameters the same in order to study the pre-breakdown phenomena as a function of E_0. We then exchanged the solution against one with a higher conductivity and again performed five discharges at the same three different initial energies. In this fashion, we covered a range of five to eight different solution conductivities. We performed the above series of experiments successively at spark gap lengths of 4, 8, 12, and 16 mm.

In order to protect the reactor wall from aggressive solutions and to vary the total volume of treated solution, a high-density polyethylene liner was installed during some experiments outside the scope of this study. Therefore all experiments were performed with and without a protective liner, since a plastic liner will have a pronounced effect on the energy loss during the initiation period.

The influence of the temperature on the pre-breakdown characteristics was investigated by filling the chamber successively with solutions with increasing temperature. Each solution was exposed to twenty discharges and then replaced. The temperature was measured after every five shots. In this manner we covered a temperature range of 5.4 - 67.9 °C. Throughout all temperature experiments the HDPE-liner was installed, the gap width was 12 mm and the initially stored energy 10 kJ. The conductivity of the solution at room temperature was 2.08 mS/cm.

Aqueous solutions were prepared from deionized water from a Milli-UV-Plus system (ρ = 18.2 MΩ cm) with $NaClO_4$ (EM Science, reagent grade) as an electrolyte. The conductivity of the solutions was monitored with a conductivity meter (Orion, model 160). The temperature of the solutions in the reactor chamber was measured using a digital thermometer equipped with a thermocouple (Omega Eng., model HH82).

Results and Discussion

Current and Voltage Transients

The electrical discharges occurring in our system exhibit two main regimes: a pre-breakdown, or initiation period (t_{ip} = 26 - 1900 μs) and the actual discharge event during which the bulk of the energy stored in a capacitor bank is released into an evolving plasma-arc (40 - 100 μs). The initiation period is characterized by a relatively slow leakage of energy in form of a low current from the hot electrode to ground as shown in the voltage transients in Figs. 2a, b. During the initiation period the potential slowly

decreases from U_0 to U_{ip} at which point a plasma arc has formed and the potential drops rapidly. The opposing ground electrode as well as the reactor wall itself serve as connections to ground, thus providing a channel for energy leakage. The energy that leaks to ground during this initiation period is a major source of inefficiency.

The slope, dU/dt, and the length of the voltage transient, t_{ip}, during its pre-breakdown stage are functions of all investigated parameters (i.e., electrical conductivity of the solution, κ, the electrode gap width, l, the initial energy stored in the capacitor bank, E_0, the solution temperature, T, and the presence of an insulating HDPE-liner). In the particular case shown in Fig. 2a (b), with κ = 4.03 mS/cm (κ = 1.08 mS/cm), l = 8 mm, E_0 = 7 kJ, and without plastic liner, the initiation period extended from t = 0 μs to t_{ip} = 288 μs (t_{ip} = 842 μs).

The reactor system during the initiation period represents an overdamped LRC circuit, with a constant resistance. Once the dielectric insulation of the water between the electrodes has disintegrated, at t = 288 μs, a short high-intensity current pulse is released into the plasma arc, Fig. 3. The breakdown of the water and the formation of a plasma arc between the electrodes dramatically decreases the resistance of the LRC circuit, causing it to become underdamped. The shape of the current transient is governed by the potential across the electrode gap just before breakdown, U_{ip}, the inductance, L, the resistance, R, and the capacitance, C, of the circuit. Since L and C are kept constant throughout all experiments, only the gap width (i.e., R) and U_{ip} have a direct influence on the voltage and current transients, once the plasma arc has formed. However, since U_{ip} is determined by U_0 as well as by dU(t)/dt and t_{ip}, all parameters varied in the experiments indirectly influence the current transients during the actual discharge period.

Since the resistance of the plasma is not constant over its lifetime, the dynamic behavior of current and voltage transients during the actual discharge period cannot be accurately described by a constant resistance LRC-circuit model. However, the behavior of the voltage transient prior to breakdown can be described as a strongly overdamped

LRC circuit with constant values for its inductance, resistance, and capacitance. This is the basis for the analysis of the initiation period behavior of the voltage transients presented in the next section.

LRC Circuit Description of the EHD

The EHD reactor can be mathematically described as an LRC circuit, i.e., the reactor system is an electrical circuit consisting of a resistance (i.e., the resistance of the submersed electrode gap), R, an inherent inductance, L, and a capacitance, C, (Fig. 1). Using Kirchhoff's voltage law (5, 6) the governing equation for the shorted circuit can be written as

$$L\frac{di(t)}{dt} + Ri(t) + \frac{1}{C}\int_0^t i(t')dt' = U_0 \tag{1}$$

where i(t) denotes the electrical current and U_0 the initial potential across the capacitor. Differentiating eq. 1 results in the homogeneous second-order differential equation

$$\frac{d^2i(t)}{dt^2} + \frac{R}{L}\frac{di(t)}{dt} + \frac{1}{LC}i(t) = 0 \tag{2}$$

Since the potential across the capacitor, U(t), is related to the circuit current by

$$i(t) = C\frac{dU(t)}{dt} \tag{3}$$

we can, alternatively to eq. 2, derive a differential equation in U(t).

$$\frac{d^2U(t)}{dt^2}+\frac{R}{L}\frac{dU(t)}{dt}+\frac{1}{LC}U(t)=0 \tag{4}$$

Eqns. 2 and 4 have the same form. Substitution of i(t) in eq. 2 and U(t) in eq. 4 with y(t) yields:

$$\frac{d^2y(t)}{dt^2}+\frac{R}{L}\frac{dy(t)}{dt}+\frac{1}{LC}y(t)=0 \tag{5}$$

The general solution of eq. 5 is given as

$$y(t)=A_1\exp\left\{\left(-\alpha+\sqrt{\alpha^2-\omega_n^2}\right)t\right\}+A_2\exp\left\{\left(-\alpha-\sqrt{\alpha^2-\omega_n^2}\right)t\right\} \tag{6}$$

where A_1 and A_2 are arbitrary constants that depend on the initial conditions, and α and ω_n are defined in terms of the parameters of the circuit:

$$\alpha=\frac{R}{2L},\quad \omega_n=\frac{1}{\sqrt{LC}} \tag{6a, b}$$

Depending on the relative magnitude of L, R, and C, three cases can be distinguished: the underdamped discharge, where $R < 2\,(L/C)^{1/2}$, the overdamped discharge, where $R > 2\,(L/C)^{1/2}$, and the critically damped discharge representing the limiting case where $R = 2\,(L/C)^{1/2}$. An overdamped discharge leads to two real solutions in eq. 6.

If we put in the values for L and C in our circuit, we can calculate a value for R_c such that the electrical discharge will be critically damped.

$$R_c = (L/C)^{1/2} = (90 \pm 4)\ m\Omega \qquad (7)$$

The pre-breakdown regime is governed by a resistance of the electrode gap that is several orders of magnitude higher than R_c leading to a highly overdamped discharge. This causes the leakage of energy from the cathode to ground during the initiation period to be relatively slow. Once the electrical breakdown has occurred, the resistance dramatically decreases and the actual discharge into the evolving plasma arc takes place. The resistance of the plasma channel, R_p, varies over its lifetime. However, a reasonable average estimate of $R_p = 30\ m\Omega$ has been obtained from the current-transient ringdown (7). Therefore the event during which the bulk of the initially stored energy is released into the solution resembles an underdamped discharge.

Analysis of the Voltage Transients During the Initiation Periods

The transients (Figs. 2a, b) during the pre-breakdown period exhibit a linear decrease of the spark gap potential, U(t), with time (as opposed to a biexponential decay, eq. 6). Also, the voltage transient decreases more steeply with $\kappa = 4.03$ mS/cm (Fig. 2a) than with $\kappa = 1.08$ mS/cm (Fig. 2b). This can be explained within the mathematical framework of an LRC circuit as shown below.

In the following few paragraphs eq. 6 is written explicitly for the given parameters and simplified whenever possible. If we focus on the voltage transients during the initiation period prior to electrical breakdown, we can determine the constants A_1 and A_2 from the initial conditions.

$$i(t = 0) = 0\,A, \quad U(t = 0) = U_0, \quad 3.85\,kV < U_0 < 19.2\,kV \qquad (8)$$

From the initial condition of the current and eq. 6 follows

$$A_2 = -A_1 \tag{9}$$

Also, for the closed circuit,

$$L\frac{di(t)}{dt} = -Ri(t) - U(t) \tag{10}$$

We determine A_1 from the initial condition and eq. 10 for t = 0

$$\frac{di(t=0)}{dt} = -\frac{1}{L}U_0 \tag{11}$$

By differentiating eq. 6 and substituting eq. 11 for di(0)/dt, the second constant can be determined

$$A_1 = \frac{U_0}{2L\sqrt{\alpha^2 - \omega_n^2}} \tag{11}$$

The exact solution of eq. 2 subject to the initial conditions given in eq. 8 is therefore

$$i(t) = \frac{U_0}{2L\sqrt{\alpha^2 - \omega_n^2}}\left[\exp\left\{\left(-\alpha + \sqrt{\alpha^2 - \omega_n^2}\right)t\right\} - \exp\left\{\left(-\alpha - \sqrt{\alpha^2 - \omega_n^2}\right)t\right\}\right] \tag{12}$$

The solution can be simplified by recognizing that during the initiation period the resistance of the electrode gap is relatively high, thus

$$\alpha^2 >> \omega^2 \Rightarrow \exp\left\{\left(-\alpha + \sqrt{\alpha^2 - \omega_n^2}\right)t\right\} >> \exp\left\{\left(-\alpha - \sqrt{\alpha^2 - \omega_n^2}\right)t\right\} \tag{13}$$

Eq. 12 may now be simplified to

$$i(t) = \frac{U_0}{2L\sqrt{\alpha^2 - \omega^2}} \exp\left\{\left(-\alpha + \sqrt{\alpha^2 - \omega_n^2}\right)t\right\} \tag{14}$$

For the given values of α and ω_n and initiation periods in the range 26 - 1900 μs (typically several hundred μs) the exponent is small. Therefore the exponential term in eq. 14 can be expanded into a MacLaurin series and truncated for terms smaller than $O(t^2)$.

$$i(t) = \frac{U_0}{2L}\left[\left(\alpha^2 - \omega_n^2\right)^{-\frac{1}{2}}(1 - \alpha t) + t + O(t^2)\right] \tag{15}$$

By expanding the root term according to

$$\left(\alpha^2 - \omega_n^2\right)^{-\frac{1}{2}} = \frac{1}{\alpha}\left(1 - \frac{\omega_n^2}{\alpha^2}\right)^{-\frac{1}{2}} = \frac{1}{\alpha} + \frac{1}{2}\frac{\omega_n^2}{\alpha^3} + O\left(\frac{\omega_n^4}{\alpha^5}\right), \quad \text{for } \alpha^2 >> \omega_n^2 \tag{16}$$

eq. 15 may be simplified further to

$$i(t) = \frac{U_0}{2L}\left[\frac{2\alpha^2 + \omega_n^2}{2\alpha^3} - \frac{1}{2}\frac{\omega_n^2}{\alpha^2}t\right] \tag{17}$$

The potential across the capacitor, U(t) is given by eq. 10. The potential across the electrode gap, $U_{gap}(t) = i(t)R$, during the initiation period is practically identical to U(t),

since the inductance of the circuit is very small (L = 275±25 nH). $U_{gap}(t)$ can now be written as

$$U(t) \cong U_{gap}(t) = U_0\left(1-\frac{t}{CR}\right) \tag{18}$$

Eq. 18 shows that the voltage transients are a linear functions of time. This mathematical result is in agreement with the observed linear potential decrease during the initiation period (Figs. 2a, b).

The combined resistance of the electrode gap and the bulk solution between the hot electrode and the chamber wall can be estimated from the slope, dU(t)/dt of the voltage transient

$$R = -\frac{U_0}{C}\left(\frac{dU(t)}{dt}\right)^{-1} \tag{19}$$

The resistance estimated from eq. 19 for the conditions of Figs. 2a, b are R = 14 Ω and R = 84 Ω respectively.

In order to relate the observed transients to the solution's conductivity, κ, which is more easily quantified than the electrode gap resistance, R, we use the following relationship between κ and R:

$$R = \frac{1}{\kappa}\frac{d}{A}, \quad \kappa = \frac{1}{\rho} \tag{20}$$

where d is the distance and A the cross-section through which the current travels, and ρ is the resistivity. Since it is difficult to determine d/A, it is customary (8) to introduce a proportionality constant, K, with dimension 1/m:

$$R = \frac{K}{\kappa} \tag{21}$$

With this definition we can rewrite eq. 19

$$U(t) = U_0\left(1 - \frac{\kappa}{KC}t\right) \tag{22}$$

$$\frac{dU(t)}{dt} = -\frac{U_0}{C}\frac{\kappa}{K} \tag{23}$$

Eq. 23 predicts a linear relationship between the electrical conductivity of the solution and the slope of the voltage transient. The experimental observations are in agreement with this prediction (Fig. 4): dU(t)/dt is a linear function of κ. This result holds for all examined gap widths as predicted. In all cases discharge was achieved with the single exception where l = 16 mm for which no electrical breakdown occurred.

The presence of the polyethylene liner does not change the linearity of the slope/conductivity relationship. However, for the unlined reactor the slope is a stronger function of κ than for the lined chamber as shown in Fig. 5. This is due to a greater K in the case of the unlined chamber where K represents the geometry of the current path. If the chamber is lined, the only path for the current is from the hot to the ground electrode, since the chamber wall is electrically insulated. In the unlined chamber current may also leak from the hot electrode directly to the reactor wall, which is at ground potential. The additional current path gives rise to a greater K and thus a stronger slope/conductivity relationship.

In addition to the linear dependence of dU(t)/dt on K and κ, eq. 23 also predicts dU(t)/dt to be a linear function of the initial potential, U_0. Again, the experimental observations (Fig. 6) are in good agreement with eq. 23.

As pointed out above, the discharge is not an instantaneous process. The initiation time, $t = t_{ip}$, is the period of time from closing the circuit, t = 0, until the actual breakdown takes place. Fig . 7 shows t_{ip} for a particular set of parameters. In general, t_{ip} decreases with increasing conductivity. The observed initiation period characteristics are summarized in Tables 1-3.

The energy lost due to current leakage during the initiation period is plotted against the conductivity for a gap width of 4 mm and three different initial energies in Figs. 8a (with liner) and 8b (without HDPE-liner). When an insulating liner is present, the energy loss, ΔE, for all three initial energies increases up to a value of k = 2 mS/cm. For $\kappa > 2$ mS/cm the increase is less steep for E_0 = 7 kJ and E_0 = 10 kJ. The curve for E_0 = 2 kJ levels off at κ = 3 mS/ cm and the energy loss, ΔE = 400 J, ceases to be a function of κ. In the case of an unlined chamber ΔE is higher by a factor of 1.5 for all three E_0 values (Fig. 8b). The general trend remains the same for E_0 = 7 kJ and E_0 = 10 kJ. However, the energy loss appears to be independent of κ over the entire range under investigation.

Tables 4-6 summarize the relative energy losses, $\Delta E/E_{0,calc}$, for the different experimental conditions in addition to the corresponding values of U_0 and U_{ip}. (Absolute energy losses, ΔE, are listed in Tables 1-3.) ΔE and $\Delta E/E_{0,calc}$ have been calculated using

$$\Delta E = \frac{1}{2} C\left(U_0^2 - U_{ip}^2\right), \qquad \frac{\Delta E}{E_{0,calc}} = 1 - \left(\frac{U_{ip}}{U_0}\right)^2 \tag{24}$$

where C = 135 μF and

$$U_{ip} = U_0 + \frac{dU(t)}{dt} t_{ip} \tag{25}$$

Throughout the entire range of experiments the discharges performed in the unlined chamber exhibited much higher absolute (Tables 1-3) as well as relative (Tables 4-6) energy losses when compared to discharges in the lined chamber. This reflects the electrical insulation of the reactor wall from the hot electrode when the liner is present. We observe further that the relative energy loss decreases for all gap lengths with increasing nominal energy, E_0. The absolute loss in energy, on the other hand, increases consistently with increasing E_0. Finally both the absolute and the relative energy losses increase with increasing gap length.

(There is a consistent, small discrepancy (i.e., $E_{0,\ calc} < E_0$) of the nominal initially stored energy E_0, and its value when calculated from the measured $U_{0,}$, according to:

$$E_{0,calc} = \frac{1}{2} C U_0^2 \tag{26}$$

We have not been able to satisfyingly explain this apparent loss of energy upon closing the circuit. However, all the presented results remain unaffected by this discrepancy, since the apparent energy loss occurs prior to recording the voltage and current data. Throughout this chapter E_0 denotes the nominal energy initially stored in the capacitor bank. The stored energy calculated from actual U_0 measurements is referred to as $E_{0,\ calc}$. The calculated initial energy is only important in the estimation of the relative energy losses (eq. 24) where it takes the place of E_0 in order to ensure consistency.)

In the preceding paragraphs we have discussed the influence of κ, K, and U_0 on the extend of the initiation period, the slope of the voltage transient and the absolute and

relative energy losses during the pre-breakdown phase. In the remainder of this section we present the observed relationships between the temperature and t_{ip}, dU(t)/dt, and ΔE.

The κ/T calibration of the conductivity meter (Fig. 9) is used to relate the measured temperature to the solution's electrical conductivity at the time of the discharge. The initiation period as a function of T is shown in Fig. 10a. The general trend is a decrease in t_{ip} with increasing T. Since the electrical conductivity of an electrolyte solution is a function of its temperature, the trend in Fig. 10a may be caused indirectly by the solutions increasing conductivity and not by its increasing temperature directly. In order to discriminate between these two possibilities, the data from Fig. 10a is re-plotted in Fig. 10b together with data obtained from discharges into solutions at constant temperature under identical experimental conditions. Fig. 10b shows that the decrease of t_{ip} with increasing T is due to a simultaneous increase in κ. The temperature of the solution does not affect the extent of the initiation period directly, but indirectly through its effect on the conductivity.

The slope of the voltage transient appears to be a linear function of the solution temperature (Fig. 11a). This can be in part explained by an increase in κ with increasing T. However, dU/dt does not increase as steeply as a sole dependence on κ would predict (i. e., a solution at room temperature with k = 4.02 mS/cm exhibits a slightly higher U(t)/dt-value of 4.86 V/μs than a solution with T = 68 °C and κ = 4.05 mS/cm (dU(t)/dt = 3.96V/μs) as shown in Fig. 11b). However, this effect is not very pronounced.

The most striking result of our temperature-dependence investigation is shown in Figs. 12a, b. It is apparent that the energy lost due to pre-breakdown leakage *decreases* with increasing solution temperature. This result suggests a strong temperature dependence of ΔE, independent from, and, in fact, overcompensating for the increase in κ with rising solution temperature. The upward trend of ΔE with increasing κ is reverted into a downward trend, when the increase in κ in accompanied by an increase in T (Fig. 12b). This observation supports the gas-pocket theory (2) of discharge initiation.

According to this theory a gas pocket has to develop within the electrode gap in order for electrical breakdown to occur. One way of generating the gas pocket is by the evaporation of water. The energy lost due to leakage from the hot electrode to the ground electrode is used in part for heating of the electrode gap, which eventually leads to the formation of the necessary gas bubble. Less energy is required for the evaporation of a quantity of hot water than for evaporation of the same quantity of cooler water, thus causing the decrease in energy loss with increasing solution temperature.

Conclusions

This work has confirmed that discharge initiation at relatively low electrical field strengths is not instantaneous, as expected (2). The observed initiation times range from 26 - 1900 μs. During this period 1.5 - 75 % of the energy stored in the capacitor (based on $E_{0,\,calc}$) is lost to current leakage. The actual discharge, during which the remainder of the energy is introduced into the evolving plasma, lasts between 40 - 100 μs. The EHD reactor resembles an LRC circuit that is strongly overdamped during the initiation period. The circuit becomes underdamped once the plasma arc has been initiated.

The initiation time decreases with increasing conductivity and decreasing gap width. The slope of the voltage transient prior to electrical breakdown has been shown to be proportional to the conductivity of the solution and the initial potential. The combined effect of initiation time and voltage slope cause the energy loss during initiation to increase with increasing conductivity. The energy loss in every case is distinctly smaller when a HDPE-liner is installed.

Discharge initiation in a low-voltage electrode gap requires the formation of a gas pocket through which charged particles may accelerate sufficiently has to be formed before the plasma channel can develop. One possible mechanism for the formation of the gas bubble is vaporization of water by local heating due to ion mobilization. A fraction

of the energy lost during the initiation period may then be accounted for as heating energy. This work has shown that less energy is lost when the discharge is carried out in a hot solution as opposed to in a cooler one with identical conductivity. This result supports the vaporization theory of gas-pocket formation. However, another possibility by which a gas bubble may form is the electrochemical formation of H_2 and O_2.

Once the actual discharge is initiated the resistance of the plasma channel (i. e., the gap width) together with the constant inductance and capacitance of the circuit dictates the energy partitioning into three events: UV radiation, steam bubble formation, and shockwave generation. (The solution's temperature and conductivity only determine the pre-breakdown energy loss.) A main goal of the EHD project is the optimization of the energy input into the generation of UV radiation and thus to maximize the indirect photochemical chemical effects. In order to enhance performance, an optimal combination of gap width, inductance, and capacitance that maximizes the rate and extent of compound degradation, needs to be determined.

A low solution conductivity, although advantageous, is not achievable with most real-world wastewaters. The solution's conductivity will be dictated by the nature of the wastewater that is to be treated. In practical applications of the EHD process, in order to minimize the prebreakdown energy loss, the discharges should be performed in wastewater with an elevated temperature in a lined chamber.

References

(1) Willberg, D. M.; Lang, P. S.; Höchemer, R. H.; Kratel, A.; Hoffmann, M. R. *Environ. Sci. Technol.*, **1995**, submitted.

(2) Naugolnykh, K., A.; Rox, N. A. *Electrical Discharges in Water: A Hydrodynamic Description*, FTD-HC-2049-74, Foreign Technology Division, Wright-Patterson Air Force Base, Ohio, 1974.

(3) Olson, A. H.; Sutton, S. P. *J. Acoust. Soc. Am.* **1993**, *94*, 4, 2226-2231.

(4) Podlesak, M. *Rev. Sci. Instrum.* **1990**, *61*, 892-896.

(5) Bobrow, L. S. *Elementary Linear Circuit Analysis*, Holt, Rinehar and Wilson: New York, 1st. ed., 1981, pp. 718.

(6) Smith, R. J. *Circuits, Devices, and Systems: A First Course in Electrical Engineering*, Wiley & Sons: New York, 2nd. ed., 1967, pp. 776.

(7) Kratel, A. personal communication, 1996.

(8) Atkins, P. W. Physical Chemistry, Oxford University Press, 3rd. ed., 1986, pp. 857.

Table 1

Pre-breakdown characteristics (i.e., initiation period, t_{ip}, voltage slope, dU(t)/dt, and energy loss, ΔE) for the 4 mm spark gap at different conductivities, κ, with initially stored energy, E_0, as parameter.

The values refer to discharges with and (without) HDPE-liner.

κ, [mS/cm]	t_{ip}, [μs]			-dU(t)/dt, [V/μs]			ΔE, [J]		
	2 kJ	7 kJ	10 kJ	2 kJ	7 kJ	10 kJ	2 kJ	7 kJ	10 kJ
1.09	497	88.3	94.4	0.52	1.03	0.76	147	0.00	3.16
(1.09)	(1352)	(175)	(149)	(1.02)	(0.69)	(0.77)	(677)	(161)	(143)
1.56	539	132	116	0.89	0.63	1.23	258	93.8	187
(1.59)	(948)	(190)	(115)	(1.57)	(2.34)	(2.34)	(692)	(448)	(326)
2.12	532	136	98.6	1.40	2.30	2.32	386	321	282
(2.10)	(711)	(144)	(86.0)	(2.11)	(3.37)	(3.55)	(691)	(484)	(370)
3.09	418	98.4	71.1	2.17	3.51	3.78	457	355	329
(3.07)	(469)	(99.3)	(65.9)	(3.21)	(5.64)	(6.34)	(691)	(556)	(431)
4.05	278	78.5	36.9	2.86	4.94	6.45	404	395	288
(4.03)	(350)	(69.0)	(50.1)	(4.24)	(7.54)	(9.44)	(699)	(519)	(563)
5.94	187	55.8	40.1	4.34	8.48	9.78	412	480	476
(5.94)	(232)	(56.9)	(36.0)	(6.29)	(12.3)	(15.2)	(665)	(686)	(649)
9.63	118	39.1	26.9	7.15	15.0	17.3	424	590	569
(9.54)	(135)	(39.4)	(29.3)	(10.6)	(21.7)	(27.5)	(662)	(833)	(951)

Table 2

Pre-breakdown characteristics (i.e., initiation period, t_{ip}, voltage slope, dU(t)/dt, and energy loss, ΔE) for the 8 mm spark gap at different conductivities, κ, with initially stored energy, E_0, as parameter.

The values refer to discharges with and (without) HDPE-liner.

κ, [mS/cm]	t_{ip}, [μs]			-dU(t)/dt, [V/μs]			ΔE, [J]		
	2 kJ	7 kJ	10 kJ	2 kJ	7 kJ	10 kJ	2 kJ	7 kJ	10 kJ
0.56	-	677	586	-	0.09	0.18	-	0.00	0.00
(-)	(-)	(-)	(-)	(-)	(-)	(-)	(-)	(-)	(-)
1.08	-	769	444	-	0.70	0.56	-	563	332
(1.07)	(-)	(1033)	(-)	(-)	(1.72)	(-)	(-)	(1658)	(-)
1.58	-	664	403	-	1.30	1.43	-	882	703
(1.57)	(-)	(762)	(-)	(-)	(2.72)	(-)	(-)	(1880)	(-)
2.09	-	528	305	-	1.89	1.96	-	994	727
(2.10)	(-)	(615)	(-)	(-)	(3.55)	(-)	(-)	(1943)	(-)
3.07	-	372	209	-	3.03	3.40	-	1123	871
(3.08)	(-)	(478)	(-)	(-)	(5.40)	(-)	(-)	(2213)	(-)
4.03	-	292	173	-	4.13	4.95	-	1192	1037
(4.03)	(-)	(380)	(-)	(-)	(7.16)	(-)	(-)	(2287)	(-)
5.97	-	197	126	-	6.30	7.80	-	1219	1172
(5.40)	(-)	(282)	(-)	(-)	(9.66)	(-)	(-)	(2294)	(-)
-	-	-	-	-	-	-	-	-	-
(7.70)	(-)	(166)	(-)	(-)	(14.3)	(-)	(-)	(2016)	(-)
9.59	-	127	82.0	-	10.7	13.8	-	1302	1335
(9.60)	(-)	(139)	(-)	(-)	(18.2)	(-)	(-)	(2016)	(-)
-	-	-	-	-	-	-	-	-	-
(18.3)	(-)	(88.8)	(-)	(-)	(33.5)	(-)	(-)	(2414)	(-)

Table 3

Pre-breakdown characteristics (i.e., initiation period, t_{ip}, voltage slope, dU(t)/dt, and energy loss, ΔE) for the 12 mm spark gap at different conductivities, κ, with initially stored energy, E_0, as parameter.

The values refer to discharges with and (without) HDPE-liner.

κ, [mS/cm]	t_{ip}, [μs]			-dU(t)/dt, [V/μs]			ΔE, [J]		
	7 kJ	10 kJ	16 kJ	7 kJ	10 kJ	16 kJ	7 kJ	10 kJ	16 kJ
1.09	1910	1216	716	0.83	0.98	1.15	1565	1442	1280
(-)	(-)	(-)	(-)	(-)	(-)	(-)	(-)	(-)	(-)
1.57	1494	902	509	1.32	1.62	1.85	1867	1712	1436
(1.60)	(-)	(1210)	(484)	(-)	(2.62)	(4.04)	(-)	(2836)	(2767)
2.09	1138	701	397	1.85	2.31	2.80	1957	1883	1675
(2.10)	(-)	(1005)	(429)	(-)	(3.89)	(5.85)	(-)	(3790)	(3792)
3.04	725	449	238	2.78	3.55	4.22	2055	1842	1538
(3.05)	(-)	(667)	(360)	(-)	(5.89)	(8.30)	(-)	(3760)	(3999)
4.02	602	351	184	3.8	4.86	6.07	2078	1957	1720
(4.02)	(-)	(530)	(238)	(-)	(7.81)	(11.5)	(-)	(3871)	(3710)
5.91	417	256	147	-	-	-	2146	2129	2190
(5.93)	(-)	(329)	(178)	(-)	(11.9)	(17.2)	(-)	(3734)	(4064)
-	-	-	-	-	-	-	-	-	-
(9.55)	(-)	(229)	(133)	(-)	(19.1)	(28.3)	(-)	(4024)	(4860)

Table 4

Initial potentials, U_0, potentials at discharge, U_{ip}, and relative energy losses, $\Delta E/E_{0,calc}$, for the 4 mm spark gap at different conductivities, κ, with initially stored energy, E_0, as parameter.

The values refer to discharges with and (without) HDPE-liner.

κ, [mS/cm]	U_0, [V]			U_{ip}, [V]			$\Delta E/E_{0,calc}$, [%]		
	2 kJ	7 kJ	10 kJ	2 kJ	7 kJ	10 kJ	2 kJ	7 kJ	10 kJ
1.09	4305	7771	9253	4047	7680	9181	12	2.3	1.5
(1.09)	(4228)	(7644)	(9072)	(2849)	(7523)	(8957)	(55)	(3.1)	(2.5)
1.56	4222	7789	9263	3742	7706	9120	21	2.1	3.1
(1.59)	(4202)	(7683)	(9070)	(2714)	(7238)	(8801)	(58)	(11)	(5.8)
2.12	4211	7757	9216	3466	7444	8987	32	7.9	4.9
(2.10)	(4173)	(7649)	(9057)	(2673)	(7164)	(8752)	(59)	(12)	(6.6)
3.09	4192	7768	9197	3285	7423	8928	39	8.7	5.8
(3.07)	(4151)	(7614)	(6053)	(2646)	(7054)	(8635)	(59)	(14)	(9.0)
4.05	4166	7740	9212	3371	7352	35	35	9.8	5.1
(4.03)	(4124)	(7590)	(9039)	(2640)	(7070)	(8566)	(59)	(13)	(10)
5.94	4162	7743	9219	3350	7270	8827	35	12	8.3
(5.94)	(4100)	(7589)	(9028)	(2068)	(6889)	(8481)	(75)	(18)	(12)
9.63	4143	7736	9190	3299	7150	8725	37	15	9.9
(9.54)	(4138)	(7657)	(9132)	(2707)	(6802)	(8326)	(57)	(21)	(17)

Table 5

Initial potentials, U_0, potentials at discharge, U_{ip}, and relative energy losses, $\Delta E/E_{0,calc}$, for the 8 mm spark gap at different conductivities, κ, with initially stored energy, E_0, as parameter.

The values refer to discharges with and (without) HDPE-liner.

κ, [mS/cm]	U_0, [V]			U_{ip}, [V]			$\Delta E/E_{0,calc}$, [%]		
	2 kJ	7 kJ	10 kJ	2 kJ	7 kJ	10 kJ	2 kJ	7 kJ	10 kJ
0.56	-	7891	9381	-	7830	9276	-	1.5	2.2
(-)	(-)	(-)	(-)	(-)	(-)	(-)	(-)	(-)	(-)
1.08	-	7920	9295	-	7382	9046	-	13	5.3
(1.07)	(-)	(7792)	(-)	(-)	(6015)	(-)	(-)	(40)	(-)
1.58	-	7885	9299	-	7022	8723	-	21	12
(1.57)	(-)	(7750)	(-)	(-)	(5677)	(-)	(-)	(46)	(-)
2.09	-	7863	9249	-	6865	8651	-	24	13
(2.10)	(-)	(7678)	(-)	(-)	(5495)	(-)	(-)	(49)	(-)
3.07	-	7949	9371	-	6822	8660	-	26	15
(3.08)	(-)	(7642)	(-)	(-)	(5061)	(-)	(-)	(56)	(-)
4.03	-	7920	9390	-	6714	8534	-	28	17
(4.03)	(-)	(7590)	(-)	(-)	(4869)	(-)	(-)	(59)	(-)
5.97	-	7881	9324	-	6640	8341	-	29	20
(5.40)	(-)	(7600)	(-)	(-)	(4876)	(-)	(-)	(59)	(-)
-	-	-	-	-	-	-	-	-	-
(7.70)	(-)	(7476)	(-)	(-)	(5102)	(-)	(-)	(53)	(-)
9.59	-	7827	9286	-	6468	8154	-	32	23
(9.60)	(-)	(7146)	(-)	(-)	(4616)	(-)	(-)	(58)	(-)
-	-	-	-	-	-	-	-	-	-
(18.3)	(-)	(7500)	(-)	(-)	(4525)	(-)	(-)	(64)	(-)

Table 6

Initial potentials, U_0, potentials at discharge, U_{ip}, and relative energy losses, $\Delta E/E_{0,calc}$, for the 12 mm spark gap at different conductivities, κ, with initially stored energy, E_0, as parameter.

The values refer to discharges with and (without) HDPE-liner.

κ, [mS/cm]	U_0, [V]			U_{ip}, [V]			$\Delta E/E_{0,calc}$, [%]		
	7 kJ	10 kJ	16 kJ	7 kJ	10 kJ	16 kJ	7 kJ	10 kJ	16 kJ
1.09	8102	9531	11850	6517	8339	11030	35	23	13
(-)	(-)	(-)	(-)	(-)	(-)	(-)	(-)	(-)	(-)
1.57	7977	9429	11740	6005	7968	10800	43	29	15
(1.60)	(-)	(8328)	(11580)	(-)	(5158)	(9625)	(-)	(62)	(31)
2.09	7932	9418	11730	5827	7799	10620	46	31	18
(2.10)	(-)	(9143)	(11530)	(-)	(5234)	(9020)	(-)	(67)	(39)
3.04	7864	9354	11660	5849	7760	10660	45	31	16
(3.05)	(-)	(9051)	(11420)	(-)	(5122)	(8432)	(-)	(68)	(45)
4.02	7869	9354	11570	5581	7648	10450	50	33	18
(4.02)	(-)	(9006)	(11410)	(-)	(4867)	(8673)	(-)	(71)	(42)
-	-	-	-	-	-	-	-	-	-
(5.93)	(-)	(9004)	(11370)	(-)	(5089)	(8308)	(-)	(68)	(47)
-									
(9.55)	(-)	(9010)	(11410)	(-)	(4636)	(7646)	(-)	(74)	(55)

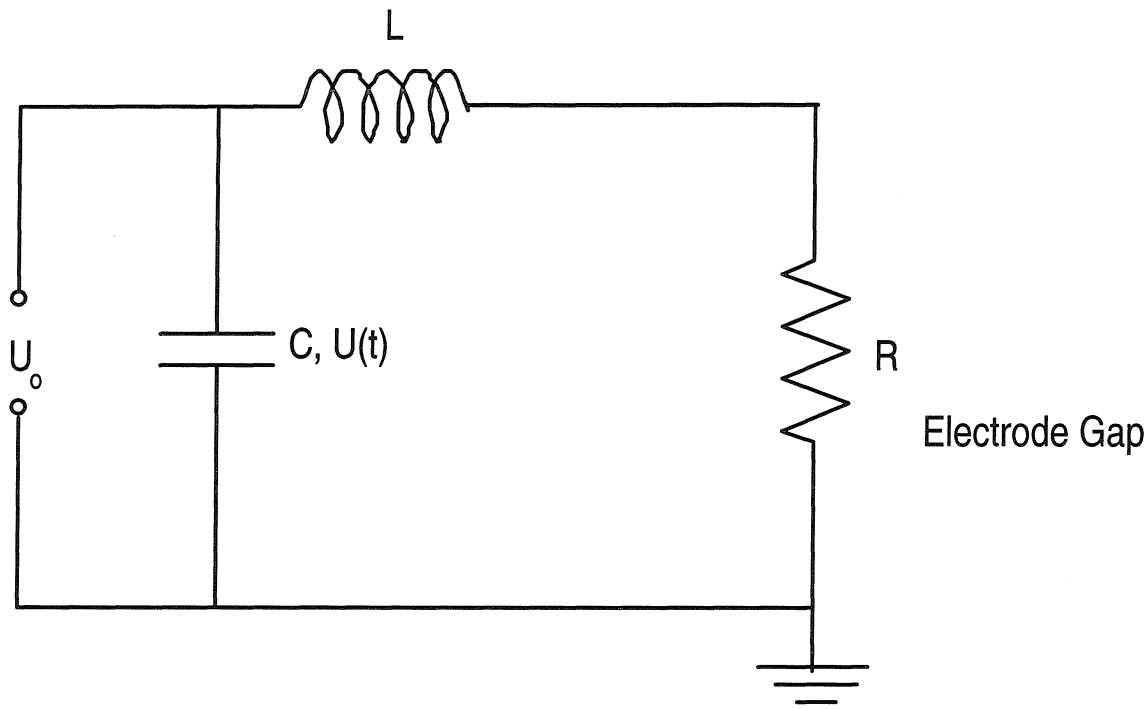

Fig. 1: Schematic LRC diagram for the EHD reactor.

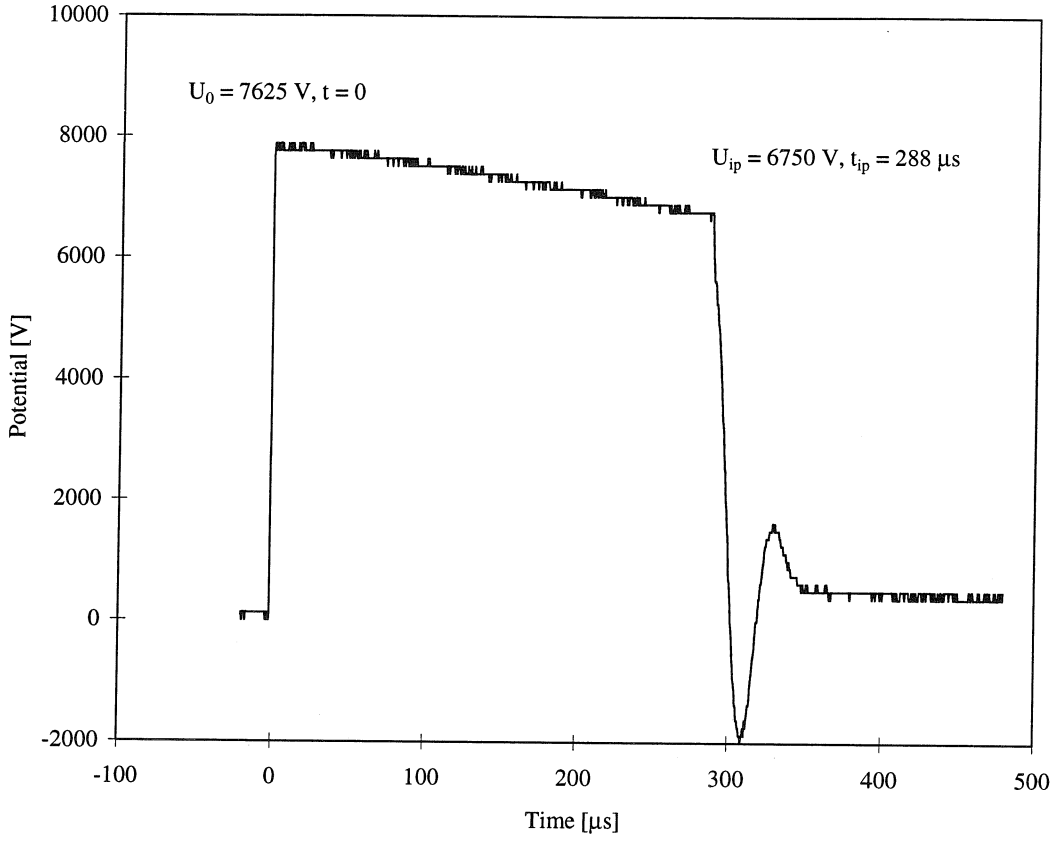

Fig. 2a: Voltage transient of an EHD event. Liner installed,

E_0 = 7 kJ, l = 8 mm, κ = 4.03 mS/cm.

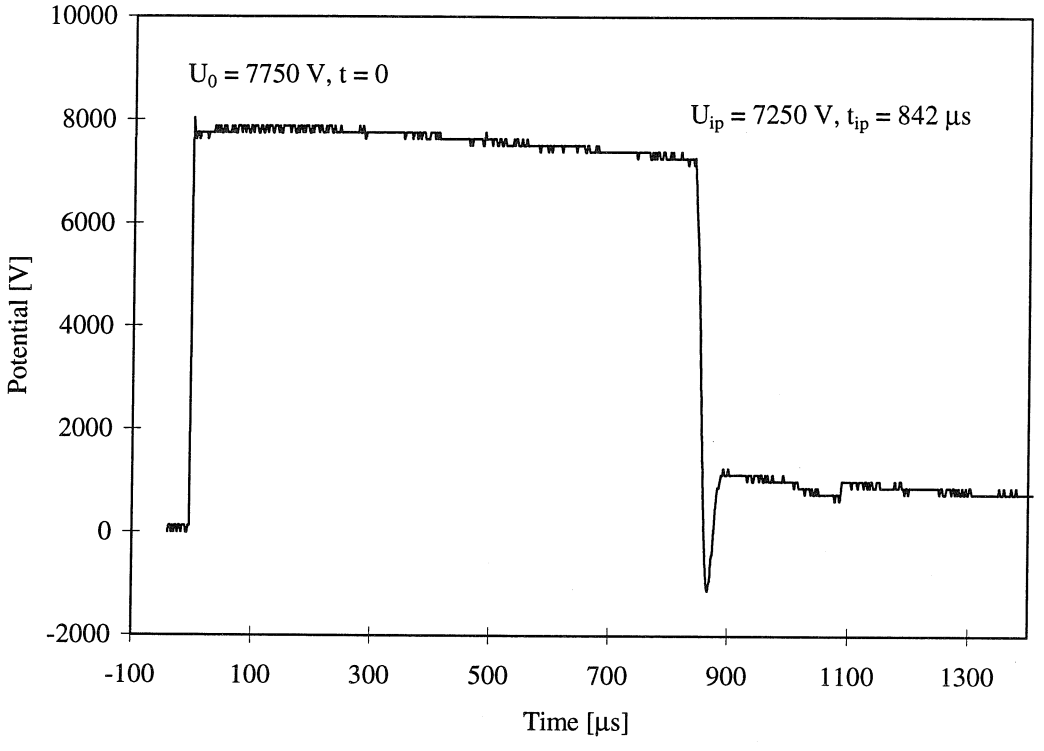

Fig. 2b: Voltage transient of an EHD event. Liner installed,

E_0 = 7 kJ, l = 8 mm, κ = 1.08 mS/cm.

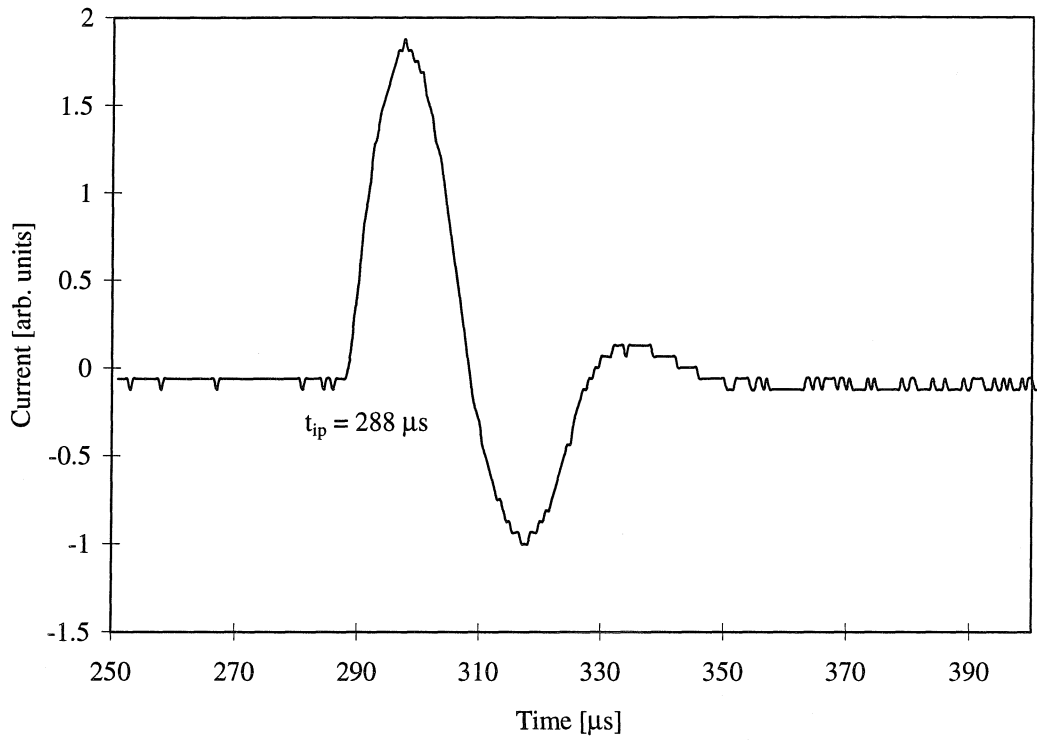

Fig. 3: Current transient of an EHD. Liner installed,

E_0 = 7 kJ, l = 8 mm, κ = 4.03 mS/cm.

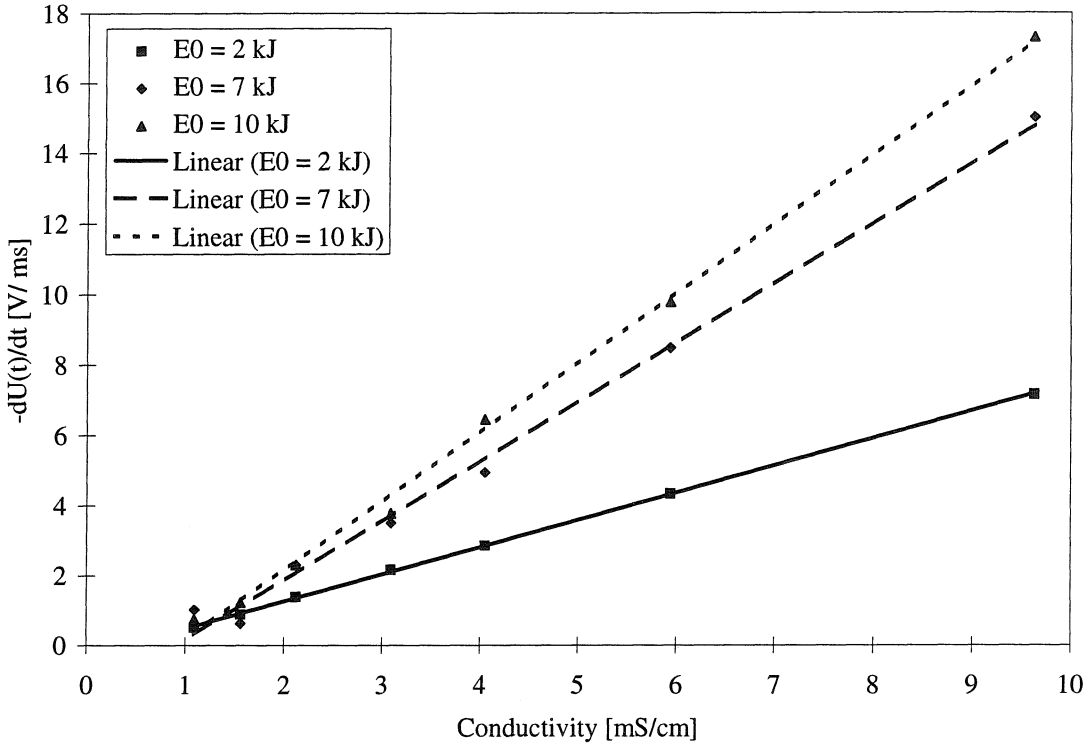

Fig. 4: Slope of the voltage transient, dU(t)/dt, as a function of the electrical conductivity of the solution. No liner installed, l = 4 mm.

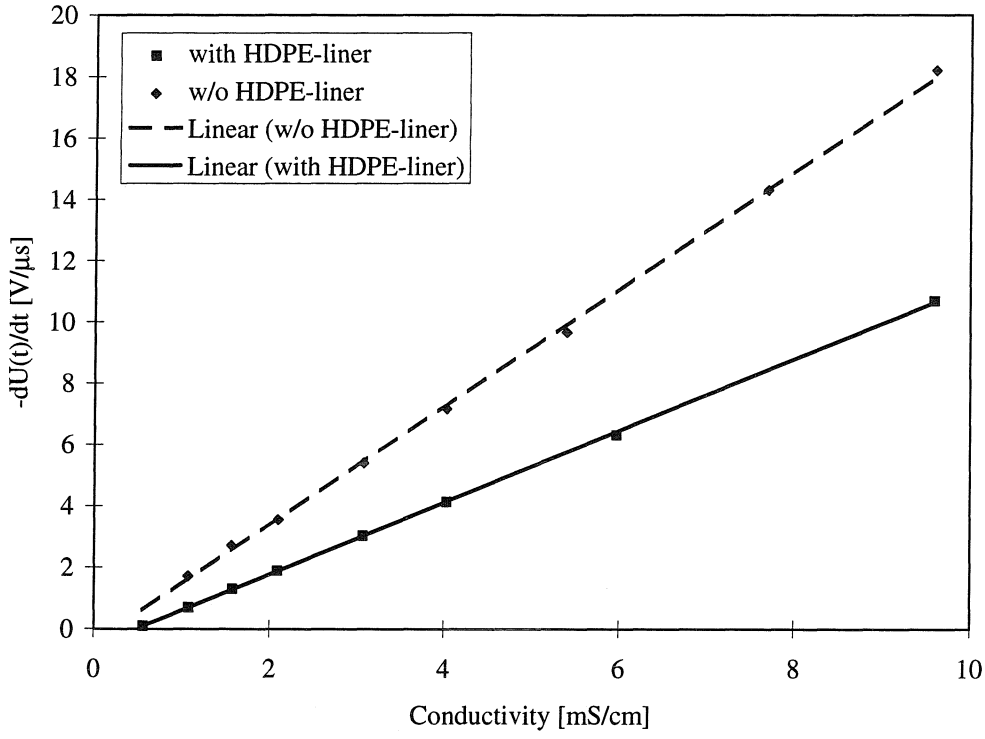

Fig. 5: Influence of an insulating HDPE-liner on the slope of the voltage transient.

E_0 = 7 kJ, l = 8 mm.

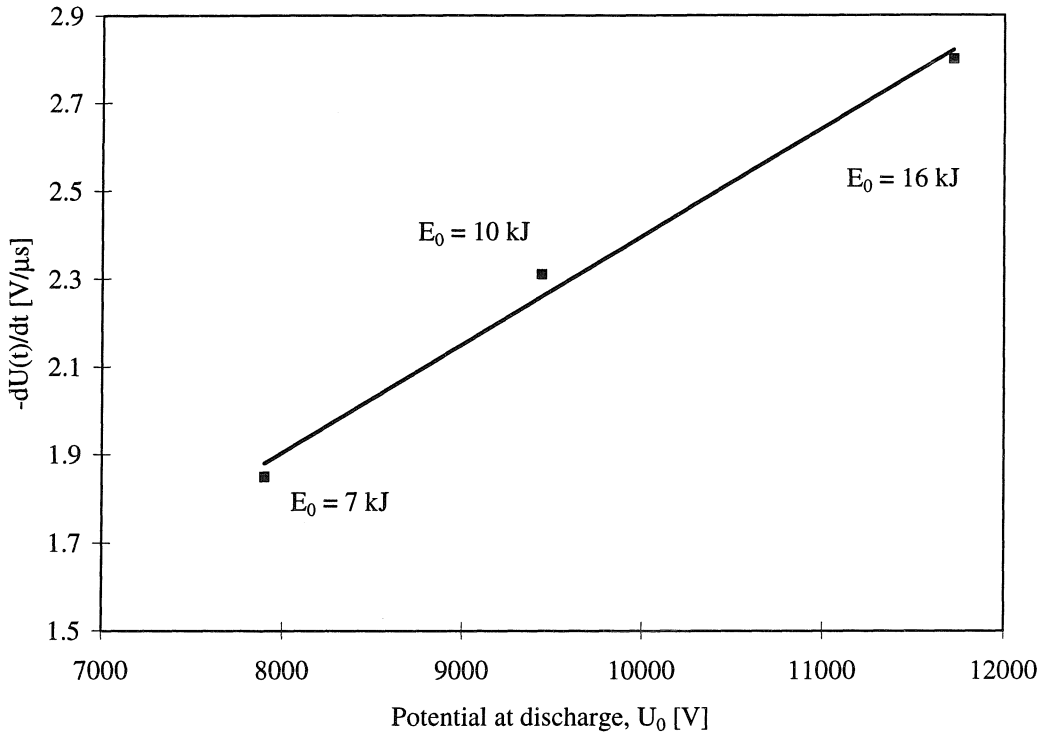

Fig. 6: Slope of the voltage transient as a function of the potential at discharge, U_{ip}. Liner installed, l = 12 mm, κ = 2.09 mS/cm.

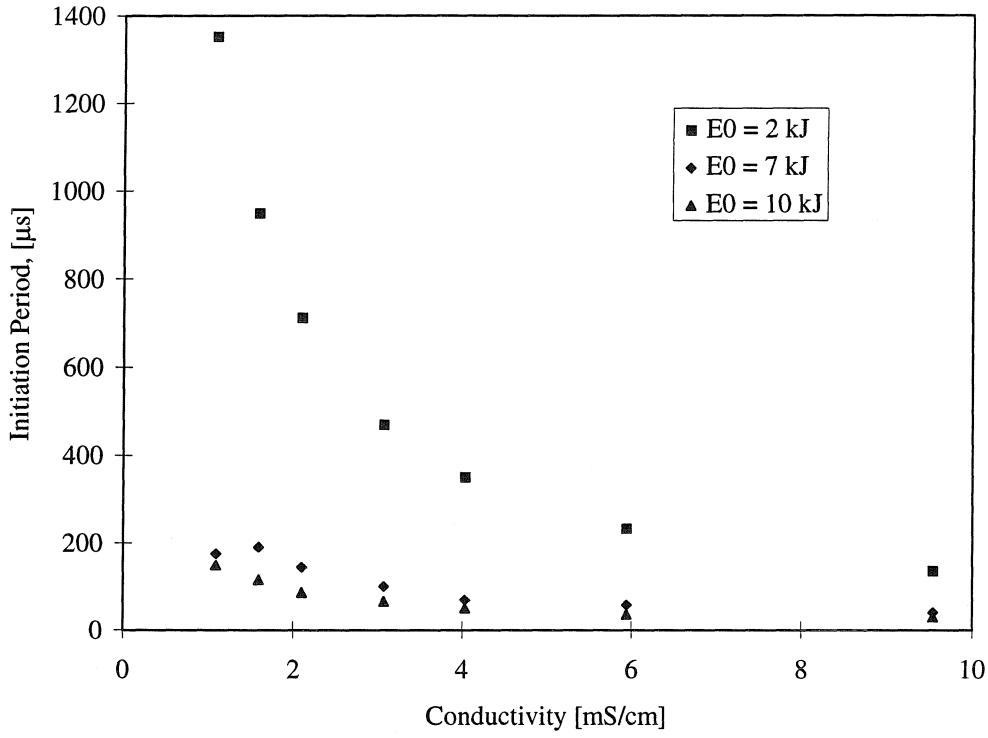

Fig. 7: Length of the initiation period as a function of electrical conductivity, with initial energy, E_0 as parameter. No liner installed, l = 4 mm.

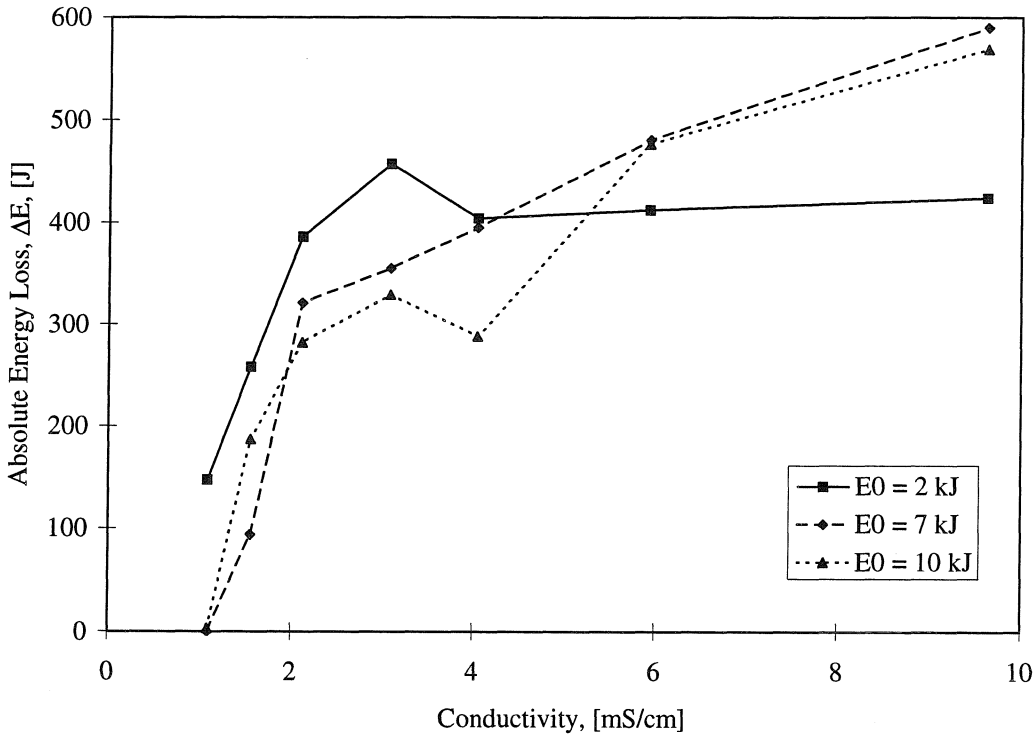

Fig. 8a: Absolute energy loss during the pre-breakdown period as a function of conductivity. Liner installed, l = 4 mm.

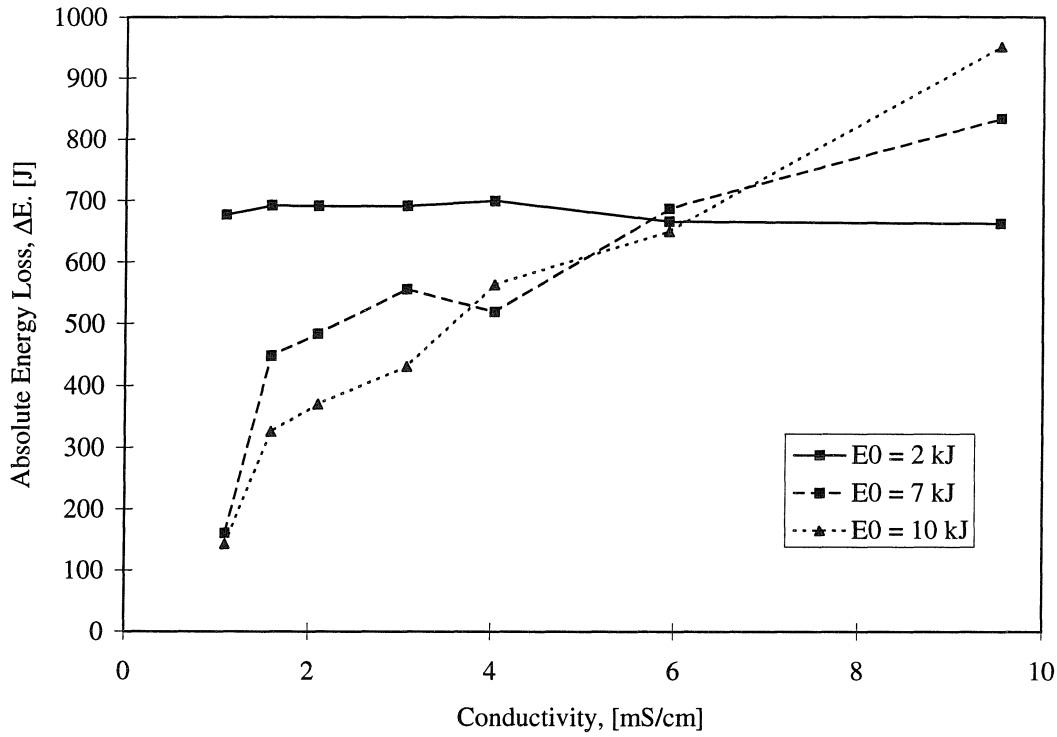

Fig. 8b: Absolute energy loss during the pre-breakdown period as a function of conductivity. No liner installed, l = 4 mm.

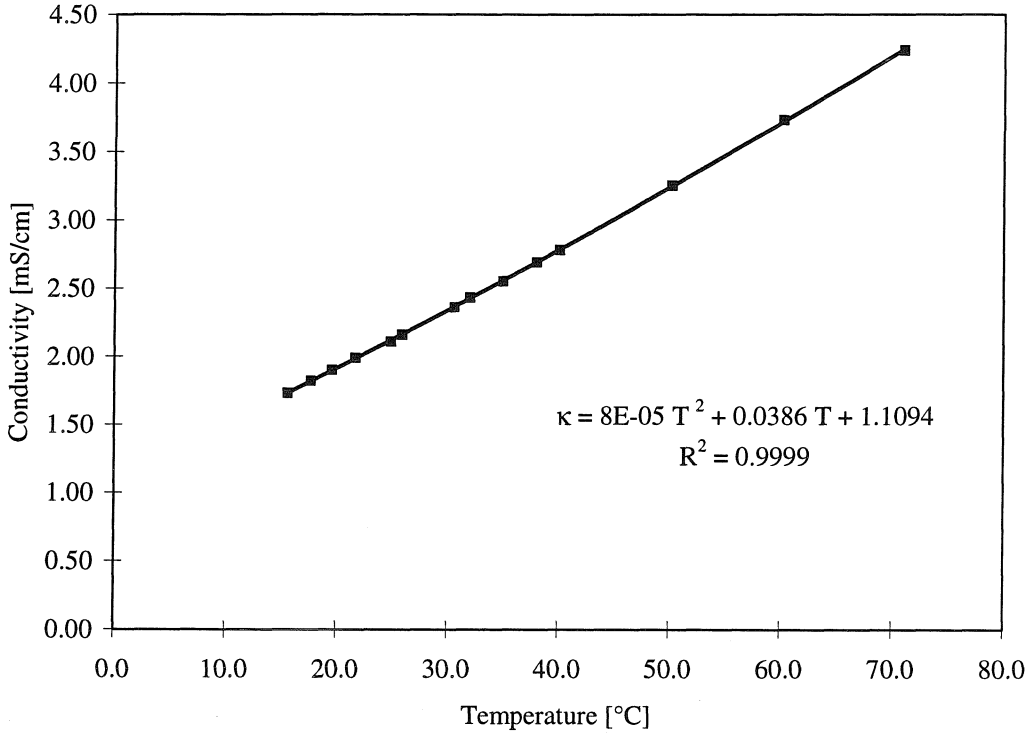

Fig. 9: Parabolic κ/T calibration curve.

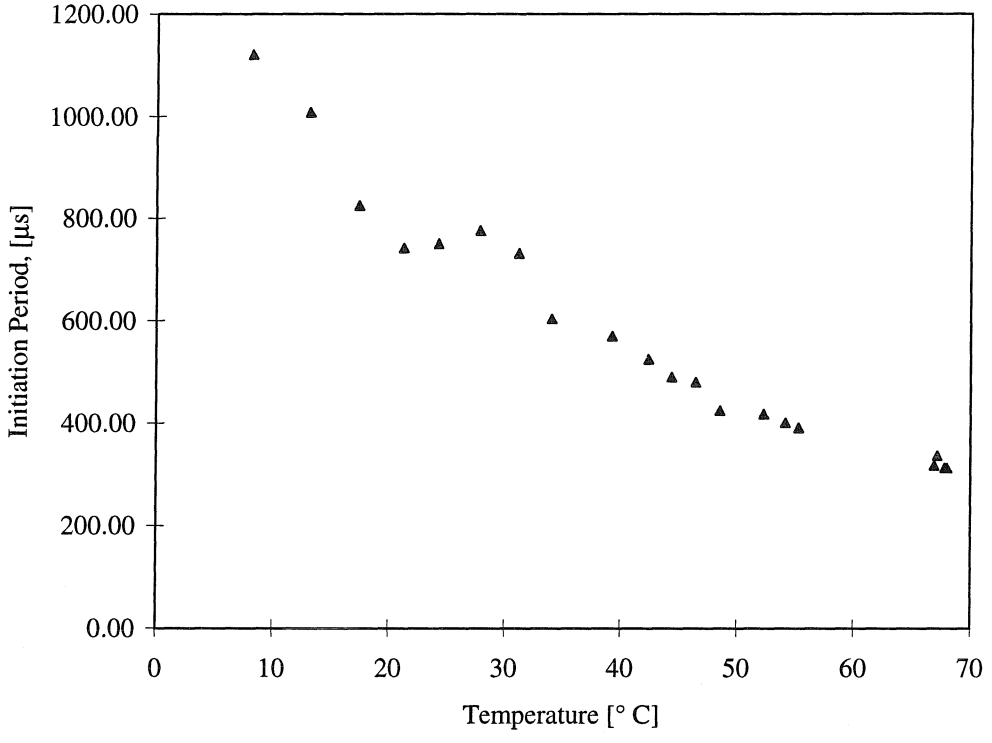

Fig. 10a: Initiation period as a function of solution temperature.

Liner is installed, E_0 = 7 kJ, l = 12 mm, κ = 2.08 mS/cm at room temperature.

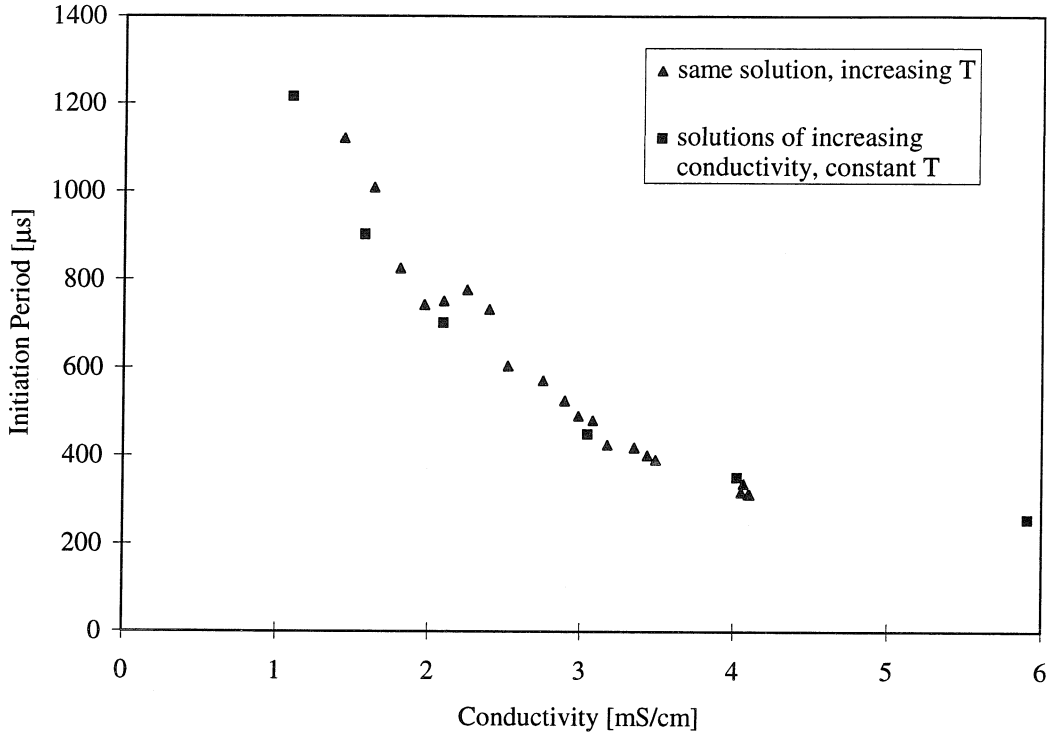

Fig. 10b: Initiation period as a function of solution conductivity.

Comparison between temperature and pure conductivity effect.

Liner is installed, E_0 = 7 kJ, l = 12 mm. The conductivity of the heated solution was 2.08 mS/cm at room temperature.

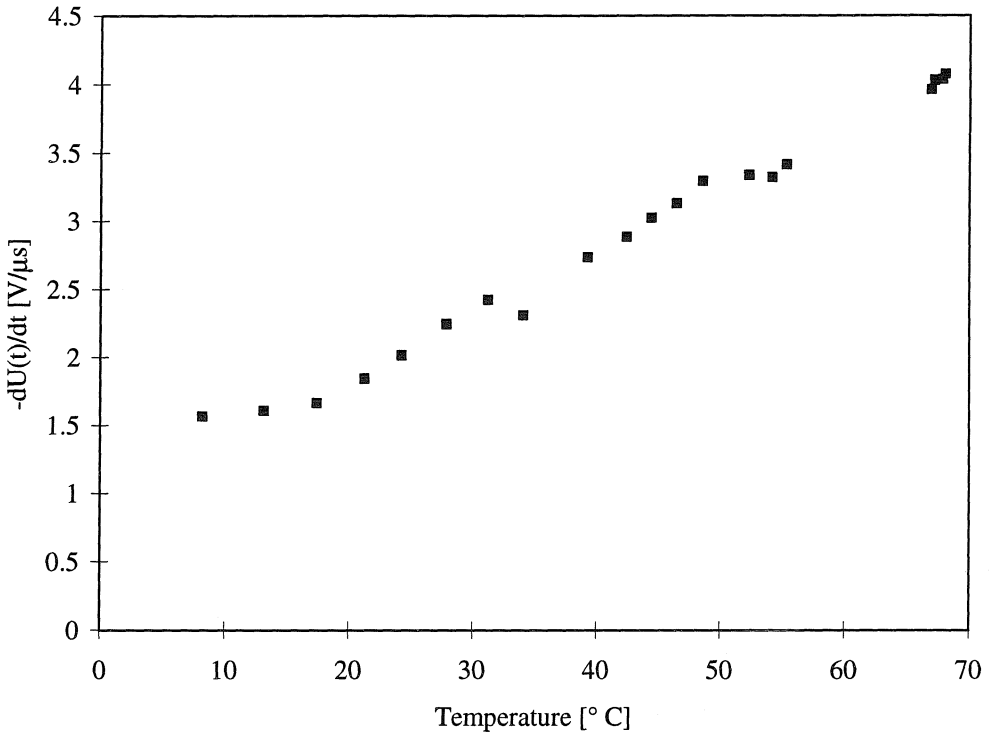

Fig. 11a: Slope of the voltage transient as a function of the solution temperature.

Liner is installed, E_0 = 7 kJ, l = 12 mm, κ = 2.08 mS/cm at room temperature.

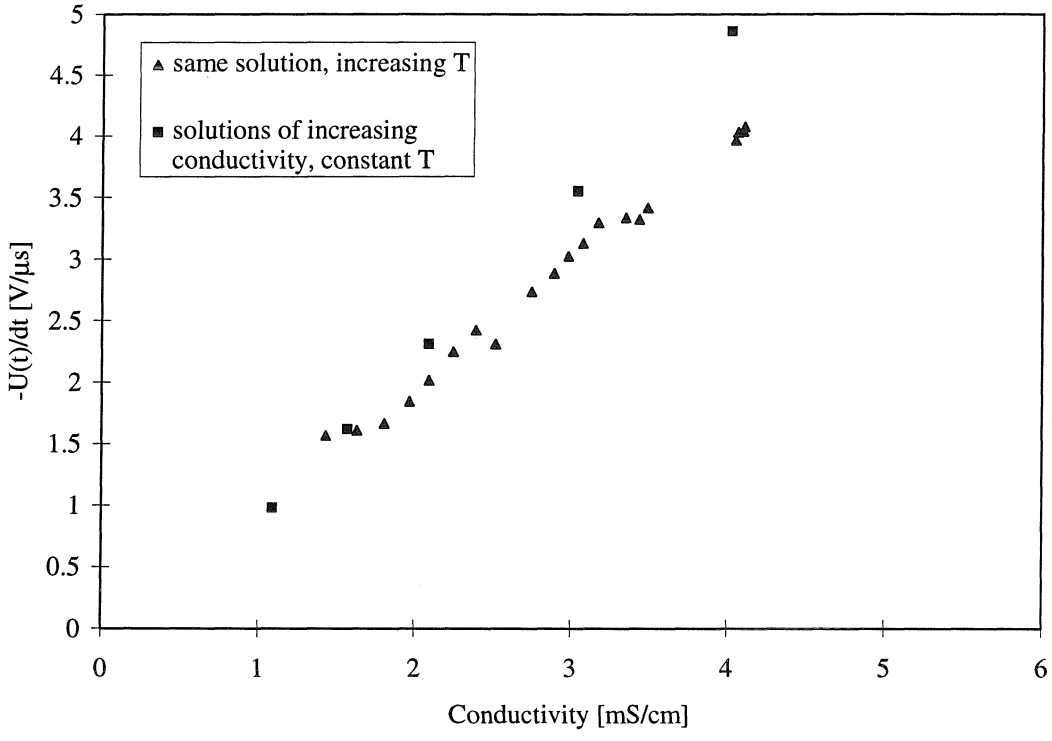

Fig. 11b: Slope of the voltage transient as a function of solution conductivity.

Comparison between temperature and pure conductivity effect.

Liner is installed, E_0 = 7 kJ, l = 12 mm. The conductivity of the heated solution was 2.08 mS/cm at room temperature.

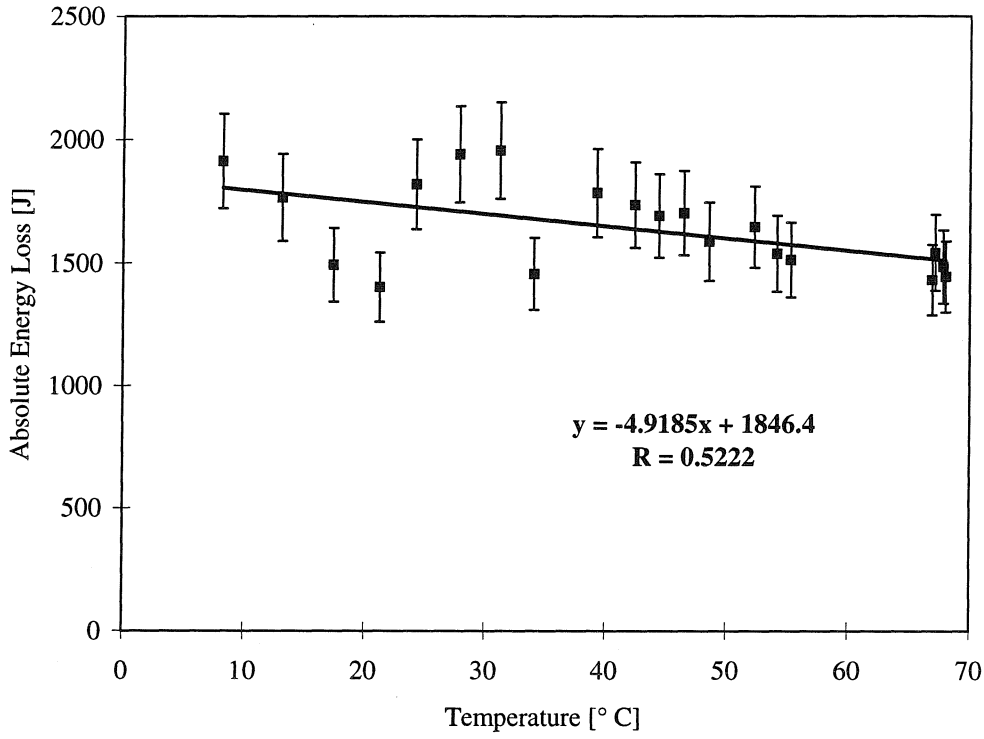

Fig. 12a: Absolute energy loss as a function of the solution temperature.

Liner is installed, E_0 = 7 kJ, l = 12 mm, κ = 2.08 mS/cm at room temperature.

Intercept at the 95 % confidence level: 1666 (low), 2027 (high).

Slope at the 95 % confidence level: -8.9 (low), -0.94 (high).

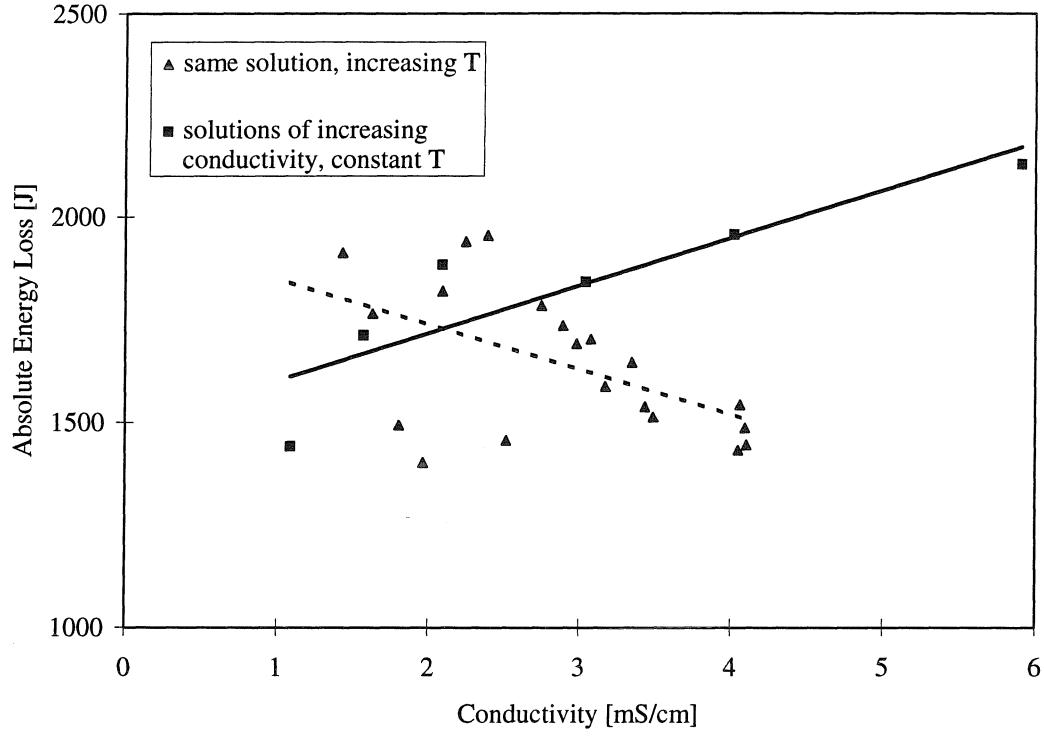

Fig. 12b: Absolute energy loss as a function of solution conductivity.

Comparison between temperature and pure conductivity effect.

Liner is installed, E_0 = 7 kJ, l = 12 mm. The conductivity of the heated solution was 2.08 mS/cm at room temperature.

- Chapter IX -

Conclusions

It has been shown that ultrasonically induced cavitation is capable of degrading a variety of chemical compounds, including p-nitrophenyl acetate, p-nitrophenol, 2,4,6-trinitrotoluene, 2,4-dinitrotoluene, 1,3,5-trinitrobenzene, 1,3-dinitrobenzene, and m-nitroaniline. The main degradation products are short-chain organic acids, nitrite, nitrate, and carbon dioxide. Depending on the substrate, different initial steps dominate the degradation reactions. The main degradation pathway for p-nitrophenol appears to be the pyrolytic cleavage of the carbon/nitrogen bond at the hot bubble/liquid interface. Trinitrotoluene and the other nitroaromatic compounds are preferentially attacked by hydroxyl radical which is generated in the cavitating aqueous solutions.

The sonochemical degradation of p-nitrophenol has been shown to be more energy efficient by a factor of approx. 20 in a parallel-plate near-field acoustical processor (NAP) when compared to the reaction in conventional probe-type reactors. The increased efficiency is ascribed to the larger surface area of the NAP which causes a larger fraction of the irradiated solution to cavitate. Also, the use of two different frequencies allow a greater number of bubbles to cavitate.

The ultrasonic degradation rate of a nitroaromatic compound appears to be proportional to the electron densitiy of its aromatic ring.

Pulsed-power discharges have the potential to become a new advanced oxidation technology. In this thesis the pre-breakdown energy losses during underwater pulsed-plasma discharges have been investigated. Circuit parameters such as the electrode gap length and the initial potential to which the capacitor bank is charged as well as the solution properties have a pronounced influence on the energy loss and the discharge characteristics. In order to maximize energy efficiency, treatment of real-life waste streams should be performed at elevated temperature in a chamber equipped with an insulating liner.

We believe direct photolysis plays the major role in the degradation of chemical compounds by pulsed-power discharges. It is therefore desirable to know the spectral distribution of the electromagnetic radiation during electrical discharges. This thesis summarizes the work towards the determination of the spectrum of the emitted light and an estimate of the plasma temperature is presented. It has been established that the electromagnetic radiation generated upon an underwater electrical discharge resembles radiation from a black-body source. A first-order estimation of the average plasma-arc temperature is given. The spectrum of the light flash has been measured using an optical multi-channel analyzer. Information about the generated radiation is essential to the further development of the EHD technology as a remediation technology, since its main chemical effects are caused by the emission of intense UV-light.

The EHD process exhibits energy efficiencies that are one to three orders of magnitude higher than the corresponding ultrasonic efficiencies. However, neither ultrasonic irradiation nor the EHD process have been optimized for maximum energy efficiency within the framework of this thesis. The EHD process has been shown to be capable of degrading various hazardous compounds. A rewarding next step in the develpoment of the EHD reactor is the optimization of the process with respect to energy efficiency.